



LUND UNIVERSITY

Detector Development, Source Characterization and Novel Applications of Laser Ion Acceleration

Senje, Lovisa

2017

Document Version:

Publisher's PDF, also known as Version of record

[Link to publication](#)

Citation for published version (APA):

Senje, L. (2017). *Detector Development, Source Characterization and Novel Applications of Laser Ion Acceleration*. [Doctoral Thesis (compilation), Atomic Physics]. Division of Atomic Physics, Department of Physics, Faculty of Engineering, LTH, Lund University.

Total number of authors:

1

General rights

Unless other specific re-use rights are stated the following general rights apply:

Copyright and moral rights for the publications made accessible in the public portal are retained by the authors and/or other copyright owners and it is a condition of accessing publications that users recognise and abide by the legal requirements associated with these rights.

- Users may download and print one copy of any publication from the public portal for the purpose of private study or research.
- You may not further distribute the material or use it for any profit-making activity or commercial gain
- You may freely distribute the URL identifying the publication in the public portal

Read more about Creative commons licenses: <https://creativecommons.org/licenses/>

Take down policy

If you believe that this document breaches copyright please contact us providing details, and we will remove access to the work immediately and investigate your claim.

LUND UNIVERSITY

PO Box 117
221 00 Lund
+46 46-222 00 00

DETECTOR DEVELOPMENT,
SOURCE CHARACTERIZATION AND
NOVEL APPLICATIONS OF
LASER ION ACCELERATION

Lovisa Senje

Doctoral Thesis
2017



LUND
UNIVERSITY

DETECTOR DEVELOPMENT,
SOURCE CHARACTERIZATION AND
NOVEL APPLICATIONS OF
LASER ION ACCELERATION

© 2017 Lovisa Senje
All rights reserved
Printed in Sweden by Media-Tryck, Lund, 2017

Division of Atomic Physics
Department of Physics
Faculty of Engineering, LTH
Lund University
P.O. Box 118
SE-221 00 Lund
Sweden

<http://www.atomic.physics.lu.se>

Lund Reports on Atomic Physics, LRAP 534

ISBN: 978-91-7753-192-0 (print)
ISBN: 978-91-7753-193-7 (pdf)
ISSN: 0281-2762



ABSTRACT

The main focus of the work presented in this thesis is on experimental studies of laser acceleration of protons and other positive ions from solid targets. The topic is explored from three different angles: firstly, the development of diagnostics adapted to the ion pulses, secondly, the characterization of the source of the energetic particles and, finally, the application of laser-accelerated protons for time-resolved radiolysis of glass and water.

Detectors that can efficiently record ion pulse parameters, such as the energy spectrum and spatial profile, were developed and implemented. One of these instruments was a modified version of a Thomson parabola spectrometer. Apart from the typical ion energy spectra provided by such an instrument, this modified diagnostic tool can also provide spatial information on pulse properties and on the spectrum of laser light transmitted through the laser-plasma interaction. The other diagnostic system developed and employed made use of plastic scintillators as a position-sensitive detector, to record either proton pulse profiles, or in combination with a dipole magnet, to record proton energy spectra, in a multiple-use, real-time feedback set-up. Laser acceleration of ions is a highly non-linear process and therefore pulse-to-pulse fluctuations are commonly large. When developing the detectors emphasis was thus placed on either being able to extract information about as many proton pulse parameters as possible simultaneously, or on being able to record large amounts of data efficiently (>100s of acquisitions over a few hours). Both these measures can be used to reduce the influence of pulse-to-pulse variations when analysing experimental results. However, they fulfil different needs, as the repetition rates of high-power lasers used for ion acceleration vary, from many laser pulses per second to one per hour or less.

To be able to control and optimize the processes that occur when energy is transferred in a plasma, from a high-intensity laser pulse to a population of energetic protons, it is vital to understand as much as possible about the acceleration mechanisms. The so-called sheath field, a \sim TV/m electric field, at the back of a solid target, in which the protons are accelerated to high energies is especially interesting. This sheath has been experimentally characterized in terms of its transverse expansion and the way in which this expansion influences the resulting proton pulse profile. It

was shown that for an angle of incidence between the laser pulse and the target foil of 45° , the transverse expansion of the sheath is asymmetric and its magnitude depends on the amount of energy contained in the laser pulse. Considerable correlation was found between the spatial properties of the laser pulse focus, the sheath and the resulting proton pulse. By splitting the laser pulse into two parts, and focusing them to two independent foci, separated by a few μm , it was possible to manipulate the shape of the sheath and thereby also the transverse divergence of the proton pulse.

Finally, experiments were performed on optically probed picosecond proton pulse radiolysis of various materials, such as glass and water. This was done by splitting each laser pulse so that one part drove an acceleration process, while the other part could be used as an intrinsically synchronised optical probe. The measurements were resolved in time by using a chirped optical probe pulse. It was found that exposure to a pulse of energetic protons, induced changes in the optical absorbance of the materials. Through these measurements it was also possible to obtain information about the proton pulse itself; in particular, the duration. Under the specific conditions used in that experiment and for a narrow energy bandwidth, the duration was found to be only 3.5 ± 0.7 ps. Compared to most other sources of high-energy protons, these laser-generated proton pulses can deliver extreme doses (kGy) in short (picosecond) pulses close to their source. In the pulsed proton radiolysis of water, indications were found that such a high dose rate affects the yield of solvated electrons, a radiolytic species.

POPULÄRVETENSKAPLIG

SAMMANFATTNING

Denna avhandling handlar om experimentella studier där kraftfulla laserpulser används till att accelerera partiklar, främst protoner, till höga energier. Det finns många olika användningsområden för högenergetiska protoner, till exempel strålbehandling inom cancerbehandling och för studier av olika materials egenskaper. Genom att studera hur protonerna accelereras av laserpulsen kan vi även bättre förstå hur intensivt ljus växelverkar med materia.

För att kunna överföra energi från laserpulsen till partiklar används ett plasma. Ett plasma är ett fjärde tillstånd för materia, förutom de tre mer välkända formerna: fast-, flytande- och gasform. Ett plasma består av negativt laddade elektroner och positiva joner, där den totala mängden positiva och negativa laddningar är lika stor. En laserpuls som är tillräckligt kraftfull kan frigöra elektroner från atomer och på så sätt skapa ett plasma. Beroende på vilket typ av material som dessa laserpulser växelverkar med och hur intensiv laserpulsen är, kan olika typer av partiklar accelereras. I några av de experiment som beskrivs i denna avhandling studeras laserbaserad elektronacceleration, men det är studier av protonacceleration som utgör grunden för avhandlingen. Då exponeras vanligtvis tunna folier, av exempelvis aluminium, som är monterade i vakuum, för laserljuset. Men faktum är att i den dominerande accelerationsprocessen i dessa fall accelereras inte partiklarna ifrån själva folien, utan ifrån ett tunt lager av vatten- och kolföreningar på baksidan av den. Om laserpulsen är tillräckligt kraftfull kommer redan den första delen av den att omvandla folien till ett plasma. Huvuddelen av laserpulsen, den mest intensiva delen, växelverkar därför med ett plasma. Genom olika processer i plasmat överförs energi från laserpulsen till elektroner. Dessa färdas sedan genom folien och fortsätter ut i vakuumet på baksidan av folien. Eftersom jonerna är kvar i plasmat uppstår en separation av de positiva och de negativa laddningarna och det byggs upp ett extremt starkt elektriskt fält. Detta fält är starkt nog att dela upp molekylerna i föreningarna i mindre beståndsdelar och på så sätt frigöra protoner som accelereras till höga energier i en mycket kort puls. En sådan protonpuls är väldigt kort, endast någon pico-sekund (miljondel av en miljondels sekund) men

kan innehålla hundratals miljarder protoner. De accelererade protonerna kan nå hastigheter som motsvarar någon eller några tiondelar av ljushastigheten. Denna accelerationsmekanism kallas på engelska för "Target Normal Sheath Acceleration" eller TNSA, och kan även användas till att accelerera tyngre joner.

Allt eftersom det har blivit tekniskt möjligt att producera mer och mer intensiva laserpulser har olika laserdrivna jonaccelerations-mekanismer observerats. För att kunna särskilja och nå djupare förståelse kring dessa mekanismer är det viktigt att det finns detektorer för de genererade partikelpulserna som är speciellt anpassade för detta ändamål. En del av denna avhandling beskriver utveckling av sådana detektorer. Med dessa kan jonpulsens egenskaper såsom energiinnehåll och spridning studeras. En typ av diagnostik som utvecklats, och finns beskriven i avhandlingen, är speciell då den möjliggör studier av dessa parameterar samtidigt. Den kan även ge information om vilka sorters joner, till exempel protoner (vätejoner) och koljoner, som accelererats. Att så mycket information som möjligt finns att tillgå för varje genererad puls är viktigt, eftersom variationerna från puls till puls av jonerna är stora.

I avhandlingen finns också beskrivet hur de laseraccelererade protonpulsernas egenskaper kan förändras genom att fördela laserpulsens energi på olika sätt, när den växelverkar med en metallfolie. Vi har studerat hur detta påverkar protonpulsens divergens. Vi ser då att vi aktivt kan öka eller minska divergensen, genom att manipulera laserpulsens. Vi har också lyckats visa att energin i laserpulsens påverkar hur det elektriska fältet på baksidan av folien utbreder sig längs med folien. Denna typ av studier har gjorts för att bättre förstå hur protonerna faktiskt accelereras, då detta leder till bättre kontroll över processen och kan möjliggöra bredare användningsområden.

Laserbaserade accelerators ger egenskaper till de högenergetiska protonerna, som skiljer sig från de protonpulser som genereras i andra, mer traditionella typer av accelerators. En är den mycket korta varaktigheten av protonpulserna som bildas. En unik möjlighet är att dela på laserpulsens och låta en del driva accelerationsprocessen och använda den andra för diagnostik. Då protonpulsens är kort, endast någon miljondel av en miljondels sekund, men perfekt synkroniserad i tiden med den del av laserpulsens som används till diagnostik går det att nå mycket hög tidsupplösning. Slutligen diskuteras i avhandlingen hur detta har utnyttjats till att studera hur olika material reagerar när de utsätts för högenergetisk protonstrålning. Speciellt intressant är hur vatten absorberar energi från protoner, eftersom vi som människor består till stor del av just vatten. I de studier vi genomfört där vatten exponerats för en protonpuls, kan vi se tecken på att processerna som sker i vattnet när protonerna passerar förändras om tillräckligt mycket energi deponeras på tillräckligt kort tid.

LIST OF PUBLICATIONS

Papers I to VI present the work on which the main part of this thesis is based. Papers VII to IX present work related to Appendix A.

I Diagnostics for studies of novel laser ion acceleration mechanisms

L. Senje, M. Yeung, B. Aurand, S. Kuschel, C. Rödel, F. Wagner, K. Li, B. Dromey, V. Bagnoud, P. Neumayer, M. Roth, C.-G. Wahlström, M. Zepf, T. Kuehl, & D. Jung.

Review of Scientific Instruments **85**, 113302 (2014).

II A setup for studies of laser-driven proton acceleration at the Lund Laser Centre

B. Aurand, M. Hansson, L. Senje, K. Svensson, A. Persson, D. Neely, O. Lundh, & C.-G. Wahlström.

Laser and Particle Beams **33**, 0263-0346/14 (2015).

III Manipulation of the spatial distribution of laser-accelerated proton beams by varying the laser intensity distribution

B. Aurand, L. Senje, K. Svensson, M. Hansson, A. Higginson, A. Gonoskov, M. Marklund, A. Persson, O. Lundh, D. Neely, P. McKenna, & C.-G. Wahlström.

Physics of Plasmas **23**, 023113 (2016).

IV Transverse expansion of the electron sheath during laser acceleration of protons

K. Svensson, F. Mackenroth, L. Senje, A. Gonoskov, C. Harvey, B. Aurand, M. Hansson, A. Higginson, M. Dalui, O. Lundh, P. McKenna, A. Persson, M. Marklund, & C.-G. Wahlström.

Manuscript.

- V **Experimental investigation of picosecond dynamics following interactions between laser accelerated protons and water**
L. Senje, M. Coughlan, D. Jung, M. Taylor, G. Nersisyan, D. Riley, C. L. S. Lewis, O. Lundh, C.-G. Wahlström, M. Zepf, & B. Dromey.
Accepted for publication in Applied Physics Letters, (2017).
- VI **Picosecond metrology of laser-driven proton bursts**
B. Dromey, M. Coughlan, L. Senje, M. Taylor, S. Kuschel, B. Villagomez-Bernabe, R. Stefanuik, G. Nersisyan, L. Stella, J. Kohanoff, M. Borghesi, F. Currell, D. Riley, D. Jung, C.-G. Wahlström, C. L. S. Lewis, & M. Zepf.
Nature Communications 7, 10642 (2016).
- VII **Supersonic jets of hydrogen and helium for laser wakefield acceleration**
K. Svensson, M. Hansson, F. Wojda, L. Senje, M. Burza, B. Aurand, G. Genoud, A. Persson, C.-G. Wahlström, & O. Lundh.
Physical Review Accelerators and Beams 19, 051301 (2016).
- VIII **Dynamics of ionization-induced electron injection in the high density regime of laser wakefield acceleration**
F. G. Desforges, B. S. Paradkar, M. Hansson, J. Ju, L. Senje, T. L. Audet, A. Persson, S. Dobosz-Dufrénoy, O. Lundh, G. Maynard, P. Monot, J.-L. Vay, C.-G. Wahlström, & B. Cros.
Physics of Plasmas 21, 120703 (2014).
- IX **Enhanced stability of laser wakefield acceleration using dielectric capillary tubes**
M. Hansson, L. Senje, A. Persson, O. Lundh, C.-G. Wahlström, F. G. Desforges, J. Ju, T. L. Audet, B. Cros, S. Dobosz Dufrénoy, and P. Monot.
Physical Review Special Topics Accelerators and Beams 17, 031303 (2014).

CONTENTS

1	Introduction	1
1.1	Motivation for this Work	2
1.2	Outline of this Thesis	3
2	Laser Ion Acceleration – The Physics and Techniques Involved	5
2.1	Electron Motion	5
2.1.1	A Single Electron in an Electromagnetic Wave	5
2.2	Laser Plasmas	6
2.2.1	Field Ionization	6
2.2.2	Ponderomotive Force	8
2.2.3	Overdense and Underdense Plasmas	9
2.2.4	Relativistic Transparency	10
2.2.5	Electron Heating Mechanisms	10
2.3	Ion Motion	11
2.3.1	Acceleration Schemes	11
2.3.2	Ion Propagation in Matter	15
2.4	Experimental Techniques	16
2.4.1	High Intensity Lasers	16
2.4.2	Focusing High Intensity Laser Pulses on Thin Foils	20
2.4.3	Diagnostics and Detectors	21
3	Experiments and Results	27
3.1	Detector Development and Related Techniques	27
3.1.1	The Online Magnetic Spectrometer	27
3.1.2	Online Spatial Profile Monitor	30
3.1.3	Modified Thomson Parabola Spectrometer	32
3.1.4	Laser Focus Optimization and Target Alignment	33
3.2	Proton Source Characterization	34
3.2.1	Split Mirror Setup	34
3.2.2	Temporal Effects on Proton Pulses Generated with a Pair of Laser Pulses	36
3.2.3	Characteristics of Proton Energy Spectra for Different Target Thicknesses	38
3.3	Novel Applications	39
3.3.1	Pump-Probe Set-up for Time-Resolved Radiolysis	41

4	Outlook	45
4.1	Future Applications	45
4.2	Laser Development	46
4.3	Target Development	47
4.4	Development of Laser Ion Acceleration	48
A	Laser Wakefield Acceleration of Electrons	51
A.1	Laser Acceleration of Electrons from a Plasma	51
A.2	Laser Wakefield Acceleration in Dielectric Capillaries	53
A.3	Densities in Supersonic Gas Flows for Laser Wakefield Acceleration	54
B	Mathematical Description of Electron in Electromagnetic Field	57
B.1	The Lorentz Force for a Relativistic Particle	57
B.2	Motion of Single Electron in Infinite, Plane, Linearly Polarized Wave	59
	The Author's Contributions to the Papers	63
	Acknowledgments	67
	References	69
	Papers	81
	Papers	83
I	Diagnostics for studies of novel laser ion acceleration mechanisms	83
II	A setup for studies of laser-driven proton acceleration at the Lund Laser Centre	91
III	Manipulation of the spatial distribution of laser-accelerated proton beams by varying the laser intensity distribution	99
IV	Transverse expansion of the electron sheath during laser acceleration of protons	109
V	Experimental investigation of picosecond dynamics following interactions between laser accelerated protons and water	115
VI	Picosecond metrology of laser-driven proton bursts	123
VII	Supersonic jets of hydrogen and helium for laser wakefield acceleration	131
VIII	Dynamics of ionization-induced electron injection in the high density regime of laser wakefield acceleration	139
IX	Enhanced stability of laser wakefield acceleration using dielectric capillary tubes	147

INTRODUCTION

This thesis describes experimental studies in which high-intensity laser pulses interact with solid and gas targets. Charged particles can be accelerated to high energies in such interactions and most of the work presented here concerns laser acceleration of protons. To understand the acceleration process and how it affects the properties of the resulting energetic particles, many different areas of physics must be considered, among them intense laser pulses, plasma physics and relativistic particle dynamics.

There are three well-known states of matter: solid, liquid and gaseous. However, when accelerating particles with a laser pulse a fourth state of matter becomes important, plasma. A plasma consists of both positive ions and electrons, and is globally charge neutral. Plasmas are found in every-day life, for example in fluorescent lamps and more spectacularly in lightning. Plasmas also exist in the sun and other stars, in interstellar and intergalactic media. A plasma can also be created by a laser pulse that is so intense that it strips electrons from the atoms in a material. If a laser pulse, propagating towards a material through vacuum is sufficiently intense, the leading edge of the pulse will ionize the material. The most intense part of the pulse then interacts with the plasma formed. Different processes may occur depending on the density profile of the plasma. For high-density plasmas, usually created in interactions between solid targets and high-intensity laser pulses, the laser pulse can drive acceleration processes, resulting predominately in energetic positive ions [1, 2]. Laser interactions with plasmas of lower densities, originating, for example, from gaseous targets, are more commonly used for the generation of high-energy electrons [3]. To efficiently accelerate charged particles, both electrons and protons, laser pulses with ultra-high intensities ($> 10^{18}$ W/cm²) are desirable.

The first laser light reported was produced by a pulsed ruby laser in 1960 [4]. Early ruby lasers typically produced pulses with durations of the order of milliseconds and energies of the order of 1 J [5], leading to pulse peak power on the kilowatt level or slightly higher. Rapid progress in laser development over the past fifty years has led to lasers that can produce pulses with terawatt (TW) and even petawatt (PW)

peak power, 12 orders of magnitude higher than the earliest lasers. To achieve ultra-high intensities, not only a high-power laser pulse is required, it is also necessary to focus it to a very small, microscopic size. If a solid or gaseous target is placed at the focus of the laser pulse, a plasma is generated. Through the processes that will be discussed in the following chapters, a directional electric field can be generated in the plasma, where energy can be transferred from the laser pulse to a population of energetic particles.

An electron is nearly 2000 times lighter than a proton. This means that an electron travelling at 2000 m/s has a similar kinetic energy to a proton with a velocity of only 45 m/s. The theory of relativity, as proposed by Albert Einstein, states that nothing can move faster than the speed of light. When a particle approaches this velocity it is said to become relativistic, and the classical relation that states that an object's velocity is proportional to the square root of its kinetic energy is no longer valid. Due to their different rest masses, a proton and an electron approach the speed of light at very different energies. In particle accelerators energy is usually transferred to particles, such as electrons and protons, with radiofrequency electric fields. However, energy can also be transferred from a very intense laser pulse. This is especially efficient for electron acceleration since electrons become relativistic at lower energies, and can co-propagate with the laser pulse, in particular with a plasma wave created behind the laser pulse in a low-density plasma, which then can continue to transfer energy to the electrons. In the case of laser-driven proton acceleration, no one has yet managed to reach relativistic energies and therefore the time window in which energy can be transferred from the laser pulse is limited approximately by the laser pulse duration. This means that it is vital to fully understand and control the acceleration process, so that the energy transfer can be maximized. High-energy protons and good control of the acceleration process broadens the range of potential applications of laser-accelerated protons.

1.1 Motivation for this Work

Laser-accelerated particles have unique properties. Pulses of protons only a few picoseconds long have been measured [6], and radioactive doses up to the kGy level can be delivered, close to the source of the pulse, in, for example water, leading to extreme dose rates that are not feasible with conventional proton sources. If a laser pulse is split into two parts and one part is used to drive the acceleration process, the other part can be used as an intrinsically synchronized probe pulse. Laser-accelerated protons thus provide a unique opportunity for optically probed radiolysis of transparent materials, motivating the experimental studies described in Papers V and VI.

As a result of advances in laser technology, leading not only to laser pulses of extremely high intensity, but also improved quality and reproducibility, novel ion acceleration mechanisms have been proposed and tested. Different mechanisms

produce ion pulses with different characteristics, in terms of their energy spectrum and spatial profile. In order to understand what mechanisms that contribute under different conditions, it is important that detectors can record a wide range of parameters. Since pulse-to-pulse fluctuations are usually large for the ion pulses, it is particularly beneficial if parameters such as the energy spectrum and spatial profile, can be recorded simultaneously. The need for suitable detection systems motivated the work presented in Papers I and II.

Increased knowledge about the source of laser-accelerated protons is vital to be able to control the acceleration process. Such knowledge can be obtained by temporally and spatially modifying the focus of the laser pulse before it interacts with a solid target, and monitoring the resulting proton pulse. This is due to the fact that the source characteristics, the laser pulse properties and proton pulse parameters are all closely correlated. This provided the motivation for the experiments discussed in Papers III and IV.

1.2 Outline of this Thesis

After this brief introduction, a short summary of the field of laser-driven ion acceleration, in terms of theoretical background, experimental methods and detectors, is given, followed by a description of the laser systems used in the experiments. An important part of all experimental work is optimization of the detection system for the specific task. Therefore, part of this thesis, together with Papers I and II, describes the development and implementation of detectors that can contribute to a better understanding of the acceleration process itself, and the parameters of the particle pulse. Another part, together with Papers III and IV, is dedicated to the experiments performed to characterize the source of the energetic particles. The final part of this thesis describes experiments in which laser-accelerated protons were used for pulsed radiolysis of glass and water. A more detailed explanation and analysis of the results obtained are given in Papers V and VI. A short introduction to laser wakefield acceleration of electrons, and to Papers VII to IX, is given in Appendix A.

LASER ION ACCELERATION – THE PHYSICS AND TECHNIQUES INVOLVED

Laser-driven ion acceleration has been explored for several decades and the knowledge accumulated, in terms of theory and experimental techniques, is considerable. The aim of this chapter is to put the work presented in the papers and in later chapters of this thesis into context. It starts with a brief overview of the physics related to laser-driven ion acceleration, then discusses some of the most common experimental methods and diagnostics, as well as the high-power lasers with which the experimental work leading to this thesis was performed.

2.1 Electron Motion

2.1.1 A Single Electron in an Electromagnetic Wave

A charged particle in an electromagnetic field, such as the field of a laser pulse, is affected by the Lorentz force:

$$\mathbf{F} = q(\mathbf{E} + \mathbf{v} \times \mathbf{B}), \quad (2.1)$$

where q is the charge of the particle, \mathbf{E} the electric field, \mathbf{v} the velocity and \mathbf{B} the magnetic field. This is also valid for relativistic particles (see App. B for a mathematical description). The relation between the electric and magnetic fields for a plane wave in vacuum is given by $|\mathbf{E}| = c|\mathbf{B}|$ and it can thus be deduced from Eq. 2.1 that the second term of the equation is only significant for very high particle velocities, i.e. relativistic particles.

A laser field can be described by its normalized vector potential, \mathbf{a} . Here, a scalar potential, ϕ , and vector potential, \mathbf{A} , are used to define the electromagnetic field as $\mathbf{E} = -\frac{\partial \mathbf{A}}{\partial t} - \nabla \phi$ and $\mathbf{B} = \nabla \times \mathbf{A}$. The expression for \mathbf{a} is given by:

$$\mathbf{a} = \frac{q\mathbf{A}}{mc}, \quad (2.2)$$

where m is the mass of the particle and c the speed of light. The amplitude of the normalized vector potential, a_0 , is a useful parameter to characterize the intensity of a laser pulse, I_1 , and can be calculated through:

$$a_0 \approx 0.86\lambda [\mu\text{m}] \sqrt{I_1 [10^{18}\text{W}/\text{cm}^2]}. \quad (2.3)$$

One reason why this is a convenient choice of parameter is because electrons exposed to the laser field oscillate with relativistic velocities if $a_0 > 1$.

For an infinite, plane wave travelling in the z -direction, and linearly polarized in the y -direction, the motion of a single electron in the field can be derived analytically (see App. B). The motion in a stationary frame is given as a function of time, t , by the expression:

$$\begin{aligned} y(t) &= \frac{ca_0}{\omega_1} \sin(\omega_1 t), \\ z(t) &= \frac{ca_0^2}{4} \left(\frac{1}{2\omega_1} \sin(2\omega_1 t) + t \right), \end{aligned} \quad (2.4)$$

where ω_1 is the laser frequency. This motion is illustrated in Fig. 2.1 for different values of a_0 and also given in a time frame co-moving with the wave. If the motion is averaged over an optical cycle, the drift velocity, v_D , in the z -direction is given by:

$$v_D = \frac{ca_0^2}{4 + a_0^2}. \quad (2.5)$$

As can be seen in Fig. 2.1, the drift velocity approaches c for large values of a_0 . For an intense laser pulse with a finite duration, a_0 varies from zero to its maximum value (corresponding to the peak intensity of the laser pulse) and back to zero. This means that the electron can be displaced from the drift in the field, but it will have no net energy gain.

2.2 Laser Plasmas

2.2.1 Field Ionization

A plasma is defined as a state of matter in which all the atoms have been ionized, it is globally charge neutral, and displays collective effects. These collective effects form the basis for laser-plasma acceleration of particles, where energy is transferred from an

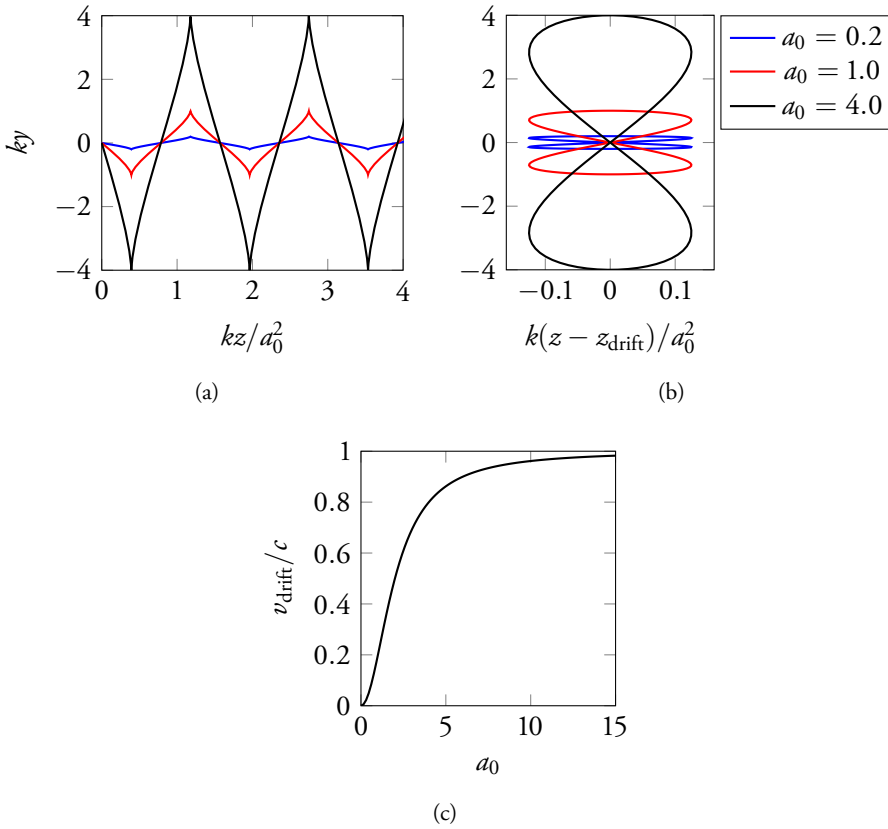


Figure 2.1 Motion of an electron in an electromagnetic wave

(a) Motion of a single electron in an infinite, plane wave, travelling along the z -direction, and polarized in the y -direction, seen from a stationary reference frame, for three different values of a_0 . k is the wavenumber and the other parameters are defined in the text. (b) As in (a) but in a reference frame co-propagating with the drift velocity of the electron along z . (c) Drift velocity along the z -axis, normalized to c , for different values of a_0 .

electromagnetic wave to particles. When a laser pulse of sufficiently high intensity interacts with a material it ionizes the atoms and/or molecules, creating a globally charge-neutral plasma consisting of positive ions and electrons. The laser intensity required depends on how strongly the electrons are bound to the atoms and varies from material to material. For free atoms and ions this process can be regarded as the potential of the electric field of the laser light suppressing the Coulomb potential of the atom or ion, in which the electrons are bound. If the laser field can suppress the potential below the ionization energy, the electron will escape and the atom becomes field ionized. The laser intensity at which this occurs is called the appearance intensity, I_{app} , and is related to the ionization energy of the atom or ion, E_{ion} , through

the relation:

$$I_{\text{app}} = \frac{c\epsilon_0^3\pi^2 E_{\text{ion}}^4}{2Z^2 e^6}, \quad (2.6)$$

where c denotes the speed of light, e the elementary charge, ϵ_0 the permittivity of free space, and Z the charge state of the created ion [7]. In the majority of the experiments described later in this thesis, laser interaction with solid aluminium foil targets was studied. When the leading edge of an intense laser pulse ionizes a solid target creating a plasma, it starts to expand. In this expanding plasma, field ionization contributes strongly to the highest charge state achieved, whereas in the bulk of the target, collisional ionization dominates [8, 9]. The peak pulse intensity from the Lund TW laser is approximately $4 \cdot 10^{19}$ W/cm² (depending on focusing optics). Ionization of outer electrons of aluminium occur before the most intense part of such laser pulse arrives at the target, and this part of the pulse therefore interacts with a plasma.

2.2.2 Ponderomotive Force

To achieve the highest possible intensity with a high-power laser pulse, it is necessary to focus it. In the experimental studies on laser interaction with solid targets discussed in this thesis, a laser focus spot size of a few to ten micrometres at full width half maximum of the intensity was typically achieved. When assuming a Gaussian intensity distribution in the focal plane, the radial intensity gradients are large. If such a laser pulse interacts with a plasma, electrons will be driven away from regions of high intensity by the so-called ponderomotive force, F_p . In a simplified picture, this can be viewed as an iterative process in which the high-amplitude electric field in the most intense region of the laser focus displaces the electron into a region with lower intensity and lower field amplitude. The restoring field can thus only partially drive the electron back towards its original position. Repeating this process results in the displacement of electrons from regions of high intensity towards those with lower intensity, and this can be represented by a force. In the non-relativistic case this force can be expressed as [10]:

$$F_p = \frac{q^2}{2\omega_1^2 m} \nabla \langle \mathbf{E} \rangle^2, \quad (2.7)$$

where ω_1 denotes the laser frequency, m the mass, q the charge and $\langle \mathbf{E} \rangle$ is the cycle averaged electric field of the laser light. As can be seen in the expression above, the force is inversely proportional to the mass of the particle. Therefore, electrons in the plasma are primarily affected, and not the heavier ions. Furthermore, it can be noted that the direction of the force is independent of the sign of the charge, and that since the laser intensity is proportional to the square of the electric field, the steeper the intensity gradients become, the stronger the force will be. A full derivation and explanation of the equivalent force in the relativistic case can be found elsewhere

[11, 12], but the resulting dynamics is essentially the same as in the classical case; light particles are driven away from regions of high laser intensity.

2.2.3 Overdense and Underdense Plasmas

Several parameters can be used to characterize a plasma. One is its frequency, ω_p , which, in the case of a plasma with a low electron temperature, can be expressed as:

$$\omega_p = \sqrt{\frac{n_e e^2}{m_e \epsilon_0}} \quad (2.8)$$

and is a function of the electron number density n_e . m_e denotes the electron mass. The plasma frequency can be described as the response of the plasma to a small perturbation, for example, that introduced by a laser field. If this perturbation displaces electrons from a slab of plasma where the ions remain stationary, the charge separation induces a restoring force leading to an oscillating motion of the electrons [13]. The magnitude of the restoring force is given by the strength of the electric field, hence the electron density is the determining factor in the process.

A laser cannot propagate through a plasma if the plasma frequency is higher than the laser frequency, i.e., if the density of the plasma is too high. The electron density at which this occurs, n_c , can easily be derived from Eq. 2.8 for a known laser frequency, ω_l :

$$n_c = \frac{\omega_l^2 m_e \epsilon_0}{e^2}. \quad (2.9)$$

This density is called the critical density, and plasmas with higher and lower densities are called overdense and underdense, respectively. This relation can be described more conveniently using units of the laser wavelength, λ_l :

$$n_c = 1.1 \cdot 10^{21} (\lambda_l [\mu\text{m}])^{-2} [\text{cm}^{-3}]. \quad (2.10)$$

When the leading edge of an intense laser pulse ionizes a solid target, the resulting plasma starts to expand. The velocity of this expansion is similar to the ion sound velocity, c_s , and can be expressed as:

$$c_s \approx \sqrt{\frac{Z k_B T_e}{m_i}} = 3 \cdot 10^7 \sqrt{\frac{Z}{A} T_e [\text{keV}]}, \quad (2.11)$$

where Z is the dominant charge state of the ions, A is the atomic mass number, T_e the electron temperature and k_B is the Boltzmann constant. This expansion causes a density gradient into which a laser pulse can propagate, until it reaches the surface corresponding to the critical density, where the laser light is either reflected or absorbed. If the laser pulse has an oblique angle of incidence, the pulse will be refracted in the gradient, and will not reach the critical surface. There is, however, an evanescent part of the electromagnetic field of the laser that can penetrate into the

overdense plasma. The depth of this penetration is called the skin depth, δ_s , and is related to the plasma frequency through:

$$\delta_s = \frac{c}{\omega_p}. \quad (2.12)$$

2.2.4 Relativistic Transparency

The plasma will be opaque to laser light if $\omega_p > \omega_l$, as stated above. However, if the laser light is sufficiently intense, the amplitude of the oscillating electrons will be sufficiently high for the electrons to become relativistic, leading to an increase in their mass. This will cause a reduction in the plasma frequency, which can lead to a plasma that is relativistically transparent. The limit of relativistic transparency for plane monochromatic light can be described by the cycle averaged Lorentz factor of the laser pulse, $\gamma = \sqrt{1 + a_0^2/2}$, as [2]:

$$\frac{n_e}{n_c \gamma} < 1 < \frac{n_e}{n_c}. \quad (2.13)$$

2.2.5 Electron Heating Mechanisms

When transferring energy from a laser pulse to electrons in an overdense plasma, several mechanisms may occur, separately, or in combination. Different heating mechanisms will dominate, depending on parameters such as the polarization of the laser pulse and the density gradient of the plasma.

As the leading edge of an intense laser pulse ionizes a solid target in vacuum, the resulting plasma starts to expand, creating a density gradient. If the laser pulse is p-polarized and the laser pulse is incident at an angle, relative to the target surface, a mechanism called resonance absorption may occur. When the most intense part of the laser pulse arrives at the plasma gradient, it will thus first propagate through an underdense region, but as the refractive index increases, with increasing plasma density, the laser pulse will gradually be deflected, and will eventually be reflected when the electron density corresponds to:

$$n_e = \cos^2(\theta)n_c, \quad (2.14)$$

where θ is the angle of incidence. Due to the p-polarization of the laser pulse, the evanescent electric field, which can tunnel towards the critical surface, is normal to the surface. It can then resonantly drive a plasma wave this region, since the plasma frequency and the laser frequency are matched at the critical surface. The energy of the wave can be transferred to particles in the plasma when the wave is damped by trapping particles or, if the intensity is sufficiently high, wavebreaking may also contribute to the damping [14]. Through empirical methods, the resulting hot-electron temperature, T_e , has been found to scale with the laser intensity, I_l , and the wavelength, λ_l , as [15]:

$$T_e \propto (I_l \lambda_l^2)^{1/3}. \quad (2.15)$$

It can thus be seen that a laser pulse with a longer wavelength heats electrons in a plasma more efficiently through resonant absorption, than a pulse of shorter wavelength.

If the plasma density gradient is very steep, another electron heating mechanism, called vacuum heating, Brunel heating, or not-so-resonant resonant absorption, may also play a part in electron heating. In this scenario, the laser field captures electrons in the underdense part of the gradient, and because of the steepness of the gradient, can accelerate them beyond the critical surface, meaning that when the laser field changes direction the electrons are out of reach of the field [16].

Both the above mentioned heating mechanisms rely on p-polarized laser pulses and oblique angles of incidence, and the resulting hot electrons propagate normally into the target. Another mechanism, through which electrons can be heated, also at normal incidence, is $\mathbf{j} \times \mathbf{B}$ -heating [17]. This kind of heating occurs due to the oscillating part of the ponderomotive force, correlated to the magnetic field, when an intense laser pulse interacts with an overdense plasma and the laser energy absorption efficiency is strongly dependent on the laser intensity. The hot-electron temperature scales with the relativistic electron ponderomotive energy [18, 19] through the relation:

$$T_e = 0.511[\text{MeV}] \left(\sqrt{1 + \frac{I_1 \lambda_1^2 [\text{W}/\text{cm}^2 \mu\text{m}^2]}{2.8 \cdot 10^{18}}} - 1 \right). \quad (2.16)$$

Unlike the case of resonant absorption and vacuum heating, the resulting hot electrons from $\mathbf{j} \times \mathbf{B}$ -heating propagate close to the laser propagation axis [20].

2.3 Ion Motion

2.3.1 Acceleration Schemes

Target Normal Sheath Acceleration

The perhaps most studied ion acceleration mechanism, and also the one utilized in most of the experimental work presented in this thesis, is target normal sheath acceleration (TNSA) [21, 22]. In this mechanism, an intense laser pulse ($I_1 \gtrsim 10^{18} \text{ W}/\text{cm}^2$ for the generation of MeV ions) interacts with a solid target, typically foils a few μm thick. Such a laser pulse can heat electrons in an overdense plasma through one, or a combination, of the different processes described in Section 2.2.5. If the electrons gain sufficient energy, they will propagate through the target foil and out of the rear surface. This charge separation of ions and electrons creates a strong, quasi-static electric field ($\sim \text{TV}/\text{m}$), directional along the target normal and called “sheath”. The electrons building up the field recirculate continuously through the foil and if the laser pulse is still ongoing when they return to the front surface they may experience repeated heating. Contamination on the rear surface of the foil, such as water vapour and hydrocarbons, will be ionized in the quasi-static field

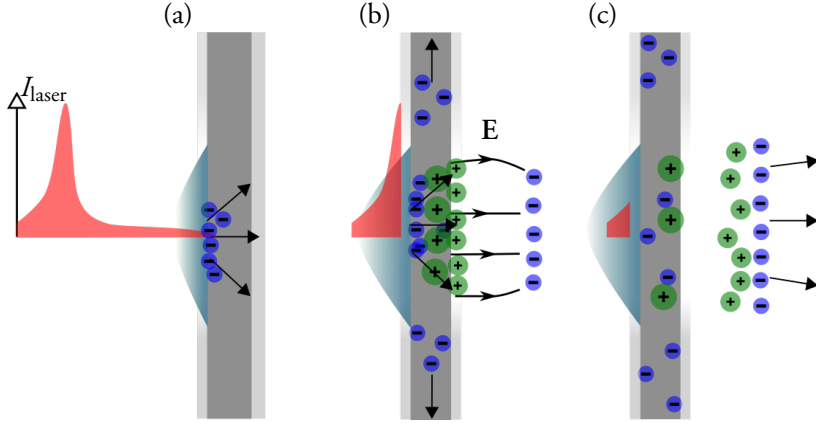


Figure 2.2 Target normal sheath acceleration

Schematic illustration of target normal sheath acceleration (TNSA). (a) The leading edge of an intense laser pulse ionizes the front surface of a solid target, and a preplasma starts to expand. The foil has layers of contaminants, such as water and hydrocarbons, on its surface. As the laser intensity increases electrons become heated through the mechanisms discussed in Section 2.2.5. Any part of the laser pulse that is not absorbed will be reflected. (b) The most intense part of the laser pulse efficiently propagates through or along the target and out into the vacuum, while the positive ions remain in the target. This causes charge separation, resulting in a strong quasi-static electric field. The surface contaminants are ionized in this field. (c) The protons (hydrogen ions) released from the ionization are accelerated to high energies in the electric field, while the heavier ions, with lower charge-to-mass ratios, are partially screened from the field by the protons and are less efficiently accelerated.

and the resulting ions can be accelerated to MeV-energies over μm -distances. The lightest ion, a proton from a hydrogen atom, will be preferentially accelerated due to its high charge-to-mass ratio, and will then partially screen the heavier ions from the electric field. It should be noted that target normal sheath acceleration can also occur on the front surface of the foil, and the ions will then be accelerated in the opposite direction to rear-surface acceleration [23]. The efficiency of front-surface acceleration is normally lower than rear-surface acceleration, but depends strongly on the preplasma expansion, and thus on the laser temporal intensity contrast.

Target normal sheath acceleration typically produces ion spectra that decay exponentially as a function of ion energy and are cut off at a certain maximum energy (see example in Fig. 2.3). A model developed by Mora [24] predicts that this cut-off energy, E_{max} , is a function of time, t , and occurs at:

$$E_{\text{max}} \simeq 2Zk_{\text{B}}T_e \left(\ln \left(\frac{2\omega_{\text{pi}}t}{\sqrt{2e}} \right) \right)^2, \quad (2.17)$$

where ω_{pi} is the plasma ion frequency, Z the charge state and e is a mathematical constant ($e \approx 2.71828$). This energy thus scales linearly with the electron temperature and with $I_1^{0.3-0.5}$ [1, 25, 26] (compare with Eq. 2.15 and Eq. 2.16).

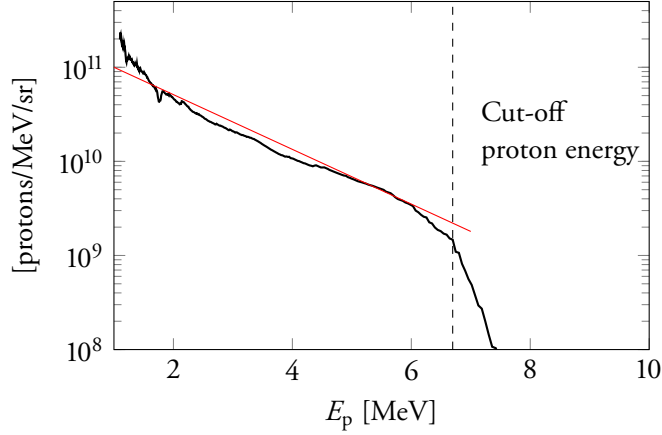


Figure 2.3 Example of typical TNSA proton energy spectrum

Energy spectrum of protons accelerated in the target normal sheath regime from a 3 μm Al foil with $I_1 = 4 \cdot 10^{19} \text{ W/cm}^2$. The dashed line indicates the cut-off energy, and the red line the approximate exponential decay of proton numbers, note the logarithmic scale, for increasing proton energies.

In order to increase the maximum proton energy by one order of magnitude, it is therefore necessary to increase the laser intensity at least by a factor of 100. The number of accelerated ions, N_i , per unit energy as a function of time is related to the electron temperature through [24]:

$$\frac{dN_i}{dE} \propto \frac{t}{\sqrt{Ek_b T_e}} \exp\left(-\sqrt{\frac{2E}{Zk_B T_e}}\right). \quad (2.18)$$

The time of acceleration, t_{acc} , for the ions of the highest energy scales with the laser pulse duration, τ , as [27]:

$$t_{\text{acc}} = 1.3 (\tau + 60) \text{ [fs]}, \quad (2.19)$$

for laser intensities $I_1 > 3 \cdot 10^{19} \text{ W/cm}^2$. It should be noted that in reality there is no limit on the acceleration time and that it is used in models to compensate for the use of a constant electron temperature. This temperature actually decreases in the acceleration process when energy is transferred to ions.

Due to the curvature of the sheath, target normal sheath acceleration produces highly divergent pulses of ions, with a half-angle up to tens of degrees. The curvature is greater close to the outer edges of the sheath, and the target normal and the direction of the electric field in the sheath do not coincide here. The correlation between the spatial appearance of the sheath and the spatial profile of the resulting proton pulses was investigated in this work (Papers III and IV). Although the pulses are divergent, the laminarity of the pulses is high and the size of the source small, leading to low transverse emittance; values below 0.004 mm mrad have been reported [28].

The laser pulse duration affects the target normal sheath acceleration mechanism. It has been found that for a specific laser pulse energy and target thickness, there is a corresponding optimum in laser pulse duration for achieving high maximum proton energies. This is implied by Eq. 2.17. Since T_e decreases with I_l , long τ leads to lower electron temperatures, and thus lower E_{\max} . On the other hand, t_{acc} increases with longer laser pulse durations, leading to increased E_{\max} . For a laser energy of 0.7 J and a 4 μm metallic target, the optimum pulse duration is ~ 250 fs, although the variation in maximum proton energies is small over a broad interval from $\tau = \sim 30$ to ~ 600 fs [29]. The dependence of optimum pulse duration with target thickness, has been confirmed through experimental studies [30, 31]. It should be noted that varying the laser pulse duration within the same laser system usually involves introducing a chirp in the pulse, which may in itself affect the acceleration process [32].

Radiation Pressure Acceleration

The scheme of radiation pressure acceleration has attracted a great deal of interest in recent years, due to the possibility of almost monoenergetic ion pulses and high energy transfer from the laser pulse to ions, which has been shown through numerical simulations [33]. In what is called the laser piston regime, an intense laser pulse ($I_l > 1.2 \cdot 10^{23} \text{ W/cm}^2$) is used to irradiate a thin foil so that, ideally, all the electrons are driven forward, away from the ions. The resulting charge separation accelerates the positive ions and if they become relativistic in one laser cycle they can co-propagate behind the electrons and the laser pulse, and the energy transfer from the laser pulse can continue. The plasma layers thus formed can be regarded as a moving reflective mirror, laser light that is reflected is thus shifted in frequency, and it is through this down-shift that the energy is transferred. The fact that the whole plasma volume is accelerated as a slab means that the ion energy spectrum can be monoenergetic. To avoid the development of instabilities during the process, the laser focal spot size must be sufficiently large that it can be considered one-dimensional, meaning that it is even more difficult to reach the high laser intensities required. Further simulations have shown that it may be possible to circumvent the intensity requirement by using a circularly polarized laser pulse [34–36] since the ponderomotive force of circularly polarized light has no fast oscillating component. Laser pulses with intensities of $I_l > 10^{20} \text{ W/cm}^2$ should then be sufficient to drive the process. A number of experimental studies have shown signatures of radiation pressure affecting the acceleration process [37–39], but no experimental study has so far been performed under conditions where the theoretical predictions of relativistic ion pulses could come true. Target deformation due to the finite size of the laser focus also poses challenges in experiments [40].

Collisionless Shock Acceleration

Radiation pressure will also affect thicker targets, but it is not possible to achieve full separation of the positive ions and the electrons in the plasma. The radiation pressure instead pushes the plasma forwards towards the target in a process called hole boring [18]. This creates an electrostatic shock wave that moves with a velocity several times higher than the ion sound velocity, see Eq. 2.11. The shock can accelerate ions through reflection. The ion energy spectra have characteristic features, typically a plateau. Due to the acceleration by reflection, the maximum achievable proton energy corresponds to twice the propagation velocity of the shock [41]. The target thickness also affects this acceleration mechanism since the recirculation of electrons through the target influences shock formation. Another characteristic of collisionless shock acceleration is that it accelerates ions from the front surface and drives them through the target. A few experimental studies on collisionless shock acceleration have been reported, where the shape of the ion energy spectra in combination with numerical modelling was used to demonstrate the contribution to the acceleration process by an electrostatic shock [42, 43].

Breakout Afterburner

Target normal sheath acceleration and radiation pressure acceleration rely on targets that are both classically and relativistically overdense, i.e., opaque to the laser light. Another acceleration mechanism, that operates in the relativistic transparency regime, is the breakout afterburner [44]. Here, the laser pulse duration and the target thickness are matched so that, ideally, the leading edge of the laser pulse interacts with an overdense plasma, where it heats electrons in a way similar to target normal sheath acceleration, while the target becomes relativistically transparent when the most intense part of the laser pulse arrives [45]. In this regime, the heated electrons can transfer momentum to heavier ions through a two-stream instability (relativistic Buneman instability [46]) in the plasma [47]. For this acceleration mechanism to occur, it is important that the target remains classically overdense for the leading edge of the laser pulse, and it is therefore vital to have high laser temporal contrast (see Section 2.4.1) so that plasma expansion prior to the arrival of the main pulse is small. The breakout afterburner acceleration scheme is particularly favourable for heavier ions, since protons are expelled from the target through volumetric heating because of their high charge-to-mass ratio. An experimental study on the generation of GeV carbon ions has been reported [48].

2.3.2 Ion Propagation in Matter

An energetic ion propagating through matter deposits energy along its path; for high-energy ions mainly through a process called electronic stopping. This occurs through inelastic collisions with electrons as the ions travel through the material. The energy may then be dissipated from the excitation of these electrons to thermal

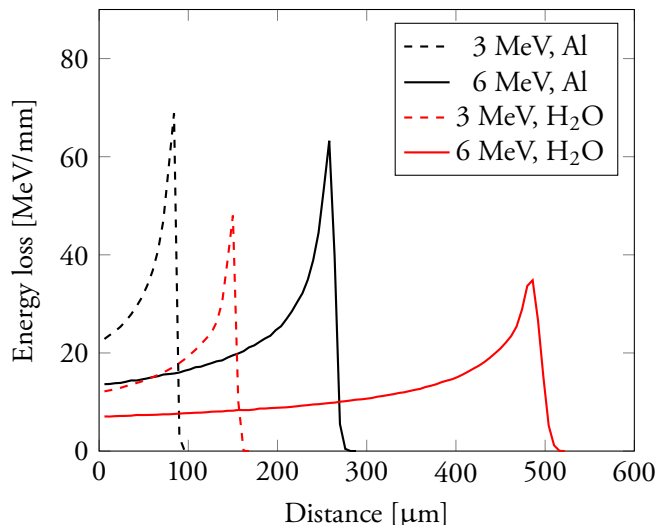


Figure 2.4 Energy deposition from energetic protons in water and aluminium

Energy loss of protons as a function of distance travelled when propagating through materials, showing the characteristic Bragg peaks at the end of their travel. The dashed and the solid curves represent protons with initial energies of 3 MeV and 6 MeV, respectively. The black curves show deposition in aluminium and the red ones deposition in water. The broadening of the peaks for the high-energy protons, the difference is especially clear between 3 and 6 MeV protons in water, is caused by greater straggling the longer the protons propagates in the material. (Adapted from SRIM [49].)

vibrations. For ions of lower energies there is also a significant contribution to the energy deposition through elastic collisions between the energetic ions and the nuclei of the atoms in the material, called the nuclear stopping power. In this process, the atom recoils from its position. The energy loss per unit distance travelled by an energetic ion increases with decreasing energy, leading to the characteristic Bragg peak. This is illustrated in Fig. 2.4. Ions of different energies therefore have well-defined ranges in different materials. The precise characteristics of energy deposition of energetic ions also varies with the type of ion.

2.4 Experimental Techniques

2.4.1 High Intensity Lasers

The experiments described in Papers II-IV were performed at the Lund High-Power Laser Facility (Sweden), whereas the experiments discussed in Paper I took place at PHELIX, GSI Helmholtz Centre for Heavy Ion Research, Darmstadt (Germany), and those reported in Papers V and VI at TARANIS, Queen's University Belfast (UK). These three lasers all produce high-power laser pulses, but have different specifications. Some of the parameters of the laser pulses from the three systems are compared in Table 2.1. Since most of the experimental work included in this thesis

Table 2.1 Laser pulse parameters

Laser pulse parameters for the terawatt laser at the Lund High-Power Laser Facility (Sweden), the PHELIX-laser at the GSI Helmholtz Centre for Heavy Ion Research, Darmstadt (Germany) and TARANIS, Queen's University Belfast (UK). The parameters given correspond to the conditions under which the experimental studies described in Papers I to VI were performed.

Pulse parameter	Lund	PHELIX	TARANIS
Amplifying medium	Ti:Sapphire	Nd:Glass	Ti:Sapphire and Nd:Glass
Duration	35 fs	500 fs	600 fs
Energy (before compression)	1.6 J	200 J	10 J
Wavelength	800 nm	1053 nm	1053 nm
Repetition rate	10 Hz	~1 shot/hour	~1 shot/10 min

was performed at the Lund High-Power Laser Facility a more detailed description of this system there is given below.

Lund High-Power Laser Facility

The multi-terawatt laser at the Lund High-Power Laser Facility is a chirped pulse amplification system [50] that delivers high-power, femtosecond laser pulses (see specifications in Table 2.1). Chirped pulse amplification is achieved by stretching ultra-short laser pulses before amplification, which leads to a lower power. This increases the maximum energy content in the pulses that the gain medium can withstand. After amplification, the pulses are compressed back down to transform-limited durations. The seeding laser pulses for later amplification stages are generated in a Kerr-lens mode-locked oscillator [51]. The laser pulses at this stage have a broad spectral bandwidth (50 nm) centred around 800 nm, they contain an energy of approximately 5 nJ and have a high repetition rate (80 MHz). A combination of a Pockels cell and a polarizer selects 10 pulses per second at the exit of the oscillator, which determines the final repetition rate of the laser system. A grating-based stretcher introduces a chirp in the pulses, thereby increasing the pulse duration to several hundred picoseconds.

The first amplification stage is a six-pass preamplifier, which is used to improve the temporal contrast of the final laser pulse by lowering the gain required in the regenerative amplifier later. The gain in this first amplifier is three to four orders of magnitude. The pulses are further amplified up to \sim mJ-level in the closed cavity of the regenerative amplifier, before they are switched out to a five-pass amplifier. Here, the laser pulse energy reaches 400 mJ, of which 200 mJ is separated and sent to other experimental set-ups. The pulses are focused through a spatial filter to remove aberrations from the wavefront, before they reach the final amplifier. In the experiments described in this thesis, the laser pulses were amplified to up to 1.6 J in a titanium-doped sapphire crystal, placed in a cryogenic cooler, and then expanded to a beam diameter of \sim 50 mm through a telescope.

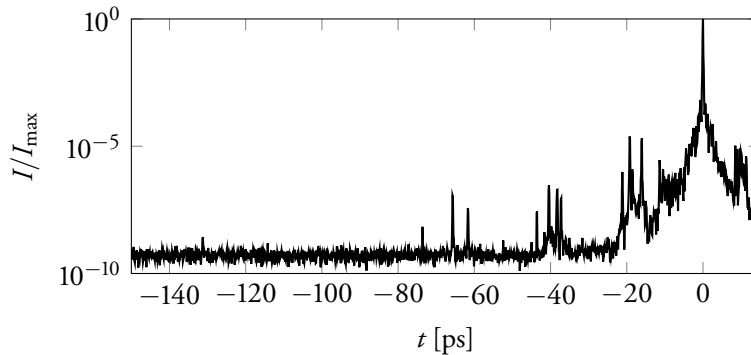


Figure 2.5 Laser temporal contrast of the TW-laser system at the Lund High-Power Laser Facility

Scan of the temporal contrast before the arrival of the main pulse with a third-order autocorrelator. It should be noted that reflections inside the autocorrelation instrument may cause some artificial pre-pulses in the measurement.

In order for the laser-pulses to reach terawatt power, they must be compressed in time. This is done in a grating compressor, which also marks the end of the chirped pulse amplification scheme. From the compressor and onwards the laser pulses are transported under vacuum since non-linear effects would arise when the high-power pulses interact with air. There are two different experimental areas, one optimized for laser interactions with gaseous targets, and one for solid targets. The laser pulses are directed to these areas with a mirror that can be flipped. The energy content of the laser pulses delivered to the experimental areas is 1 J or slightly below.

Laser Pulse Duration

The laser pulse duration, τ , is determined by its spectral content through a Fourier transform. For a chirp-free pulse, the broader the spectral bandwidth of the pulse, the shorter the pulse duration. The bandwidth of a pulse from the multi-terawatt laser in Lund is approximately 40 nm after compression, which has a transform limit of ~ 35 fs.

The duration of a femtosecond laser pulse can be estimated with a second-order intensity autocorrelator. The pulse is split into two parts and sent along two different arms, where their relative delay can be varied. They are then spatially overlapped inside a non-linear crystal. If there is also a temporal overlap between the pulses, a frequency-doubled harmonic is generated. If there is an angle between the axes of propagation of the two pulses, the width of the region with temporal overlap, and thus the width of the harmonic, can be used to determine the pulse duration.

Laser Temporal Contrast

In laser-driven ion acceleration from thin foils, the temporal contrast of the laser pulse determines the shape and density of the plasma with which the most intense part of the laser pulse will interact. If a sufficiently high amount of energy is deposited onto the foil before the arrival of the main pulse, the expansion of the plasma damps or even prevents the ion acceleration mechanisms, and it is therefore generally desirable to achieve the highest possible temporal contrast at short times before the main pulse arrives at the foil [30]. There are, however, some cases where it is desirable to deposit a controlled amount of energy onto the target before the main pulse arrives, in order to create a plasma with an optimized density. This can increase the absorption of laser energy, thereby increasing the hot-electron temperature, and enhancing the maximum ion energies [52].

Several factors affect the laser contrast in a high-power laser system. Amplified spontaneous emission is caused by spontaneous propagation of photons that are amplified in the laser cavities. This causes a pre-pedestal, typically between 5 and 10 orders of magnitude below the maximum intensity, at times between 150 and 20 ps before the arrival of the main pulse in Fig. 2.5. Optical switches, such as Pockels cells, can be used to gate this emission down to nanosecond time-scales, but on the picosecond time-scale it is more challenging to reduce the intensity before the arrival of the main pulse. Pre-pulses from stray reflections in the laser system also affect the temporal contrast of the laser pulse, as well as non-compressible parts of the laser pulse spectrum.

The temporal contrast of a laser pulse can be measured with a third-order autocorrelator. A third-order process is needed, due to asymmetry in the temporal contrast before and after the main pulse, unlike the pulse duration measurements, where symmetry is assumed. Using a third-order instrument also enables high dynamic range and temporal contrast up to 10 orders of magnitude, or even slightly higher, can be determined.

Apart from efforts to improve the temporal contrast that can be made within the laser system itself, such as the use of a preamplifier before the regenerative amplifier, it is also possible to implement one, or several, plasma mirrors [53]. A plasma mirror works as a sub-picosecond optical switch for intense laser pulses. It consists of a sheet of glass with properties such that the laser light should initially be transmitted, i.e. anti-reflection coated for the polarization used and/or mounted at Brewster's angle. The pre-pedestal of the laser pulse is thus transmitted. When the laser light becomes sufficiently intense to ionize the substrate, an overdense, highly reflective, plasma is formed. The plasma expansion occurring over a femtosecond laser pulse duration is negligible and the surface thus becomes a high-flatness mirror. In this way the most intense part of the laser pulse is cleaned of the pre-pedestal. The efficiency of this “cleaning”-process is determined by the quality of the anti-reflection coating, an improvement in the laser temporal contrast of two orders of magnitude per plasma mirror can be usually achieved [54]. However, there have been reports of contrast

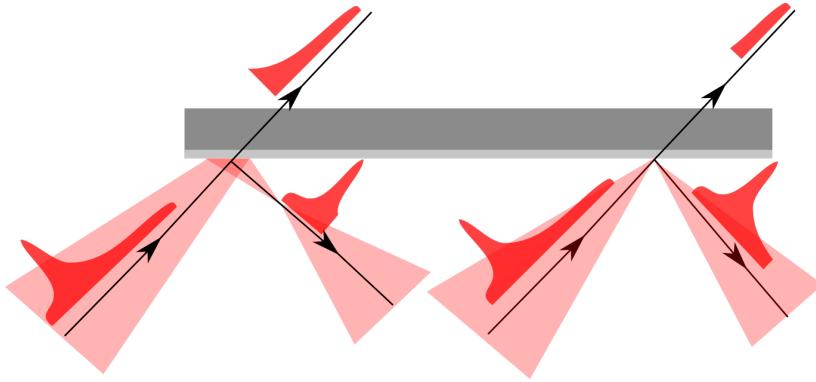


Figure 2.6 Illustration of the use of a plasma mirror

Schematic illustration of how a plasma mirror separates the main part of the laser pulse from the pre-pedestal. The onset of plasma formation with respect to the arrival of the main pulse can be varied by changing the distance from the focal plane to the mirror. In the scenario on the left, the plasma mirror is placed far from the focal plane and contrast enhancement therefore continues until close to the arrival of the main pulse, but more of the pulse energy is lost. In the scenario on the right, the plasma mirror is placed very close to the focal plane of the laser, and contrast enhancement ceases earlier with respect to arrival of the main pulse, however, the energy throughput is higher.

enhancement of four orders of magnitude, measured at 1 ps before the arrival of the main pulse, for a single plasma mirror using state-of-the-art coatings [55].

2.4.2 Focusing High Intensity Laser Pulses on Thin Foils

High-power ($>TW$), ultra-short laser pulses must be focused with reflective optics since the interactions between the laser light and the glass in a lens would severely affect the pulse and damage the lens. Typically, off-axis parabolic mirrors are used to focus these high-power pulses. These mirrors are characterized by their f -number, defined as the focal length divided by the aperture of the focusing optics. The focusing properties of the parabolic mirror can be determined from the f -number for a laser pulse with a certain wavelength. If a Gaussian spatial beam profile is assumed for a laser pulse that fills the whole aperture of the mirror, the smallest achievable focal spot size with a radius w_{focus} , can be related to the f -number, F_{number} , through:

$$w_{\text{focus}} \approx \frac{2}{\pi} \lambda_l F_{\text{number}}. \quad (2.20)$$

The radius w is defined as the radial point at which the intensity has fallen by a factor $1/e^2$ from its peak value and the spot size, $2w$, for a Gaussian beam is a factor ~ 1.7 larger than the the full width at half maximum of the intensity.

The Rayleigh range, d_{Rayleigh} , which describes the distance from the focal plane at which the spot size is doubled, is given by:

$$d_{\text{Rayleigh}} = \frac{4\lambda_l}{\pi} F_{\text{number}}^2. \quad (2.21)$$

Achieving a small focal spot is crucial to maximize the intensity in the laser pulse, used to accelerate ions from solid targets. Therefore, a parabolic mirror with a small f-number is commonly used. In the experimental studies presented in Papers I to VI, focusing optics with f-numbers between 1 and 3 were used. Using such focusing optics leads to short Rayleigh ranges, assuming that the diameter of the mirror is matched to the size of the unfocused laser pulse. This means that the target must be placed with high (μm) precision in the focal plane of the laser pulse.

A deformable mirror can be used to optimize the quality of the laser focus and such a mirror is part of the TW-laser system at the Lund High-Power Laser Facility. This deformable mirror consists of 32 actuators located behind a thin, reflecting substrate. Applying a voltage over one of the actuators causes a slight force on the substrate, changing the shape of the reflective surface. The mirror is imaged onto a wavefront sensor (PHASICS, SID4). Using a feedback loop from the wavefront sensor, the deformable mirror can be used to correct for aberrations in the near-field of the laser pulse, ideally creating a flat wavefront, to optimize the laser focus quality. This optimization process helps to achieve the highest possible laser intensity at the focus, by ensuring a small spot size, close to the diffraction limit.

Experiments in which the influence of the laser focal spot size and shape on the target normal sheath acceleration process was studied are presented in Papers III and IV and are discussed in the next chapter.

Thin Foils

All the experimental studies on laser-driven ion acceleration presented in this thesis were performed using μm -thick metallic foils, apart from that described in Paper I. The reason for this is that metallic foils, which are conducting, lead to smooth proton pulse profiles. In contrast, using μm -thick insulating target foils causes filamented proton pulse profiles, since the electron current may exhibit instability when propagating through the target foil [56]. Using target foils that are a few micrometres or slightly thicker, also enables the acquisition of large amounts of data with low influence of the amplified spontaneous emission. If thinner, sub-micrometre foils are used, it is usually, depending on laser temporal contrast, necessary to implement a plasma mirror, since the pre-pedestal of the laser pulse might damage these foils prior to the arrival of the main pulse. This makes the experimental set-up more complex and typically lowers the repetition rate of the ion pulses.

2.4.3 Diagnostics and Detectors

Thomson Parabola Spectrometer for Laser-Accelerated Ions

As can be seen from the Lorentz equation (Eq. 2.1), a charged particle moving in an electric and/or magnetic field is subject to a force. This can be used to characterize energetic ion pulses, by allowing the ion pulse to propagate through an external

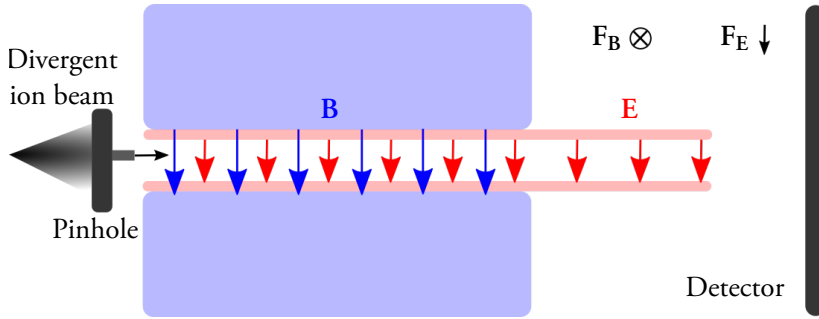


Figure 2.7 Thomson parabola spectrometer

Schematic illustration of a Thomson parabola spectrometer. A collimated part of a divergent pulse of positive ions is selected with a pinhole. The ions propagate through parallel electric and magnetic fields onto a position-sensitive detector. The electric and magnetic fields exert forces on the ions, displacing them from their original direction of propagation. The deflection resulting from the electric-field is used to determine the charge-to-mass ratio of the ions and the displacement caused by the magnetic field is related to the ion energies.

electric and magnetic field. These are commonly set up parallel to each other, and perpendicular to the axis of ion propagation, with strong permanent magnets (up to ~ 1 T) and high-voltage electrodes (kV) (see Fig. 2.7). The $q(\mathbf{v} \times \mathbf{B})$ -term in the equation gives rise to a force acting on the ion in a direction perpendicular to both \mathbf{v} and \mathbf{B} , which increases with increasing velocity and thus with increasing energy. However, a particle with high energy is less affected since it spends less time in the magnetic field. Associated with the $q(\mathbf{E})$ -term is a force along the axis of the electric field that is determined by the charge of the ion. The ions are hence accelerated by the electric field according to their charge-to-mass ratio. Therefore, if the displacement caused by these forces is measured with a 2-dimensional position-sensitive detector, the energy and charge-to-mass ratio of the ions can be deduced. Such an instrument is called a Thomson parabola spectrometer, after its inventor J. J. Thomson [57]. It should be noted that in the non-relativistic case, an ion with higher energy spends less time in the electric field, than an ion of lower energy which travels slower, and is therefore subject to the force arising from the electric field for a shorter time, causing a smaller deflection. There is thus an energy-dependence, not only of the deflection from the magnetic field, but also from the electric field.

For a non-relativistic ion with velocity v , charge q and mass m , initially propagating along the z -axis, through an electric field E_x of length l_E , and a magnetic field B_x of length l_B , the deflection at the plane of detection can be expressed through a first-order Taylor expansion as:

$$\begin{aligned} x &= \frac{qE_x l_E (d_E + 0.5l_E)}{mv^2}, \\ y &= \frac{qB_x l_B (d_B + 0.5l_B)}{mv}, \end{aligned} \quad (2.22)$$

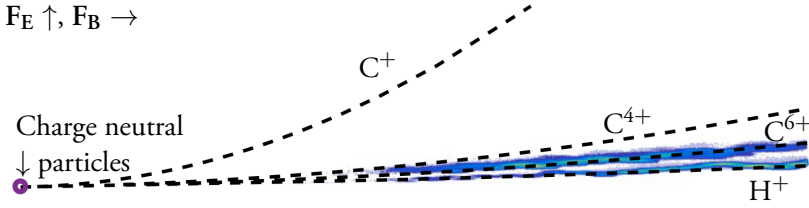


Figure 2.8 Particle traces from a Thomson parabola spectrometer

Example of ion traces, marked in blue, from Thomson parabola spectrometer of laser-accelerated ions on position-sensitive detector. Only protons (H^+) and C^{6+} were detected in this particular experimental set-up, but for illustrative purposes the parabolic traces of two lower charge states of carbon ions (C^{4+} and C^+) are marked with dashed curves as well. The position where the different traces overlap, corresponds to where charge neutral particles, or particles of infinite energy, arrive at the detector.

where d_E and d_B denote the drift from the end of the electric and magnetic field, respectively, to the plane of detection. Combining these equations and eliminating v gives a parabolic equation which, for a fixed set-up of the spectrometer, is unique for each charge-to-mass ratio:

$$y^2 = \frac{q B_x^2 l_B^2 (d_B + 0.5 l_B)^2}{m E_x l_E (d_E + 0.5 l_E)} x. \quad (2.23)$$

However, the equation is not uniquely defined for ions of different species that have the same charge-to-mass ratio, for example C^{6+} and O^{8+} . Examples of parabolic ion traces can be seen in Fig. 2.8.

Thomson parabola spectrometers can be adapted for the characterization of ion pulses of different energies. The requirement on instrument energy acceptance commonly ranges from a few MeV per nucleon [58] up to 100 MeV per nucleon [59, 60] for laser-accelerated ions. Optimization of the resolution for a specific energy range is primarily done by adjusting the drift distances, d_E and d_B , and the lengths of the electric and magnetic field, l_E and l_B . Although the equations given here are for non-relativistic particles, it is possible to perform a similar, but numerical, analysis for relativistic ions. Paper I presents an alternative set-up of a Thomson parabola spectrometer, which will be further discussed in the next chapter. Under experimental conditions where only one type of ion is present, the electric field of the Thomson parabola spectrometer can be excluded; such a set-up is described in Section 3.1.

Radiochromic Films, CR39 and Scintillators

There are several methods of detection for energetic ions, one of the most commonly used for laser accelerated ions is called Radiochromic Film (RCF). Radiochromic film consists of a thin layer of radiosensitive dye (tens of micrometres), between two polyester-based layers (hundreds of micrometres). When this film is exposed to

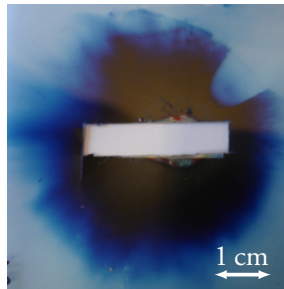


Figure 2.9 Radiochromic film

A $5 \times 5 \text{ cm}^2$ radiochromic film exposed to a pulse of laser-accelerated ions. The central part of the pulse propagates through the slit and on to further diagnostics. The “dent” in the ion pulse profile in the upper right corner is caused by a mechanical object obstructing the ion pulse.

radiation, such as energetic ions, it changes colour. It is also sensitive to other types of radiation, commonly produced when accelerating ions with lasers, for example, energetic electrons and x-rays. Scanning the films after exposure to radiation allows the dose deposited at different positions to be calculated, provided there is a means of calibration. If several films are stacked together, so that the low-energy ions are completely stopped and incrementally filtered away, layer by layer, it is also possible to resolve the spatial profile of the ion pulse for different energy intervals [61, 62], (cf. Fig. 2.4). This also provides a means of distinguishing between the signal from ions and that from electrons or x-rays, since the energy deposition characteristics and ranges of electrons and x-rays differ from those of ions. Radiochromic film was used as a detector in the studies described in Papers V and VI.

Another material commonly used to detect radiation, is CR39. This is made out of sheets of plastic (Polyallyl diglycol carbonate), also commonly used in the lenses of eyeglasses. When an energetic ion deposits its energy in a CR39-detector bonds are broken in the polymer. After exposure, the CR39 is placed in a bath of sodium hydroxide (typically 20 % NaOH and 80 % H₂O at 90°C) where the broken polymers are etched away from the rest of the plastic. This creates micrometre-sized pits that can be seen under a microscope (Fig. 2.10(b)). Areas with high pit density also appears less transparent to the naked eye (see Fig. 2.10(a)). Unlike radiochromic film, CR39-detectors are not sensitive to x-rays or electrons, although they can affect the etch rate and pit diameter [63]. A disadvantage of both these detectors is that they can only be used once and must be replaced for new measurements. Remotely controlled mechanical solutions can be employed when running experiments under vacuum, but there is a limit to the number of recordings that can be made before the vacuum chamber in which the experiment is being performed must be opened. For laser systems that produce only a few laser pulses per day, this is not a limiting problem. However, when working with a high-repetition-rate laser system, this can seriously limit the amount of data that can be acquired. Another drawback is that they provide no real-time feedback on the exposure.

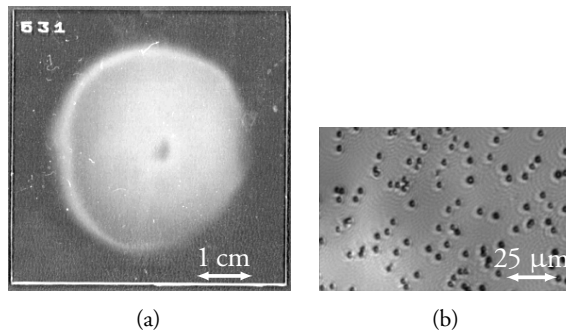


Figure 2.10 CR39 track detector

(a) Image of a $5 \times 5 \text{ cm}^2$ CR39 track detector, that has been exposed to a pulse of laser accelerated ions and etched in sodium hydroxide. The round white area is the ion pulse imprint on the detector. The black dot in the centre is due to slight over-etching, leading to pits merging together and appearing less “milky” in the image. (b) Ion pits in a CR39-detector imaged in a microscope with 40 times magnification.

Plastic scintillators are detectors that can be used many times and, in combination with a camera, they can provide real-time data. In the experiments described in Papers II and IV, plastic scintillators (BC400 and BC408, Saint Gobain) were used. These scintillators emit light when energy from a proton is deposited in the plastic, and provided that the proton is completely stopped in the plastic, the response depends on the initial energy of the proton. These scintillators can also be employed for detecting other ion species, but carbon ions, for example, generate a significantly lower response per unit energy than protons. The implementation of plastic scintillators for the detection of laser-accelerated protons is further discussed in Chapter 3.

EXPERIMENTS AND RESULTS

The purpose of this chapter is to describe the experimental techniques and present the results of the attached publications. Work that has not yet been published will also be presented in greater detail. The first section is dedicated to detector development, and is followed by a section describing experiments to characterize the source of laser-accelerated protons. The last section of the chapter addresses the application of laser-accelerated protons for radiolysis.

3.1 Detector Development and Related Techniques

3.1.1 The Online Magnetic Spectrometer

In order to achieve an online detection system that can provide real-time information on proton energies, an online magnetic spectrometer was implemented at the High-Power Laser Facility in Lund. This consists of a dipole magnet, a plastic scintillator (St Gobain, BC-408) and an EMCCD-camera (Princeton, “PhotonMAX1024”) and was used in the experiments reported in Papers II and III. The magnet was placed 45 cm from the interaction area in the target-normal direction. A 1 mm opening slit was mounted on the front of the magnet. The 1 mm thick scintillator was covered with an aluminium foil and fastened onto a window in the vacuum chamber, 7 cm behind the end of the magnet. The rear-side of the scintillator was imaged through the window, with a 50 mm $f/1.4$ objective, onto the EMCCD-camera. The principle behind the system was thus that high-energy protons emerging from the laser-plasma interaction were propagating through the entrance slit, into the dipole magnetic, where their trajectories were dispersed according to their energies. The position at which each proton hits the scintillator is therefore determined by its energy. The thickness of the protective aluminium foil covering the scintillator is chosen so that heavier ions, accelerated in the same sheath field as the protons, are completely

blocked by the foil. The high-energy protons impinging on the scintillator cause scintillation and the emitted light is captured by the camera.

Calibration

In order to calibrate the detection system in terms of both the energy dispersion of the magnet and the response of the scintillator to high-energy protons, a 1 mm thick piece of CR39 was attached to the scintillator. It was positioned so that it covered half of the width of the expected proton trace. The CR39 was covered with the same type of aluminium foil as the scintillator up to the optical axis, where the plastic was left bare in order to create a imprint from uncharged particles and debris from target, that are not deflected in the magnetic field.

The CR39 was then etched in a NaOH solution. Using a microscope objective with 40 times magnification and a CCD camera, a series of images of the CR39 were recorded along the proton trace, i.e. the rectangle of proton pits on the CR39 where one dimension corresponds to the width of the slit, and the other to the different proton energies (comparable to a proton trace on a scintillator, as can be seen in Fig. 3.2(a)).

The spacing between the centre of the different images was 500 μm . Each image corresponds to 130 μm x 83 μm of the CR39. The pits in the images were counted separately for each image, and up to 300 pits were recorded in a single image. As protons with higher energies deposit less energy close to the surface of the CR39, it was etched several times, and the images corresponding to higher proton energies were analysed. Finally, the traces were merged using the imprint of uncharged particles as a reference.

The distance from the centre of the imprint to the position where the protons with sufficiently high energy to just penetrate the Al foil (i.e. the lower cut-off of the trace) was measured, to determine the effective strength of the magnetic field inside the dipole magnet. Assuming a constant 5 cm long field, the effective magnetic field was calculated to be 0.83 T, consistent with Hall probe measurements. Based on these measurements, a dispersion curve could be calculated, see Fig. 3.1(b), using the Larmor radius, R :

$$R = \frac{p}{qB}, \quad (3.1)$$

where p is the momentum of the ion, q is the charge and B is the strength of the magnetic field. If the proton enters the dipole magnet perpendicular to the magnetic field, the displacement on the scintillator, d , due to the magnetic field, can be expressed for non-relativistic ion energies as:

$$d = R - \sqrt{R^2 - a^2} + \frac{ab}{\sqrt{R^2 - a^2}}, \quad (3.2)$$

where a is the length of the magnetic field and b is the distance from the back of the magnet to the plane of detection.

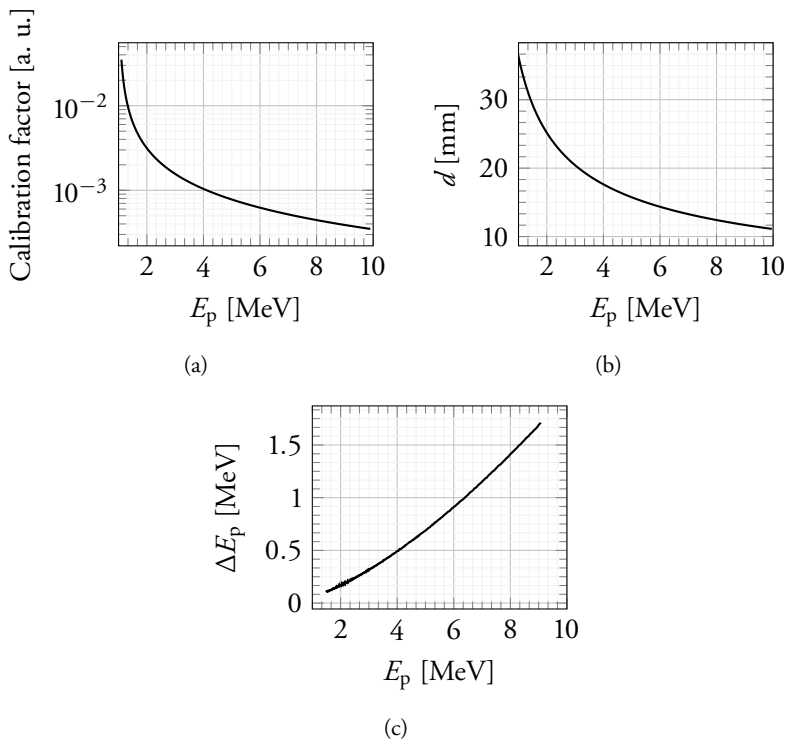


Figure 3.1 Online magnetic spectrometer

(a) Calibration curve for the plastic scintillator, used as detector for the online magnetic spectrometer, as a function of proton energy. The curve is used to convert light output (counts on EMCCD detector) to number of protons. (b) Deflection of protons by the dipole magnet in the detection plane. (c) The energy resolution of the spectrometer for different proton energies, limited by the slit width.

The opening of the entrance slit limits the resolution of the spectrometer. The imprint of uncharged particles and debris on the CR39 has a height of 1.08 mm. The geometric resolution of the spectrometer is calculated assuming that this is the case for all proton energies (i.e. a completely monoenergetic proton pulse will make a 1.08 mm high imprint on the scintillator), see Fig. 3.1(c).

A proton energy spectrum can be produced from the dispersion curve and the images of the proton trace on the CR39. The number of protons per MeV per steradian was calculated by determining the energy width that each of the images corresponds to, and the solid angle taken up by the image ($130 \mu\text{m} \times 83 \mu\text{m} / (568 \text{ mm})^2 = 3.3 \times 10^{-8} \text{ sr}$).

The number of photons emitted from the scintillator per proton depends on the amount of energy deposited in the scintillator. As protons produced in the current experimental set-up at the High-Power Laser Facility in Lund, are all assumed to be completely stopped in the 1 mm thick scintillator, the fluorescence depends on the initial energy of the protons. Filtering is used to remove “hot pixels” resulting from

x-rays hitting the sensor of the camera, and the background is then subtracted. The background level is determined from a region in the image adjacent to the proton trace. To be able to compare the proton spectra from the CR39 and the scintillator, the scintillator trace is compensated for the energy dispersion of the magnet and also for the energy width of each pixel.

The CR39 spectrum is divided by the scintillator spectrum to obtain a calibration curve, as shown in Fig. 3.1(a). Due to the noise in the scintillator spectrum a least-squares fit was made to the experimental calibration curve, which is then extrapolated to higher energies (<10 MeV).

By applying the same methods and corrections to other proton traces recorded from the scintillator, calibrated spectra can be obtained by multiplication with the calibration curve. The various steps involved in obtaining a calibrated proton spectrum from the raw image provided by the scintillator are illustrated in Fig. 3.2.

3.1.2 Online Spatial Profile Monitor

When investigating laser-driven ion acceleration mechanisms, not only the proton energy spectrum is of interest. Knowledge of the spatial profile of the proton pulse can provide further understanding. Therefore, an online spatial pulse profile monitor was developed and used at the High-Power Laser Facility in Lund, for the experiments described in Papers III and IV. This detector consists of a scintillator (St Gobain, BC-408) placed only a few centimetres from the target foil, which is imaged onto a CCD camera. The size of the scintillator is large enough to capture the whole of the diverging proton pulse at this distance. The scintillator is covered with a $12\ \mu\text{m}$ thick protecting aluminium foil, and placed at the entrance of a light-sealed box. The protective foil also prevents heavier ions with lower energies from reaching the scintillator. An optical fibre bundle is used to transport the light emitted from the scintillator, when struck by high energy protons, to a camera outside the vacuum chamber. Two objectives, one mounted on the end of the fibre bundle facing the scintillator, and one mounted on the camera, image the scintillator onto the CCD sensor. To distinguish between the signals from the detector caused by protons and by electrons, an aluminium grid is placed directly in front of the scintillator. The thickness of the grid is chosen so that it completely stops all the protons with the energies expected in the experiment, while the background caused by high-energy electrons is not significantly affected. The spatial profile of the proton pulse and the electron pulse can then be calculated by interpolation over the grid lines in the analysis process. It is, however, difficult to obtain the absolute number of protons at different positions within the pulse from the scintillator image. All protons with energies below 10 MeV, as measured in the experiments described in Papers III and IV, are fully stopped in the 1 mm thick scintillator and the number of photons emitted per proton depends on the initial energy of the proton. Due to this convoluted signal between the number of protons and their energies it is important

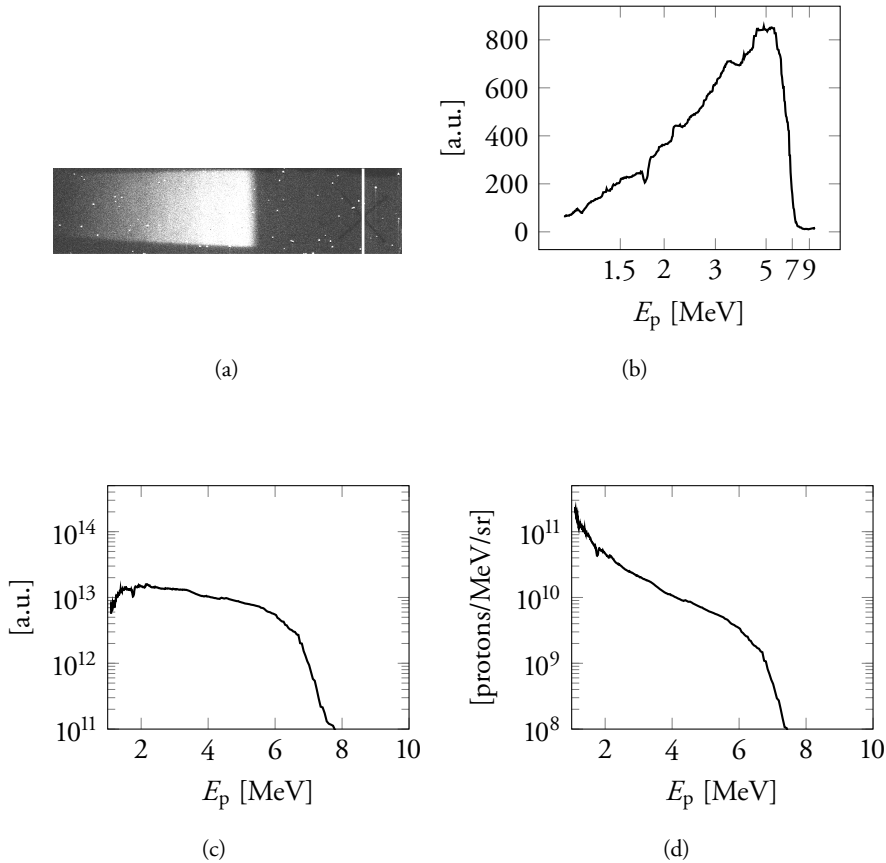


Figure 3.2 Derivation of proton spectra from the scintillator image

(a) Image of the scintillator when struck by a proton pulse accelerated from a 3 μm thick Al foil and dispersed by a dipole magnet with an entrance slit that blocks off-axis protons. The vertical white line indicates the position of protons with infinite energy. (b) Corresponding background-subtracted, vertically integrated signal. Dispersion and scintillator response are not corrected for. Note the non-linear energy axis. (c) Proton spectrum which is corrected for energy dispersion in the dipole magnet, but not for scintillator response. (d) Final calibrated proton spectrum.

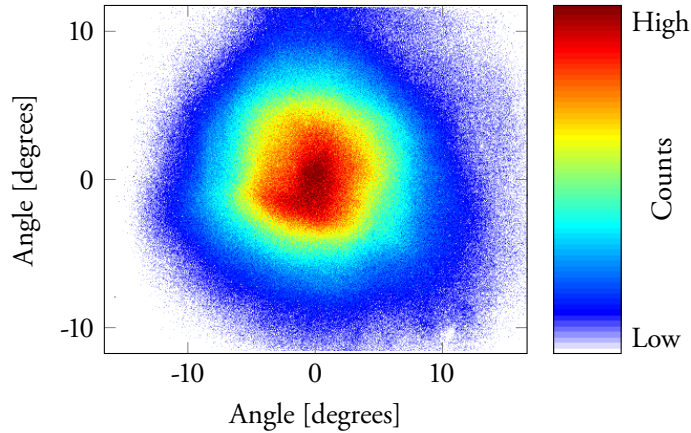


Figure 3.3 Proton pulse profile

Pulse energy profile from the online spatial detector of protons with energies above ~ 1 MeV, accelerated in the target normal sheath acceleration regime from a $3 \mu\text{m}$ thick Al foil. The peak laser pulse intensity was $2 \cdot 10^{19} \text{ W/cm}^2$.

to complement the online spatial profile detector with other instruments, such as a magnetic proton spectrometer or a Thomson parabola spectrometer, to aid in the interpretation of the image.

3.1.3 Modified Thomson Parabola Spectrometer

In order to distinguish between different laser-driven ion acceleration mechanisms, such as target normal sheath acceleration, radiation pressure acceleration and the breakout afterburner, it is vital to be able to characterize the different signatures of each mechanism. For example, the ion spectra resulting from radiation pressure acceleration show monoenergetic peaks [36], those from the breakout afterburner off-axis angular effects [64], and in all of them the laser radiation can be spectrally modified in different ways when reflected from, or transmitted through, the target. Two common diagnostic tools used when studying laser ion acceleration are stacks of RCF, which provides a spatial profile and a crude energy spectrum, but cannot distinguish between different ion species, and Thomson parabola spectrometers, which can separate ion species, but provide no spatial information. It is, however, preferable to study as many features as possible in a single laser-plasma interaction.

An electric field directed parallel to the magnetic field allows different ions to be spatially separated according to their charge-to-mass ratio, as in a Thomson parabola spectrometer, (see Section 2.4.3). This is usually done with an entrance pinhole mounted on the magnet [59]. If a slit is used instead of a pinhole, separating the different ion species becomes more complex. The advantage of using a slit is that it allows 1D spatial features to be resolved, in addition to recording the ion energies. The permanent magnets can also be mounted at an angle to each other, to further

extend the spatial acceptance angle to tens of degrees, in an ion wide-angle magnetic spectrometer [65]. An electric field can also be applied after the detection plane of the ion wide-angle magnetic spectrometer, as described in Paper I. In this way, it is possible to separate and detect multiple ion species along selected axes without losing the capability of spatial resolution. Further information on the laser-plasma interaction can also be obtained if a pick-up mirror is inserted slightly above the optical axis after the dipole magnet. Laser light transmitted through the target foil is diffracted by the ion spectrometer slit and can, be directed by the mirror to an optical spectrometer. Such a diagnostic system provides the opportunity to study multiple aspects of the laser-plasma interaction simultaneously, and was successfully implemented and tested during an experiment performed at the PHELIX-laser (reported in Paper I).

3.1.4 Laser Focus Optimization and Target Alignment

In the set-up used for the experimental studies described in Papers III and IV, overlapping laser focus optimization system and target alignment system were implemented at the High-Power Laser Facility in Lund. The experimental chamber used in this configuration is illustrated in Figure 1 in Paper II. A $10\times$ magnification infinity corrected objective (10X Mitutoyo Plan Apo NIR) was used in combination with a $1\times$ magnification tube lens to image the laser focus of a strongly attenuated laser beam onto a camera (Point Grey, Firefly FMVU-03MTM-CS). An advantage of using an infinity-corrected objective is that it allows the camera to be placed outside the vacuum chamber, more than 0.5 m from the laser focus.

The same optical system was used to image the deformable mirror (discussed in Section 2.4.2), located inside the laser pulse compressor, onto a wavefront sensor. The deformable mirror can thus also be used to correct the laser pulse wavefront for aberrations introduced by the focusing mirror, since the wavefront sensor is placed after the off-axis parabolic mirror. The diffraction limit for the off-axis parabolic mirror, with a 152 mm focal length, and the 50 mm diameter, 800 nm wavelength laser pulses is $\sim 2\ \mu\text{m}$, assuming a Gaussian beam. After running the feedback loop, a $3\ \mu\text{m}$ (FWHM) laser focus is commonly achieved.

Apart from imaging and optimizing the laser focus, the third purpose of this system is to position the thin foils used for proton acceleration in the target normal sheath acceleration regime, at the focus of the laser pulse. The rear surface of the target foil is illuminated with a red light-emitting diode, and an image is obtained in the aforementioned camera. In the experiments described in Papers III and IV, the horizontal angle of incidence of the laser pulses onto the target foils was 45° . The target foil is thus mounted at an angle with respect to microscope objective and the imaging system. Due to the shallow depth of focus of the imaging system, only a thin vertical line of the target foil is in focus in the camera image. By superimposing this line on the position of the laser focus, recorded previously with the same camera, it is possible to position the target with an accuracy better than $\pm 10\ \mu\text{m}$, (see Fig.

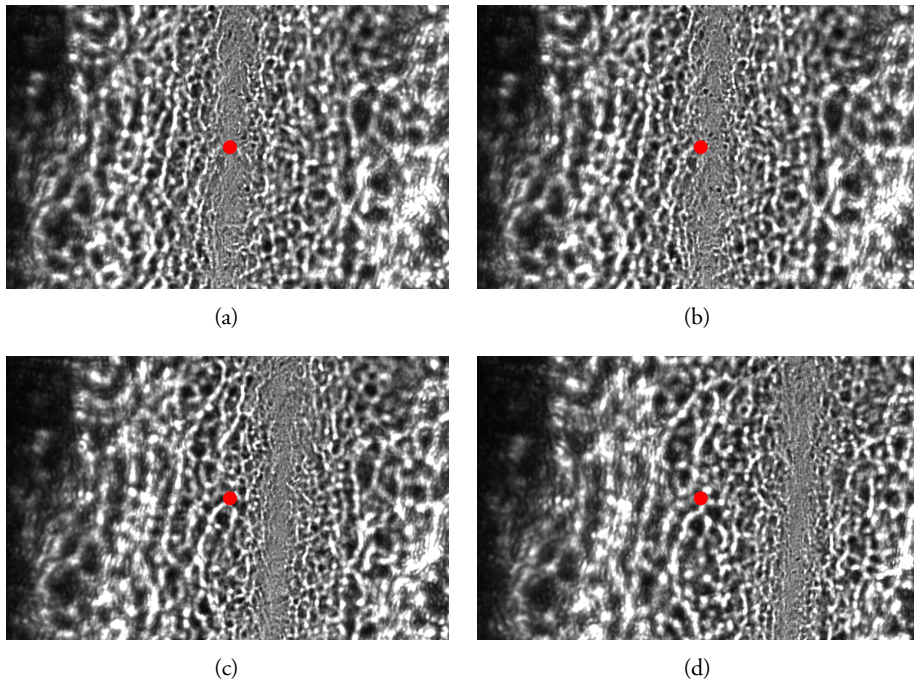


Figure 3.4 Target alignment

3 μm Al target foil positioned (a) in the laser focus (marked by the red dot), (b) 10 μm behind the laser focus, (c) 50 μm behind the laser focus and (d) 100 μm behind the laser focus.

3.4). This can be compared with the Rayleigh range of the laser pulse focus which is $\sim 35 \mu\text{m}$. Using the same system to control the laser focus and target alignment ensures that no errors are introduced by misalignments of the overlap of two separate systems.

3.2 Proton Source Characterization

One of the main goals of research in the field of laser-driven ion acceleration is to achieve better control of the laser-plasma interaction so that the accelerated ions can be used more efficiently for applications. This requires better understanding of the ion source, and Papers III and IV in this thesis describe experimental studies in which the actual acceleration mechanism was steered. After an introduction to the results of these papers, further unpublished experimental studies regarding source characterisation are discussed.

3.2.1 Split Mirror Setup

The method of manipulating the target normal sheath acceleration process, which was designed for, and implemented in, the experimental studies described in Papers II

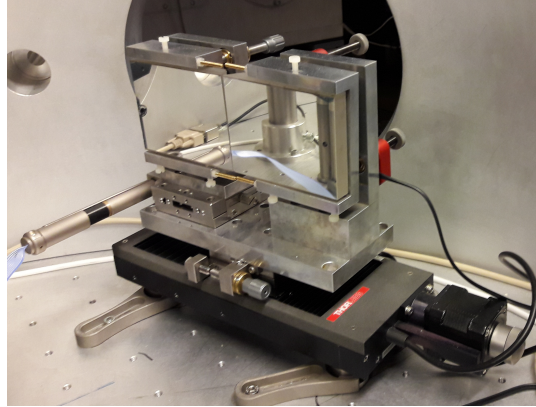


Figure 3.5 The split mirror

Image of the split mirror mounted in the experimental chamber at the Lund High-Power Laser Facility. One of the mirrors can be tipped/tilted and moved backwards/forwards with respect to the other, to introduce either a spatial or temporal separation in a laser pulse that is reflected by the mirror. The mirror can also be translated sideways to vary the energy ratio between the two parts of the reflected laser pulse.

to IV, involves separating the laser pulse in two parts. This allows the sheath formation to be steered by depositing the two portions of the energy contained in the laser pulse on the target, at slightly different points in time and space. A tool enabling these types of investigations is the split mirror described in Paper II. It consists of two mirrors mounted side by side separated by only a few hundred micrometres. One of the mirrors can be tipped or tilted with respect to the other. When the laser pulse is aligned onto the split mirror, placed before the focusing optic, in such a way that it is reflected from both parts, two foci will result, and the separation of the foci can be accurately controlled by tipping/tilting one part of the mirror. It is also possible to move both parts of the mirror sideways to vary the amount of energy contained in each part of the laser pulse, allowing the relative intensity at the two foci to be continuously varied. A third option is to move one mirror forward into the laser propagation axis, thus creating a temporal separation between the two parts of the laser pulse. All these options have been utilized in this work to study laser-driven ion acceleration mechanisms, and are presented below.

Paper III describes how the shape and size of the laser focus influence the spatial profile of the sheath on the back of the target foil and, consequently, the divergence of the proton pulse. The relative distance between the two foci, each containing 50% of the total laser pulse energy, was varied. As the distance is increased, the proton pulse becomes more collimated in the direction along the foci separation. This can be explained by the correlation between the proton pulse divergence and the shape of the sheath. Protons are accelerated perpendicular to the front of the sheath. The protons deriving from the central part of the sheath are thus more collimated than those originating from the edges. Separating the two laser foci leads to elongation of

the sheath, causing a collimating effect along the longer axis of the sheath. The spatial profile of the proton pulse was recorded for different separations of the laser foci. When they completely overlap the profile is essentially circular. An example of such profile, recorded with the spatial detector described in Section 3.1.2, can be seen in Fig. 3.3. Increasing the distance to 3 times the focal spot diameter causes an elliptical profile, while at larger separations the profile becomes circular once again. At these larger separations, two separate sheaths are formed, resulting in two independent and overlapping circular pulses. These results were verified through simulations of sheath formation, as described in the paper.

The transverse expansion of the sheath along the foil surface was studied in the experiment described in Paper IV. The laser focus was divided into two parts, using the split mirror, and these were vertically separated by a distance corresponding to approximately twice the full width at half the maximum intensity laser spot size. The two laser pulses interacted with an aluminium target foil at an angle of incidence of 45° and the intensity ratio between the two foci is set to 1.6. The non-normal angle of incidence causes the transverse sheath expansion to be different in the two horizontal directions, and the different intensities of the two foci leads to a greater transverse expansion of the part of the sheath generated from the focus with the greater energy. The measured resulting proton pulse energy profiles are thus elliptical and tilted, due to the asymmetrical and tilted shape of the sheath. It is also possible to control the tilt by varying the intensity ratio between the two foci.

3.2.2 Temporal Effects on Proton Pulses Generated with a Pair of Laser Pulses

As discussed in Section 3.2.1, the split mirror can be used to delay part of the laser pulse with respect to the other. This was implemented in order to investigate the temporal evolution of the laser-driven proton acceleration mechanism. According to Fuchs et al. [27], the time it takes for the most energetic protons to be accelerated in the target normal sheath regime, t_{acc} , depends on the intensity and duration of the laser pulse. In the set-up for laser-driven proton acceleration at the High-Power Laser Facility in Lund t_{acc} would be approximately 130 fs. Depositing more energy onto the target, in the form of a second laser pulse, after 130 fs or longer, might thus increase the number of protons, but should not affect the maximum energy of the proton pulse. However, the acceleration time is a parameter introduced in theoretical models, to compensate for the decrease in hot electron temperature through energy transfer to the protons. It is thus interesting to investigate whether this acceleration time actually has any bearing in experimental studies.

In the experiments, a 38 fs (FWHM) laser pulse was split into two parts that were completely spatially overlapped at the focus. The size of the overlapped focus was $4 \times 6 \mu\text{m}^2$. The angle of incidence between the laser axis and the Al target foil was 45° . Each of the two parts contained 400 mJ, and could be continuously separated in time up to a few picoseconds. The effect of changing the relative delay between the

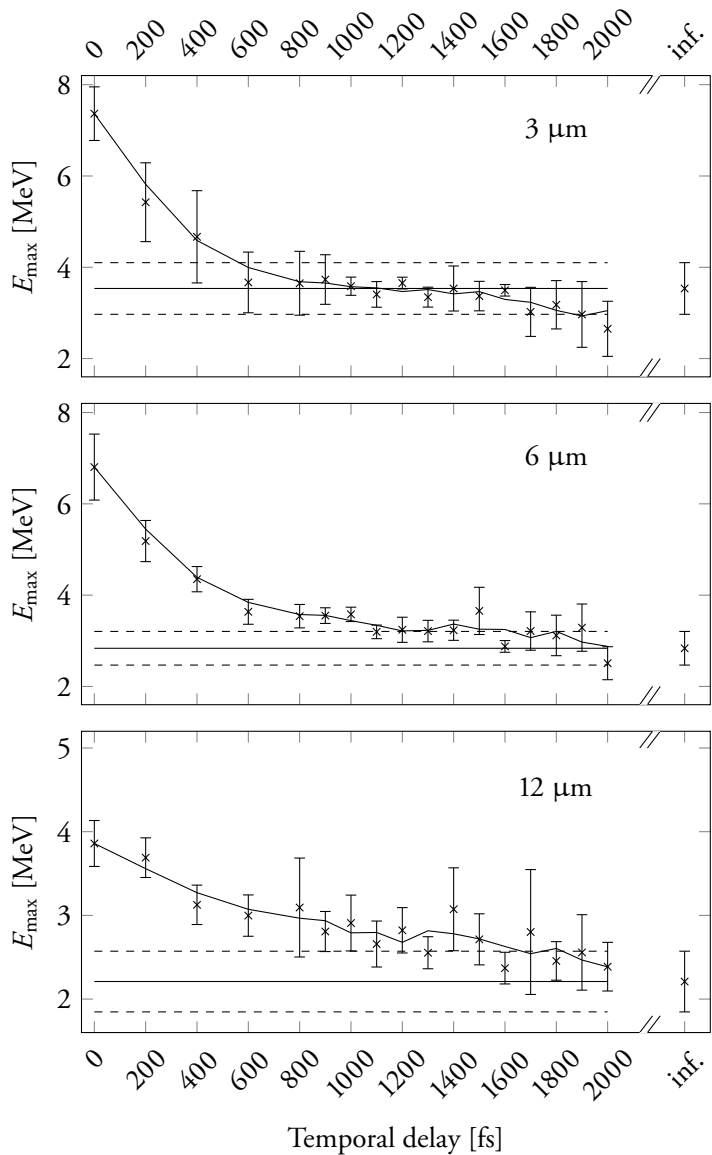


Figure 3.6 Maximum proton energy after acceleration by a pair of identical laser pulses with varying temporal delay

Maximum proton energy as a function of the relative delay between two laser pulses that are spatially overlapped at the focus. The mean value of 5 recordings, for each delay, is indicated by a cross, and the error bars show the standard deviation. The value at infinity represents an infinite delay between the pulses, i.e. only one laser pulse reaches the target foil. The solid horizontal line indicates the average infinity value, and the dashed lines indicate the standard deviation. Three different aluminium foil thicknesses were investigated: 3 μm (top), 6 μm (middle) and 12 μm (bottom).

two parts of the laser pulse on the maximum energy of the resulting proton spectra is shown in Fig. 3.6. If it can be assumed that the acceleration process is only affected by the second pulse while the process is still ongoing, then measuring how long the second laser pulse influences the maximum energy of the proton pulse will provide information on the duration of the acceleration process. It was also investigated whether the thickness of the target foil influences the temporal evolution of the acceleration process. In Fig. 3.6 zero temporal delay represents the scenario when the two pulses are fully overlapped both spatially and temporally; in other words they essentially constitute one pulse with twice the energy. An infinite delay means that only the first of the two laser pulses reaches the target foil. As the temporal delay is increased, the maximum proton energy decreases. However, this occurs much more slowly than in the model proposed by Fuchs et al. for all three target foil thicknesses investigated. There is also a clear indication that increasing target thickness causes a slower decrease in maximum proton energy. The maximum proton energy with an infinite relative delay can be used as a reference to determine when the second pulse no longer influences the acceleration process.

It was also studied how the total number of accelerated protons ($E_p > 1$ MeV) along the target-normal direction varied with the delay, and it was found to be possible to influence the number of protons with a second pulse over the whole time frame measured (2 ps). This indicates that the protons are not completely depleted from the sheath area from the first pulse, and that the second pulse may set up a second sheath, accelerating more protons. At longer time scales ($t > 2$ ps) plasma expansion will eventually prevent this.

3.2.3 Characteristics of Proton Energy Spectra for Different Target Thicknesses

The proton energy spectra vary, depending on the thickness of the target foil. This could be the result of the acceleration mechanism that comes into play, but even within the target normal sheath acceleration regime, the choice of target affects the sheath formation and thus the properties of the accelerated ions. If the temporal laser contrast is sufficiently high not to destroy the target foil before the arrival on the main pulse, the thinner the foil (at least down to the nm scale), the higher the proton energy [66]. This can be explained by the divergence of the electron beam propagating through the target; a thicker target leads to a larger sheath, and thus a lower electric field strength. It can additionally be explained with recirculation of the high-energy electrons, as they oscillate back through the foil. If the target is sufficiently thin, the laser pulse will still be ongoing, and can further heat the returning electrons. The radius of the sheath, r_s , can be expressed as:

$$r_s = r_0 + l \tan \alpha, \quad (3.3)$$

where r_0 is the radius of the laser focus, l is the thickness of the target and α the divergence half-angle of the electron beam in the target, which can range from $\sim 10^\circ$

up to a few tens of degrees [1, 52, 67].

The effect of target thickness on the shape of the proton energy spectrum, measured in the target-normal direction, was investigated in this work, and the results are presented in Fig. 3.7. Three different features can be seen: I) the proton pulses generated from 3 and 6 μm Al foils clearly have a higher maximum energy than those from 12 μm ; II) the number of low-energy protons ($E_p < 2 \text{ MeV}$) increases with foil thickness; and III) the proton spectra from the 3 μm foil decay approximately exponentially with increasing proton energy (i.e., they appear linear on the semi-logarithmic scale in Fig. 3.7), which is not the case for 6 and 12 μm thick foils.

Feature I) is in accordance with the results reported by of Neely et al. [66] discussed above. Feature II) can be explained by Eq. 3.3, and is, to some degree, a consequence of I). A larger sheath with a lower maximum field strength accelerates more protons, but to lower energies. This is based on the assumption that the sheath does not fully deplete the proton population on the back of the foil for any of the foil thicknesses studied, and that the efficiency of energy transfer from the laser to the sheath does not depend on the target thickness. The explanation of feature III) is, however, less intuitive. One explanation could be two separate hot-electron populations, driven by different heating mechanisms. If these heating mechanisms have different directionality, such as resonance absorption and $\mathbf{j} \times \mathbf{B}$ heating (see Section 2.2.5), a thicker target would enhance the spatial separation between the two populations. These two populations of energetic electrons would set up two sheaths, which could be partially overlapping, and thus accelerating proton bunches with slightly different properties. The proton spectra measured in this study, along the target-normal direction, would be expected to show contributions from protons originating from both sheaths, and will therefore deviate from the expected exponentially decaying energy spectrum. Similar results have been reported by Fang et al. [43], using a comparable set-up. They explained the plateaux observed in the proton energy spectra as being due to the simultaneous occurrence of two different ion acceleration mechanisms: target normal sheath acceleration and collisionless shock acceleration.

Simulations are being carried out to determine how our proton spectra were generated, and to better understand the observed change in spectral shape.

3.3 Novel Applications

Laser-driven proton acceleration is a growing field, in which novel applications in materials and medical sciences are becoming a reality. Methods utilizing the unique properties of laser-accelerated protons to study the interaction between energetic protons and different materials are described in Papers VI and V.

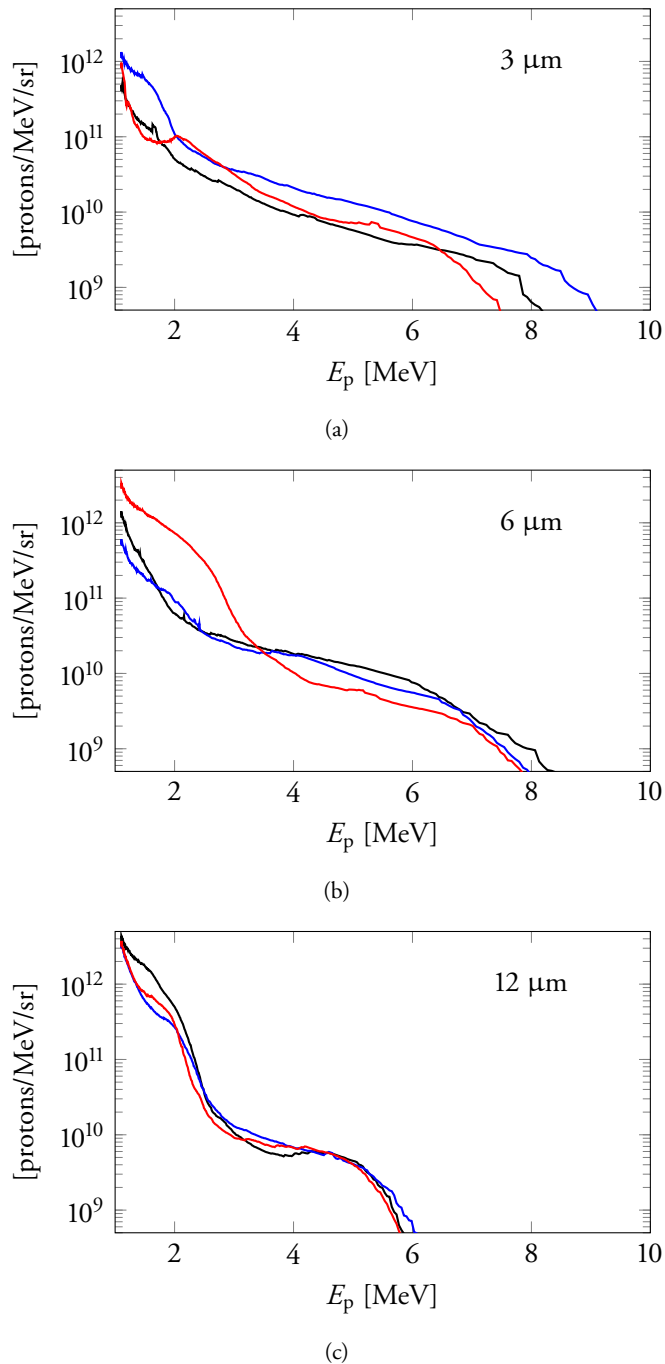


Figure 3.7 Comparison of proton spectra from target foils with different thicknesses
Proton spectra from (a) 3 μm Al foil, (b) 6 μm Al foil, (c) 12 μm Al foil. Three representative proton spectra for each foil thickness are shown. The laser energy on the target was 0.65 J, the laser pulse duration was 38 fs (FWHM), and the laser temporal contrast was $3 \cdot 10^{-9}$ measured 100 ps before the arrival of the main pulse. The laser focus size was 3.5 μm (FWHM). The appearance of the proton spectra changes with increasing target thickness, from a simple exponential decay to a double structure.

3.3.1 Pump-Probe Set-up for Time-Resolved Radiolysis

One of the unique advantages of laser-accelerated protons is that it is possible to split the laser pulse before interacting with the target, and use one part to drive the acceleration process, and the other as an optical probe with variable time delay, but without temporal jitter. Studies have been conducted in which the optical probe is used to image the plasma dynamics with shadowgraphy [68–70]. Paper VI presents a scheme in which the optical probe is used to image the interaction of laser-accelerated protons with an optically transparent material. A chirp is introduced into the probe pulse, such that different frequencies pass through the interaction volume at different times, thereby enabling temporal resolution of the interaction mechanisms through the use of an imaging spectrometer. For this scheme to work, the absorption and/or scattering of the probe pulse wavelength(s) in the investigated material must change when the material is exposed to high-energy protons. To determine any changes in the transmission of the probe pulse, it is recorded twice: once with high-energy protons present in the material and once without. The ratio between the two recordings represents the change in transmission, where each wavelength corresponds to different points in time.

Jitter makes it difficult to electronically synchronize two pulses much below the nanosecond timescale, and this also limits the time resolution. The main advantage of studying how different materials react to proton radiation with the method described here, is that the probe pulse and the driving pulse come from the same source, and are therefore intrinsically synchronized in time. This allows sub-picosecond temporal resolution to be achieved, as reported in Paper VI. Other advantages are the short pulse-durations of laser accelerated protons and the very high dose rates; these will be further discussed in the sections below.

Picosecond Radiolysis of Glass with Laser Accelerated Protons

Optical opacity was induced in fused silica (SiO_2) and borosilicate glass (BK7) by using laser-accelerated protons, as described in Paper VI. Energetic protons deposit their energy in the glass and excite electrons from the valence band to the conduction band. If the probe pulse arrives at the interaction volume before these electrons recombine, the electrons contribute to the absorption of the optical radiation through free-free absorption. This happens when a free electron gains energy by absorbing a photon while colliding with an ion.

The lifetime of the electrons in the conduction band can be deduced by studying the change in the transmission of the probe pulse, when the glass is exposed to proton radiation and directly thereafter. It was previously only possible to carry out such experiments with picosecond time resolution using photoexcitation [71]. Using laser-accelerated protons allows for investigations of differences in the way which the glass reacts to irradiation by photons and ions. In the experiment described in Paper VI, the lifetime of electrons in the conduction band was measured and found to be <

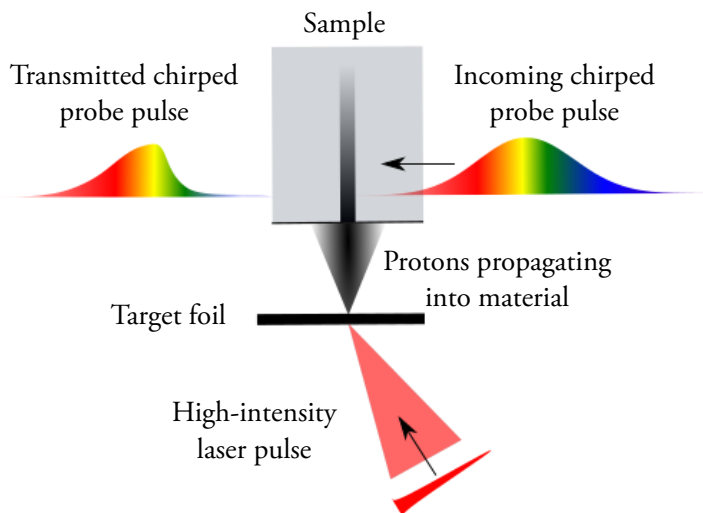


Figure 3.8 Pump-probe set-up

Schematic illustration of the way in which an intense laser pulse can accelerate protons, and a chirped pulse, originating from the same source, is used to probe processes induced in a material by the energetic protons. Proton pulses accelerated in the target normal sheath acceleration regime are divergent, therefore, a collimating entrance slit is placed in front of the sample. In the experiments described in Papers VI and V, the bandwidth of the chirped probe pulse is only a few nanometres, but it is illustrated here with different colours for clarity. Due to the chirp, different frequencies arrive at the interaction volume at different times. Separating the frequencies with a spectrometer thus gives the temporal evolution of the change in transmission induced by the laser-accelerated protons. In the case illustrated here, the high-energy protons arrive at the material when approximately half the probe pulse has passed through the material, modifying the intensity profile of the second part of the transmitted probe pulse. When an imaging spectrometer is used to image the probe pulse in the sample, with the entrance slit oriented along the proton propagation axis, both spatial and temporal information can be recorded in a single shot.

0.2 ps in fused silica. The very fast recovery of this material makes it suitable for use in proton pulse duration diagnostics, which further discussed in the section below. In contrast to fused silica, the borosilicate glass was found to have a much longer lifetime, of > 400 ps. This is, however, still considerably shorter than previously published results of 5000 ps, obtained by photoexcitation [71].

Proton Pulse Diagnostics

As mentioned above, the short lifetime of the electrons in the conduction band in fused silica, thus also the proton-induced opacity, makes it suitable for proton pulse diagnostics. In the experiments reported in Paper VI, protons were accelerated in the target normal sheath acceleration regime. The proton pulses, in this case ranging up to ~ 10 MeV, have an exponentially decaying energy spectrum. These protons are non-relativistic, meaning that protons of different energies travel with different

velocities. While the high-energy protons propagate from the target foil to the fused silica sample, the pulse duration will increase due to energy dispersion. However, the range of a high-energy proton in a material depends on its initial energy. The protons with the highest energies reach furthest into the material, meaning that, at this depth, the proton pulse becomes essentially monoenergetic, and its duration is the same as at its source. By measuring the duration of the change in transmission at the depth in the material that only protons within an energy bandwidth of 0.5 MeV could reach, the proton pulse duration was determined to be 3.5 ± 0.7 ps. The laser pulse driving the acceleration process had a duration of 600 fs. To calculate the acceleration time from Eq. 2.19, a correction should be made, since the peak laser intensity (approximately $1 \cdot 10^{19}$ W/cm²) was slightly below the value of $I_1 = 3 \cdot 10^{19}$ W/cm² required. With this correction, the equation becomes $t_{\text{acc}} \approx 2.5(\tau + 60)$ [fs] [27], leading to an acceleration time of $t_{\text{acc}} = 1650$ fs, which is significantly shorter than the measured value of 3.5 ± 0.7 ps. Thus, the two fundamentally different methods of measuring t_{acc} described in this thesis, the other was discussed in Section 3.2.2, both indicate that fitting the acceleration time to compensate for the temperature decay of hot electrons does not fully describe the physical processes.

Picosecond Radiolysis of Water with Laser-Accelerated Protons

Paper V presents experiments in which the unique properties of laser-accelerated protons were utilized to study how picosecond bunches of energetic protons interact with water; an area of physics especially interesting due to its interdisciplinary relevance in biology and radiation medicine.

The experimental pump-probe scheme, described above, allows investigations, with unsurpassed time resolution, of the ultrafast mechanisms occurring in water radiolysis by protons, that have previously only been accessible through simulations. When an energetic proton propagates in water, it deposits energy by ionizing water molecules. The electrons released in this process will become thermalized and later solvated in the water. These electrons, and other radiolytic species, form along the proton tracks in so-called spurs. Some properties of solvated electrons in water are well known [73], but their structure and the underlying physics are still the subject of debate. It has not been demonstrated whether a solvated electron can be modelled by an electron in a cavity surrounded by water molecules [74], or the opposite, an electron in a volume with an increased density of water molecules [75]. One of the signatures of solvated electrons in water is the broad optical absorption spectrum (see Fig. 3.9), peaking around 700 nm and extending from the ultraviolet into the infrared region [76]. The transmission of a near-infrared probe pulse in water, as in the experiment described in Paper V, thus changes when the water sample is irradiated with protons. These variations in transmission were recorded and studied in an attempt to understand how the high radiation doses delivered in short proton pulses (kGy dose delivered in < 80 ps) affect the ultrafast yield of solvated electrons.

If laser-accelerated protons are to be used in radiation medicine, it is important

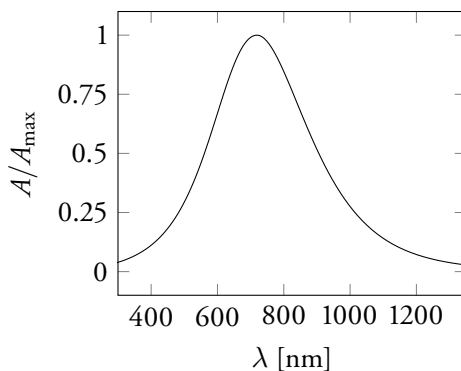


Figure 3.9 Absorption spectrum of solvated electrons in water

Absorption spectrum of solvated electrons in water at room temperature for different wavelengths, λ , adapted from parameters given by Jou et al. [72]. The level of absorption, A , is normalized to the maximum absorption, A_{\max} .

to understand how the dose rate affects cell damage, bearing in mind the short proton pulse duration. The yield of solvated electrons is an indicator of this, since the precursors of solvated electrons have been suggested to play a role in the damage of biomolecules [77]. Simulations of the change in the yield of solvated electrons when two proton tracks are close, in both time and space, have been published [78], showing a decrease in the yield for decreasing track separation. Paper V presents experimental data that support these simulations. It should, however, be noted that the difference in yield is mainly important for dose calculation purposes, and does not prevent the use of laser-accelerated protons for radiation therapy.

OUTLOOK

This chapter discusses future prospects of laser-driven ion acceleration. Apart from the fundamental aim of increasing our understanding of how intense light interacts with matter, there are several areas where considerable progress should be possible over the next few years, and others where progress may take a little longer. In this chapter, some potential applications of laser-accelerated ions are presented, together with some developments in lasers, targets and acceleration mechanisms that may facilitate the implementation of such applications.

4.1 Future Applications

A great deal of effort has been devoted to developments aimed at the use of laser-accelerated ions for cancer treatment, in the form of radiotherapy, as a cost-efficient alternative to cyclotron accelerators [78–83]. However, higher ion energies, around 250 MeV for non-superficial tumours [80], and better control of pulse parameters are required before treatment schemes based on laser-accelerated ions can be successfully implemented in hospitals. It is also desirable to keep the duration of each therapy session short, meaning that the repetition rate of the delivered proton pulses should be high.

Another possible future application of laser-accelerated ions is in fast ignition of fusion targets [84], where the energy deposition characteristics of ions in materials are utilized to locally ignite a pre-compressed fuel pellet. By matching the energy of the proton pulse, and thus the corresponding Bragg peak, to the desired point of ignition in the pellet, it should be possible to limit the ignition to a small volume. The advantages of using laser-accelerated ions, over ions from a radio-frequency accelerator, are the ultrashort pulse duration and high dose rate, leaving little time for the development of instabilities during ignition.

Another area in which laser-accelerated protons could be used is in the production of short-lived radioactive isotopes used for positron emission tomography (PET). In this case, the energetic protons are used to drive nuclear reactions. To achieve the required activity of the isotopes it is again important to increase the laser and the proton pulse repetition rate [85].

The application of pulses of laser-accelerated protons for time-resolved radiolysis of different materials, can also be further developed. It is, for example, possible to investigate other materials, and also to use laser pulses with broader bandwidths, thus enabling better time resolution in the probing.

4.2 Laser Development

Existing lasers with the highest power output, such as Vulcan (The Rutherford Appleton Laboratory, UK), the Texas Petawatt laser (The University of Texas at Austin, USA), LFEX (Osaka University, Japan) and PHELIX (GSI, Darmstadt, Germany), are capable of delivering laser pulses with repetition rates up to a few shots per hour, and it is from this type of laser the highest proton energies have been achieved so far (>85 MeV) [86]. Reasonable average beam currents can be achieved by either improving the conversion of laser energy to ion energy, and using lasers with already high repetition rates, but lower output power, more efficiently to accelerate protons, or further development of the laser technology, to increase the repetition rate of petawatt lasers. Some steps towards higher repetition rates will be implemented in a 10 petawatt laser at the Extreme Light Infrastructure Beamlines facility in Prague, currently under construction, by more efficient cooling of the glass discs commonly used for laser amplification. Repetition rates of one laser pulse per minute have been achieved with this novel glass-disc cooling technique [87], but this is still far below the repetition rates of conventional radio-frequency accelerators. The recently operational CETAL-laser in Romania has a slightly lower output power (1 PW), but can deliver 25 fs pulses at a rate of 0.1 Hz [88], and the 1 petawatt BELLA laser (Berkeley, USA) runs at a repetition rate of 1 Hz.

Apart from achieving higher laser energies and repetition rates, it is also vital, due to the non-linear nature of the acceleration process, to improve the control of laser pulse parameters, such as pointing, wavefront, pulse duration and energy content, in order to achieve reproducible proton pulses.

High laser temporal contrast is especially important for the efficient acceleration of ions from solid targets. Efforts to improve this parameter, while maintaining a high laser intensity at the focus, include the implementation of ellipsoidal plasma mirrors [89]. However, implementation of such mirrors is difficult in high-repetition-rate systems.

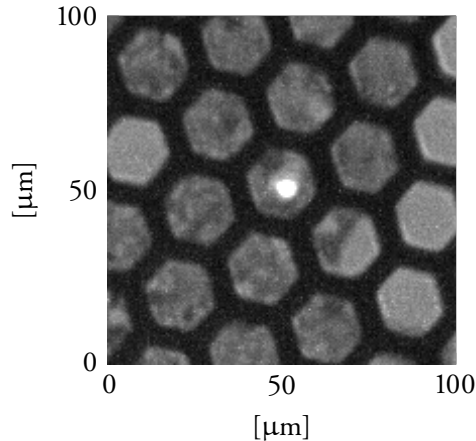


Figure 4.1 Graphene

1- to 7-layer graphene on a supporting copper grid, mounted at a position overlapping the laser focus in the experimental target chamber at the Lund High-Power Laser Facility. The lighter hexagons on the right contain no graphene. The bright spot in the centre is a focused attenuated femtosecond laser pulse transmitted through the graphene. (Photo courtesy of Hannes Pahl.)

4.3 Target Development

Over recent years, a variety of target designs for laser ion acceleration have been suggested to increase the maximum ion energy, and to control other ion pulse parameters. The use of density gradients on the front of targets, for example, using a foam layer, to increase laser absorption, have shown promising results in simulations [90], but the fabrication of such targets with sufficiently high quality has until now been difficult. An improved technique for the manufacture of foam targets has led to almost a doubling of ion energies compared with the energetic ions originating from a flat foil under the same conditions [91]. This suggests that it might be possible in the near future to significantly increase ion energies in the target normal sheath acceleration regime, if it is possible to achieve similar results with other laser systems, i.e., other laser parameters. Other novel target designs include foils with nanoparticles [92, 93] or gratings [94], and mass-limited targets [95]. However, due to the limited increase in ion energies from such designs, it seems unlikely that they will enable new high-energy applications, but could instead contribute to applications that require small source sizes or collimated pulses.

An interesting option in the development of targets is the use of graphene [96]. This could be used, for example, as the thin layer for chirped standing-wave acceleration, described in Section 4.4 below, or as a single target for acceleration mechanisms such as radiation pressure acceleration, or in acceleration schemes in the relativistic transparency regime. However, it is not known whether the collective effects of a traditional 3-dimensional plasma would persist due to its very thin nature;

in single-layer graphene only one atomic layer thick. It should, however, be borne in mind that unless graphene is handled in ultra-high vacuum, there may be a few atomic layers of contamination such as water and hydrocarbons. One problem in the manufacture of graphene is to make free-standing areas that are sufficiently large to focus a laser pulse onto without interacting with the supporting grid (see Fig. 4.1). Another challenge lies in obtaining the level of laser temporal contrast required for the main laser pulse to interact with the target, before it is damaged by the pulse prepulse.

4.4 Development of Laser Ion Acceleration

One of the main hurdles to be overcome in laser-driven ion acceleration, as mentioned in the introduction, is that non-relativistic ions travel more slowly than the laser pulse, thereby limiting the time frame in which energy transfer is possible between the ion pulse and the laser pulse. This problem could be solved by achieving relativistic energies through novel or improved laser-driven ion acceleration mechanisms, or by schemes circumventing the problem such as those proposed by Mackenroth et al. [97] and Isaacs et al. [98] and mentioned below. Another solution would be to somehow accelerate ions in an environment where the light group velocity is reduced, so-called “slow light” [99], which could co-propagate with non-relativistic ions.

A novel laser acceleration mechanism called chirped standing wave acceleration has recently been proposed [97]. The fundamental idea behind this scheme is to reflect a broadband, intense chirped laser pulse off a substrate at quasi-normal incidence, and to place a thin film layer at the first node of the resulting standing wave. In order to create a standing wave, the thin layer must become relativistically transparent to the laser pulse. Electrons from the layer are locked in the node by the ponderomotive force, and move as the chirp causes the node to move, and charge separation will cause the ions to follow. Simulations have shown peaked ion energy spectra around 100 MeV for 10 J laser pulses, but technical difficulties, such as target mounting, must be overcome before the concept can be experimentally realized. Another proposed acceleration scheme is proton acceleration in a slow wakefield [98]. In this case, two laser pulses of different durations collide in a plasma with a spatial density gradient. The resulting beating creates a slow-moving wakefield where ions can be accelerated, comparable to the case of laser wakefield acceleration of electrons.

Another suggested way forward is the regime of single-cycle laser acceleration, where an ultrashort (a few femtoseconds) petawatt laser pulse is used to avoid the development of instabilities in acceleration mechanisms such as radiation pressure acceleration [100]. There are currently no single-cycle petawatt lasers anywhere in the world, but a proposed compression scheme, relying on a laser pulse with top-hat near-field profile, to compress it in several stages from ~ 30 fs to ~ 2 fs using sheets of sub-millimetre plastic films to spectrally broaden the pulse, may make such pulses

possible in the future [101].

LASER WAKEFIELD ACCELERATION OF ELECTRONS

This appendix provides a brief introduction to laser wakefield acceleration of electrons, in relation to the experimental studies presented in Papers VII, VIII and IX.

A.1 Laser Acceleration of Electrons from a Plasma

The ponderomotive force of a laser pulse propagating through an underdense plasma drives electrons away from the most intense regions (see Sec. 2.2.2). Since the force increases with decreasing mass, the heavier, positively charged ions remain almost stationary compared to the electrons. Behind the laser pulse, the electrons will oscillate back and forth around the equilibrium, creating a plasma wave with a phase velocity similar to the laser group velocity, close to the speed of light in vacuum. The separation of electrons from positive ions gives rise to a strong electric field, up to several 100 GV/m, into which electrons can be injected and accelerated to high energies. The accelerating field is lower than in the case of laser-driven ion acceleration (typically \sim TV/m), but the lighter electrons can become relativistic and co-propagate with the laser, and can thus be accelerated over longer distances (millimetres compared to tens of micrometres). The concept of electron accelerators based on processes in laser plasmas was first proposed by Tajima and Dawson in 1979 [102]. Experimental progress was made over the following decades, in particular, once so-called “wavebreaking” had been discovered [103]. Wavebreaking occurs when the amplitude of the plasma wave becomes so high that it cannot be sustained, and electrons start moving forwards, in the frame of the wave, and into the electric field. This takes place when the phase velocity of the plasma wave is lower than the velocity of the electrons. These electrons are injected into the accelerating electric field and may deform the plasma wave, which prevents further wavebreaking, and

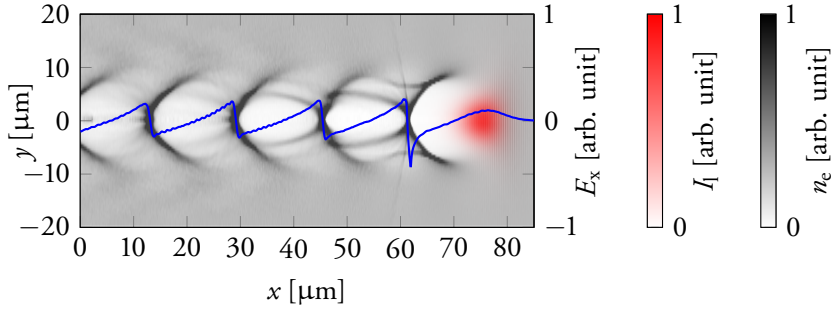


Figure A.1 Laser wakefield

Particle-in-cell simulation of a high-intensity laser pulse propagating through an underdense plasma, performed with CALDER-Circ [107]. The greyscale indicates electron density, n_e , and the red colour scale the laser intensity, I_l . The laser pulse propagates from left to right, along the x -axis. The ponderomotive force drives electrons away from the intense laser light, creating a void of electrons behind the laser pulse. Since the heavier positive ions in the plasma are much less affected, this leads to charge separation. The resulting longitudinal electric field, E_x , is represented by the blue line. If electrons are injected into this field at a position where they experience a force along the laser propagation axis, they can be accelerated to relativistic energies. Examples of electron injection mechanisms are given in the text. (Figure courtesy of Henrik Ekerfelt.)

the electrons become trapped. However, the first demonstrations of laser wakefield acceleration of electron bunches with low energy spread were not reported until 2004 [104–106]. This was attributed to localized injection of electrons in the accelerating field, where the electrons are consequently accelerated over the same distance and reaching the same energy.

Many different processes determine the way in which an intense laser pulse propagates through an underdense plasma, and the acceleration process depends on them all. A laser pulse passing through a tight focus in vacuum will be highly divergent, due to diffraction, but in an underdense plasma contributions from other processes complicate the dynamics. The refractive index of the plasma depends on the electron density. The laser pulse reaches its highest intensity in the central part of the focus, where field ionization will be most effective. Depending on the ion species and the laser intensity required for field ionization of inner electrons, this may cause a radial electron density gradient, and thus a gradient in refractive index, corresponding to a negative lens. This is called ionization defocusing. This effect is greater for heavier atoms and molecules, since lighter ones, with fewer electrons, usually become fully ionized by the intense laser, and ionization defocusing then only occurs in the wings of the focus. However, the laser pulse has lower intensity out of the focal plane and ionization defocusing may take place here.

A relativistic effect that counteracts both ionization defocusing and diffraction of the laser pulse is self-focusing. The increased mass of the electrons in the plasma as they reach relativistic energies, due to oscillation, will affect the refractive index of the plasma. The greater the electron mass, the greater the increase in the refractive

index [108]. The radial variation in intensity in the laser focus will lead to an effect comparable to that of a positive lens. This effect can guide an intense laser pulse through an underdense plasma over distances corresponding to several Rayleigh ranges.

The electron density also varies longitudinally in the plasma wave, leading to different group velocities within the laser pulse. The front of the pulse experiences a higher electron density, leading to a lower group velocity, than the back, which causes temporal compression of the pulse.

Dephasing limits the energy gain of the electrons. Electrons that are injected into the accelerating field experience an increase in energy and as their velocity approaches speed of light, they outrun the accelerating phase of the plasma wave and end up in a decelerating region, if the phase velocity of the wave is lower than the velocity of the electrons [3]. For the negatively charged electrons, the electric field, E_x , shown by the blue line in Fig. A.1, accelerates in the positive direction for negative values of E_x .

Another factor that limits the acceleration length is pump depletion. As energy is transferred from the laser pulse, i.e. the pump, to the plasma wave, where it will be dissipated through thermal effects, the laser pulse will decrease in intensity until it can no longer drive the wave. The depletion length, corresponding to the distance over which the laser pulse loses all its energy, is proportional to the inverse of the electron density.

Electrons in the wakefield may have transverse momentum and wiggle due to a restoring force resulting from charge separation. Charged particles that oscillate emit radiation, and laser wakefield acceleration of electrons can therefore also produce x-rays. In the experiments described in Paper VIII these x-rays were used as a tool to diagnose the acceleration process.

Underdense plasmas for laser wakefield acceleration are typically produced from gas jets. Paper VII discusses the technical aspects of how the choice of gas influences the acceleration process. Papers VIII and IX describe experimental studies where the laser wakefield acceleration process was guided inside thin dielectric capillary tubes.

A.2 Laser Wakefield Acceleration in Dielectric Capillaries

There are several advantages of performing laser wakefield acceleration inside a waveguide. Since self-focusing is not necessary to guide the laser pulse, the plasma density can be arbitrarily low. This means that the depletion length can become very long, and the group velocity of the laser approaches c . Another advantage is the shock-free gas flow inside the capillary [109]. It is also possible to choose the capillary diameter and plasma density so that energy from the wings of the laser focus is reflected off the walls and contributes to increased self-focusing, compared to similar conditions in a gas cell or jet [110].

In the experimental study described in Paper IX the stability of the resulting electron pulses from laser wakefield acceleration in capillary tubes was compared with the stability of electrons accelerated from a gas jet. The capillaries had inner diameters between 150 and 260 μm , and lengths of 10 to 20 mm. It was found that the use of capillary tubes enhanced the stability of the electron pulses in terms of both charge and divergence.

By allowing the laser pulse to interact with a gas mixture of different species, it is possible to inject electrons into the wakefield in another way than wavebreaking. In this case, one gas with low atomic number, such as helium, which will be completely ionized by the leading edge of the laser, is mixed with a small amount of another gas consisting of molecules or atoms that require higher intensities for field ionization of the inner electrons. Electrons will be released from the heavier gas atoms when the most intense part of the laser pulse reaches the interaction volume and will be immediately trapped in the wake behind the laser pulse. For example, helium can be completely ionized by a laser field with an intensity of $I_1 = 8.8 \cdot 10^{14} \text{ W/cm}^2$, whereas the two innermost electrons of nitrogen require an intensity of $I_1 = 1.0 \cdot 10^{19}$ and $I_1 = 1.6 \cdot 10^{19} \text{ W/cm}^2$ for field ionization. In the experiments the peak laser intensity was $I_1 = 4.4 \cdot 10^{18} \text{ W/cm}^2$, without taking self-focusing or pulse compression into account, which will increase the intensity. In this case one, or even two, of the inner electrons of the nitrogen atom may experience fields sufficiently intense for ionization.

Paper VIII presents an experimental study of the ionization injection mechanism. This was done by investigating the x-ray emission volume in the plasma. The divergent x-ray pulses were shadowed by the edges of the capillary tube exit, and recorded images of the x-rays showed circular shapes corresponding to the exit of the capillary. Assuming the divergence to be constant from shot to shot, the diameter of this circle can be used to determine where the x-ray emission took place. When comparing these images with x-rays from self-injected electrons and from ionization-injected electrons it became clear that ionization injection occurs earlier.

A.3 Densities in Supersonic Gas Flows for Laser Wakefield Acceleration

To create a gaseous target of suitable density for the formation of underdense plasmas and laser wakefield acceleration of electrons, gas with a high backing pressure (tens of bars) is released through a pulsed gas nozzle (up to several mm diameter). This leads to the formation of a high-density supersonic gas jet.

Two of the most common choices of gas targets for laser wakefield acceleration are hydrogen and helium. Since hydrogen gas consists of H_2 molecules, completely ionized gases of hydrogen and helium at the same pressure should release the same number of electrons, and the underdense plasmas formed should have the same properties. The Coulomb repulsion between the two protons released from each

ionized H_2 molecule, occurs on timescales that are much longer than those for plasma wave formation and the acceleration process. Laser wakefield acceleration should thus work similarly in hydrogen and helium at the same gas concentration. However, the results from experimental studies using the same backing pressure for the gas jets of helium and hydrogen, from which an underdense plasma is created and electrons are accelerated, reported in Paper VII, showed different electron pulse properties. The difference was found to originate in fluid mechanical properties of hydrogen and helium, which have different constants for specific heat. Using the same backing pressure for the same nozzle thus results in different gas densities, and different electron number densities in the plasmas formed. This was confirmed by probing the plasmas with a beam from a HeNe laser and measuring the induced phase shift with a wavefront sensor.

MATHEMATICAL DESCRIPTION OF ELECTRON IN ELECTROMAGNETIC FIELD

This appendix includes the mathematical description of some of the physics presented in Sec. 2.1.

B.1 The Lorentz Force for a Relativistic Particle

A scalar and a vector potential can be used to describe electric and magnetic fields.

$$\mathbf{A} = \mathbf{A}(t, \mathbf{r}) - \text{Vector potential}, \quad (\text{B.1})$$

$$\phi = \phi(t, \mathbf{r}) - \text{Scalar potential}. \quad (\text{B.2})$$

Here t denotes time and \mathbf{r} is a room vector. The electric and magnetic fields, \mathbf{E} and \mathbf{B} respectively, are related to the potentials through:

$$\mathbf{B} = \nabla \times \mathbf{A}, \quad (\text{B.3})$$

$$\mathbf{E} = -\frac{\partial \mathbf{A}}{\partial t} - \nabla \phi. \quad (\text{B.4})$$

The relativistic Lagrangian, \mathcal{L} , for a particle with charge q and invariant mass m moving in an electromagnetic field with a velocity, \mathbf{v} , is then given by:

$$\mathcal{L}(\mathbf{r}, \mathbf{v}, t) = E_{\text{kin}}(\mathbf{r}, \mathbf{v}, t) - E_{\text{pot}}(\mathbf{r}, \mathbf{v}, t) = -mc^2 \sqrt{1 - \frac{\mathbf{v}^2}{c^2}} + q\mathbf{v} \cdot \mathbf{A} - q\phi, \quad (\text{B.5})$$

where c is the speed of light.

The Euler-Lagrange equation states that:

$$\frac{d}{dt} \frac{\partial \mathcal{L}}{\partial \mathbf{v}} - \frac{\partial \mathcal{L}}{\partial \mathbf{r}} = 0. \quad (\text{B.6})$$

The different derivatives in Eq. B.6 are calculated stepwise:

$$\begin{aligned} \frac{\partial \mathcal{L}}{\partial \mathbf{v}} &= \frac{\partial}{\partial \mathbf{v}} \left(-mc^2 \sqrt{1 - \frac{\mathbf{v}^2}{c^2}} + q\mathbf{v} \cdot \mathbf{A} \right) \\ &= mc^2 \frac{1}{2} \frac{1}{\sqrt{1 - \frac{\mathbf{v}^2}{c^2}}} \frac{2\mathbf{v}}{c^2} + q \frac{\partial}{\partial \mathbf{v}} (v_x A_x + v_y A_y + v_z A_z) \\ &= m\mathbf{v} \frac{1}{\sqrt{1 - \frac{\mathbf{v}^2}{c^2}}} + q \left(\frac{\partial}{\partial v_x} (v_x A_x), \frac{\partial}{\partial v_y} (v_y A_y), \frac{\partial}{\partial v_z} (v_z A_z) \right) \\ &= \mathbf{p} + q\mathbf{A}, \end{aligned} \quad (\text{B.7})$$

$$\begin{aligned} \frac{d}{dt} \left(\frac{\partial \mathcal{L}}{\partial \mathbf{v}} \right) &= \frac{d}{dt} (\mathbf{p} + q\mathbf{A}) = \dot{\mathbf{p}} + q\dot{\mathbf{A}} = \dot{\mathbf{p}} + \frac{\partial \mathbf{A}}{\partial t} + \nabla \mathbf{A} \mathbf{i} \\ &= \dot{\mathbf{p}} + \frac{\partial \mathbf{A}}{\partial t} + \nabla \mathbf{A} \mathbf{v}, \end{aligned}$$

$$\frac{\partial \mathcal{L}}{\partial \mathbf{r}} = q \left(v_x \frac{\partial A_x}{\partial r_x}, v_y \frac{\partial A_y}{\partial r_y}, v_z \frac{\partial A_z}{\partial r_y} \right) - q \nabla \phi = q (\nabla \mathbf{A})^T \mathbf{v} - q \nabla \phi,$$

where \mathbf{p} is the relativistic momentum.

Inserting the different derivatives into the Euler-Lagrange equation, it gives that:

$$\frac{d}{dt} \frac{\partial \mathcal{L}}{\partial \mathbf{v}} - \frac{\partial \mathcal{L}}{\partial \mathbf{r}} = \dot{\mathbf{p}} + q \frac{\partial \mathbf{A}}{\partial t} + q \nabla \mathbf{A} \mathbf{v} - q (\nabla \mathbf{A})^T \mathbf{v} + q \nabla \phi = 0. \quad (\text{B.8})$$

Solving the equation for $\dot{\mathbf{p}}$ leads to:

$$\begin{aligned} \dot{\mathbf{p}} &= q \left(-\frac{\partial \mathbf{A}}{\partial t} - \nabla \mathbf{A} \mathbf{v} + (\nabla \mathbf{A})^T \mathbf{v} - \nabla \phi \right) \\ &= q \left(-\frac{\partial \mathbf{A}}{\partial t} - \nabla \phi - \nabla \times \mathbf{A} \times \mathbf{v} \right) \\ &= q (\mathbf{E} + \mathbf{v} \times \mathbf{B}). \end{aligned} \quad (\text{B.9})$$

Remembering that the time derivative of momentum gives a force, \mathbf{F} ($\mathbf{F} = \frac{d\mathbf{p}}{dt}$), it is then possible to see that the force on a charged particle in an electromagnetic field is given by:

$$\mathbf{F} = q (\mathbf{E} + \mathbf{v} \times \mathbf{B}), \quad (\text{B.10})$$

the so-called Lorentz force.

B.2 Motion of Single Electron in Infinite, Plane, Linearly Polarized Wave

Assuming an infinite, plane, linearly polarized wave it is possible to find out the pattern of motion for a single electron by finding constants of motion for the system. The vector potential for a wave that is polarized in the y -direction and propagating along the z -axis is given by $\mathbf{A} = A(z - ct)\hat{y}$ whereas the scalar potential is equal to zero.

Under the conditions mentioned above the following must be true:

$$\frac{d}{dt} \frac{\partial \mathcal{L}}{\partial v_y} = 0. \quad (\text{B.11})$$

which means that $\frac{\partial \mathcal{L}}{\partial v_y}$ is a constant of motion. In section B.1 it can be seen that this derivative can be represented as:

$$\frac{\partial \mathcal{L}}{\partial v_y} = p_y(t) + qA_y(t). \quad (\text{B.12})$$

Combining Eq. B.11 and Eq. B.12 it is easy to conclude that:

$$p_y(t) + qA_y(t) = p_y(0) + qA_y(0). \quad (\text{B.13})$$

For an electron initially at rest the following condition must then apply:

$$p_y(t) = -qA_y(t). \quad (\text{B.14})$$

Another constant of motion can be derived from the fundamental relation in Hamiltonian mechanics below:

$$\frac{\partial \mathcal{L}}{\partial t} + \frac{\partial \mathcal{H}}{\partial t} = 0, \quad (\text{B.15})$$

where \mathcal{H} is the Hamiltonian of the system, describing its total energy, E_{tot} . Recalling that $\mathbf{A} = A(z - ct)\hat{y}$ it is possible to determine the time-derivative of the energy of the electron:

$$\frac{dE_{\text{tot}}}{dt} = \frac{\partial \mathcal{H}}{\partial t} = -\frac{\partial \mathcal{L}}{\partial t} = c \frac{\partial \mathcal{L}}{\partial z}. \quad (\text{B.16})$$

Considering *only* the z -component in Eq. B.6 (Euler-Lagrange equation) and that \mathbf{A} has previously been assumed not to have any z -component, the last expression can be modified:

$$c \frac{\partial \mathcal{L}}{\partial z} = c \frac{d}{dt} \frac{\partial \mathcal{L}}{\partial v_z} = c \frac{dp_z}{dt}. \quad (\text{B.17})$$

Finally the constant of motion can be found:

$$\frac{d}{dt} (E_{\text{tot}} - cp_z) = 0. \quad (\text{B.18})$$

If the electron is further assumed to be stationary before the arrival of the laser pulse, its total energy is given by:

$$E_{\text{tot}}(t) = E_{\text{pot}} + cp_z(t) = mc^2 + cp_z(t). \quad (\text{B.19})$$

The more traditional way to describe the energy of the relativistic electron would be $E_{\text{tot}} = mc^2\gamma = mc^2\sqrt{1 + \frac{p^2}{m^2c^2}}$, where p is the magnitude of the momentum. Together with the former expression, p_z is then derived as a function of the normalized vector potential, $\mathbf{a} = \frac{q\mathbf{A}}{mc}$:

$$\begin{aligned} mc^2 + cp_z &= \sqrt{(mc^2)^2 + c^2p_y^2 + c^2p_z^2}, \\ &\implies \\ (mc^2)^2 + 2mc^3p_z + c^2p_z^2 &= (mc^2)^2 + c^2p_y^2 + c^2p_z^2, \\ &\iff \\ p_z &= \frac{p_y^2}{2mc} = \frac{q^2A_y^2}{2mc} = \frac{mca_y^2}{2}. \end{aligned} \quad (\text{B.20})$$

Electron trajectories

Assuming that $\mathbf{a} = (0, a_y, 0)$ it is possible to use the constants of motion derived above to determine the trajectories of charged particles in an electromagnetic wave:

$$\begin{aligned} p_x &= 0, \\ p_y &= qA_y = q\frac{mc}{q}a_y = mca_y, \\ p_z &= \frac{mc}{2}a_y^2. \end{aligned} \quad (\text{B.21})$$

Another way of writing \mathbf{p} is as $\mathbf{p} = \gamma m\mathbf{v}$. Eq. B.21 is thus possible to rewrite:

$$\begin{aligned} \gamma \frac{dx}{dt} &= 0, \\ \gamma \frac{dy}{dt} &= ca_y, \\ \gamma \frac{dz}{dt} &= c\frac{a_y^2}{2}. \end{aligned} \quad (\text{B.22})$$

Finding the relation between γ and a_y :

$$\begin{aligned} E_{\text{kin}} = E_{\text{tot}} - mc^2 &= mc^2\gamma - mc^2 = mc^2(\gamma - 1) = p_zc, \\ &\iff \\ \gamma - 1 &= \frac{p_z}{mc}, \\ &\iff \\ \gamma &= \frac{a_y^2}{2} + 1, \end{aligned} \quad (\text{B.23})$$

a change of variable from t to $\tau = t - z(t)/c$ can be performed. First it is necessary to find how the time-derivative can be expressed in this new variable:

$$\begin{aligned} \gamma \frac{d}{dt} &= \gamma \frac{d\tau}{dt} \frac{d}{d\tau} = \left(\gamma - \frac{\gamma}{c} \frac{dz}{dt} \right) \frac{d}{d\tau} = \left(\gamma - \frac{1}{2} a_y^2 \right) \frac{d}{d\tau} \\ &= \left(1 + \frac{a_y^2}{2} - \frac{a_y^2}{2} \right) \frac{d}{d\tau} = \frac{d}{d\tau}. \end{aligned} \quad (\text{B.24})$$

It is then clear that Eq. B.22 is equivalent with:

$$\begin{aligned} \frac{dx}{d\tau} &= 0, \\ \frac{dy}{d\tau} &= ca_y, \\ \frac{dz}{d\tau} &= c \frac{a_y^2}{2}. \end{aligned} \quad (\text{B.25})$$

It is further assumed that $a_y = a_0 \cos(\omega\tau)$, which makes it possible to integrate Eq. B.25 to find the trajectory of an electron in an electromagnetic wave in the y - and z -directions.

$$\begin{aligned} y(\tau) &= \int_0^\tau ca_0 \cos(\omega\tau') d\tau' = \frac{ca_0}{\omega} \left[\sin(\omega\tau') \right]_0^\tau = \frac{ca_0}{\omega} \sin(\omega\tau), \\ z(\tau) &= \int_0^\tau \frac{ca_0^2}{2} \cos^2(\omega\tau') d\tau' = \frac{ca_0^2}{2} \int_0^\tau \frac{\cos(2\omega\tau') + 1}{2} d\tau' \\ &= \frac{ca_0^2}{4} \left[\frac{1}{2\omega} \sin(2\omega\tau') + \tau' \right]_0^\tau = \frac{ca_0^2}{4} \left(\frac{1}{2\omega} \sin(2\omega\tau) + \tau \right). \end{aligned} \quad (\text{B.26})$$

The expressions above describe how the electron moves in a stationary frame of reference. The motion can be averaged over a laser-cycle to find the drift velocity in the z -direction. The sine-function has a time average of zero and the following relation is valid:

$$\begin{aligned} z &= \frac{ca_0^2}{4} \tau, \\ &\iff \\ z &= \frac{ca_0^2}{4} (t - z/c), \\ &\iff \\ z \left(1 + \frac{a_0^2}{4} \right) &= \frac{ca_0^2}{4} t. \end{aligned} \quad (\text{B.27})$$

Differentiating implicitly with respect to t gives the drift velocity, $v_{\text{D}, z\text{-dir}}$:

$$\begin{aligned} \dot{z} \left(1 + \frac{a_0^2}{4} \right) &= \frac{ca_0^2}{4}, \\ &\iff \\ v_{\text{D}, z\text{-dir}} &= \frac{ca_0^2}{4 + a_0^2}. \end{aligned} \tag{B.28}$$

THE AUTHOR'S CONTRIBUTIONS TO THE PAPERS

I Diagnostics for studies of novel laser ion acceleration mechanisms

I took an active part in constructing the set-up and performing the experiment, in which the diagnostics was implemented and tested. I analysed the data, wrote the manuscript, and was the corresponding author in the submission and review process.

II A setup for studies of laser-driven proton acceleration at the Lund Laser Centre

I planned and designed parts of the set-up, in particular the optical system for combined laser focus optimization and target alignment, and the proton spectrometer. I participated actively in discussions of the manuscript.

III Manipulation of the spatial distribution of laser-accelerated proton beams by varying the laser intensity distribution

I participated actively in setting up and performing the experiment. I analysed the proton energy spectra and contributed to the analysis and interpretation of the experimental data. I did not participate in the numerical modelling of the underlying physics.

IV Transverse expansion of the electron sheath during laser acceleration of protons

I participated actively in setting up and performing the experiment. I contributed to the interpretation of the experimental data and gave feedback on the manuscript. I did not participate in the numerical modelling of the underlying physics.

V Experimental investigation of picosecond dynamics following interactions between laser accelerated protons and water

I contributed actively to setting up and performing the experiment. In particular, I designed the target-foil holder, I built the target-foil alignment system and I ensured the correct alignment of the experimental set-up on a daily basis. I analysed the data, interpreted most of the results, and created a model describing the change in the absorbance when the energy of a pulse of high-energy protons is deposited in water. I wrote the manuscript and responded to the comments in the review process.

VI Picosecond metrology of laser-driven proton bursts

I contributed actively to setting up and performing the experiment. In particular, I designed the target-foil holder, I built the target-foil alignment system and I ensured the correct alignment of the experimental set-up on a daily basis. I developed the basis for a time-resolved model to simulate the propagation of a multi-energy proton pulse through a material, including its slowing down and stopping. I did not participate in the analysis of proton energy deposition in the different glass materials, or how the materials differed from each another. I gave constructive feedback on the manuscript.

The papers presented below are related to Appendix A.

VII Supersonic jets of hydrogen and helium for laser wakefield acceleration

I participated in the performance of the experiment and contributed through discussions and constructive feedback on the manuscript.

VIII Dynamics of ionization-induced electron injection in the high density regime of laser wakefield acceleration

IX Enhanced stability of laser wakefield acceleration using dielectric capillary tubes

Papers VIII and IX are based on results from the same experimental campaign, and I participated in setting up and performing the experiments. In particular, I set up a spectrometer for the analysis of the spectral content of the laser pulse on each shot. I provided constructive feedback on the manuscript.

ACKNOWLEDGMENTS

Modern experimental physics is a team effort, and none of the work presented in this thesis would have been possible without the support of many people.

I would especially like to thank my main supervisor Claes-Göran Wahlström, for his support during the years, and for so enthusiastically introducing me to the world of Atomic Physics when I was an engineering student. I appreciate the enormous care with which every aspect of my work was regarded and his comprehensive and instructive feedback. I would also like to express my gratitude to my co-supervisor Olle Lundh, who made my Master's project so interesting that I wanted to continue in the research group.

Another very important person, without whom running the laser system would have been impossible, is Anders Persson. Thank you for your constant kindness and helpfulness!

Other members of the research group have been very important in bringing this PhD-project to conclusion and I would especially like to thank Kristoffer Svensson, for being so easy to work with, and for helping me with the formatting of this thesis. I would also like to thank Isabel Gallardo Gonzalez, for her positivity and for answering all my stupid questions about the laser system after a year on parental leave, Martin Hansson, for being generous with his knowledge, and Henrik Ekerfelt for his willingness to discuss everything from plasma physics to recruitment processes. I am also grateful to all the other former and present members for their support and collaboration, including, Jonas Björklund Svensson, Malay Dalui, Hannes Pahl, Alexander Permogorov, Franck Wodja, Matthias Burza, Bastian Aurand, Elnaz Yazdani and Guillaume Genoud. I would also like to take this opportunity to thank everyone at the Division of Atomic Physics for creating such a pleasant working environment, and extend my gratitude to Åke Johansson, Harriet Lindahl, Camilla Nilsson, Anne Petersson-Jungbeck and Jakob Testad for making everything run so perfectly.

I have had the great pleasure of performing experimental campaigns outside of Lund and I would in particular like to thank Brendan Dromey and Matthew Zepf for their hospitality at Queen's University, Belfast, and for letting me learn things about water I could never have imagined. I would also like to thank the groups of

Brigitte Cros, David Neely and Paul McKenna that have come to Lund to perform experiments, for pleasant collaboration.

The PLIONA project has been inspiring, and I would like to thank all the members for making attending the workshops a pleasant (and informative) experience.

I am also grateful to other people, who have been far more than colleagues: Linnea, when physics, or other parts of life, were driving me insane, I knew I could always come to you. Even early in the morning. Very, very early in the morning. Jenny, thank you for always being positive about doing things, also on short notice, and for making me feel that I could tell you anything without being judged. You're are both fantastic friends, and I will always feel nostalgic about the time we were all living at Väster.

I would like to thank my parents for their generous and never-failing support. Mamma, for teaching me to deal not only with the easy parts of life, but also the importance of not ignoring things that are difficult, and also for teaching me to appreciate things. Pappa, for puzzling all those puzzles with me and for making me feel that I could solve any problem if I just put my mind and heart to it.

Finally, an infinite amount of thanks to the best family anyone could ever wish for. Daniel, from the very first day you listened to and considered my opinions, regardless of whether it was the orientation of a wave-plate or what cake to buy. For this I love you. In particular, thank you for dealing with everyday life so that I could deal with this thesis. Elise, tack för att du gjorde det omöjligt att bara vara fysiker. Du är utan tvekan det bästa resultatet av min tid som doktorand.

REFERENCES

1. H. Daido, M. Nishiuchi and A. S. Pirozhkov. *Review of laser-driven ion sources and their applications*. Rep. Prog. Phys. **75**, 056401 (2012).
2. A. Macchi, M. Borghesi and M. Passoni. *Ion acceleration by superintense laser-plasma interaction*. Rev. Mod. Phys. **85**, 751–793 (2013).
3. E. Esarey, C. Schroeder and W. Leemans. *Physics of laser-driven plasma-based electron accelerators*. Rev. Mod. Phys. **81**, 1229–1285 (2009).
4. T. H. Maiman. *Stimulated optical radiation in ruby*. Nature **187**, 493–494 (1960).
5. R. H. Milburn. *Electron scattering by an intense polarized photon field*. Phys. Rev. Lett. **10**, 75–77 (1963).
6. B. Dromey, M. Coughlan, L. Senje, M. Taylor, S. Kuschel, B. Villagomez-Bernabe, R. Stefanuik, G. Nersisyan, L. Stella, J. Kohanoff, M. Borghesi, F. Currell, D. Riley, D. Jung, C.-G. Wahlström, C. L. S. Lewis and M. Zepf. *Picosecond metrology of laser-driven proton bursts*. Nat. Commun. **7**, 10642 (2016).
7. P. Gibbon. *Short pulse laser interactions with matter: an introduction*. Imperial College Press (2005).
8. A. Zhidkov and A. Sasaki. *Effect of field ionization on interaction of an intense subpicosecond laser pulse with foils*. Phys. Plasmas **7**, 1341–1344 (2000).
9. G. M. Petrov, J. Davis and T. Petrova. *Ionization dynamics of high-intensity laser-target interactions*. Plasma Phys. Control. Fusion **51**, 095005 (2009).
10. W. L. Kruer. *The physics of laser plasma interaction*. Allan M. Wylde (1988).
11. B. Quesnel and P. Mora. *Theory and simulation of the interaction of ultraintense laser pulses with electrons in vacuum*. Phys. Rev. E **58**, 3719–3732 (1998).

12. E. A. Startsev and C. J. McKinstrie. *Multiple scale derivation of the relativistic ponderomotive force*. Phys. Rev. E **55**, 7527–7535 (1997).
13. S. Eliezer. *The interaction of high-power lasers with plasmas*. Institute of Physics Publishing (2002).
14. F. Ferroni, L. A. Gizzi and M. Missiroli, editors. *Proceedings of the international school of physics, Enrico Fermi. Laser-plasma Acceleration*. IOS Press and Società Italiana di Fisica (2012).
15. F. N. Beg, A. R. Bell, A. E. Dangor, C. N. Danson, A. P. Fews, M. E. Glinsky, B. A. Hammel, P. Lee, P. A. Norreys and M. Tatarakis. *A study of picosecond laser-solid interactions up to 10^{19} W/cm²*. Phys. Plasmas **4**, 447–457 (1997).
16. F. Brunel. *Not-so-resonant, resonant absorption*. Phys. Rev. Lett. **59**, 52–55 (1987).
17. W. L. Kruer and K. Estabrook. *$\mathbf{j} \times \mathbf{B}$ heating by very intense laser light*. Phys. Fluids **28**, 430–432 (1985).
18. S. C. Wilks, W. L. Kruer, M. Tabak and A. B. Langdon. *Absorption of ultra-intense laser pulses*. Phys. Rev. Lett. **69**, 1383–1386 (1992).
19. G. Malka and J. L. Miquel. *Experimental confirmation of ponderomotive-force electrons produced by an ultrarelativistic laser pulse on a solid target*. Phys. Rev. Lett. **77**, 75–78 (1996).
20. M. I. K. Santala, M. Zepf, I. Watts, F. N. Beg, E. Clark, M. Tatarakis, K. Krushelnick, A. E. Dangor, T. McCanny, I. Spencer, R. P. Singhal, K. W. D. Ledingham, S. C. Wilks, A. C. Machacek, J. S. Wark, R. Allott, R. J. Clarke and P. A. Norreys. *Effect of the plasma density scale length on the direction of fast electrons in relativistic laser-solid interactions*. Phys. Rev. Lett. **84**, 1459–1462 (2000).
21. S. C. Wilks, A. B. Langdon, T. E. Cowan, M. Roth, M. Singh, S. Hatchett, M. H. Key, D. Pennington, A. MacKinnon and R. A. Snavely. *Energetic proton generation in ultra-intense laser-solid interactions*. Phys. Plasmas **8**, 542–549 (2001).
22. M. Passoni, L. Bertagna and A. Zani. *Target normal sheath acceleration: theory, comparison with experiments and future perspectives*. New J. Phys. **12**, 045012 (2010).
23. T. Ceccotti, A. Lévy, H. Popescu, F. Réau, P. D’Oliveira, P. Monot, J. P. Geindre, E. Lefebvre and P. Martin. *Proton acceleration with high-intensity ultrahigh-contrast laser pulses*. Phys. Rev. Lett. **99** (2007).

24. P. Mora. *Plasma expansion into a vacuum*. Phys. Rev. Lett. **90**, 185002 (2003).
25. L. Robson, P. T. Simpson, R. J. Clarke, K. W. D. Ledingham, F. Lindau, O. Lundh, T. McCanny, P. Mora, D. Neely, C.-G. Wahlstrom, M. Zepf and P. McKenna. *Scaling of proton acceleration driven by petawatt-laser-plasma interactions*. Nat. Phys. **3**, 58–62 (2007).
26. M. Allen, Y. Sentoku, P. Audebert, A. Blazevic, T. Cowan, J. Fuchs, J. C. Gauthier, M. Geissel, M. Hegelich, S. Karsch and et al. *Proton spectra from ultraintense laser-plasma interaction with thin foils: Experiments, theory, and simulation*. Phys. Plasmas **10**, 3283–3289 (2003).
27. J. Fuchs, Y. Sentoku, E. d’Humières, T. E. Cowan, J. Cobble, P. Audebert, A. Kemp, A. Nikroo, P. Antici, E. Brambrink, A. Blazevic, E. M. Campbell, J. C. Fernández, J.-C. Gauthier, M. Geissel, M. Hegelich, S. Karsch, H. Popescu, N. Renard-LeGalloudec, M. Roth, J. Schreiber, R. Stephens and H. Pépin. *Comparative spectra and efficiencies of ions laser-accelerated forward from the front and rear surfaces of thin solid foils*. Phys. Plasmas **14**, 053105 (2007).
28. T. E. Cowan, J. Fuchs, H. Ruhl, A. Kemp, P. Audebert, M. Roth, R. Stephens, I. Barton, A. Blazevic, E. Brambrink, J. Cobble, J. Fernández, J.-C. Gauthier, M. Geissel, M. Hegelich, J. Kaae, S. Karsch, G. P. Le Sage, S. Letzring, M. Manclossi, S. Meyroneinc, A. Newkirk, H. Pépin and N. Renard-LeGalloudec. *Ultralow emittance, multi-MeV proton beams from a laser virtual-cathode plasma accelerator*. Phys. Rev. Lett. **92**, 204801 (2004).
29. J. Schreiber, F. Bell, F. Grüner, U. Schramm, M. Geissler, M. Schnürer, S. Ter-Avetisyan, B. M. Hegelich, J. Cobble, E. Brambrink, J. Fuchs, P. Audebert and D. Habs. *Analytical model for ion acceleration by high-intensity laser pulses*. Phys. Rev. Lett. **97**, 045005 (2006).
30. A. Flacco, T. Ceccotti, H. George, P. Monot, P. Martin, F. Réau, O. Tcherbakoff, P. d’Oliveira, F. Sylla, M. Veltcheva and et al. *Comparative study of laser ion acceleration with different contrast enhancement techniques*. Nucl. Instr. Meth. Phys. Res. A **620**, 18–22 (2010).
31. K. Zeil, S. D. Kraft, S. Bock, M. Bussmann, T. E. Cowan, T. Kluge, J. Metzkes, T. Richter, R. Sauerbrey and U. Schramm. *The scaling of proton energies in ultrashort pulse laser plasma acceleration*. New J. Phys. **12**, 045015 (2010).
32. S. Y. Kalmykov, A. Beck, X. Davoine, E. Lefebvre and B. A. Shadwick. *Laser plasma acceleration with a negatively chirped pulse: all-optical control over dark current in the blowout regime*. New J. Phys. **14**, 033025 (2012).
33. T. Esirkepov, M. Borghesi, S. V. Bulanov, G. Mourou and T. Tajima. *Highly efficient relativistic-ion generation in the laser-piston regime*. Phys. Rev. Lett. **92**, 175003 (2004).

34. A. Macchi, F. Cattani, T. V. Liseykina and F. Cornolti. *Laser acceleration of ion bunches at the front surface of overdense plasmas*. Phys. Rev. Lett. **94**, 165003 (2005).
35. O. Klimo, J. Psikal, J. Limpouch and V. T. Tikhonchuk. *Monoenergetic ion beams from ultrathin foils irradiated by ultrahigh-contrast circularly polarized laser pulses*. Phys. Rev. ST Accel. Beams **11**, 031301 (2008).
36. A. P. L. Robinson, M. Zepf, R. G. Kar, S. Evans and C. Bellei. *Radiation pressure acceleration of thin foils with circularly polarized laser pulses*. New J. Phys. **10**, 013021 (2008).
37. A. Henig, S. Steinke, M. Schnürer, T. Sokollik, R. Hörlein, D. Kiefer, D. Jung, J. Schreiber, B. M. Hegelich, X. Q. Yan, J. Meyer-ter Vehn, T. Tajima, P. V. Nickles, W. Sandner and D. Habs. *Radiation-pressure acceleration of ion beams driven by circularly polarized laser pulses*. Phys. Rev. Lett. **103**, 245003 (2009).
38. S. Kar, K. F. Kakolee, B. Qiao, A. Macchi, M. Cerchez, D. Doria, M. Geissler, P. McKenna, D. Neely, J. Osterholz, R. Prasad, K. Quinn, B. Ramakrishna, G. Sarri, O. Willi, X. Y. Yuan, M. Zepf and M. Borghesi. *Ion acceleration in multispecies targets driven by intense laser radiation pressure*. Phys. Rev. Lett. **109**, 185006 (2012).
39. C. A. J. Palmer, J. Schreiber, S. R. Nagel, N. P. Dover, C. Bellei, F. N. Beg, S. Bott, R. J. Clarke, A. E. Dangor, S. M. Hassan, P. Hilz, D. Jung, S. Kneip, S. P. D. Mangles, K. L. Lancaster, A. Rehman, A. P. L. Robinson, C. Spindloe, J. Szerypo, M. Tatarakis, M. Yeung, M. Zepf and Z. Najmudin. *Rayleigh-Taylor instability of an ultrathin foil accelerated by the radiation pressure of an intense laser*. Phys. Rev. Lett. **108**, 225002 (2012).
40. F. Dollar, C. Zwick, A. G. R. Thomas, V. Chvykov, J. Davis, G. Kalinchenko, T. Matsuoka, C. McGuffey, G. M. Petrov, L. Willingale, V. Yanovsky, A. Maksimchuk and K. Krushelnick. *Finite spot effects on radiation pressure acceleration from intense high-contrast laser interactions with thin targets*. Phys. Rev. Lett. **108**, 175005 (2012).
41. L. O. Silva, M. Marti, J. R. Davies, R. A. Fonseca, C. Ren, F. S. Tsung and W. B. Mori. *Proton shock acceleration in laser-plasma interactions*. Phys. Rev. Lett. **92**, 015002 (2004).
42. A. Henig, D. Kiefer, M. Geissler, S. G. Rykovanov, R. Ramis, R. Hörlein, J. Osterhoff, Z. Major, L. Veisz, S. Karsch, F. Krausz, D. Habs and J. Schreiber. *Laser-driven shock acceleration of ion beams from spherical mass-limited targets*. Phys. Rev. Lett. **102**, 095002 (2009).

43. Y. Fang, T. Yu, X. Ge, S. Yang, W. Wei, T. Yuan, F. Liu, M. Chen, J. Liu, Y. Li and et al. *Combined proton acceleration from foil targets by ultraintense short laser pulses*. Plasma Phys. Contrl. F. **58**, 045025 (2016).
44. L. Yin, B. J. Albright, B. M. Hegelich and J. C. Fernández. *GeV laser ion acceleration from ultrathin targets: The laser break-out afterburner*. Laser Part. Beams **24**, 291–298 (2006).
45. A. Henig, D. Kiefer, K. Markey, D. C. Gautier, K. A. Flippo, S. Letzring, R. P. Johnson, T. Shimada, L. Yin, B. J. Albright, K. J. Bowers, J. C. Fernández, S. G. Rykovanov, H.-C. Wu, M. Zepf, D. Jung, V. Kh. Liechtenstein, J. Schreiber, D. Habs and B. M. Hegelich. *Enhanced laser-driven ion acceleration in the relativistic transparency regime*. Phys. Rev. Lett. **103**, 045002 (2009).
46. O. Buneman. *Dissipation of currents in ionized media*. Phys. Rev. **115**, 503–517 (1959).
47. B. J. Albright, L. Yin, Kevin J. Bowers, B. M. Hegelich, K. A. Flippo, T. J. T. Kwan and J. C. Fernandez. *Relativistic Buneman instability in the laser breakout afterburner*. Phys. Plasmas **14**, 094502 (2007).
48. D. Jung, L. Yin, D. C. Gautier, H.-C. Wu, S. Letzring, B. Dromey, R. Shah, S. Palaniyappan, T. Shimada, R. P. Johnson, J. Schreiber, D. Habs, J. C. Fernández, B. M. Hegelich and B. J. Albright. *Laser-driven 1 GeV carbon ions from preheated diamond targets in the break-out afterburner regime*. Phys. Plasmas **20**, 083103 (2013).
49. www.srim.org (2013).
50. D. Strickland and G. Mourou. *Compression of amplified chirped optical pulses*. Opt. Comm. **55**, 447–449 (1985).
51. D. E. Spence, J. M. Evans, W. E. Sleat and W. Sibbett. *Regeneratively initiated self-mode-locked Ti:sapphire laser*. Opt. Lett. **16**, 1762 (1991).
52. M. Kaluza, J. Schreiber, M. I. K. Santala, G. D. Tsakiris, K. Eidmann, J. Meyer-ter Vehn and K. J. Witte. *Influence of the laser prepulse on proton acceleration in thin-foil experiments*. Phys. Rev. Lett. **93**, 045003 (2004).
53. B. Dromey, S. Kar, M. Zepf and P. Foster. *The plasma mirror: A subpicosecond optical switch for ultrahigh power lasers*. Rev. Sci. Instrum. **75**, 645–649 (2004).
54. C. Thauray, F. Quéré, J.-P. Geindre, A. Levy, T. Ceccotti, P. Monot, M. Bougeard, F. Réau, P. d'Oliveira, P. Audebert, R. Marjoribanks and P. Martin. *Plasma mirrors for ultrahigh-intensity optics*. Nat. Phys. **3**, 424–429 (2007).

55. S. Inoue, K. Maeda, S. Tokita, K. Mori, K. Teramoto, M. Hashida and S. Sakabe. *Single plasma mirror providing 10^4 contrast enhancement and 70% reflectivity for intense femtosecond lasers*. Appl. Opt. **55**, 5647 (2016).
56. M. Manclossi, J. J. Santos, D. Batani, J. Faure, A. Debayle, V. T. Tikhonchuk and V. Malka. *Study of ultraintense laser-produced fast-electron propagation and filamentation in insulator and metal foil targets by optical emission diagnostics*. Phys. Rev. Lett. **96**, 125002 (2006).
57. J.J. Thomson. *XXVI. Rays of positive electricity*. Phil. Mag. Series 6 **21**, 225–249 (1911).
58. K. Harres, M. Schollmeier, E. Brambrink, P. Audebert, A. Blazevic, K. Flippo, D. C. Gautier, M. Geissel, B. M. Hegelich, F. Nurnberg, J. Schreiber, H. Wahl and M. Roth. *Development and calibration of a Thomson parabola with microchannel plate for the detection of laser-accelerated MeV ions*. Rev. Sci. Instrum. **79**, 093306 (2008).
59. D. Jung, R. Hörlein, D. Kiefer, S. Letzring, D. C. Gautier, U. Schramm, C. Hubsch, R. Ohm, B. J. Albright, J. C. Fernandez, D. Habs and B. M. Hegelich. *Development of a high resolution and high dispersion Thomson parabola*. Rev. Sci. Instrum. **82**, 013306 (2011).
60. A. Alejo, S. Kar, A. Tebartz, H. Ahmed, S. Astbury, D. C. Carroll, J. Ding, D. Doria, A. Higginson, P. McKenna, N. Neumann, G. G. Scott, F. Wagner, M. Roth and M. Borghesi. *High resolution Thomson parabola spectrometer for full spectral capture of multi-species ion beams*. Rev. Sci. Instrum. **87**, 083304 (2016).
61. F. Nürnberg, M. Schollmeier, E. Brambrink, A. Blazevic, D. C. Carroll, K. Flippo, D. C. Gautier, M. Geissel, K. Harres, B. M. Hegelich, O. Lundh, K. Markey, P. McKenna, D. Neely, J. Schreiber and M. Roth. *Radiochromic film imaging spectroscopy of laser-accelerated proton beams*. Rev. Sci. Instrum. **80**, 033301 (2009).
62. D. Kirby, S. Green, F. Fiorini, D. Parker, L. Romagnani, D. Doria, S. Kar, C. Lewis, M. Borghesi and H. Palmans. *Radiochromic film spectroscopy of laser-accelerated proton beams using the FLUKA code and dosimetry traceable to primary standards*. Laser Part. Beams **29**, 231–239 (2011).
63. J. Rojas-Herrera, H. G. Rinderknecht, A. B. Zylstra, M. Gatu Johnson, D. Orozco, M. J. Rosenberg, H. Sio, F. H. Seguin, J. A. Frenje, C. K. Li and R. D. Petrasso. *Impact of x-ray dose on the response of CR-39 to 1-5.5 MeV alphas*. Rev. Sci. Instrum. **86**, 033501 (2015).
64. L. Yin, B. J. Albright, D. Jung, K. J. Bowers, R. C. Shah, S. Palaniyappan, J. C. Fernandez and B. M. Hegelich. *Mono-energetic ion beam acceleration in solitary*

- waves during relativistic transparency using high-contrast circularly polarized short-pulse laser and nanoscale targets.* Phys. Plasmas **18**, 053103 (2011).
65. D. Jung, R. Hörlein, D. C. Gautier, S. Letzring, D. Kiefer, K. Allinger, B. J. Albright, R. Shah, S. Palaniyappan, L. Yin, J. C. Fernandez, D. Habs and B. M. Hegelich. *A novel high resolution ion wide angle spectrometer.* Rev. Sci. Instrum. **82**, 043301 (2011).
66. D. Neely, P. Foster, A. Robinson, F. Lindau, O. Lundh, A. Persson, C.-G. Wahlström and P. McKenna. *Enhanced proton beams from ultrathin targets driven by high contrast laser pulses.* Appl. Phys. Lett. **89**, 021502 (2006).
67. J. Fuchs, T. E. Cowan, P. Audebert, H. Ruhl, L. Gremillet, A. Kemp, M. Allen, A. Blazevic, J.-C. Gauthier, M. Geissel, M. Hegelich, S. Karsch, P. Parks, M. Roth, Y. Sentoku, R. Stephens and E. M. Campbell. *Spatial uniformity of laser-accelerated ultrahigh-current MeV electron propagation in metals and insulators.* Phys. Rev. Lett. **91**, 255002 (2003).
68. P. M. Nilson, L. Willingale, M. C. Kaluza, C. Kamperidis, S. Minardi, M. S. Wei, P. Fernandes, M. Notley, S. Bandyopadhyay, M. Sherlock, R. J. Kingham, M. Tatarakis, Z. Najmudin, W. Rozmus, R. G. Evans, M. G. Haines, A. E. Dangor and K. Krushelnick. *Magnetic reconnection and plasma dynamics in two-beam laser-solid interactions.* Phys. Rev. Lett. **97**, 255001 (2006).
69. A. Flacco, A. Guemnie-Tafo, R. Nuter, M. Veltcheva, D. Batani, E. Lefebvre and V. Malka. *Characterization of a controlled plasma expansion in vacuum for laser driven ion acceleration.* J. Appl. Phys. **104**, 103304 (2008).
70. C. A. J. Palmer, N. P. Dover, I. Pogorelsky, M. Babzien, G. I. Dudnikova, M. Ispiryan, M. N. Polyanskiy, J. Schreiber, P. Shkolnikov, V. Yakimenko and Z. Najmudin. *Monoenergetic proton beams accelerated by a radiation pressure driven shock.* Phys. Rev. Lett. **106**, 014801 (2011).
71. A. Horn, E. W. Kreutz and R. Poprawe. *Ultrafast time-resolved photography of femtosecond laser induced modifications in BK7 glass and fused silica.* Appl. Phys. A **79**, 923–925 (2004).
72. F.-Y. Jou and G. R. Freeman. *Temperature and isotope effects on the shape of the optical absorption spectrum of solvated electrons in water.* J. Phys. Chem. **83**, 2383–2387 (1979).
73. B. Abel, U. Buck, A. L. Sobolewski and W. Domcke. *On the nature and signatures of the solvated electron in water.* Phys. Chem. Chem. Phys. **14**, 22 (2011).
74. L. Turi and A. Madarasz. *Comment on "Does the hydrated electron occupy a cavity?".* Science **331**, 1387–1387 (2011).

75. R. E. Larsen, W. J. Glover and B. J. Schwartz. *Does the hydrated electron occupy a cavity?* Science **329**, 65–69 (2010).
76. M. Assel, R. Laenen and A. Laubereau. *Retrapping and solvation dynamics after femtosecond UV excitation of the solvated electron in water.* J. Chem. Phys. **111**, 6869 (1999).
77. E. Alizadeh and L. Sanche. *Precursors of solvated electrons in radiobiological physics and chemistry.* Chem. Rev. **112**, 5578–5602 (2012).
78. M. S. Kreipl, W. Friedland and H. G. Paretzke. *Interaction of ion tracks in spatial and temporal proximity.* Radiat. Environ. Biophys. **48**, 349–359 (2009).
79. S. V. Bulanov, T. Z. Esirkepov, V.S. Khoroshkov, A. V. Kuznetsov and F. Pegoraro. *Oncological hadrontherapy with laser ion accelerators.* Phys. Lett. A **299**, 240–247 (2002).
80. K. Ledingham, P. Bolton, N. Shikazono and C.-M. Ma. *Towards laser driven hadron cancer radiotherapy: A review of progress.* Appl. Sci. **4**, 402–443 (2014).
81. S. Kawata, T. Izumiyama, T. Nagashima, M. Takano, D. Barada, Q. Kong, Y. J. Gu, P. X. Wang, Y. Y. Ma and W. M. Wang. *Laser ion acceleration toward future ion beam cancer therapy - Numerical simulation study -.* Laser Ther. **22**, 103–114 (2013).
82. E. Fourkal, T. Tajima, M. Ding and C. M. Ma. *PIC simulation of laser proton acceleration for radiotherapy.* Med. Phys. **29**, 2788 (2002).
83. U. Linz and J. Alonso. *What will it take for laser driven proton accelerators to be applied to tumor therapy?* Phys. Rev. ST Accel. Beams **10** (2007).
84. M. Roth, T. E. Cowan, M. H. Key, S. P. Hatchett, C. Brown, W. Fountain, J. Johnson, D. M. Pennington, R. A. Snavely, S. C. Wilks, K. Yasuike, H. Ruhl, F. Pegoraro, S. V. Bulanov, E. M. Campbell, M. D. Perry and H. Powell. *Fast Ignition by Intense Laser-Accelerated Proton Beams.* Phys. Rev. Lett. **86**, 436–439 (2001).
85. I. Spencer, K. W. D. Ledingham, R. P. Singhal, T. McCanny, P. McKenna, E. L. Clark, K. Krushelnick, M. Zepf, F. N. Beg, M. Tatarakis, A.E. Dangor, P.A. Norreys, R.J. Clarke, R.M. Allott and I.N. Ross. *Laser generation of proton beams for the production of short-lived positron emitting radioisotopes.* Nucl. Instr. Meth. Phys. Res. B **183**, 449–458 (2001).
86. F. Wagner, O. Deppert, C. Brabetz, P. Fiala, A. Kleinschmidt, P. Poth, V. A. Schanz, A. Tebartz, B. Zielbauer, M. Roth, T. Stöhlker and V. Bagnoud. *Maximum proton energy above 85 MeV from the relativistic interaction of laser pulses with micrometer thick CH₂ targets.* Phys. Rev. Lett. **116**, 205002 (2016).

87. J. Wallace. *National Energetics' 10 petawatt laser system passes major milestone*. LaserFocusWorld (2016).
88. M. G. Florescu, O. G. Dului, D. Pantazi, C. M. Ticos, D. Sporea, R. Vasilache, V. Ionescu and M. Oane. *Radiological safety assesment for the experimental area of a hyper-intense laser with peak-power of 1 PW - CETAL*. Radiat. Prot. Dosimetry (2016).
89. R. Wilson, M. King, R. J. Gray, D. C. Carroll, R. J. Dance, C. Armstrong, S. J. Hawkes, R. J. Clarke, D. J. Robertson, D. Neely and et al. *Ellipsoidal plasma mirror focusing of high power laser pulses to ultra-high intensities*. Phys. Plasmas **23**, 033106 (2016).
90. A. Sgattoni, P. Londrillo, A. Macchi and M. Passoni. *Laser ion acceleration using a solid target coupled with a low-density layer*. Phys. Rev. E **85** (2012).
91. M. Passoni, A. Sgattoni, I. Prencipe, L. Fedeli, D. Dellasega, L. Cialfi, I. W. Choi, I. J. Kim, K. A. Janulewicz, H. W. Lee, J. H. Sung, S. K. Lee and C. H. Nam. *Toward high-energy laser-driven ion beams: Nanostructured double-layer targets*. Phys. Rev. Accel. Beams **19**, 061301 (2016).
92. D. Margarone, O. Klimo, I. J. Kim, J. Prokúpek, J. Limpouch, T. M. Jeong, T. Mocek, J. Pšikal, H. T. Kim, J. Proška, K. H Nam, L. Štolcová, I. W. Choi, S. K. Lee, J. H. Sung, T. J. Yu and G Korn. *Laser-driven proton acceleration enhancement by nanostructured foils*. Phys. Rev. Lett. **109**, 234801 (2012).
93. L. Torrasi, M. Cutroneo and G. Ceccio. *Effect of metallic nanoparticles in thin foils for laser ion acceleration*. Phys. Scripta **90**, 015603 (2014).
94. T. Ceccotti, V. Floquet, A. Sgattoni, A. Bigongiari, O. Klimo, M. Raynaud, C. Riconda, A. Heron, F. Baffigi, L. Labate, L. A. Gizzi, L. Vassura, J. Fuchs, M. Passoni, M. Květon, F. Novotny, M. Possolt, J. Prokúpek, J. Proška, J. Pšikal, L. Štolcová, A. Velyhan, M. Bougeard, P. D'Oliveira, O. Tcherbakoff, F. Réau, P. Martin and A. Macchi. *Evidence of resonant surface-wave excitation in the relativistic regime through measurements of proton acceleration from grating targets*. Phys. Rev. Lett. **111**, 185001 (2013).
95. T. M. Ostermayr, D. Haffa, P. Hinz, V. Pauw, K. Allinger, K.-U. Bamberg, P. Böhl, C. Bömer, P. R. Bolton, F. Deutschmann, T. Ditmire, M. E. Donovan, G. Dyer, E. Gaul, J. Gordon, B. M. Hegelich, D. Kiefer, C. Klier, C. Kreuzer, M. Martinez, E. McCary, A. R. Meadows, N. Moschüring, T. Rösch, H. Ruhl, M. Spinks, C. Wagner and J. Schreiber. *Proton acceleration by irradiation of isolated spheres with an intense laser pulse*. Phys. Rev. E **94**, 033208 (2016).
96. K. S. Novoselov. *Electric field effect in atomically thin carbon films*. Science **306**, 666–669 (2004).

97. F. Mackenroth, A. Gonoskov and M. Marklund. *Chirped-standing-wave acceleration of ions with intense lasers*. Phys. Rev. Lett. **117**, 104801 (2016).
98. J. Isaacs and P. Sprangle. *Proton acceleration in a slow wakefield*. App. Phys. Lett. **110**, 024101 (2017).
99. L. V. Hau, S. E. Harris, Z. Dutton and C. H. Behroozi. *Light speed reduction to 17 metres per second in an ultracold atomic gas*. Nature **397**, 594–598 (1999).
100. M. L. Zhou, X. Q. Yan, G. Mourou, J. A. Wheeler, J. H. Bin, J. Schreiber and T. Tajima. *Proton acceleration by single-cycle laser pulses offers a novel monoenergetic and stable operating regime*. Phys. Plasmas **23**, 043112 (2016).
101. G. Mourou, S. Mironov, E. Khazanov and A. Sergeev. *Single cycle thin film compressor opening the door to Zeptosecond-Exawatt physics*. Eur. Phys. J. Spec. Top. **223**, 1181–1188 (2014).
102. T. Tajima and J. M. Dawson. *Laser electron accelerator*. Phys. Rev. Lett. **43**, 267–270 (1979).
103. A. Modena, Z. Najmudin, A. E. Dangor, C. E. Clayton, K. A. Marsh, C. Joshi, V. Malka, C. B. Darrow, C. Danson, D. Neely and F. N. Walsh. *Electron acceleration from the breaking of relativistic plasma waves*. Nature **377**, 606–608 (1995).
104. C. G. R. Geddes, C. Toth, J. van Tilborg, E. Esarey, C. B. Schroeder, D. Bruhwiler, C. Nieter, J. Cary and W. P. Leemans. *High-quality electron beams from a laser wakefield accelerator using plasma-channel guiding*. Nature **431**, 538–541 (2004).
105. S. P. D. Mangles, C. D. Murphy, Z. Najmudin, A. G. R. Thomas, J. L. Collier, A. E. Dangor, E. J. Divall, P. S. Foster, J. G. Gallacher, C. J. Hooker, D. A. Jaroszynski, A. J. Langley, W. B. Mori, P. A. Norreys, F. S. Tsung, R. Viskup, B. R. Walton and K. Krushelnick. *Monoenergetic beams of relativistic electrons from intense laser-plasma interactions*. Nature **431**, 535–538 (2004).
106. J. Faure, Y. Glinec, A. Pukhov, S. Kiselev, S. Gordienko, E. Lefebvre, J.-P. Rousseau, F. Burgy and V. Malka. *A laser-plasma accelerator producing monoenergetic electron beams*. Nature **431**, 541–544 (2004).
107. A. F. Lifschitz, X. Davoine, E. Lefebvre, J. Faure, C. Rechatin and V. Malka. *Particle-in-cell modelling of laser-plasma interaction using Fourier decomposition*. J. Comp. Phys. **228**, 1803–1814 (2009).
108. P. Sprangle, E. Esarey and A. Ting. *Nonlinear interaction of intense laser pulses in plasmas*. Phys. Rev. A **41**, 4463–4469 (1990).

-
109. J. Osterhoff, A. Popp, Z. Major, B. Marx, T. P. Rowlands-Rees, M. Fuchs, M. Geissler, R. Hörlein, B. Hidding, S. Becker, E. A. Peralta, U. Schramm, F. Grüner, D. Habs, F. Krausz, S. M. Hooker and S Karsch. *Generation of stable, low-divergence electron beams by laser-wakefield acceleration in a steady-state-flow gas cell*. Phys. Rev. Lett. **101**, 085002 (2008).
 110. G. Genoud, K. Cassou, F. Wojda, H. E. Ferrari, C. Kamperidis, M. Burza, A. Persson, J. Uhlig, S. Kneip, S. P. D. Mangles, A. F. Lifschitz, B. Cros and C.-G. Wahlström. *Laser-plasma electron acceleration in dielectric capillary tubes*. Appl. Phys. B **105**, 309–316 (2011).

PAPERS

Diagnostics for studies of novel laser ion acceleration mechanisms

L. Senje, M. Yeung, B. Aurand, S. Kuschel, C. Rödel, F. Wagner, K. Li, B. Dromey, V. Bagnoud, P. Neumayer, M. Roth, C.-G. Wahlström, M. Zepf, T. Kuehl, & D. Jung.

Review of Scientific Instruments **85**, 113302 (2014).



Diagnostics for studies of novel laser ion acceleration mechanisms

Lovisa Senje,¹ Mark Yeung,² Bastian Aurand,¹ Stephan Kuschel,² Christian Rödel,² Florian Wagner,³ Kun Li,⁴ Brendan Dromey,⁵ Vincent Bagnoud,^{2,6} Paul Neumayer,⁴ Markus Roth,³ Claes-Göran Wahlström,¹ Matthew Zepf,^{2,5} Thomas Kuehl,^{4,6,7} and Daniel Jung⁵

¹Department of Physics, Lund University, P. O. Box 118, S-221 00 Lund, Sweden

²Helmholtz-Institut Jena, D-07743 Jena, Germany

³Technische Universität Darmstadt, D-64289 Darmstadt, Germany

⁴Extreme Matter Institut, D-64291 Darmstadt, Germany

⁵Department of Physics and Astronomy, Queen's University, Belfast BT7 1NN, United Kingdom

⁶GSI Helmholtzzentrum für Schwerionenforschung GmbH, D-64291 Darmstadt, Germany

⁷Universität Mainz, D-55099 Mainz, Germany

(Received 8 August 2014; accepted 17 October 2014; published online 5 November 2014)

Diagnostic for investigating and distinguishing different laser ion acceleration mechanisms has been developed and successfully tested. An ion separation wide angle spectrometer can simultaneously investigate three important aspects of the laser plasma interaction: (1) acquire angularly resolved energy spectra for two ion species, (2) obtain ion energy spectra for multiple species, separated according to their charge to mass ratio, along selected axes, and (3) collect laser radiation reflected from and transmitted through the target and propagating in the same direction as the ion beam. Thus, the presented diagnostic constitutes a highly adaptable tool for accurately studying novel acceleration mechanisms in terms of their angular energy distribution, conversion efficiency, and plasma density evolution. © 2014 Author(s). All article content, except where otherwise noted, is licensed under a Creative Commons Attribution 3.0 Unported License. [<http://dx.doi.org/10.1063/1.4900626>]

I. INTRODUCTION

The field of laser-based ion acceleration has made significant advances over the last years.¹ Protons and other ions can be accelerated to high energies (MeVs) on a micrometre scale (compared to metre scale in conventional radio frequency accelerators) in plasmas from different materials placed in the focus of a high intensity laser beam. One of the currently most studied mechanisms for laser ion acceleration is target normal sheath acceleration^{2,3} (TNSA), where ions are accelerated to tens of MeV from foils with thicknesses on the micrometre scale. Other acceleration schemes have been proposed and investigated through particle in cell (PIC) simulations, such as Radiation Pressure Acceleration^{4,5} (RPA) and the Break-Out Afterburner^{6,7} (BOA), and ions could here reach significantly higher energies of hundreds of MeV. These mechanisms demand very high laser intensities and/or high temporal laser contrast and only recent improvements in available laser systems^{8,9} have allowed to experimentally study them.^{10–15} With these new mechanisms characteristics significantly different from those of TNSA appear, such as monoenergetic ion spectra for RPA¹⁶ and off-axis angular effects in ion beam profiles for BOA.¹⁷ Further appearing, for both RPA and BOA, is the possibility to more efficiently accelerate heavier ions and changes in the characteristics of the laser radiation that is transmitted or reflected from the target.^{18,19}

However, to distinguish and quantify the differences between the different acceleration mechanisms requires dedicated diagnostics. This is challenging to achieve, especially considering the often large angle of divergence of beams of laser accelerated ions of up to 40°. Traditionally, stacks of radiochromatic film (RCF),²¹ which changes color when absorbing radiation, and Thomson parabolas²² have been used

as main diagnostics. The disadvantages of these are that the RCF stacks provide limited energy resolution, have no means of separating different ion species, and make it difficult to simultaneously measure the laser spectrum, and that the Thomson parabola lacks angular resolution. Previously, the ion wide angle spectrometer²³ (iWASP) has been introduced as an initial cover of this need. Here, angularly resolved proton spectra can be obtained and a second ion species can also be recorded, although without charge information, making separation of multiple heavier ion species nearly impossible.

In this article, we present novel diagnostics that allow to experimentally distinguish different laser ion acceleration mechanisms: proton and ion spectra (for multiple species) along selected axes can be recorded simultaneously with the wide angle spectrum and the reflected and transmitted laser spectra. This diagnostic thereby makes it possible to study all the characteristics discussed above, simultaneously.

II. DESIGN

The design of the diagnostics has been made with focus on features particularly important to investigate in order to distinguish different laser ion acceleration mechanisms: (I) Angularly resolved energy spectra for protons and one more ion species, (II) Spectrum for each ion species present along selected axes, and (III) Characteristics of laser radiation transmitted and reflected from the target.

A. Ion wide angle spectrometer

Charged particles, such as ions, passing through a magnetic dipole field obtain a curved trajectory characterised by



the Larmor radius, which can be derived from the magnetic part of the Lorentz equation,

$$\vec{F} = q(\vec{v} \times \vec{B}), \quad (1)$$

where \vec{F} is the force exerted on a particle with charge, q , and velocity, \vec{v} , by the magnetic field, \vec{B} . Such magnetic field can, for example, be set up between two parallel permanent magnets, acting as a basic ion spectrometer. As mentioned before, beams of laser accelerated ions can be highly divergent and a pinhole or a slit at the entrance of the ion spectrometer is thus necessary in order to separate the different ion energies with sufficient resolution. With such a spectrometer it is however not possible to resolve angular features in the divergent beams of laser accelerated ions and thereby not meeting requirement (I). In an iWASP, this is resolved by using a wide entrance slit and an angle between the magnets, see Fig. 1, and thus allowing a larger part of a divergent beam to reach the detector. A major difference between the iWASP and a standard ion spectrometer is thereby the much larger solid angle covered.^{23,24}

The magnetic field in an iWASP is not exactly equal for all angles α , see Fig. 1(b), and, in addition, particles moving in different directions travel different distances both inside and outside the iWASP before reaching the detector. For small particle deflections inside the magnetic field, the vertical displacement of a non-relativistic ion with mass m , on a detector located a distance d_B after the end of the magnetic field is given by

$$D_B(\alpha) = \frac{qB_{\perp}(\alpha)L_B(\alpha)}{mv_{\alpha}} \left(\frac{L_B(\alpha)}{2} + d_B(\alpha) \right), \quad (2)$$

where D_B is the displacement, B_{\perp} is the component of the magnetic field in the horizontal plane directed perpendicular to the ion trajectory, v_{α} is the velocity component directed at an angle α from the z -direction, and L_B is the length of the magnetic field.

In the detector plane of the iWASP, the ion energies are thus given by their vertical position and their angular properties along the horizontal axis. Along the axis of the entrance slit the iWASP thereby gives an angularly resolved ion energy spectrum (requirement (I) above).

B. Ion separation extension (ISE)

The magnetic fields of neither a basic magnetic ion spectrometer nor an iWASP, can separate multiple different ion species. This can be remedied by letting the ions pass through an electric field \vec{E} , which exerts a force

$$\vec{F} = q\vec{E} \quad (3)$$

on a particle with charge q .

Traditionally, in a Thomson parabola, where a magnetic ion spectrometer is combined with high voltage electrodes, only one detector plane is used and electrodes are placed inside or directly after the magnet. This is not possible with an iWASP since the traces of different ion species would be overlapping.

To fulfil requirement (II) above and separate multiple ion species, and at the same time maintaining requirement (I), a thin, vertical slit is made in the detector plane of the iWASP,

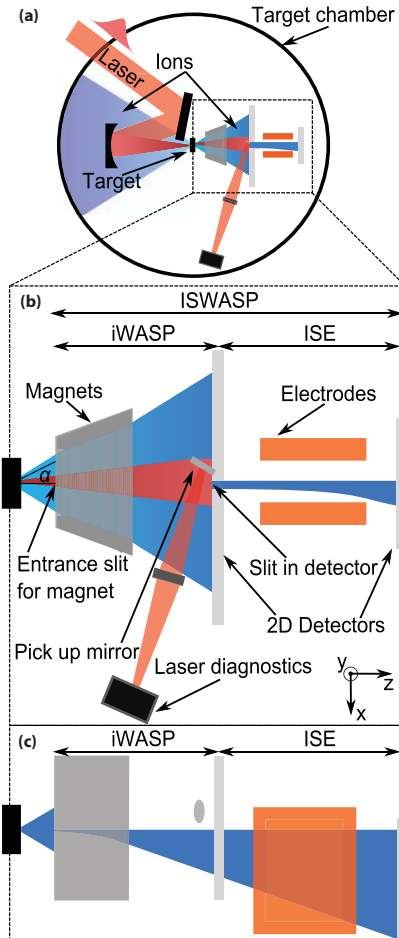


FIG. 1. (a) A schematic topview of a possible experiment chamber where the incoming laser beam is focused onto the target at normal incidence by an off-axis parabolic mirror. (b) Topview of close-up of laser and ion diagnostics (ISWASP). The ions first pass through an ion wide angle spectrometer (iWASP), providing energy dispersion. Some of the ions propagate through a slit in the first detector plane, into an ion separation extension (ISE) unit. Here, the ions pass through an electric field, providing separation according to the ions' charge to mass ratio, onto a second detector. The 2-dimensional detectors could, for example, consist of image plates and/or nuclear track detectors (CR39). Laser radiation transmitted through the target is diffracted in the entrance slit of the iWASP and thereafter picked up by a mirror located outside the ion beam and guided onto laser diagnostics. (c) Sideview of (b). In this dimension, the divergence of the ion beam is reduced due to the entrance slit of the iWASP. The laser light is here omitted for clarity but the pick-up mirror is shown above the ion beam.

positioned in the target normal direction (0°) in Fig. 1. It could however be placed along any arbitrary axis directed at an angle α from the target normal, inside the acceptance angle of the iWASP. The slit is perpendicular to the entrance slit of the iWASP and they are thereby together forming a

rectangular “pinhole.” Behind this “pinhole” two high voltage copper electrodes are placed. This extension separates the different ion species in a direction perpendicular to the magnetic displacement when a high voltage is applied to the electrodes. The deviation from the original axis for a non-relativistic ion caused by the \vec{E} -field is given by

$$D_E = \frac{qE_x L_E}{m v_x^2} \left(\frac{L_E}{2} + d_E \right), \quad (4)$$

where D_E denotes the displacement, m is the mass of the ion, L_E is the length of the electric field, and d_E is the distance to the detector plane from the end of the electric field.

After the electrodes an additional detector is located to record the ion traces. With this extension we add the capability of ion separation and of recording spectra for several ion types to the iWASP, together forming the ion separation wide angle spectrometer (ISWASP). It is further also possible to use several extensions in different directions in a multi-ISWASP configuration.

The resolution of the ISE is limited by properties of the electric field, such as strength and length, and the size of the rectangular “pin hole.” The height of the first slit determines the energy resolution whereas the width of the second slit affects the width of the traces and thereby how well the ion traces from different species are separated. The vertical slit should be chosen as wide as possible, while still allowing the different ion traces to be separated, in order to maximize the signal to noise level on the detector.

The distances between the different components of the diagnostics can be varied, as well as the voltages applied to the electrodes, making it possible to tune the diagnostic for different circumstances. It is therefore a versatile instrument suitable to use with a wide range of particle energies.

C. Characterization of transmitted and reflected laser radiation

In the presented design, we utilize the fact that a significant amount of laser light can be collected through the entrance slit of the ISWASP to cover requirement (III). This allows simultaneous recording of the laser light transmitted and reflected from the target along with the ion spectra. A pick-up mirror is placed in front of the first detector plane. We exploit that any part of the laser pulse transmitted through the target foil will diffract in the slit of the ISWASP, making it possible to place a pick-up mirror in such a way that it does not affect or clip the ion beam or the zero-order (neutral particles that are unaffected by the electric and magnetic field), see Fig. 1(c). The pick-up mirror reflects the light into an optical diagnostic instrument. The incident laser light which is reflected on the target is recollimated by the focusing optics and a fraction is picked up by a leakage from one of the mirrors in the beam path.

In a simple version, integrating diagnostic can be used for both the transmitted and reflected laser light. In order to fully resolve the dynamics, an auto-correlator or a Frequency-Resolved Optical Gating²⁵ (FROG) could be used, providing further information about the temporal evolution of the transient plasma dynamics.

III. IMPLEMENTATION

The proposed design of the ISWASP has been tested at the PHELIX laser²⁶ at GSI Helmholtzzentrum für Schwerionenforschung GmbH, Germany. Protons and carbon ions were accelerated from nanometre thin parylene foils^{27,28} by a 80 J, 500 fs laser pulse with a central wavelength of 1053 nm, which could be made circularly polarized by using a quarter-wave plate. The laser pulse was interacting with the target at normal incidence.

Ion and proton spectra were recorded simultaneously with the ISWASP. The iWASP-section used consists of two 10 cm long permanent magnets mounted in an iron yoke with a half angle of 15° and a horizontal entrance slit positioned on the front. The magnetic field between the magnets is approximately 0.4 T. The detector plane of the iWASP was positioned 500 mm from the source. In the implementation of this design, the particle detectors of the iWASP were image plates²⁹ covered with a layer of 1 mm thick CR39³⁰ in the region where protons above 10 MeV are expected. Protons with such energies will pass through the layer onto the image plate, whereas the heavier ions will be stopped in the CR39. The damage in the CR39 caused by protons at these energies is negligible and only visible after long etching times. The angularly resolved proton spectrum and the spectrum of the carbon ions were detected on the image plate and CR39, respectively. The entrance slit of the ISE measured 120 μm and was positioned in the target normal direction, $\alpha = 0^\circ$. The electrodes of the ISE were 100 mm long, separated by 16 mm, and had an applied voltage of 7 kV. The detector of the ISE was placed 800 mm from the source and consists of an image plate. Ion traces in the ISE were obtained for protons, C^{6+} and C^{5+} , see Fig. 2. The optical axis is not visible in the figure but corresponds to the point where both \vec{E} -field and \vec{B} -field deflections are zero. The diagnostics can easily be adjusted for different target materials, giving other ion species, by changing the voltage on the electrodes and/or the distance from the electrodes to the detector plane.

The traces on the image plate can be analysed starting from Eqs. (2) and (4) and the spectra for each ion species can thus be obtained. Spectra corresponding to the ion traces in Fig. 2 are found in Fig. 3. In the analysed spectra, a maximum energy of ~28 MeV was determined for protons and

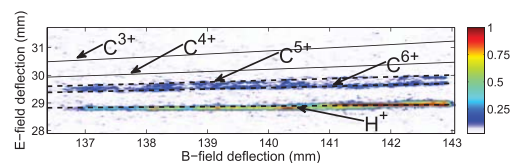


FIG. 2. Image plate with experimentally obtained ion traces from the ion separation extension (ISE) in combination with the ion wide angle spectrometer (iWASP). The dashed lines indicate simulated traces of H^+ , C^{6+} , and C^{5+} , whereas the thin, solid lines indicate the simulated traces of C^{4+} and C^{3+} . The latter two traces and subsequently also carbon ions in lower charge states, were below the detection threshold for the experimental conditions under which the ISWASP was tested, as most carbon ions were then fully ionized. The color scale gives the photo stimulated luminescence of the image plate where one corresponds to the strongest signal.

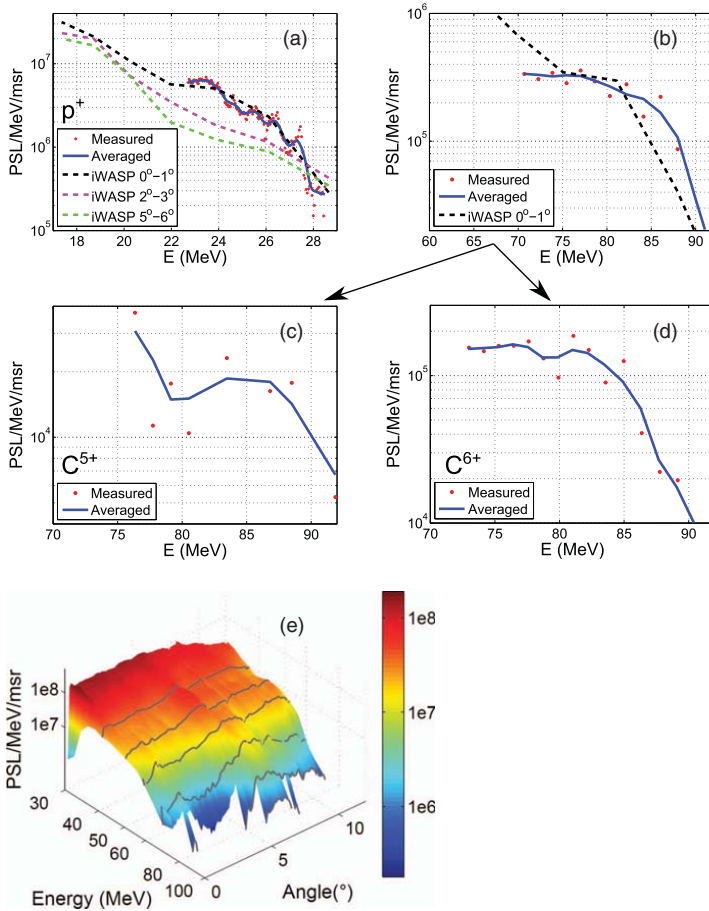


FIG. 3. Ion spectra obtained with an iWASP, analysed from raw traces shown in Fig. 2. From the ISE-unit, the red dots indicate actual data points whereas the solid blue line is a moving average over several data points and are recorded from the ion separation extension. The dashed lines are spectra recorded with only the iWASP. On the vertical axes PSL stands for the photo stimulated luminescence of the image plates. For conversion of PSL to absolute particle numbers, an equipment specific calibration is required. (a) Proton spectra, the different angular intervals are defined so that 0° is directed in the target normal direction. (b) The carbon ion traces recorded with iWASP and CR39 as detector and the ISE using an image plate, in both cases assuming that only C⁶⁺ is present. Then in (c) (C⁵⁺) and (d) (C⁶⁺) the different species have been separated. (e) Carbon wide angle spectrum from iWASP, again assuming that only C⁶⁺ is present.

~90 MeV for both detected carbon charge states. It can also be seen in Fig. 3 that, as expected, the proton spectra from the iWASP converges into the one from the ISE as the angle moves towards 0° where the extension was placed. In the detector plane of the iWASP, carbon ions are detected with a CR39. The analysis of this has been done assuming that all carbon atoms were fully ionised to C⁶⁺. In order to be able to compare with the ISE, the carbon traces in Fig. 2 were first analysed as if they both were C⁶⁺. These spectra are shown together in Fig. 3(b). In Figs. 3(c) and 3(d), spectra can be seen from the ISE, where the two different charge states of carbon ions have been separated. From these spectra, the ratio between the number of C⁵⁺ and C⁶⁺ can also be deduced (in spectra from Fig. 3 this ratio is ~13%) and

thereby giving an error estimate of the spectra in Figs. 3(b) and 3(e).

If a higher voltage is applied to the electrodes in the ISE, the separation between the different ion traces in Fig. 2 would become larger and thereby making the analysis easier for cases where there are many different species present.

The laser spectrum was recorded with optical spectrometers, both in the transmitted and the reflected direction, see Fig. 4 where the second order harmonic is shown. Red and blue-shifts can be compared for different shots for both the transmitted and reflected light and from this information about the plasma expansion from the laser-target interaction can be deduced. Shot to shot variations in the intensity ratio between the two light components can also be analysed.

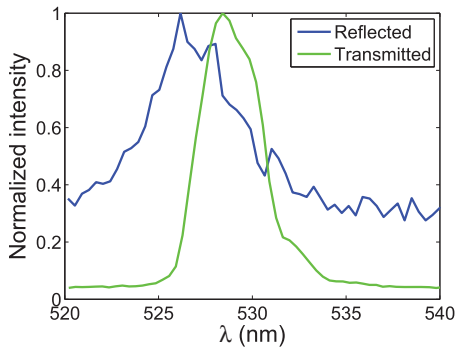


FIG. 4. The second order harmonic of the laser spectrum reflected from (blue) and transmitted through (green) the target. The former recollimated by the focusing optics and recorded through a leakage of a mirror in the laser beam path and the latter picked up from diffraction from the entrance slit of the ISWASP.

IV. CONCLUSIONS

A novel diagnostics, the ISWASP, is presented with the major advantage that multiple parameters can be investigated simultaneously, minimizing the impact of shot-to-shot fluctuations. This is especially important when taking into account the current repetition rate at many high power laser facilities (commonly as low as $\sim 1/h$), which makes it challenging to acquire large data sets. The diagnostic presented here gives highly useful additional information compared to only using a RCF stack, a Thomson parabola, or an iWASP, in particular for distinguishing between different laser ion acceleration mechanisms. In this first experiment, the ISE was used only along the optical axis, but it could be positioned along any axis in the detection plane of the iWASP and multiple extensions could also be used simultaneously allowing ion separation along different axes.

ACKNOWLEDGMENTS

The research leading to these results has received funding from LASERLAB-EUROPE (Grant Agreement No. 284464, EC's Seventh Framework Programme) and the Swedish Research Council. L. Senje acknowledges financial support from SILMI, European Science Foundation (ESF).

- ¹A. Macchi, M. Borghesi, and M. Passoni, *Rev. Mod. Phys.* **85**, 751–793 (2013).
- ²S. P. Hatchett, C. G. Brown, T. E. Cowan, E. A. Henry, J. S. Johnson, M. H. Key, J. A. Koch, A. B. Langdon, B. F. Lasinski, R. W. Lee, A. J. Mackinnon, D. M. Pennington, M. D. Perry, T. W. Phillips, M. Roth, T. C. Sangster, M. S. Singh, R. A. Snavely, M. A. Stoyer, S. C. Wilks, and K. Yasuike, *Phys. Plasmas* **7**, 2076 (2000).
- ³S. C. Wilks, A. B. Langdon, T. E. Cowan, M. Roth, M. Singh, S. Hatchett, M. H. Key, D. Pennington, A. MacKinnon, and R. A. Snavely, *Phys. Plasmas* **8**, 542 (2001).
- ⁴T. Esirkepov, M. Borghesi, S. V. Bulanov, G. Mourou, and T. Tajima, *Phys. Rev. Lett.* **92**, 175003 (2004).

- ⁵A. Macchi, F. Cattani, T. V. Liseykina, and F. Cornolti, *Phys. Rev. Lett.* **94**, 165003 (2005).
- ⁶L. Yin, B. J. Albright, B. M. Hegelich, K. J. Bowers, K. A. Flippo, T. J. T. Kwan, and J. C. Fernandez, *Phys. Plasmas* **14**, 056706 (2007).
- ⁷B. J. Albright, L. Yin, K. J. Bowers, B. M. Hegelich, K. A. Flippo, T. J. T. Kwan, and J. C. Fernandez, *Phys. Plasmas* **14**, 094502 (2007).
- ⁸R. C. Shah, R. P. Johnson, T. Shimada, K. A. Flippo, J. C. Fernandez, and B. M. Hegelich, *Opt. Lett.* **34**, 2273 (2009).
- ⁹A. Jullien, O. Albert, F. Burgy, G. Hamoniaux, J.-P. Rousseau, J.-P. Chambaret, F. Aug-Rochereau, G. Chriaux, J. Etchepare, N. Minkovski *et al.*, *Opt. Lett.* **30**, 920 (2005).
- ¹⁰A. Henig, S. Steinke, M. Schürer, T. Sokollik, R. Hörlein, D. Kiefer, D. Jung, J. Schreiber, B. M. Hegelich, X. Q. Yan, J. Meyer-ter Vehn, T. Tajima, P. V. Nickles, W. Sandner, and D. Habs, *Phys. Rev. Lett.* **103**, 245003 (2009).
- ¹¹D. Jung, L. Yin, D. C. Gautier, H.-C. Wu, S. Letzring, B. Dromey, R. Shah, S. Palaniyappan, T. Shimada, R. P. Johnson, J. Schreiber, D. Habs, J. C. Fernández, B. M. Hegelich, and B. J. Albright, *Phys. Plasmas* **20**, 083103 (2013).
- ¹²B. Aurand, S. Kuschel, O. Jäckel, C. Rödel, H. Y. Zhao, S. Herzer, A. E. Paz, J. Bierbach, J. Polz, B. Elkin *et al.*, *New J. Physics* **15**, 033031 (2013).
- ¹³B. Aurand, S. Kuschel, O. Jäckel, C. Rödel, H. Zhao, S. Herzer, A. Paz, J. Bierbach, J. Polz, B. Elkin *et al.*, *Nucl. Instrum. Methods Phys. Res. A* **740**, 83–86 (2014).
- ¹⁴C. A. J. Palmer, N. P. Dover, I. Pogorelsky, M. Babzien, G. I. Dudnikova, M. Isiriyan, M. N. Polyanskiy, J. Schreiber, P. Shkolnikov, V. Yakimenko, and Z. Najmudin, *Phys. Rev. Lett.* **106**, 014801 (2011).
- ¹⁵S. Kar, K. F. Kakolee, B. Qiao, A. Macchi, M. Cercez, D. Doria, M. Geissler, P. McKenna, D. Neely, J. Osterholz, R. Prasad, K. Quinn, B. Ramakrishna, G. Sarri, O. Willi, X. Y. Yuan, M. Zepf, and M. Borghesi, *Phys. Rev. Lett.* **109**, 185006 (2012).
- ¹⁶A. P. L. Robinson, M. Zepf, R. G. Kar, S. Evans, and C. Bellei, *New J. Phys.* **10**, 013021 (2008).
- ¹⁷L. Yin, B. J. Albright, K. J. Bowers, D. Jung, J. C. Fernández, and B. M. Hegelich, *Phys. Rev. Lett.* **107**, 045003 (2011).
- ¹⁸S. Palaniyappan, B. M. Hegelich, H.-C. Wu, D. Jung, D. C. Gautier, L. Yin, B. J. Albright, R. P. Johnson, T. Shimada, S. Letzring, D. T. Offermann, J. Ren, C. Huang, R. Hörlein, B. Dromey, J. C. Fernandez, and R. C. Shah, *Nat. Phys.* **8**, 763 (2012).
- ¹⁹A. Macchi, S. Veghini, T. V. Liseykina, and F. Pegoraro, *New J. Phys.* **12**, 045013 (2010).
- ²⁰A. Maksimchuk, S. Gu, K. Flippo, and D. Umstadter, *Phys. Rev. Lett.* **84**, 4108–4111 (2000).
- ²¹F. Nürnberg, M. Schollmeier, E. Brambrink, A. Blazevic, D. C. Carroll, K. Flippo, D. C. Gautier, M. Geissel, K. Harres, B. M. Hegelich, O. Lundh, K. Markey, P. McKenna, D. Neely, J. Schreiber, and M. Roth, *Rev. Sci. Instrum.* **80**, 033301 (2009).
- ²²J. J. Thomson, *Philos. Mag. Ser. 6* **22**, 469 (1911).
- ²³D. Jung, R. Hörlein, D. C. Gautier, S. Letzring, D. Kiefer, K. Allinger, B. J. Albright, R. Shah, S. Palaniyappan, L. Yin, J. C. Fernandez, D. Habs, and B. M. Hegelich, *Rev. Sci. Instrum.* **82**, 043301 (2011).
- ²⁴D. Gwynne, S. Kar, D. Doria, H. Ahmed, M. Cercez, J. Fernandez, R. J. Gray, J. S. Green, F. Hanton, D. A. MacLellan *et al.*, *Rev. Sci. Instrum.* **85**, 033304 (2014).
- ²⁵D. Kane and R. Trebino, *IEEE J. Quantum Electron.* **29**, 571–579 (1993).
- ²⁶V. Bagnoud, B. Aurand, A. Blazevic, S. Borneis, C. Bruske, B. Ecker, U. Eisenbarth, J. Fils, A. Frank, E. Gaul *et al.*, *Appl. Phys. B* **100**, 137–150 (2010).
- ²⁷B. Aurand, B. Elkin, L.-O. Heim, B. Lommel, B. Kindler, M. Tomut, C. Rödel, S. Kuschel, O. Jäckel, J. Barz *et al.*, *J. Polym. Sci. Part B: Polym. Phys.* **51**, 1355–1360 (2013).
- ²⁸B. Aurand, B. Elkin, L.-O. Heim, B. Lommel, B. Kindler, M. Tomut, C. Rödel, S. Kuschel, O. Jäckel, and T. Kuehl, *J. Radioanal. Nucl. Chem.* **299**, 965 (2014).
- ²⁹I. J. Paterson, R. J. Clarke, N. C. Woolsey, and G. Gregori, *Meas. Sci. Technol.* **19**, 095301 (2008).
- ³⁰R. L. Fleischer, P. B. Price, and R. M. Walker, *J. Appl. Phys.* **36**, 3645 (1965).

PAPER II

A setup for studies of laser-driven proton acceleration at the Lund Laser Centre

B. Aurand, M. Hansson, L. Senje, K. Svensson, A. Persson, D. Neely, O. Lundh, & C.-G. Wahlström.

Laser and Particle Beams 33, 0263-0346/14 (2015).

A setup for studies of laser-driven proton acceleration at the Lund Laser Centre

B. AURAND,¹ M. HANSSON,¹ L. SENJE,¹ K. SVENSSON,¹ A. PERSSON,¹ D. NEELY,² O. LUNDH,¹
 AND C.-G. WAHLSTRÖM¹

¹Department of Physics, Lund University, Lund, Sweden

²Central Laser Facility, STFC Rutherford Appleton Laboratory, Didcot, United Kingdom

(RECEIVED 8 September 2014; ACCEPTED 26 October 2014)

Abstract

We report on a setup for the investigation of proton acceleration in the regime of target normal sheath acceleration. The main interest here is to focus on stable laser beam parameters as well as a reliable target setup and diagnostics in order to do extensive and systematic studies on the acceleration mechanism. A motorized target alignment system in combination with large target mounts allows for up to 340 shots with high repetition rate without breaking the vacuum. This performance is used to conduct experiments with a split mirror setup exploring the effect of spatial and temporal separation between the pulses on the acceleration mechanism and on the resulting proton beam.

Keywords: Laser-ion acceleration; Mirror design; Radiation detectors

INTRODUCTION

Within the last decade, tremendous progress has been made in the field of laser ion acceleration. First demonstrated *Wilks et al., 2001* by the mechanism of target normal sheath acceleration (TNSA) nowadays provides a source for ultra-short proton bunches with energies up to several tens of MeV (*Daido et al., 2012; Passoni et al., 2010*). An ultra-intense laser pulse ($I > 10^{16}$ W/cm²) which interacts with the front-side of a μm -thick target foil drives a massive electron current toward the rear-side of the target. The electrons exiting the target on the scale of the Debye-length create a charge separation field between them and the positively charged remaining bulk. This generates an electric field in the order of a few TV/m. In this field, which can be considered static on the timescale of a several 100's of fs up to a few ps (*Schreiber et al., 2006*), protons and heavier ions like carbon or oxygen — mainly from the hydrocarbon contamination layer on the target — are accelerated.

Numerous studies on the mechanism of TNSA have been made so far, e.g., the investigation of the dependence on laser parameters like the focal spot size (*Brenner et al., 2011*), energy (*Coury et al., 2012*), or pulse duration (*Robson et al., 2007*), studies on the electron current driven in the

target (*Tresca et al., 2011; Coury et al., 2013*), or different target geometry (*Schwoerer et al., 2006; Ramakrishna et al., 2010; Hegelich et al., 2006; Burza et al., 2011*). In our current study on TNSA acceleration, we focus on the influence of two independent laser pulses with different temporal and spatial separation, interacting with the target and driving the acceleration. In this paper we describe the technical part of the setup, which includes laser and particle diagnostics as well as the target and optical probing system.

LASER SYSTEM

The Lund terawatt laser is a Ti:Sapphire based CPA (*Strickland & Mourou, 1985*) laser system with four amplification stages situated in the basement of the Physics Department at Lund university. A dedicated diagnostic table setup next to the compressor allows the verification of the laser beam parameters on a daily basis. The pulse duration is measured with a second order single-shot autocorrelator. A third order scanning autocorrelator (Amplitude, Sequoia[®]) is used to measure the laser contrast. Besides that, the spectrum (RGB, Qwave[®]) and the spectral phase (Avesta, SPIDER SP-120) are recorded. A mirror in the beam line with a designed leakage of 1.5% allows for on-shot recording of autocorrelation and laser spectrum. Typical pulse parameters are an energy $E_L = 0.9$ J at a pulse duration of $\tau_L = 35$ fs. The laser contrast is $0.5\text{--}1 \times 10^{-9}$ up to 50 ps before the main

Address correspondence and reprint request to Bastian Aurand, Department of Physics, Lund University, 22100 Lund, Sweden.
 E-mail: bastian.aurand@uni-duesseldorf.de

pulse. A beam position system controls piezo mirrors in the amplifier chain and compensates for long term drifts which helps to keep laser parameters stable during operation.

A deformable mirror (DM) with a clear aperture of 65 mm, segmented in 32 piezo controlled areas (NightN Ltd., DM2-65-32) in the beam line enables corrections of the wavefront downstream. The 45 mm diameter beam is guided in vacuum and can be delivered into two different target areas by flipping one of the beam line mirrors. One of the target areas is mainly dedicated to laser wakefield acceleration (LWFA) (Desforges *et al.*, 2014; Hansson *et al.*, 2014) experiments, whereas the other target area mainly for proton experiments. The radiation shielding allows simultaneous experiments on electrons in one room and preparation of ion acceleration experiments in the other room. Both cylindrical experimental chambers with an inner diameter of 108 cm and a height of 37 cm are accessible by removing the lid or flanges on the side of the vacuum vessel. In the following, we will focus on the proton setup only (Fig. 1).

TARGET SYSTEM

Below the proton chamber is a housing containing an electrically insulated and Faraday-shielded xyz-linear stage system (Newport, GTS70). Using optical encoded position sensors and double-shielded cables, malfunction events due to electro-magnetic pulses do not occur. All stages have a

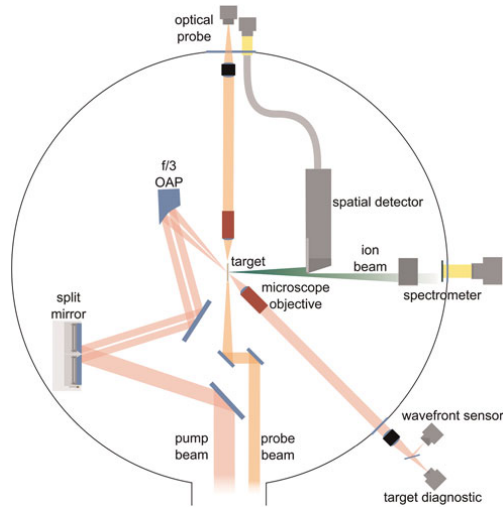


Fig. 1. Experimental setup for proton acceleration in the TNSA regime. The incident laser pulse is divided by a split-mirror into two beams which can be spatially and temporally shifted with respect to each other. Both beams are focused by the same OAP onto the target. The accelerated protons can be sent to a spectrometer for an energy measurement or a spatial detector in order to determine the beam profile. An independent optical probe can be used to do shadowgraphy or interferometry of the target rear surface.

travel range of 70 mm at a velocity of up to 50 mm/s with an on-axis accuracy of $\pm 1\mu\text{m}$ and a bi-directional position reproducibility of 100 nm. The upper part of the target mount holds a three-point load, multi-purpose holder on which different kinds of self-centering targets can be mounted. Additional tip/tilt screws enable target adjustments perpendicular to the motion axis which is checked for every target with a micrometer caliper. Primarily used is an matrix target mount with 340 (17×20) independent target positions of 1 mm diameter and 2.5 mm separation (Fig. 2a). The mount consists of two comb shaped plates where a target foil can be clamped in between (Fig. 2b). Using an additional spacer, double layered target configurations or grids for proton imaging purposes can be realized.

The position of the target chamber center (TCC) which is the dedicated focus position is defined by the overlap of two external lasers beams, each referenced to the center of two opposed flanges on the chamber wall. This position is transferred to an alignment needle on the target mount and verified during major rebuilds. The target is aligned in the TCC using the laser focus diagnostic, observing the

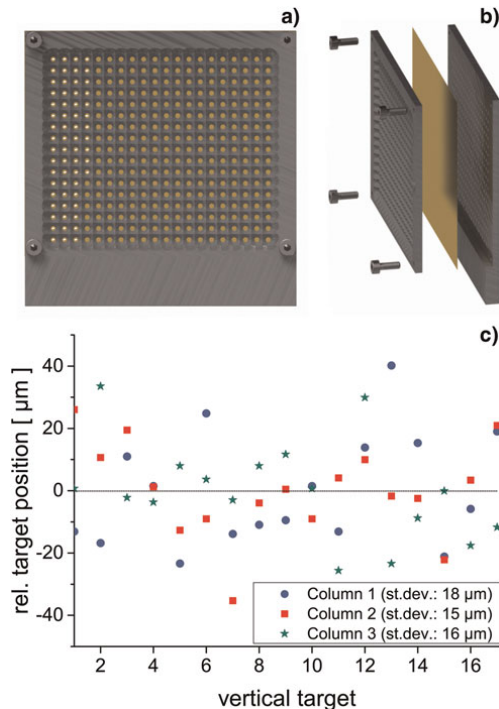


Fig. 2. (a) Matrix target mount with 340 (17×20) independent target positions. (b) The mount consists of two comb shaped plates where the target foil is clamped in between (c) Scan of the relative focal position for a column wise vertical movement of a $3\mu\text{m}$ Al foil. The standard deviation in each column is less than $18\mu\text{m}$.

reflection of a monochromatic light source from the target rear surface at an angle of 45° . This diagnostic is based on an infinity corrected 10 \times objective (Mitutoyo, Plan Apo NIR) with a working distance of 31 mm, imaging the laser focal plane onto a camera outside the vacuum vessel. Alternatively, for the laser alignment, the beam can be sent to a modified Hartmann sensor (Hartmann, 1900; Primot *et al.*, 1995) (Phasics, SID4) to measure the wavefront. Note that within this setup using a DM, wavefront corrections for all optical elements up to the final focusing parabola can be included. The small depth of the focus diagnostic ($4.1 \mu\text{m}$) and the additional observation angle allow for a position accuracy of $2\text{--}3 \mu\text{m}$ with respect to the objective.

The typical procedure in order to take a series of shots is a columnwise pre-inspection of the target, regarding foil condition and possible wrinkles. This allows for a burst-mode of up to 17 shots within 1 min by moving the target vertically to the next position without any further inspection. Measurements of the focus position (Fig. 2c) for a pre-aligned target show a deviation of less than $18 \mu\text{m}$, which is significantly smaller than the Rayleigh-length. This deviation is mainly given by imperfections during manufacturing of the target mount. The complete remote control of the target alignment enables a scan with a complete target in less than 1.5 h. Simultaneous monitoring and controlling of the laser parameters guarantee stable laser conditions. Further automated control of the target system, e.g., by target positioning via chromatic-confocal sensing (Ruprecht, A.K. *et al.* 2005) could increase the repetition rate and precision of the alignment.

SPLIT MIRROR SETUP

Focusing of the laser is done by an off-axis parabolic mirror with 152 mm focal length (SORL, OAP 06-02-03/MMOA-3) giving a focal spot of $5 \mu\text{m}$ (FWHM) corresponding to a maximum intensity of $2 \times 10^{19} \text{ W/cm}^2$ on the target and a measured Rayleigh-length of ($z_R \approx 50 \mu\text{m}$). One of the mirrors inside the experimental chamber consists of a specially designed split-mirror to generate two independent beams which can be spatially and temporally shifted with respect to each other (Fig. 3a). The setup is based on two protected silver mirrors sized $70 \times 90 \text{ mm}$ which have a thin edge to place them side by side, leaving a vertical gap of only a few tenths of a millimetre. Both mirrors are mounted separately and can be tilted horizontally and vertically using piezo-linear actuators (Newport, Picomotor). In addition, one of the mirrors is mounted on a linear stage allowing for a translation perpendicular to its surface. The introduced path difference of up to 20 mm in either direction at an incidence angle of $\approx 12^\circ$ corresponds to a temporal delay of max. $\pm 68 \text{ ps}$ with respect to the fixed pulse. Finally, both mirrors can be moved sideways simultaneously to change the fraction of the incident beam on each mirror and therefore the energy ratio between the two pulses.

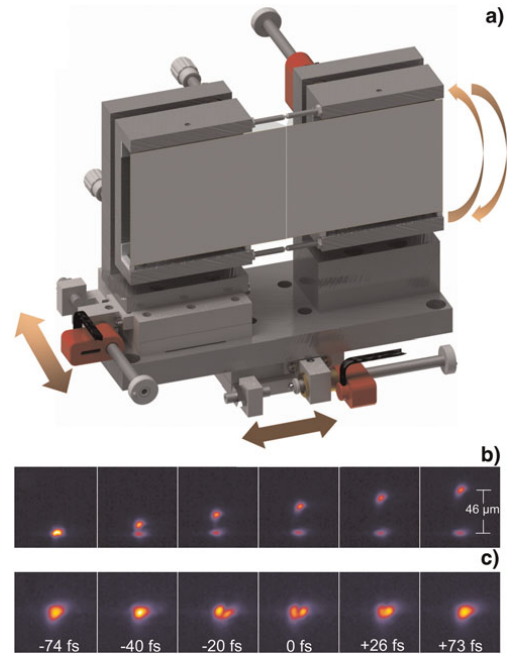


Fig. 3. (a) Split mirror setup generating two independent beams, which can be spatially and temporally shifted against each other. In addition the amount of energy in both parts can be changed. (b) Vertical focus separation by movement of one beam. (c) Interference structures are visible when the beams overlap within $\Delta t = \pm 20 \text{ fs}$ relative timing.

We deduce the minimal vertical movement of the beam in the focal plane to 150 nm/steps of the piezomotor tilting the mirror. In the given geometry, a vertical separation does not significantly change the length of each beam path, so it is not changing the relative timing between the two pulses. The bi-directional repeatability due to hysteresis effects in the mount is in the order of $5\text{--}6 \mu\text{m}$. To avoid this effect, scans are always performed in one direction of movement (Fig. 3b).

The temporal overlap of the pulses is verified by the observation of an interference structure while both beams are spatially overlapped. The interference pattern is visible within a spatial range of $20 \mu\text{m}$ corresponding to $\approx 60 \text{ fs}$ temporal range, showing a symmetric maximum (Fig. 3c). This method allows for a relative timing with a sub-pulse duration accuracy which is higher compared to methods like transverse probing of the generated plasma (Aurand *et al.*, 2014).

Advantageous for all kinds of measurement series done with this setup are the common beam line and the focusing system downstream of the split-mirror, making the measurements insensitive to beam pointing fluctuations. Even if the absolute focus position of the system undergoes a small spatial jitter, the relative spatial and temporal separation of the beams remained fixed.

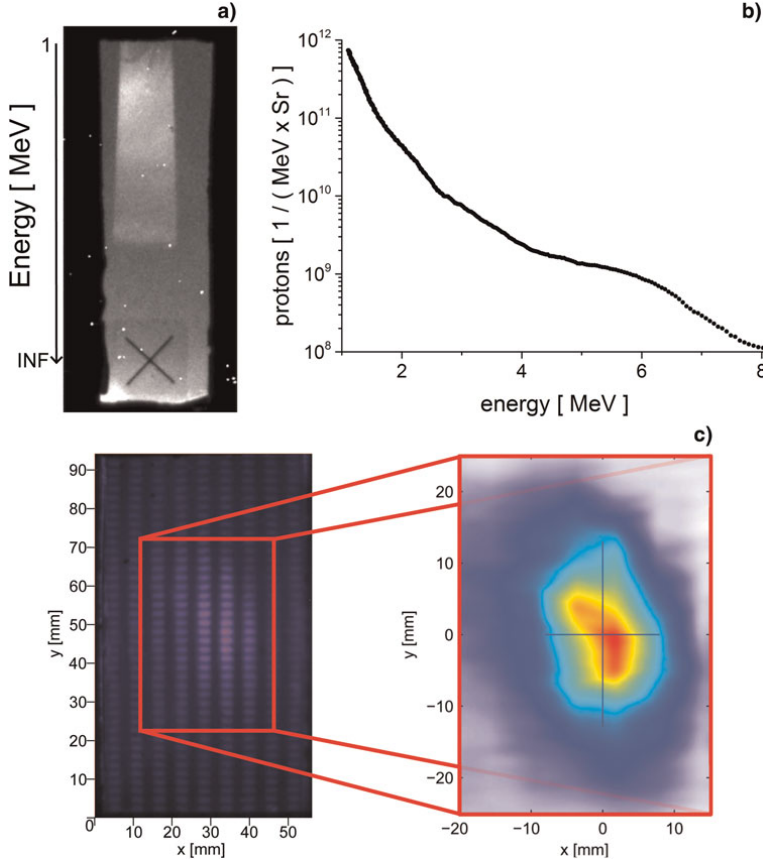


Fig. 4. Proton energy measurement from a $3\ \mu\text{m}$ Al foil. (a) The raw data image obtained by the fluorescence of energy dispersed protons in a BC-408 scintillator in target normal direction. (b) Evaluated proton spectra using the calculated deflection curve and a cross calibration with CR-39 to get the absolute particle number. (c) Using the spatial detector, a beam profile of the accelerated particles can be taken. An Al filter grid in front of the detector allows for the subtraction of the electron background and a reconstruction of the proton beam profile.

ION DIAGNOSTIC

Ions are accelerated from the target rear surface. In order to be able to match the high repetition rate and the high number of shots per target, all diagnostics used in this setup have digital readouts.

The proton energy is determined by deflection of the proton beam in a magnetic field with an effective strength of $B_{\text{eff}} = 0.69\ \text{T}$ and a length of 6 cm, which is situated in the target normal direction (47 ± 0.5) cm behind the target. A 1 mm horizontal entrance slit covers a solid angle of (8×10^{-5}) sr. Heavier ions are blocked by a $6\ \mu\text{m}$ Al filter in front of the scintillator (St. Gobain, BC-408). The fluorescence signal is imaged by a 16-bit camera (Princeton, “PhotonMAX 1024”) (Fig. 4a). To obtain the absolute particle number, a cross-calibration using a CR-39 trace detector

was done (Cartwright *et al.*, 1978) (Fig. 4b). The lowest detectable energy, determined by the setup geometry, is 1.2 MeV. The highest resolvable energy is ≈ 10 MeV.

The proton beam profile is measured by moving a scintillator (St. Gobain, BC-408) with a thickness of $500\ \mu\text{m}$ into to the beam at a position of (65 ± 2) mm behind the target. The scintillator is placed in a light-shielded aluminum box with a $12\ \mu\text{m}$ thick Al entrance window and an acceptance angle of 28° . The scintillator is imaged by an objective inside the box onto an optical fiber bundle, which transfers the signal out of the vacuum chamber onto a camera (Fig. 4c). Using a grid of Al bars with different thicknesses in front of the scintillator allows for an analytical subtraction of the electron background, superimposed with the signal, by taking the different stopping power for electrons and protons into account. In

contrast to a stack of radiochromic film (RCF), the energy selectivity of the scintillator is not very high. The signal is a superposition of all protons which are passing the filter and thus being transmitted or being stopped in the scintillator ($d_{\text{Scint}} = 0.5 \text{ mm}$; $0.9 \text{ MeV} \leq E_{\text{Stop}} \leq 7 \text{ MeV}$). In the future, a stack of scintillators with various thickness which are fluorescing at different wavelengths could be used to obtain an energy resolved signal (Green *et al.*, 2011). Note that the response from a scintillator depends both on particle number and particle energy, which needs to be taken into account calculating absolute particle numbers (Green *et al.*, 2011).

OPTICAL PROBE SETUP

A small amount ($\approx 10 \text{ mJ}$) of the stretched pulse can be coupled from the last amplification stage of the laser system and sent to a separate pulse compressor. This part is compressed to roughly 60 fs and can optionally be frequency doubled ($\lambda_{2\omega} = 400 \text{ nm}$). A specially designed curved target mount allows for probing along the target rear surface without being affected by the bright plasma on the front surface (Fig. 5a). A motorized linear stage with 150 mm travel enables controlled delay scans in a time window of up to 1 ns. The probe imaging system consists of a 20 \times infinity corrected objective (Mitutoyo, Plan Apo NIR) with a working distance of 20 mm. The image is collected by a camera outside the vacuum vessel. In this configuration, shadowgraphy can be obtained, with a resolution of 1 μm (Fig. 5b). By adding a Wollaston prism (Small *et al.*, 1973) and two polarizers outside the chamber, Nomarski-interferometry can be done to determine the electron density (Fig. 5c).

OUTLOOK

The double pulse setup described above was developed and implemented within the last year and has been used for experiments. More than 4000 shots on targets have been conducted so far, investigating changes in particle-energy

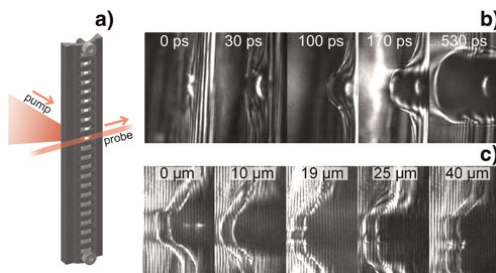


Fig. 5. (a) Curved target mount for transverse optical probing of the target rear surface. (b) High resolution shadowgraphy of an evolving plasma-plume, probed at different times compared to the pump-pulse. (c) Raw image by the Nomarski interferometric setup of two plasma-plumes for a fixed time but different separations, done by the split-mirror setup.

distribution and proton beam profile. Tentative results show a clear dependence of particle energy and proton beam divergence on the spatial separation of the two foci. A detailed analysis and comparison to numerical simulations is currently under investigation and will be reported accordingly.

ACKNOWLEDGMENTS

We gratefully thank the Knut and Alice Wallenberg Foundation, the Swedish Research Council and the Swedish Foundation for Strategic Research for financial support. D. Neely acknowledges financial support by the UK Grant program: EP/K022415/1 (Advanced laser-ion acceleration strategies towards next generation healthcare).

REFERENCES

- AURAND, B., KUSCHEL, S., JÄCKEL, O., RÖDEL, C., ZHAO, H.Y., HERZER, S., PAZ, A.E., BIERBACK, J., POLZ, J., ELKIN, B., KAMAKAR, A., GIBBON, P., KALUZA, M.C. & KUEHL, T. (2014). Enhanced radiation pressure-assisted acceleration by temporally tuned counter-propagating pulses. *Nucl. Inst. Meth. A* **740**, 033031.
- BRENNER, C.M., GREEN, J.S., ROBINSON, A.P.L., CARROLL, D.C., DROMEY, B., FOSTER, P.S., KAR, S., LI, Y.T., MARKEY, K., SPINDLOE, C., STREETER, M.J.V., TOLLEY, M., WAHLSTRÖM, C.-G., XU, M.H., ZEPF, M., MCKENNA, P. & NEELY, D. (2011). Dependence of laser accelerated protons on laser energy following the interaction of defocused, intense laser pulses with ultra-thin targets. *Lasers Part. Beams* **29**, 345–351.
- BURZA, M., GONOSKOV, A., GENOUD, G., PERSSON, A., SVENSSON, K., QUINN, M., MCKENNA, P., MARKLUND, M. & WAHLSTRÖM, C.-G. (2011). Hollow microspheres as targets for staged laser-driven proton acceleration. *New J. Phys.* **13**, 013030.
- CARTWRIGHT, B.G. & SHIRK, E.K. (1978). A nuclear-track-recording polymer of unique sensitivity and resolution. *Nucl. Inst. Meth. A* **153**, 457–460.
- COURY, M., CARROLL, D.C., ROBINSON, A.P.L., YUAN, X.H., BRENNER, C.M., BURZA, M., GRAY, R.J., QUINN, M.N., LANCASTER, K.L., LI, Y.T., LIN, X.X., TRESKA, O., WAHLSTRÖM, C.-G., NEELY, D. & MCKENNA, P. (2012). Influence of laser irradiated spot size on energetic electron injection and proton acceleration in foil targets. *Appl. Phys. Lett.* **100**, 074105.
- COURY, M., CARROLL, D.C., ROBINSON, A.P.L., YUAN, X.H., BRENNER, C.M., BURZA, M., GRAY, R.J., QUINN, M.N., LANCASTER, K.L., LI, Y.T., LIN, X.X., TRESKA, O., WAHLSTRÖM, C.-G., NEELY, D. & MCKENNA, P. (2013). Injection and transport properties of fast electrons in ultra-intense laser-solid interactions. *Phys. Plasmas* **20**, 043104.
- DAIDO, H., NISHIUCHI, M. & S. PIROZHKO, S. (2012). Review of laser-driven ion sources and their applications. *Rep. Prog. Phys.* **75**, 056401.
- DESFORGES, F.G., HANSSON, M., JU, J., SENJE, L., AUDEY, T.L., DOBOSZ-DUFRENOY, S., PERSSON, A., LUNDH, WAHLSTRÖM, C.-G. & CROS, B. (2014). Reproducibility of electron beams from laser wakefield acceleration in capillary tubes. *Nucl. Instrum. Meth. A* **740**, 54–59.
- GREEN, J., BORGHESE, M., BRENNER, C.M., CARROLL, D.C., DOVER, N.P., FOSTER, P.S., GALLEGOS, P.L., GREEN, S., KIRBY, D., KIRKBY, K.J., MCKENNA, P., MERCHANT, M.J., NAIMUDIN, Z., PALMER, C.A.J., PARKER, D., PRASAD, R., QUINN, K.E., RAJEV,

- P.P., READ, M.P., ROMAGNANI, L., SCHREIBER, J., STREETSE, M.J.V., TRESKA, O., WAHLSTRÖM, C.-G., ZEFT, M. & NEELY, D. (2011). Scintillator-based ion beam profiler for diagnosing laser-accelerated ion beams. *SPIE Proc.* **8079**, 807991.
- HANSSON, M., SENJE, L., PERSO, A., LUNDH, O., WAHLSTRÖM, C.-G., DESFORGES, F.G., JU, J., AUDET, T.L., CROS, B., DOBOSZ, S. & MONOT, P. (2014). Enhanced stability of laser wakefield acceleration using dielectric capillary tubes. *Phys. Rev. STAB* **17**, 031303.
- HARTMANN, J. (1900). Bemerkungenüber den Bau und die Justirung von Spektrographen. *Z. Instrumentenkunde* **20**, 17–27, 47–58.
- HEGELICH, B.M., ALBRIGHT, B.J., COBBLE, J., FLIPPO, K., LETZRING, S., PAFFETT, M., RUHL, H., SCHREIBER, J., SCHULZE, R.K. & FERNÁNDEZ, J.C. (2006). Laser acceleration of quasi-monoenergetic MeV ion beams. *Nat.* **439**, 441–444.
- PASSONI, M., BERTAGNA, L. & ZANI, A. (2010). Target normal sheath acceleration: Theory, comparison with experiments and future perspectives. *New J. Phys.* **12**, 045012.
- PRIMOT, J. & SOGNO, L. (1995). Achromatic three-wave (or more) lateral shearing interferometer. *Z. JOSA A* **12**, 2679–2685.
- RAMAKRISHNA, B., MURAKAMI, M., BORGHESI, M., EHRENTAUF, L., NICKLES, P.V., SCHÜRER, M., STEINKE, S., PSIKAL, J., TIKHONCHUK, V. & TER-AVETISYAN, S. (2010). Laser-driven quasimonoenergetic proton burst from water spray target. *Phys. Plasmas* **17**, 083113.
- ROBSON, L., SIMPSON, P.T., CLARKE, R.J., LEDINGHAM, K.W.D., LINDAU, F., LUNDH, O., MCCANNY, T., MORA, P., NEELY, D., WAHLSTRÖM, C.-G., ZEPF, M. & MCKENNA, P. (2007). Scaling of proton acceleration driven by petawatt-laser plasma interactions. *Nat. Phys.* **3**, 58–62.
- RUPRECHT, A.K., PRUSS, C., TIZIANI, H.J., WOLFGAN, O., PETER, L., ARNDT, L., MOHR, J. & LEHMANN, P. (2005). Confocal micro-optical distance sensor: Principle and design. *Z. SPIE Proc.* **5856**, 128–135.
- SCHREIBER, J., BELL, F. GRÜNER, F., SCHRAMM, U., GEISSLER, M., Schnüger, TER-AVETISYAN, S., HEGELICH, B.M., COBBLE, J., BRAMBRINK, E., FUCHS, J., AUDEBERT, P. & HABS, D. (2006). Analytical model for ion acceleration by high-intensity laser pulses. *Phys. Rev. STAB* **97**, 045005.
- SCHWOERER, H., PFOTENHAUER, S. JÄCKEL, O., AMTHOR, K.-U., LIESFELD, B., ZIEGLER, W., SAUERBREY, R., LEDINGHAM, K.W.D. & ESIRKEPOV, T. (2006). Laser-plasma acceleration of quasi-monoenergetic protons from microstructured targets. *Nat.* **439**, 445–448.
- SMALL, R.D., SERNAS, V.A. & PAGE, R.H. (1972). Single beam Schlieren interferometer using a Wollaston prism. *Appl. Opt.* **11**, 858–862.
- STRICKLAND, D. & MOUROU, G. (1985). Compression of amplified chirped optical pulses. *Opt. Commun.* **56**, 219–221.
- TRESKA, O., CARROLL, D.C., YUAN, X.H., AURAND, B., BAGNOUD, V., BRENNER, C.M., COURRY, M., FILS, J., GRAY, R.J., KÜHL, T., LI, C., LI, Y.T., LIN, X.X., QUINN, M.N., EVANS, R.G., ZIELBAUER, B., ROTH, M., NEELY, D. & MCKENNA, P. (2011). Controlling the properties of ultra-intense laser proton sources using transverse refluxing of hot electrons in shaped mass-limited targets. *Plasma Phys. Contr. Fusion* **53**, 105008 .
- WILKS, S.C., LANGON, A.B., COWAN, T.E., ROTH, M., SINGH, M., HATCHETT, S., KEY, M.H., PENNINGTON, D., MACKINNON, A. & SNAVERLY, R.A. (2001). Energetic proton generation in ultra-intense laser solid interactions. *Phys. Plasmas* **8**, 542–549.

PAPER III

Manipulation of the spatial distribution of laser-accelerated proton beams by varying the laser intensity distribution

B. Aurand, L. Senje, K. Svensson, M. Hansson, A. Higginson, A. Gonoskov, M. Marklund, A. Persson, O. Lundh, D. Neely, P. McKenna, & C.-G. Wahlström.

Physics of Plasmas **23**, 023113 (2016).



Manipulation of the spatial distribution of laser-accelerated proton beams by varying the laser intensity distribution

B. Aurand,^{1,2,a)} L. Senje,¹ K. Svensson,¹ M. Hansson,¹ A. Higginson,³ A. Gonoskov,⁴ M. Marklund,⁴ A. Persson,¹ O. Lundh,¹ D. Neely,⁵ P. McKenna,³ and C.-G. Wahlström¹

¹Department of Physics, Lund University, P.O. Box 118, 22100 Lund, Sweden

²Institut für Laser- und Plasmaphysik, Heinrich-Heine Universität, 40225 Düsseldorf, Germany

³SUPA Department of Physics, University of Strathclyde, Glasgow G4 0NG, United Kingdom

⁴Department of Applied Physics, Chalmers University of Technology, 41296 Gothenburg, Sweden

⁵Central Laser Facility, STFC, Rutherford Appleton Laboratory, OX11 0QX Didcot, United Kingdom

(Received 25 October 2015; accepted 20 January 2016; published online 18 February 2016)

We report on a study of the spatial profile of proton beams produced through target normal sheath acceleration using flat target foils and changing the laser intensity distribution on the target front surface. This is done by either defocusing a single laser pulse or by using a split-pulse setup and irradiating the target with two identical laser pulses with variable spatial separation. The resulting proton beam profile and the energy spectrum are recorded as functions of the focal spot size of the single laser pulse and of the separation between the two pulses. A shaping of the resulting proton beam profile, related to both an increase in flux of low-energy protons in the target normal direction and a decrease in their divergence, in one or two dimensions, is observed. The results are explained by simple modelling of rear surface sheath field expansion, ionization, and projection of the resulting proton beam. © 2016 Author(s). All article content, except where otherwise noted, is licensed under a Creative Commons Attribution (CC BY) license (<http://creativecommons.org/licenses/by/4.0/>). [<http://dx.doi.org/10.1063/1.4942032>]

I. INTRODUCTION

More than a decade ago, first experimental results^{1,2} showed the possibility to accelerate protons to tens of MeV kinetic energy over a sub-mm length by using ultra-intense laser pulses irradiating the front side of μm -thick metal foils. The laser pulse forms a megaampere electron current inside the target penetrating through the rear surface and expanding into vacuum, leading to a charge separation on the scale of the Debye length. In the resulting electric field—which is of the order of up to a few TV/m—protons, mainly from the hydrocarbon contamination layer on the target rear surface, are quickly accelerated to high energies.^{3,4}

This process, the target-normal-sheath-acceleration (TNSA) mechanism,⁵ creates a continuous, Boltzmann-like, energy distribution up to a cut-off energy, which has attracted considerable interest, partly from a fundamental plasma physics point of view and partly because of its great potential for novel applications. It represents a very compact source of energetic ions. The pulse duration, at the source, is short, and the transverse emittance is very low.^{6–8} Potential applications in medicine, material science, accelerator physics, and industry, for example, have been widely discussed.^{3,9} However, in order to become a useful source for applications, a number of parameters must be greatly improved. For example, the shot-to-shot stability, the maximum proton energies, and the laser-to-proton energy conversion efficiencies must be increased. At the same time, the beam divergence should be reduced. In addition, for many applications, the proton energy distributions must be reduced, and ideally, a narrow

energy spread achieved. All these improvements require further experimental and theoretical studies and enhanced understanding of the fundamental processes involved.

In typical TNSA experiments, using a flat metallic target foil irradiated on the front surface by a tightly focused laser pulse, the beam of protons leaves the target's rear surface centred along the target's normal (TN) direction. The maximum proton energy, E_{PROT} , within the beam depends on the peak laser intensity I_L and, thus, for a given laser pulse duration, both on the pulse energy and the irradiated spot size on the target. Brenner *et al.*¹⁰ show that increasing I_L by increasing the pulse energy has a significantly larger influence on the total flux of protons than the same increase in intensity obtained by reducing the laser spot size. Xu *et al.*¹¹ and Green *et al.*¹² show that, with constant laser pulse energy and pulse duration, the total flux of protons can be increased by defocusing the laser at the target, even though the peak laser intensity is decreased. The proton beam divergence depends on the laser parameters and on the proton energies; the most energetic protons exhibit the smallest divergence.¹³ Schollmeier *et al.*¹⁴ used micro-structured target foils as a tool to demonstrate the effect of defocusing the laser beam on the generated proton beam. Several more studies have been reported in the literature regarding the proton beam divergence and laminarity¹⁵ and how they can be manipulated, e.g., via the use of curved targets.^{16,17} In this paper, we report on experimental studies of how the angular/spatial distribution of the proton beams can be manipulated without changing the target shape or composition, and instead by varying spatially the laser intensity distribution on the target's front surface. We keep the target and laser parameters fixed and vary the intensity distribution while monitoring the

^{a)}Electronic mail: Bastian.Aurand@uni-duesseldorf.de



spatial proton beam profile. In recent studies, it was shown that by using a fixed, hollow, doughnut-like laser beam profile, the beam divergence, and energy profile could be manipulated.¹⁸ Here, we vary the intensity distribution either by defocusing the laser on the target or by dividing the focused laser pulse into two spatially separated pulses, with a separation that can be continuously varied. In the first case, we find that the proton beam divergence can be significantly reduced by optimally defocusing the laser pulse, and in the second case that, with optimized separation between the two foci, the proton beam divergence is reduced in the direction of the separation of the foci, resulting in an elliptically shaped proton beam. These collimation effects, in one or two dimensions, are found to be mainly affecting the relatively large number of low energy protons. The number of low energy protons in the target's normal direction increases while their divergence decreases, resulting in intense beams of low-energy protons, collimated in one or two dimensions.

II. EXPERIMENTAL SETUP AND METHODS

The experiments were carried out using the Lund 10Hz multi-terawatt laser system; a chirped-pulse amplification (CPA) based Ti:sapphire laser with a pulse duration of 35 fs and a temporal contrast better than 1×10^{-9} 50 ps before the main pulse. In the experiments presented here, the energy per pulse, on target, was kept fixed at 0.6J. The experimental setup¹⁹ is shown in Fig. 1(a). After compression, the 45 mm diameter beam was guided into the interaction chamber and sent onto a split-mirror setup (Figure 1(b)) before reaching an off-

axis parabolic (OAP) focusing mirror. For the first part of the investigation, the split-mirror setup was positioned in a way that the full laser beam was reflected on one of the mirrors, and thus, only one focal spot was produced. Instead, the target foil was moved to different positions along the optical axis around the beam waist. For the second part of the investigation, the split-mirror setup was positioned such that each laser pulse was divided into two halves, resulting in two identical focused laser pulses hitting the target foil. The foil was then positioned in the focal plane of the focusing mirror while the separation between the two foci was varied between shots.

The split-mirror setup consists of two planes, protected silver mirrors of standard optical quality ($\lambda/10$ flatness). They have a vertically oriented wedged shaped edge in order to enable the mirrors to be mounted very close to each other, with a gap of only a few tenths of a millimetre, but with the possibility to move freely relative to each other. Due to a separate mounting, the mirrors can be tilted independently in vertical and horizontal directions. In addition, one of the mirrors is mounted on a linear translation stage, which moves the mirror perpendicular to its surface, enabling the relative optical path length and therefore the relative timing of the pulses to be accurately controlled. The complete split-mirror setup is further mounted on another linear translation stage moving it transversely with respect to the laser beam. This enables the split ratio of the pulses to be varied. Both beams are sent onto the same off-axis parabolic mirror, with 152 mm focal length and focused to a circular spot with radius $r_L = 2.5 \mu\text{m}$ (HWHM) reaching a peak intensity of $I_L = 2 \times 10^{19} \text{ W/cm}^2$.

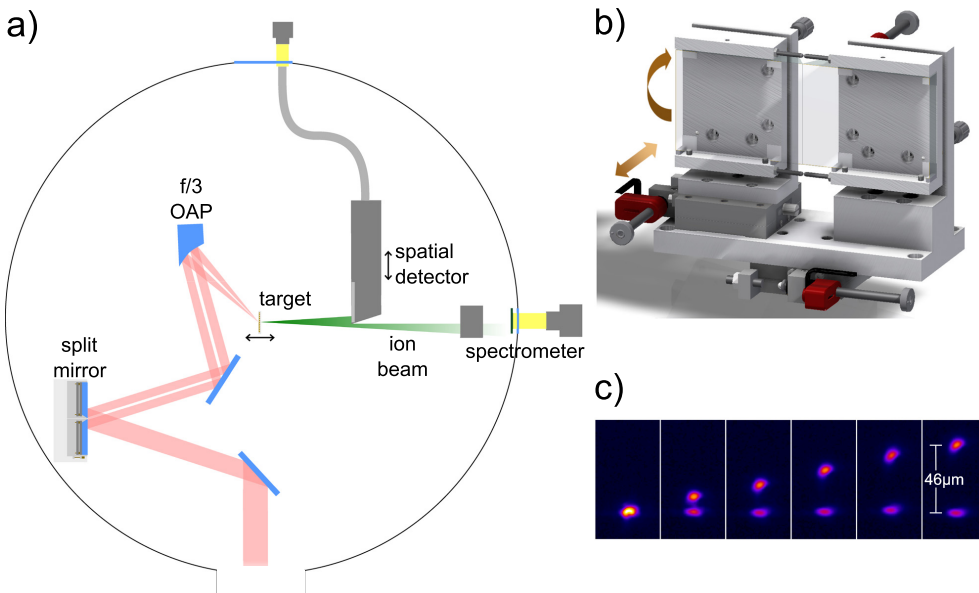


FIG. 1. (a) Experimental setup: The laser beam is guided onto the split-mirror and separated into two parts which are focused by an $f/3$ parabolic mirror onto the target. For diagnostics, either a spectrometer, consisting of a dipole magnetic field, a scintillator, and a camera, or a spatial detector to image the beam profile is used. (b) The split-mirror consists of two independently adjustable rectangular mirrors with a gap of a few tenths of a millimetre in between. (c) By tilting one of the mirrors, the spatial separation of the beams and the resulting foci can be varied.

Applying angular tilts in one direction to one of the mirrors, the two foci can be separated in that direction of the focal plane (Figure 1(c)). Note that this tilt is induced more than 1 m upstream of the interaction point and is in the order of some μ -rad. Neither a significant pulse front tilt nor a significant relative temporal difference between the beams is induced. By use of a deformable mirror in the beam line, the phase was corrected to ensure a good quality of the focus in the overlapped case. The slight horizontal elongation of the beam, which can be seen in Figure 1(c), is independent of the tilt direction. Fine adjustment of the temporal overlap can be done by adjustments of the relative path length while monitoring the interference patterns occurring in the focal plane when the foci have a spatial overlap. In the studies reported here, the splitting ratio was fixed at either 100:0 or 50:50, and the relative time delay $\Delta t = 0$.

As a target, we used $3\ \mu\text{m}$ -thick Al foils mounted in a matrix target holder realizing 340 independent targets and where each new target can be aligned within a few seconds, with an accuracy of better than $18\ \mu\text{m}$ (standard deviation) with respect to the laser focus position. The target is mounted at 45° , horizontally tilted, with respect to the laser axis.

In order to take advantage of the high repetition rate of the laser and the fast target alignment procedure, only online proton diagnostics were used. A magnetic-field based proton spectrometer disperses the protons, after passing through a 1 mm entrance pinhole, depending on their energy onto a scintillator (St. Gobain: BC-408; $500\ \mu\text{m}$ thick), wrapped in a $12\ \mu\text{m}$ thick aluminum foil to block heavy ions, which is monitored by a 16-bit camera (Princeton: PhotonMAX1024). The proton signal is collected in the target's normal direction covering a solid angle of 8×10^{-5} sr, and the energy uncertainty due to the pinhole size is $\Delta E/E \approx 10\%$. In addition, a spatial detector is used to monitor the spatial-intensity distribution of the proton beam.²⁰ A scintillator (St. Gobain: BC-408; $500\ \mu\text{m}$ thick) is positioned (65 ± 2) mm behind the target in a light shielded box with a $12\ \mu\text{m}$ thick and light tight Al entrance window. The scintillator emission is imaged onto an optical fibre bundle, which allows for the image to be transferred onto a 12-bit CCD camera placed outside the vacuum chamber. This enables a reconstruction of the two-dimensional proton beam spatial profile. With this detector

setup, the signal is not energy selective, but represents a superposition of all protons, which are stopped in the scintillator ($0.9\ \text{MeV} < E_{\text{Stop}} < 7\ \text{MeV}$). We typically investigate protons with maximum kinetic energies of $E \leq 6\ \text{MeV}$, so most protons are stopped in the scintillator. The signal from the detector is thus not representing the number of protons, but rather the deposited energy. By adding additional bars of aluminum with different thicknesses in front of the detector allowed us to distinguish between electrons and protons in the detector, which was used to calibrate the device.

III. EXPERIMENTAL RESULTS

A. Defocus scan with a single laser focus

When we use only one laser focus and move the target foil along the laser propagation axis, i.e., through the focus, we find, as expected, that the highest proton energy is obtained with the target at best focus ($r_{0,\mu\text{m}} \approx 2.5\ \mu\text{m}$), where the peak intensity is the highest. The proton beam is then centered along the TN direction, and the profile, integrating over all protons with $E > 0.9\ \text{MeV}$, is spatially round and smooth. However, the divergence dramatically decreases when the target foil is positioned at $\pm 375\ \mu\text{m}$ ($r_{375,\mu\text{m}} \approx 8.5\ \mu\text{m}$) or at $\pm 450\ \mu\text{m}$ ($r_{450,\mu\text{m}} \approx 10.5\ \mu\text{m}$) from best focus (see Figure 2(a)). This corresponds to approximately three to four Rayleigh lengths, and the peak laser intensity is reduced by roughly one order of magnitude. The laser beam profile was carefully investigated in order to ensure a homogeneous distribution of energy over the enlarged irradiated spot. The small difference in the intensity of the proton beam distribution, which can be seen in Figure 2(a) for target positions before and behind the focus, is not systematically different for the full measurement campaign, but they differ systematically within one measurement run with the same laser alignment. This might result mainly from the fact that a laser beam profile for a real laser is not only perfectly Gaussian but also to a smaller extent that a real focussing element is not perfectly parabolic. In this case, it can be shown by ray-tracing that there are small differences in local divergence and intensities on small scales within the beam profile.

The observed decrease in the proton beam divergence is not due to the decrease in the laser intensity, which is easily verified by reducing the laser energy with the target at a best

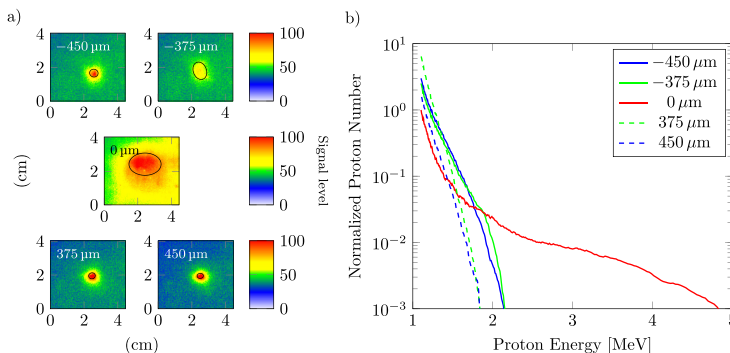


FIG. 2. (a) The proton beam profile for five representative shots measured with the spatial detector for the target foil positioned at best focus (middle) ($r_{0,\mu\text{m}} \approx 2.5\ \mu\text{m}$), $375\ \mu\text{m}$ ($r_{375,\mu\text{m}} \approx 8.5\ \mu\text{m}$), and $450\ \mu\text{m}$ ($r_{450,\mu\text{m}} \approx 10.5\ \mu\text{m}$) before and after the focus (upper/lower). In the defocused case, the proton beam is collimated compared to best focus. The corresponding proton energy distribution in the TN direction is shown in (b).

focus. Instead, it represents a significant relative increase in the number of low energy protons propagating close to the TN direction. The overall lower proton energy results from the de-focusing and therefore the reduced sheath field strength.

Figure 2(b) shows the proton energy distribution observed in the TN direction with the target both at the best focus and defocused by $375\ \mu\text{m}$. This shows the significant relative increase in the number of low energy protons and a corresponding decrease in protons with the highest energies. This resembles the finding in Ref. 11, but here, it is evident that the increase in low-energy protons in the TN direction is partly due to a reduction in divergence of these protons. Defocusing the laser pulse thus leads to reduced divergence and a significantly increased relative flux of low energy protons in the centre of the beam, even though the maximum proton energy is reduced. Using different aluminum filters in front of the spatial detector reveals as well the finding that in the defocused case, the energy of the protons in the center of the beam decreases, while their particle number increases.

B. Two foci of equal intensity and variable separation with the target foil at the best focus

Using similar measurement methods compared to the previous paragraph, we find as expected that the highest proton energy is obtained with zero separation, i.e., when the two foci overlap and give rise to the highest peak intensity on target. The spatial beam profile is then round in the TN direction, and with the highest energy protons having the smallest divergence, consistent with several previous reports.^{2,21,22} When separating the two foci in one direction,

we find that the proton beam shape changes from circular to elliptical, with the minor axis in the direction of separation. When the separation is increased further, the proton beam profile becomes round again (see Figure 3(a)). Since this effect occurs both for horizontal and vertical tilt, it is concluded that it is not due to the incidence angle between the laser and target, e.g., caused by an elongated beam profile due to the projection on the target surface. The degree of ellipticity, defined as the ratio between the major and the minor axis of an ellipse fitted to 80% level in each proton dose distribution, is shown in Figure 3(a) for different separation of the foci. When placing a filter in front of the spatial detector, stopping protons with energy below 1.7 MeV, we find that the elliptical shape disappears and we are left with a significantly weaker but circular proton beam, for all values of foci separation.

This observation is similar to the case of defocusing as discussed above, where we observed a collimation in two dimensions of low energy protons when defocusing the laser on the target foil. Here, we also find a collimation of low energy protons, but now only in one direction. This is further verified by measuring the proton energy distribution in the TN direction, as a function of separation between the two foci. Figure 3(b) shows two plots of the proton energy distribution in the TN direction with the two foci separated at $9\ \mu\text{m}$ and $30\ \mu\text{m}$ divided by the distribution obtained with the two overlapping foci. The inset shows the original signal. These plots show the significant increase in the number of low energy protons obtained with the optimum separation, accompanied by a relative decrease in protons with the highest energies. With large separation ($30\ \mu\text{m}$) between the two foci, two independent proton sources are obtained, with the

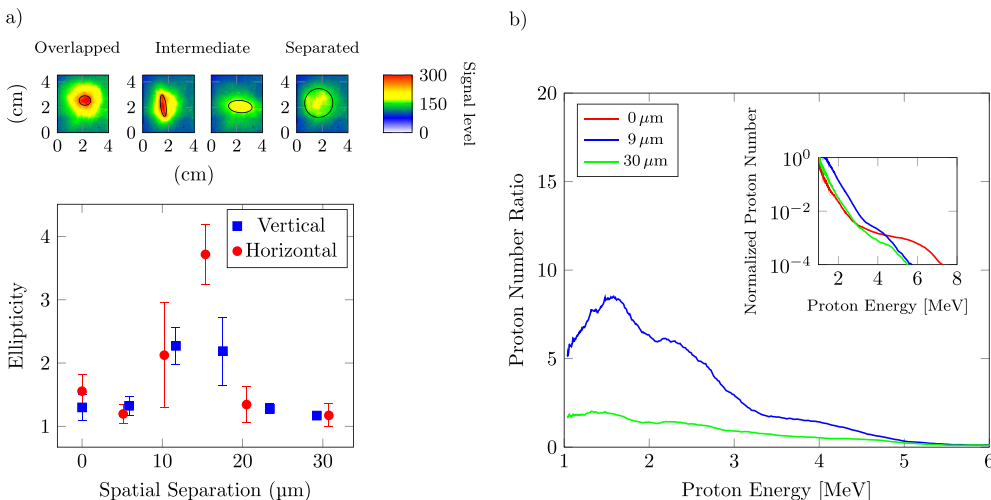


FIG. 3. (a) The upper figures show the measured proton beam profile for the case of two foci being overlapped or separated (horizontally or vertically). For an intermediate separation of ~ 3 focus diameters, the resulting beam profile becomes elliptical. Overlapping or separating the foci further results in a circular shaped profile. Calculating the ellipticity from the beam profile for different spatial separations in horizontal and vertical direction illustrates the change in the beam profile. (b) The inset shows the proton energy distribution in the forward direction for three different separations between the two focal spots. The large plot gives the energy distribution measured for the different separations divided by the corresponding distribution obtained in the case that both foci overlap (red curve $0\ \mu\text{m}$ separation). For a separation of $9\ \mu\text{m}$, the number of low energy protons is increased.

same reduction in the maximum energy as for the optimum separation, but without the enhancement in proton flux at low energies. These graphs show that the elliptical shape observed with the spatial detector actually represents a collimation effect, with an increase in proton number in TN direction, and that this collimation mainly affects the low energy protons.

IV. MODELLING

A numerical model was developed to investigate how the size of the laser focus and the separation of the laser foci in the case of two beams may be expected to influence the resulting proton beam distribution. The model (an earlier version of which is described in Ref. 23) calculates how the evolving fast electron density distribution on a grid corresponding to the target rear surface maps into the beam of protons accelerated by TNSA. Fast electrons produced at the target front side in a given laser focus are assumed to be ballistically transported through the target in a beam with a fixed divergence angle. Transport phenomena such as collisions and self-generated fields are not accounted for, but are expected to have a limited effect in relatively thin targets.²⁴ Recirculation or refluxing of fast electrons within the foil is also neglected. It was validated in simulations that refluxing for a 35 fs-duration laser pulse will occur essentially only for target thicknesses of more than $3\ \mu\text{m}$. The rear-surface fast electron sheath dynamics, field-ionization of hydrogen, and the direction of projection of the resulting protons are calculated. Unlike more computationally intensive 3D Particle-in-Cell (PIC) modelling, this simpler approach enables a range of parametric scans to be performed relatively quickly, to explore the expected changes to the proton beam profile.

The initial diameter of the fast electron distribution at the target rear side, arising from a laser focal spot of radius r_L at the front side, is given by $d_e = 2(r_L + D \tan \theta_{1/2})$, where $\theta_{1/2}$ is the divergence half-angle of the electron beam as it propagates within the target of thickness D . The sheath profile due to the single laser focus is assumed to be parabolic.²⁴ In the case of two laser foci, two fast electron distributions are generated at the target rear, with the degree of overlap depending on the separation of the laser foci and the magnitude of $\theta_{1/2}$. In the calculations below, $D = 3\ \mu\text{m}$ and $\theta_{1/2}$ is set to 30° . The target rear surface is defined as a spatial grid of 80×80 cells of $0.025\ \mu\text{m}$ size, centred at $X = Y = 0$. Electrons arrive over the duration of the laser pulse, which is set equal to 35 fs. The magnitude of the sheath field increases with the increase in the fast electron number density over the first half (rising edge) of the laser pulse and thereafter decreases with time due to lateral expansion of the electron population. The maximum field strength is calculated (assuming a sharp boundary) as $E_{max} = E_0 \sqrt{2/e_N}$, where e_N is Euler's number (2.7183), $E_0 = \sqrt{n_{e0} k_B T_e / \epsilon_0}$, ϵ_0 is the vacuum permittivity, and T_e and n_{e0} are the fast electron temperature and maximum density, respectively (as derived in Ref. 25). The fast electron temperature is determined from ponderomotive scaling.²⁶ The number of fast electrons generated, and thus the fast electron density, is calculated assuming a laser pulse energy of 0.6 J and a laser-to-fast electron energy conversion efficiency of 20%. The conversion efficiency is fixed at this value in the

intensity range explored in this study, based on measurements reported in Ref. 27. The initial transverse sheath expansion velocity is set equal to $0.7c$ (as determined from a previous experiment⁸ and simulations²⁸), and it decreases exponentially with a $1/e$ time constant of 60 fs. The rate of reduction in the transverse expansion velocity is based on time- and space-resolved interferometry measurements of a probe beam reported in Ref. 8, scaled to the shorter laser pulse used in the present work. The sheath evolution is calculated in 0.8 fs steps.

Free protons are released by field ionization of a uniform layer of hydrogen, as calculated using the Ammosov-Delion-Krainov (ADK) rate²⁹ at each time step. Changes in the proton front due to the evolving electric field are calculated, and the local gradient to this front is used to determine the projection of the resulting beam of protons. The detector plane is defined by a $3\ \text{cm} \times 3\ \text{cm}$ spatial grid with a resolution equal to $100\ \mu\text{m}$ and is set 6.5 cm from target, to match the experimental conditions. The 2D proton beam spatial-intensity distributions calculated after 200 fs are compared with the measurements.

A. Defocusing

The simulations show that as the laser pulse is defocused, the maximum kinetic energy in the proton beam is reduced, but the number of low-energy protons increases. In addition, more gradual gradients in the sheath field lead to a reduction in the beam divergence. The result is therefore, at the optimum amount of defocusing, a narrow and intense beam of low energy protons. This is illustrated in Figure 4. Further defocusing reduces the laser intensity too much, and the proton beam quickly reduces in brightness. In the simulation, the proton distribution can be analyzed separately for different proton energies. When this is done, it is found that the observed intense and narrow beam is due to protons with kinetic energy less than 70% of the maximum energy obtained at best focus. This is in agreement with the experimental finding.

B. Two spatially separated foci

For the purposes of modelling the case of the two spatially separated foci, it is assumed that the fast electron population produced by each laser spot passes through the thin foil without interaction with the other and emerges at the rear side. The electron density at the rear surface is summed in regions of overlap, which enhances the sheath field. The results of these simulations show that as the spot separation is increased, the proton beam becomes elliptical, with the minor axis in the direction parallel to the separation direction (Figure 5). The maximum degree of ellipticity is obtained when the separation is ~ 3 focal spot diameters. As the separation is further increased, the two spots each give rise to independent circular proton beams. The spatial separation of these is not noticeable in the far-field detection plane, where a single round proton distribution is therefore observed. These simulation results are in excellent agreement with the experimental finding. In the simulation, the proton distribution can be analyzed separately for different proton energies. When this is done, it is found that the observed ellipticity is

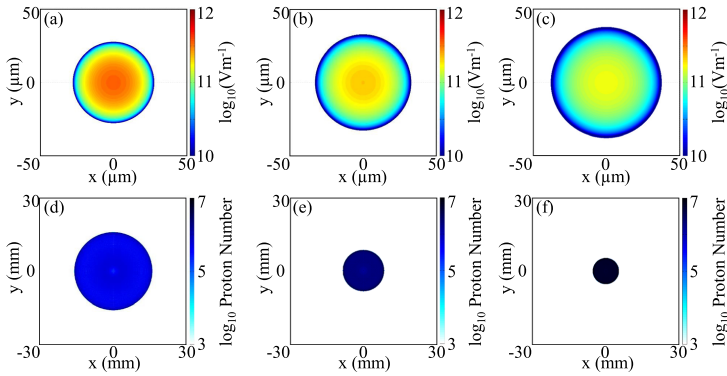


FIG. 4. Simulation results showing the electrostatic sheath field distribution after 200 fs for: (a) $r_L = 5 \mu\text{m}$, (b) $r_L = 10 \mu\text{m}$, and (c) $r_L = 15 \mu\text{m}$. The corresponding proton beam profiles, integrated over the full proton energy range, are shown in (d)–(f), respectively. In the defocused case, the sheath field is larger and weaker, resulting in a proton beam with smaller divergence.

due to protons with kinetic energy less than 70% of the maximum energy. Analyzing only the high energy range of the proton energy distribution, circular beam profiles are found independently of spot separation. This is also in agreement with the experimental findings.

V. CONCLUSION

This article addresses the influence of defocusing and focus shaping of the laser pulse on the generated proton beam profile and the proton energy distribution. Defocusing a single laser beam by a few Rayleigh lengths on the target front surface results in a spatially larger electron distribution directed towards the target rear surface, which has a lower average energy due to the lower initial laser intensity. As a result, the created sheath field on the rear surface covers a larger area, resulting in a larger proton source size, but is weaker than in the case of a focused laser beam. The secondary accelerated beam of protons is more collimated, due to the larger electron

distribution at the target rear side leading to a lesser electrostatic sheath field gradient, and therefore more directed electric field distribution. At the same time, the proton flux is increased due to the larger source size of protons being accelerated. This however results in a reduction of the electric field strength, leading to an overall lower proton energy.

By using two laser beams, to create two foci separated by a few laser spot diameters, we could transfer this effect of beam-shaping to a tool in order to generate a customized proton beam of high flux in one direction. In that case, the superposition of the shape of the two foci as well as the resulting electron distribution driven through the target forms an expanded sheath field in one direction at the target rear surface. The beam of accelerated protons is produced with a lower divergence in only one direction. We demonstrated that for our experimental parameters, this effect occurs for a focal spot separation between the two foci of approximately three focal spot diameters. A larger beam separation results in two independent proton sources,³⁰ each

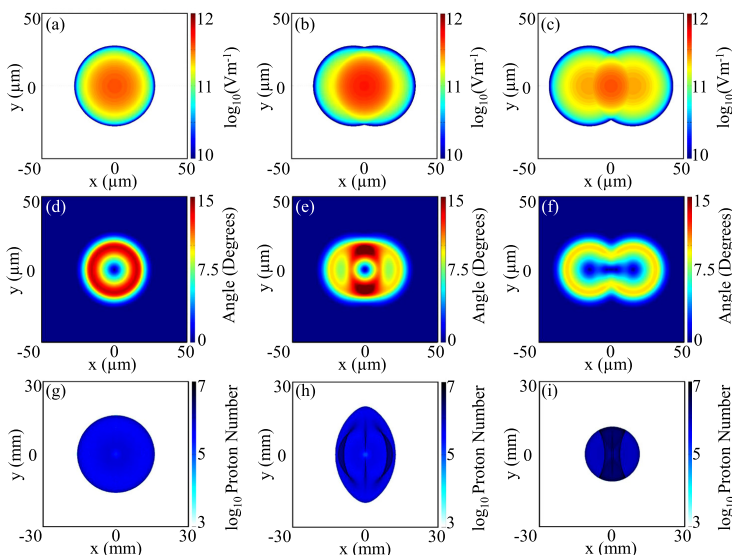


FIG. 5. Simulation results showing the electrostatic sheath field distribution after 200 fs for focal spot separation equal to: (a) $0 \mu\text{m}$, (b) $15 \mu\text{m}$, and (c) $30 \mu\text{m}$. The corresponding angular proton distributions at the target surface are shown in (d)–(f), respectively, and the resulting proton beam distributions in the detector plane are shown in (g)–(i), respectively. At an optimum foci separation, corresponding to case (b), the divergence in the x-direction is significantly reduced.

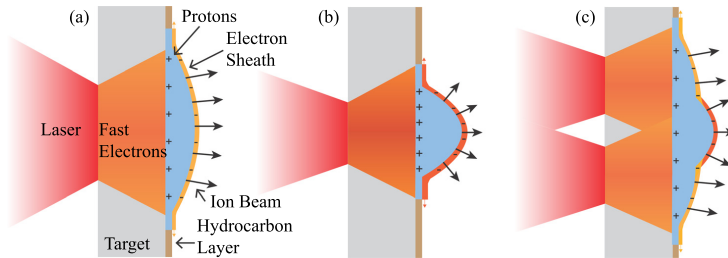


FIG. 6. Schematic illustration of the sheath fields formed by (a) a single defocused laser pulse; (b) two overlapped laser foci; and (c) two laser foci at a separation close to optimum to modify the sheath profile.

with high divergence but relative low energy. A smaller separation results in one proton source with high divergence and high energy, due to the addition of both laser beams. Figure 6 illustrates schematically the sheath expansion in three of the cases investigated experimentally. These results obtained by laser beam splitting presents an indirect measurement of the sheath field size, which was estimated to be in the order of $20\ \mu\text{m}$. This is in agreement with the results obtained in Ref. 31 using a laser system with a similar pulse duration as in our study, i.e., a few tens of femtoseconds. For longer laser pulse durations, where the electrons can be accelerated and recirculated within the target during the pulse duration, the sheath field becomes larger, as, e.g., obtained in Refs. 32 and 33.

In summary, the proton beam can be shaped by this effect, increasing the proton flux for the low energy proton part. The cost of this effect is a reduction in the maximum proton energy. For distinct applications which do not need high proton energies but a high proton flux with a shaped beam profile (e.g., proton beam writing³⁴ or radioisotope production³⁵), this method might be sufficient to at least preform the beam profile before using collimators to create the desired shape. This enhances the process efficiency and reduces the number of protons which need to be dumped away creating unnecessary activation or radiation at the collimator. Using this technique on high energy lasers could be a scheme to accelerate protons as a fast ignition driver. Here, as well primarily a high proton flux is needed.

In the case studied above, both laser beams interact with the target at the same time. In further studies, one can introduce a temporal delay between the two pulses, which may result not only in a collimation but also in a change of direction of the proton beam due to a possible tilt of the sheath field front at the target rear surface. This may allow for a new method of combined beam collimation and shaping. Exploring the influence of varying the relative intensities of the two pulses is additional options for further studies.

ACKNOWLEDGMENTS

We gratefully thank the Knut and Alice Wallenberg Foundation, including their funding of the PLIONA project, the Swedish Research Council, and the Swedish Foundation for Strategic Research for financial support. We also acknowledge support from EPSRC (Grant No. EP/J003832/1) and Laserlab-Europe/CHARPAC (Grant Agreement No. 284464).

¹E. L. Clark, K. Krushelnick, J. R. Davies, M. Zepf, M. Tatarakis, F. N. Beg, A. Machacek, P. A. Norreys, M. I. K. Santala, I. Watts, and A. E. Dangor, *Phys. Rev. Lett.* **84**, 670 (2000).

²R. A. Snavely, M. H. Key, S. P. Hatchett, T. E. Cowan, M. Roth, T. W. Phillips, M. A. Stoyer, E. A. Henry, T. C. Sangster, M. S. Singh, S. C. Wilks, A. MacKinnon, A. Offenberger, D. M. Pennington, K. Yasuike, A. B. Langdon, B. F. Lasinski, J. Johnson, M. D. Perry, and E. M. Campbell, *Phys. Rev. Lett.* **85**, 2945 (2000).

³H. Daido, M. Nishiuchi, and A. S. Prizhkov, *Rep. Prog. Phys.* **75**, 056401 (2012).

⁴M. Passoni, L. Bertagna, and A. Zani, *New J. Phys.* **12**, 045012 (2010).

⁵S. C. Wilks, A. B. Langdon, T. E. Cowan, M. Roth, M. Singh, S. Hatchett, M. H. Key, D. Pennington, A. MacKinnon, and R. A. Snavely, *Phys. Plasmas* **8**, 542 (2001).

⁶J. Fuchs, P. Antici, E. d'Humilres, E. Lefebvre, M. Borghesi, E. Brambrink, C. A. Cecchetti, M. Kaluza, V. Malka, M. Manclossi, S. Meyroneinc, P. Mora, J. Schreiber, T. Toncian, H. Pepin, and P. Audebert, *Nat. Phys.* **2**, 48 (2006).

⁷J. Fuchs, C. A. Cecchetti, M. Borghesi, T. Grismayer, E. d'Humilres, P. Antici, S. Atzeni, P. Mora, A. Pipahl, L. Romagnani, A. Schiavi, Y. Sentoku, T. Toncian, P. Audebert, and O. Willi, *Phys. Rev. Lett.* **99**, 015002 (2007).

⁸S. Buffechoux, J. Psikal, M. Nakatsutsumi, L. Romagnani, A. Andreev, K. Zeil, M. Amin, P. Antici, T. Burris-Mog, A. Compant-La-Fontaine, E. d'Humieres, S. Fourmaux, S. Gaillard, F. Gobet, F. Hannachi, S. Kraft, A. Mancic, C. Plaisir, G. Sarri, M. Tarisien, T. Toncian, U. Schramm, M. Tampo, P. Audebert, O. Willi, T. E. Cowan, H. Pépin, V. Tikhonchuk, M. Borghesi, and J. Fuchs, *Phys. Rev. Lett.* **105**, 015005 (2010).

⁹K. W. D. Ledingham, P. R. Bolton, N. Shikazono, and C. M. C. Ma, *Appl. Sci.* **4**, 402 (2014).

¹⁰C. M. Brenner, J. S. Green, A. P. L. Robinson, D. C. Carroll, B. Dromey, P. S. Foster, S. Kar, Y. T. Li, K. Markey, C. Spindloe, M. J. V. Streeter, M. Tolley, C.-G. Wahlström, M. H. Xu, M. Zepf, P. McKenna, and D. Neely, *Laser Part. Beams* **29**, 345 (2011).

¹¹M. H. Xu, Y. T. Li, D. C. Carroll, P. S. Foster, S. Hawkes, S. Kar, F. Liu, K. Markey, P. McKenna, M. J. V. Streeter, C. Spindloe, Z. M. Sheng, C.-G. Wahlström, M. Zepf, J. Zheng, J. Zhang, and D. Neely, *Appl. Phys. Lett.* **100**, 084101 (2012).

¹²J. S. Green, D. C. Carroll, C. Brenner, B. Dromey, P. S. Foster, S. Kar, Y. T. Li, K. Markey, P. McKenna, D. Neely, A. P. L. Robinson, M. J. V. Streeter, M. Tolley, C.-G. Wahlström, M. H. Xu, and M. Zepf, *New J. Phys.* **12**, 085012 (2010).

¹³J. Fuchs, T. E. Cowan, P. Audebert, H. Ruhl, L. Gremillet, A. Kemp, M. Allen, A. Blazevic, J.-C. Gauthier, M. Geissel, M. Hegelich, S. Karsch, P. Parks, M. Roth, Y. Sentoku, R. Stephens, and E. M. Campbell, *Phys. Rev. Lett.* **91**, 255002 (2003).

¹⁴M. Schollmeier, K. Harres, F. Nürnberg, A. Blazevic, P. Audebert, E. Brambrink, J. C. Fernández, K. A. Flippo, D. C. Gautier, M. Geibel, B. M. Hegelich, J. Schreiber, and M. Roth, *Phys. Plasmas* **15**, 053101 (2008).

¹⁵T. E. Cowan, J. Fuchs, H. Ruhl, A. Kemp, P. Audebert, M. Roth, R. Stephens, I. Barton, A. Blazevic, E. Brambrink, J. Cobble, J. Fernández, J.-C. Gauthier, M. Geissel, B. M. Hegelich, J. Kaae, S. Karsch, G. P. Le Sage, S. Letzring, M. Manclossi, S. Meyroneinc, A. Newkirk, H. Pépin, and N. Renard-LeGalloudec, *Phys. Rev. Lett.* **92**, 204801 (2004).

¹⁶P. K. Patel, A. J. Mackinnon, M. H. Key, T. E. Cowan, M. E. Foord, M. Allen, D. F. Price, H. Ruhl, P. T. Springer, and R. Stephens, *Phys. Rev. Lett.* **91**, 125004 (2003).

¹⁷M. Roth, A. Blazevic, M. Geissel, T. Schlegel, T. E. Cowan, M. Allen, J.-C. Gauthier, P. Audebert, J. Fuchs, J. Meyer-ter-Vehn, B. M. Hegelich,

- S. Karsch, and A. Pukhov, *Phys. Rev. Spec. Top. - Accel. Beams* **5**, 061301 (2002).
- ¹⁸C. Brabetz, S. Busold, T. Cowan, O. Deppert, D. Jahn, O. Kester, M. Roth, D. Schumacher, and V. Bagnoud, *Phys. Plasmas* **22**, 013105 (2015).
- ¹⁹B. Aurand, M. Hansson, L. Senje, K. Svensson, A. Persson, D. Neely, O. Lundh, and C.-G. Wahlström, *Laser Part. Beams* **33**, 59 (2015).
- ²⁰J. S. Green, M. Borghesi, C. M. Brenner, D. C. Carroll, N. P. Dover, P. S. Foster, P. Gallegos, S. Green, D. Kirby, K. J. Kirkby, P. McKenna, M. J. Merchant, Z. Najmudin, C. A. J. Palmer, D. Parker, R. Prasad, K. E. Quinn, P. P. Rajeev, M. P. Read, L. Romagnani, J. Schreiber, M. J. V. Streeter, O. Tresca, C.-G. Wahlström, M. Zepf, and D. Neely, *Proc. SPIE* **8079**, 807991 (2011).
- ²¹F. Nürnberg, M. Schollmeier, E. Brambrink, A. Blazevic, D. C. Carroll, K. Flippo, D. C. Gautier, M. Geißel, K. Harres, B. M. Hegelich, O. Lundh, K. Markey, P. McKenna, D. Neely, J. Schreiber, and M. Roth, *Rev. Sci. Instrum.* **80**, 033301 (2009).
- ²²J. Schreiber, S. Ter-Avetisyan, E. Risse, M. P. Kalachnikov, P. V. Nickles, W. Sandner, U. Schramm, D. Habs, J. Witte, and M. Schnürer, *Phys. Plasmas* **13**, 033111 (2006).
- ²³M. N. Quinn, D. C. Carroll, X. H. Yuan, M. Borghesi, R. J. Clarke, R. G. Evans, J. Fuchs, P. Gallegos, L. Lancia, and K. Quinn, *Plasma Phys. Controlled Fusion* **53**, 124012 (2011).
- ²⁴X. H. Yuan, A. P. L. Robinson, M. N. Quinn, D. C. Carroll, M. Borghesi, R. J. Clarke, R. G. Evans, J. Fuchs, P. Gallegos, L. Lancia, D. Neely, K. Quinn, L. Romagnani, G. Sarri, P. A. Wilson, and P. McKenna, *New J. Phys.* **12**, 063018 (2010).
- ²⁵T. Grismayer and P. Mora, *Phys. Plasmas* **13**, 032103 (2006).
- ²⁶S. C. Wilks, W. L. Krueer, M. Tabak, and A. B. Langdon, *Phys. Rev. Lett.* **69**, 1383 (1992).
- ²⁷P. M. Nilson, W. Theobald, J. Myatt, C. Stoeckl, M. Storm, O. V. Gotchev, J. D. Zuegel, R. Betti, D. D. Meyerhofer, and T. C. Sangster, *Phys. Plasmas* **15**, 056308 (2008).
- ²⁸P. McKenna, D. C. Carroll, R. J. Clarke, R. G. Evans, K. W. D. Ledingham, F. Lindau, O. Lundh, T. McCanny, D. Neely, A. P. L. Robinson, L. Robson, P. T. Simpson, C.-G. Wahlström, and M. Zepf, *Phys. Rev. Lett.* **98**, 145001 (2007).
- ²⁹M. V. Ammosov, N. B. Delone, and V. P. Krainov, *Sov. Phys. - JETP* **64**, 1191 (1986).
- ³⁰O. Lundh, Y. Glinec, C. Homann, F. Lindau, A. Persson, C.-G. Wahlström, D. C. Carroll, and P. McKenna, *Appl. Phys. Lett.* **92**, 011504 (2008).
- ³¹O. Jäckel, J. Polz, S. M. Pfotenhauer, H.-P. Schlenvoigt, H. Schwöerer, and M. C. Kaluza, *New J. Phys.* **12**, 103027 (2010).
- ³²J. Schreiber, M. Kaluza, F. Grüner, U. Schramm, B. M. Hegelich, J. Cobble, M. Geissler, E. Brambrink, J. Fuchs, P. Audebert, D. Habs, and K. Witte, *Appl. Phys. B* **79**, 1041 (2004).
- ³³M. Borghesi, A. J. Mackinnon, D. H. Campbell, D. G. Hicks, S. Kar, P. K. Patel, D. Price, L. Romagnani, A. Schiavi, and O. Willi, *Phys. Rev. Lett.* **92**, 055003 (2004).
- ³⁴F. Watt, M. B. H. Breese, A. A. Bettioli, and J. A. van Kan, *Mater. Today* **10**(6), 20 (2007).
- ³⁵R. Clarke, S. Dorkings, D. Neely, and I. Musgrave, *Proc. SPIE* **8779**, 87791C (2013).

PAPER IV

Transverse expansion of the electron sheath during laser acceleration of protons

K. Svensson, F. Mackenroth, L. Senje, A. Gonoskov, C. Harvey, B. Aurand, M. Hansson, A. Higginson, M. Dalui, O. Lundh, P. McKenna, A. Persson, M. Marklund, & C.-G. Wahlström.

Manuscript.

Transverse Expansion of the Electron Sheath during Laser Acceleration of Protons

K. Svensson,¹ F. Mackenroth,^{2,3} L. Senje,¹ A. Gonoskov,³ C. Harvey,³ B. Aurand,^{1, a)} M. Hansson,¹ A. Higginson,⁴ M. Dalui,¹ O. Lundh,¹ P. McKenna,⁴ A. Persson,¹ M. Marklund,³ and C.-G. Wahlström^{1, b)}

¹⁾*Department of Physics, Lund University, 221 00 Lund, Sweden*

²⁾*Max Planck Institute for the Physics of Complex Systems, Nöthnitzer Str. 38, 01187 Dresden, Germany*

³⁾*Chalmers University of Technology, 412 58 Gothenburg, Sweden*

⁴⁾*SUPA Department of Physics, University of Strathclyde, Glasgow, G4 0NG, United Kingdom*

(Dated: 23 February 2017)

Transverse expansion of the electrostatic sheath during target normal sheath acceleration (TNSA) of protons is investigated experimentally using a setup with two synchronized laser pulses. The laser pulses are focused onto 3 μm thick aluminum foils at oblique angle of incidence in the horizontal plane. With the pulses spatially separated by less than three laser spot diameters, the resulting proton beam profiles become elliptical. By introducing a small intensity difference between the two pulses the ellipses are rotated, by a certain angle, but only if the spatial separation of the two pulses is in the vertical direction. The rotation angle is shown to depend on the relative intensity of the two pulses. The observed effects are found to be dependent on high temporal contrasts of the laser pulses. A simple model describing how the size of the electron sheath on the rear of the target depends on the relative intensity between the foci is presented. The model assumes that the transverse expansion of the sheath, produced by each focus, has a preferred direction, which is in the forward direction of the laser pulse projected onto the target, in the case of $J \times B$ heating. The model assumptions are verified and the unknown dependence of the transverse extents of the sheaths are estimated self-consistently through a series of high resolution, two-dimensional particle-in-cell simulations.

The study of compact sources of laser-driven energetic proton beams is an active area of research, with many potential applications, such as medical treatment of cancer¹, production of short-lived isotopes², and ion implantation³. One acceleration process, called target normal sheath acceleration (TNSA), has been explored in a number of experimental and numerical studies^{4,5}. The process incorporates a short laser pulse, typically shorter than 1 ps, which carries an energy on the order of 1 J. The laser is focused onto the front surface of a thin foil, which instantly ionizes and becomes a plasma. The resulting plasma electron density, n_e , has a gradient along the target normal direction, and eventually becomes higher than the critical density, $n_c = \epsilon_0 m_e \omega^2 / e^2$, for the laser radiation, where ϵ_0 is the permittivity of free space, m_e is the electron mass, ω is the laser angular frequency, and e is the elementary charge. This has the effect that the laser pulse cannot propagate through the full length of the plasma and is partly reflected. However, some of its energy is absorbed and heats electrons, which can traverse the target. There are different heating mechanisms contributing to the hot electron population, such as resonant absorption⁶, vacuum heating⁷, and $J \times B$ heating⁸. For high intensities and short plasma scale lengths, $J \times B$ heating is expected to dominate, which accelerates hot electrons along the laser propaga-

tion axis. As the electrons exit the rear of the target, they set up strong electrostatic sheath fields in which positively charged particles, present on the rear of the target, can be accelerated in the target normal direction.

In a recent study⁹, we showed that, by varying the laser intensity distribution on the front of the target, the divergence of the resulting proton beam can be controlled. Irradiating the target simultaneously with two identical, focused laser pulses, spatially separated by less than three spot diameters, the resulting proton beam obtained an elliptical transverse profile, with its major axis perpendicular to the foci separation axis. However, separating the foci by more than three spot diameters resulted in two independent proton sources on the rear of the target, and the detected proton beam profiles became circular, just as if only one focus was used. In this paper, we extend that study and present new experimental results obtained by altering the intensity ratio between the two separated laser foci. We find that under certain conditions the orientation of the ellipse rotates, which allows us to determine how the transverse expansion of the electron sheath field depends on laser pulse intensity.

The experimental investigation was performed using the multi-terawatt laser system at the Lund Laser Centre, which for this study delivered p-polarized laser pulses with full-width at half-max (FWHM) durations of 40 fs, and temporal contrasts higher than 10^9 on the 100 ps time scale. The total energy on target for each laser pulse was 0.7 J. The experimental setup¹⁰ is illustrated in Fig. 1, in which a split mirror divides the incoming laser pulse in two separate pulses, and both are focused

^{a)}Present address: Institut für Laser- und Plasmaphysik, Heinrich-Heine Universität, 40225 Düsseldorf, Germany

^{b)}Electronic mail: claes-goran.wahlstrom@fysik.lth.se

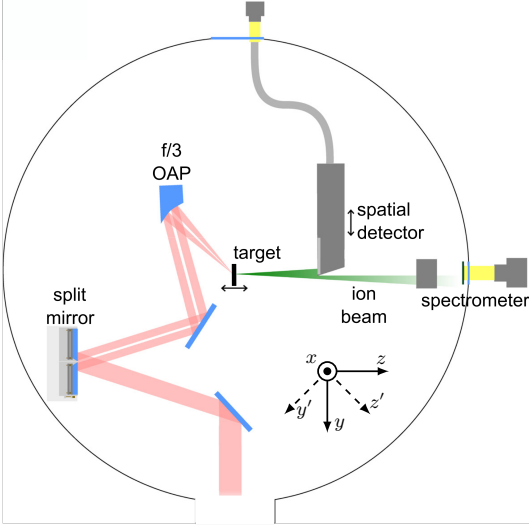


FIG. 1. The p-polarized laser pulse was guided onto the split mirror, where it was divided in two parts. Both of them were then sent towards an f/3 off-axis parabolic mirror, which focused the laser pulses onto the front of a 3 μm thick aluminum target foil. The accelerated protons were detected by a spatial detector, situated 6.5 cm from the rear of the target. The illustration is taken from a publication⁹ describing the experimental setup in greater detail.

by the same f/3 off-axis parabolic mirror (OAP) onto the front of a 3 μm aluminum foil at 45° incidence angle, resulting in two spots, each with a size (intensity FWHM) of 5 μm . By introducing a small tilt in one part of the split mirror, it is possible to separate the two foci horizontally and vertically. Their relative intensity can also be varied by moving the split mirror along its surface. During the experimental study, the accelerated protons were detected by a spatial detector situated 6.5 cm from the rear of the target. The spatial detector consists of a scintillating screen (Saint-Gobain, BC-408), which is imaged onto one end of an optical fiber bundle. The other end is imaged by a 12 bit camera, positioned outside the experimental vacuum chamber. The scintillator is covered by a 13 μm aluminum foil in order to protect it from residual laser light and target debris. This foil also stopped protons with energies lower than ~ 1 MeV. The spatial detector can also be moved, such that the central

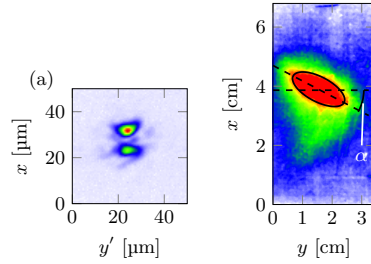


FIG. 2. Laser foci vertically separated 8.5 μm with (a) higher intensity on top ($\rho = 1.6$), and the corresponding transverse proton beam profile depicted in (b). The proton beam profile rotation angle in (b) is approximately -25° . The ellipse is fitted to the 65% signal level. All color scales are normalized to the maximum signal in each image, and the proton beam profile is detected 6.5 cm from the target foil.

part of the proton beam propagates through a permanent magnet with an effective length of 5 cm and field 0.8 T field strength. The protons are dispersed according to their energies in this field, and finally detected by a setup consisting of a scintillator (Saint-Gobain, BC-408) and a 16-bit EMCCD camera. The scintillator is covered by a 6 μm aluminum foil, which stops protons with energies lower than 0.5 MeV.

When the two vertically separated laser pulses had equal intensity, the resulting spatial profile of the proton beam was elliptical with its major axis oriented horizontally. This is in perfect agreement with the findings by Aurand et al⁹. Introducing a small intensity difference between two pulses, as shown in Fig. 2a, the elliptical proton beam profile, shown in Fig. 2b, became tilted by an angle α . If the rotation angle of the elliptical beam profile depends on differences in laser spot characteristics between the two foci, inverting their positions should mirror the proton beam profile about the horizontal axis. This was experimentally verified, and the orientation of the elliptical proton beam profile was indeed mirrored when the two foci were interchanged. For horizontal separation of the laser foci, the elliptical proton beam profile was oriented vertically. However, introducing an intensity difference for this configuration did not result in any significant rotation of the ellipse from its vertical orientation.

To determine how α is affected by the relative foci alignment, we positioned the separated laser foci, with equal intensities, at an angle φ relative to the vertical axis. By keeping the separation distance fixed and varying φ from 0° to 90°, we found that the resulting α followed φ as a one-to-one relation. Thus, the observed effect, shown in Fig. 2, is significantly larger than can be accounted for by any misalignments, estimated to less than $\pm 5^\circ$, of the laser foci separation seen in Fig. 2a. However, for horizontal separation of the foci, any tilt was well within the alignment precision regardless of the intensity ratio.

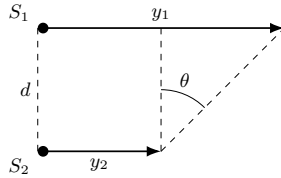


FIG. 3. A model where the two laser spots, S_1 and S_2 , are separated vertically by a distance d . Each laser spot creates a sheath which extends in the forward direction by y_1 and y_2 , respectively. The figure illustrates the situation after a given expansion time, when the intensity of the laser pulse in S_1 was higher than in S_2 .

The observations can be explained if the electrostatic sheath field, responsible for proton acceleration, is tilted. Since the angle of incidence of the laser is 45° in the horizontal plane, the sheath expansion is expected to have a preferred direction along the y -axis. This preference can be seen as a combination of the finite size of the laser spot, and that the laser pulse strikes the target at an angle. Also, if $J \times B$ heating dominates, the sheath would preferentially expand in that direction, since the electrons are driven in the laser propagation (z') direction, see Fig. 1. Thus, separating the foci vertically (along the x -axis), and introducing a difference in expansion through an intensity difference, the leading edge of the resulting electron sheath is expected to become tilted. Separating the foci horizontally (along the y' -axis), on the other hand, does not result in any tilt of the front of the electrostatic sheath field.

To describe the effect quantitatively, we construct a simple model describing the transverse sheath expansion. We start from the basic assumption that for each laser focus, the spatial size of the resulting sheath field depends on the laser energies E_1 and E_2 contained in the focus S_1 and S_2 , respectively. We neglect any changes in laser spot sizes and assume the pulse duration to remain unaffected by the splitting of the laser pulse. Then, separating the foci by a distance d , their different front edge positions y_1 and y_2 , respectively, lead to an effective tilting of the leading edge of the sheath by an angle θ , as indicated in Fig. 3. Since the major axis of the elliptical proton beam profile for equal intensity in the two foci, was found to be perpendicular to the orientation of the elongated sheath field⁹, we assume here that $\alpha = -\theta$. From geometrical considerations we read off Fig. 3:

$$\tan(\theta) = \frac{y_1 - y_2}{d}. \quad (1)$$

Assuming the edge position scaling with laser pulse intensity to be equivalent and independent in the two laser spots, from now on it is sufficient to consider only one spot, in order to derive analytically the dependency of θ on the ratio, $\rho = I_1/I_2$, between the intensity in respective foci, and the total laser energy $E_{\text{tot}} = E_1 + E_2$.

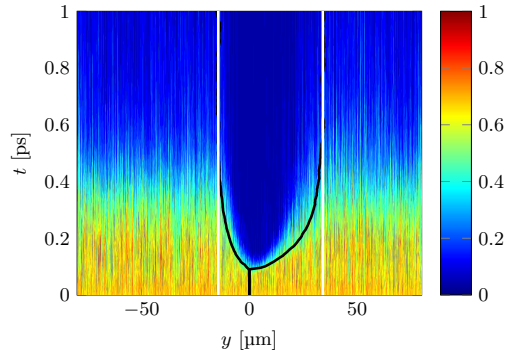


FIG. 4. Example of PIC simulation results for a single laser pulse with energy 1.1 J, showing the proton density as a function of both y , and time, t . The electron edge position is extracted from the region void of protons, and the fitted edge position for each time step is shown as black lines, with the saturated size shown as white lines.

We model the edge position of the sheath arising in a single laser spot to depend linearly on the pulse energy it contains. Below, we confirm this assumption to be well reproduced by numerical simulations in the parameter range under study. Then, the energy-dependent edge position on the rear side of the target is parametrized as

$$y(E) = kE + C, \quad (2)$$

where k and C are constants. Inserting Eq. 2 into Eq. 1, we find θ to be given by

$$\tan(\theta) = \frac{k}{d} E_{\text{tot}} \frac{\rho - 1}{\rho + 1}. \quad (3)$$

The only unknown parameter in Eq. 3 is the proportionality constant k . To determine it self-consistently, we invoke numerical simulations. Since we are only interested in the sheath dynamics in the plane of incidence of the laser pulse (yz -plane), a two-dimensional cut through the laser spot is expected to provide a good model of the expanding sheath. We perform a series of two-dimensional particle-in-cell (PIC) simulations, using the code PICADOR¹¹ (see Fig. 4). We model a linearly polarized laser pulse with central wavelength $\lambda = 810$ nm and a Gaussian envelope in time with 66 fs FWHM pulse duration and focal spot diameter $5 \mu\text{m}$ incident under a 45° angle onto a $3 \mu\text{m}$ thick, preionized target. On the front of the target, we model a preplasma of scale length $L = 0.1 \mu\text{m}$, composed of electrons (mass m_e , charge $-e$) and protons (mass m_p , charge e). The target bulk is composed of electrons and highly ionized heavy ions (mass to charge ratio $4.5m_p/e$). We checked that higher ionisation states in the target bulk as are expected to occur in the experiment, i.e., lower mass to charge ratios in the simulations, do not significantly alter the simulation results. We use a simulation box with 4096×1024 cells and a

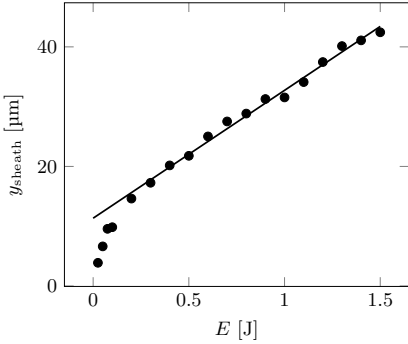


FIG. 5. Fitted edge positions in the forward direction for the performed PIC simulations. The solid line is a linear fit for $E > 0.1$ J, with slope $k = 21 \mu\text{m J}^{-1}$.

size of $160 \mu\text{m} \times 60 \mu\text{m}$ to resolve the small scale plasma heating dynamics as well as the large spatial extent of the sheath expansion. We initialize the simulation such that at its start, the center of the laser pulse is placed $15 \mu\text{m}$ from the front of the target, to suppress artificial penetration of the main laser pulse into the target.

All parameters are kept unchanged in all simulations, except for the total energy content of laser pulse. Then, for each separate simulation the proton density on the rear side of the target is recorded as a function of time, with an example displayed in Fig. 4. Clearly visible is a structure with significantly reduced proton density growing over time. We interpret this lack of protons being due to the expanding electron cloud accelerating them away from the rear side of the target. The sheath field is subsequently shielded by the accelerated protons whence no protons are pulled back into the sheath region over the times studied here, and a proton void signifies the spatial extent of the sheath on the rear side of the target. We then use an automated fitting routine to fit a smeared out step profile of the form $\sigma_p(y) = \sigma_{p,0} (1 - \exp[-\sigma_\delta y^4])$ to the proton distribution in positive as well as negative y -direction, where σ_p is the proton density on the rear side of the target and $\sigma_{p,0}$, σ_δ are fitting parameters. For each time step in the simulation, we identify the edge position as the position y_{sheath} where the fitted step profile has reached $\sigma_p(y_{\text{sheath}}) = 0.9\sigma_{p,0}$ (black lines in Fig. 4). Apparently, the edge position saturates to a constant value long after the laser pulse has passed. This is interpreted as the equilibrium edge position in positive as well as negative y -direction (white lines in Fig. 4).

The resulting energy dependent sheath edge positions in the positive y direction are well reproduced by a linear fit, shown in Fig. 5, for laser energies $E > 0.1$ J, whence we limit the use of the presented linear model to laser energies larger than this threshold. In this regime, however, we find Eq. 2 to provide a good reproduction of the energy dependent edge positions. The unknown proportionality constant in Eq. 3 is then determined to be

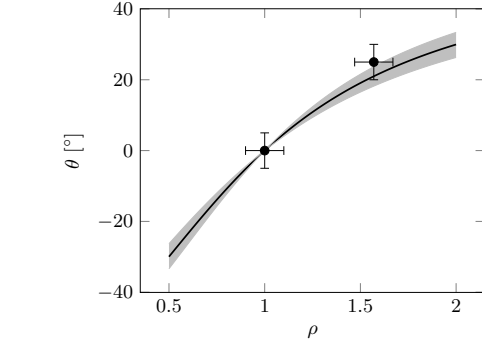


FIG. 6. Rotation angle of the front edge of the electron sheath, θ , as predicted by Eq. 3 as function of foci energy ratio, ρ , is shown for $E_{\text{tot}} = 0.7$ J. The gray area surrounding the line shows how the corresponding θ changes when E_{tot} is changed by ± 0.1 J. The rotation angles measured experimentally are shown as circles, assuming the relation $\theta = -\alpha$, with error bars indicating estimated uncertainties. The uncertainty of θ is estimated to $\pm 5^\circ$, and arises from the fact that θ depends on the signal level for the fitting routine. In ρ , the uncertainty is given by using different methods for calculating the energy ratio.

$k = 21 \mu\text{m J}^{-1}$.

Next, we compare the predictions of our model to our experimental measurement seen in Fig. 2b for $E_{\text{tot}} = 0.7$ J, and $\rho = 1.6$. In Fig. 6, θ is plotted as a function of ρ for $E_{\text{tot}} = 0.7$ J using $d = 8.5 \mu\text{m}$. The experimentally measured rotation angles are shown as black dots, and are in excellent agreement with our model.

It is also worth noting that θ is very sensitive to changes in the energy ratio close to $\rho = 1$ for larger E_{tot} , i.e. for high laser energy. This effect agrees with the experimental observation that the rotation angle was very sensitive to even small differences in energy between the two laser spots. The effect of the elliptical beam profiles and their rotation was also found to be very sensitive to the temporal contrast of the laser pulses. This is expected to be related to the plasma expansion on the front of the target. If the expanded plasma has a long scale length, the foci separation is effectively washed out. The model describing the rotation of the elliptical proton beam profiles also assumes a preferred sheath expansion direction. If $J \times B$ heating is the dominating mechanisms, this effect is expected to vanish if there is considerable plasma expansion on the front of the target prior to the arrival of the main part of the laser pulse. The presented model is a rather primitive one. As explicitly mentioned, we neglect all dependency of the laser spots on the varying laser energy. Furthermore, assuming that the tilt of the total sheath field to be only due to varying steady state edge positions in forward direction disregards more com-

PAPER V

Experimental investigation of picosecond dynamics following interactions between laser accelerated protons and water

L. Senje, M. Coughlan, D. Jung, M. Taylor, G. Nersisyan, D. Riley, C. L. S. Lewis, O. Lundh, C.-G. Wahlström, M. Zepf, & B. Dromey.

Accepted for publication in Applied Physics Letters, (2017).

Experimental investigation of picosecond dynamics following interactions between laser accelerated protons and water

L. Senje,¹ M. Coughlan,² D. Jung,² M. Taylor,² G. Nersisyan,² D. Riley,² C.L.S. Lewis,² O. Lundh,¹ C.-G. Wahlström,¹ M. Zepf,^{2,3} and B. Dromey^{2, a)}

¹⁾*Department of Physics, Lund University, P. O. Box 118, S-221 00 Lund, Sweden*

²⁾*School of Mathematics and Physics, Queens University Belfast, Belfast BT7 1NN, UK*

³⁾*Helmholtz-Institut Jena, D-07743 Jena, Germany*

(Dated: 1 March 2017)

We report direct experimental measurements with picosecond time resolution of how high energy protons interact with water at extreme dose levels (kGy), delivered in a single pulse with a duration of less than 80 ps. The unique synchronisation possibilities of laser accelerated protons with an optical probe pulse were utilized to investigate energy deposition of fast protons in water on a time scale down to only a few picoseconds. This was measured using absorbance changes in the water, induced by a population of solvated electrons created in the tracks of the high energy protons. Our results indicate that for sufficiently high doses delivered in short pulses, intertrack effects will affect the yield of solvated electrons. The experimental scheme allows for investigation of the ultrafast mechanisms occurring in proton water radiolysis, an area of physics especially important due to its relevance in biology and for proton therapy.

The field of laser based ion acceleration has made rapid progress in the past decade.^{1,2} As control over ion beam parameters increases, it becomes possible to find and develop applications utilizing their unique properties. Ion pulses from laser particle accelerators are created on the time scale of a picosecond³ and although they commonly have a broad energy spectrum, close to their source they are significantly shorter⁴ than the ion beams from conventional accelerators. Further it is possible to synchronise multiple laser pulses, provided they come from the same source, with time jitter that is negligible on the picosecond time scale, and thus enabling the possibility to use one laser pulse to drive the acceleration process and one as a probe, in a pump/probe-configuration.⁴ Until now, studies have been conducted probing or imaging the actual acceleration process with shadowgraphy or using the accelerated protons to probe laser generated dense plasmas.⁵ In this letter we present results where the short pulse duration, in combination with the exceptional synchronisation properties are utilized to investigate how energetic protons interact with water with a time resolution of only a few picoseconds.

Experimental research of proton radiolysis in water has so far been limited in time resolution by available proton pulse durations and by electronic synchronisation between the proton pulse and a separate probe. This has made it impossible to make direct experimental studies of processes that are faster than a few hundred picoseconds. Another option is to use indirect scavenging techniques, where a chemical scavenger is employed to measure the yields of radiolytic species in the tracks of high energy protons.⁶ By varying the concentration of the scavenger, the yields can be accurately determined at different times

using the rate constant for the reaction between the scavenger and the radicals. For picosecond time scales, however, this method becomes less reliable due to the very high concentration of scavengers needed. Traditionally, such experiments were performed in combination with Monte Carlo simulations^{7,8} to study the early effects of the high energy protons on water.

As high energy protons propagate into water, the absorbance of the water changes for certain wavelengths. This process occurs when the protons deposit energy through ionising the water molecules and thereby releasing electrons. In the water these secondary electrons will first become thermalized and then subsequently solvated/hydrated and, among other things, have the property of absorbing light in the visible and near-infrared region.⁹ Even though the existence of solvated electrons has been known for decades, their exact properties and behaviour is not fully understood and are to some extent still debated.^{10–12} From a biological perspective the study of how high energy protons interact with water is highly relevant since as much as 66% of radiation deposited into a cell is initially absorbed by water molecules. The radicals and solvated electrons formed in this interaction can then react with and damage the DNA in the cell.¹³

In the proton pulse radiolysis experiment we present here, protons were accelerated from thin aluminium foils in the target normal sheath acceleration (TNSA) regime.^{14,15} Here the leading edge of an ultrashort high intensity laser pulse fully ionises the front surface of a target foil and turns it into a plasma. The ponderomotive force of the laser pulse pushes electrons through the plasma and sets up a quasi-static electric field on the back of the foil. Contaminations, such as hydrocarbons and water, that can be found here become ionised and preferentially the protons (H^+) are accelerated in the electric field to MeV-energies. This gives a characteristically broad, exponentially decaying, and in our case,

^{a)}Electronic mail: b.dromey@qub.ac.uk

non-relativistic proton energy spectrum, meaning that the protons within a pulse travel with different velocities. This proton pulse is also divergent. Due to these factors, it is important to study the proton-water interaction as close to the proton source as possible, to fully take advantage of the short proton pulses and also to reach the highest dose levels.

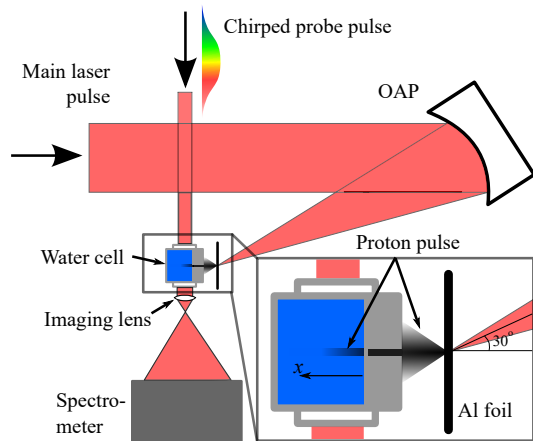


FIG. 1. Schematic sketch of the experimental setup. A high energy infrared laser pulse, compressed in the time domain to 600 fs (full width at half maximum), is focused by an off-axis parabolic mirror (OAP) onto a 12 μm thick Al target foil, at 30° angle of incidence. Protons are accelerated through the TNSA process. The ~ 0.1 mm central part of the proton pulse is allowed to enter through a 0.2 mm thick window of teflon into a cell filled with water. The non-central protons are stopped in a several millimetre thick cover of teflon. Perpendicular to the propagation direction of the protons in the water, along the x -axis, a chirped laser pulse is entering the water cell through a thin optical window. This pulse propagates through the volume where the accelerated protons interact with the water. Since the pulse is chirped, different frequencies will reach this volume at different times, thus giving a time resolution. The interaction volume is imaged and magnified by a lens onto the entrance slit of a Czerny-Turner imaging spectrometer. The main laser pulse and the probe pulse come from the same laser source and are therefore fully synchronised in time from shot to shot.

The experiments were performed at the TARANIS laser at Queen’s University, Belfast, UK. The laser delivered 10 J in 600 fs long pulses with a central wavelength of 1053 nm and a repetition rate of approximately 1 pulse per 10 min. The laser pulses were focused with an $f/2$ off-axis parabolic mirror onto a 12 μm thick aluminium foil at 30° angle of incidence. Protons were accelerated to energies up to ~ 10 MeV, which was measured with stacks of radiochromic film,¹⁶ that change color when absorbing radiation. 1 cm behind the target a water-cell was placed, see Fig. 1. The optical absorbance of the water in this cell was probed, perpendicular to the proton prop-

agation direction, with a 1 ns long chirped laser pulse, originating from the same source as the main pulse. The chirp in the probe pulse was introduced in a double pass grating stretcher and was tuned in a dedicated grating compressor. In the beam path of the probe pulse, two mirrors were placed on a translation stage so that the relative delay between the proton pulse and the probe pulse could be varied over a few ns. The interaction area was imaged by a lens with 8 times magnification onto the entrance slit of a 1 m imaging Czerny-Turner spectrometer with a 10×10 cm², 1200 lines/mm grating. The width of the proton beam, which the optical probe beam propagates through, is on the order of one hundred micrometers and the transmission is assumed to be constant over this distance. Different wavelengths passed through the interaction area at different times, since the probe pulse was chirped. The wavelength bandwidth of the probe pulse is only a few nm and its optical spectrum is fully enclosed in the much broader spectral region of absorption of the solvated electrons. The spectrometer then separated the frequencies spatially, thus creating a time-resolved image of the interaction. The images were captured at the exit of the spectrometer by a 16-bit CCD camera with 2048² pixels on a 27.6 \times 27.6 mm² sensor, with one axis corresponding to the time domain and the other axis the propagation depth of the laser-accelerated protons into the water. Unlike some other similar techniques which probe radiolytic processes with a chirped optical probe,^{17,18} our scheme includes an intrinsic temporal synchronization between the chirped pulse and a proton pulse. To determine the time resolution of the system, the spectrum of the chirped probe pulse was cut at a certain wavelength, thereby creating a step function in the wavelength domain. The 10%-90% rise time of the response in the spectrometer (giving the limit for the lowest resolvable time structures) was then corresponding to 12 ps \pm 1.5 ps for a probe pulse duration of 1 ns. In a similar way the spatial resolution was determined, by imaging a sharp edge placed in the position of the water cell, to be 2.5 μm \pm 0.5 μm . Our experimental scheme thus allows for imaging both the temporal and spatial evolution, along the proton propagation axis, of the optical absorbance as the proton pulse propagates through the water cell.

For each set of data attained during the experiment, two recordings of the probe pulse were made. One with the proton pulse in the water and one without. By comparing the two images the change in transmission induced by the interaction between the high energy protons and the water could be deduced (Fig. 2). In the analysis process the probe pulse intensities are set to be equal before the arrival of the proton pulse in the water cell, to account for small fluctuations in the probe pulse intensity between the two recordings.

The absorbance, A , of a material is given by the relation

$$A = -\log_{10}(T) = \epsilon c l \quad (1)$$

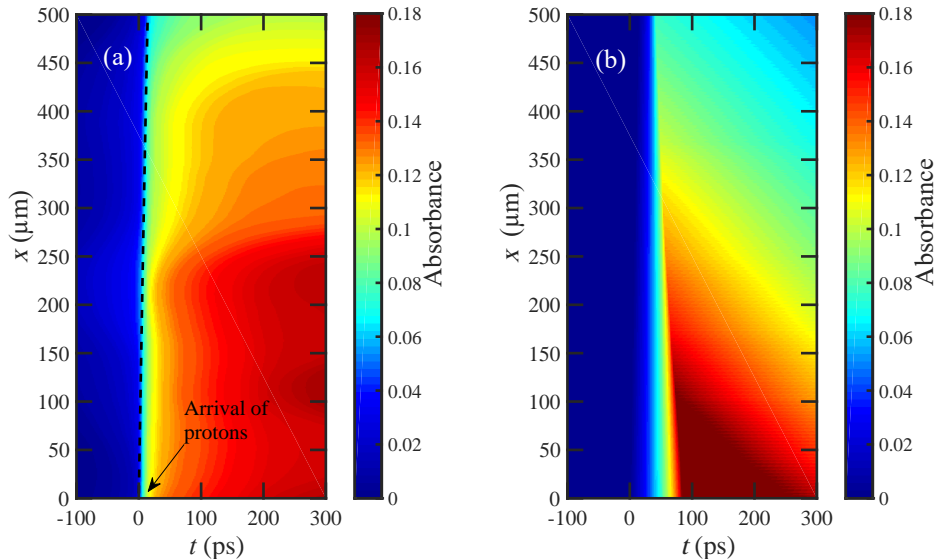


FIG. 2. (a) Experimental recording of induced absorbance in water to a chirped optical probe ($\lambda=1053$ nm) when exposed to a pulse of high energy protons (arriving at $t=0$ ps). The protons in the pulse have an exponentially decaying energy spectrum reaching up to approximately 10 MeV. The horizontal axis, t , represents the temporal evolution of the absorbance and the vertical axis, x , the spatial evolution along the axis of propagation of the energetic protons. The color scale indicates level of absorbance, where 0 corresponds to full transmission. The dashed, black line shows how a proton with an initial energy of 10 MeV would propagate through the water. Small fluctuations in the spectrum of the probe pulse give high frequency noise in the analysis process. This has been removed from the image with an edge-preserving moving median-filter for illustrative purposes, but all analysis has made with unfiltered data. The image has been truncated from the full ns-duration of the probe pulse for clarity. (b) Model of absorbance in (a) based on extrapolation of expected yields^{6,8} (approximately 4 solvated electrons per 100 eV of deposited energy, decreasing with increasing linear energy transfer) and decay kinetics^{19,20} of solvated electrons from studies with lower dose rates and measured at similar or longer times. The initial, exponentially decaying, proton energy spectrum is assumed to be similar to what was recorded during the experiment with a maximum proton energy of ~ 10 MeV. The point in time when the absorbance reaches its highest level for each value of x , is determined by the decreasing proton pulse duration at increasing propagation depths.

where T is the transmittance, ϵ denotes the molar attenuation coefficient, c the absorbant concentration and l the path length. In our case the absorbing species, at the probe pulse wavelength, is solvated electrons. The concentration of solvated electrons mainly depends on the amount of energy deposited into the water by the laser accelerated protons, but also somewhat on the linear energy transfer, i.e. the yield of solvated electrons is halved for protons close to the end of their tracks.⁶ The energy spectrum of the proton beam in these experiments is exponentially decaying, meaning that the highest amount of deposited energy per volume unit (highest dose) is found where the protons enter the water cell. This means that c , and by extension A , are in fact functions of the position along the proton propagation axis in the water cell, x .

The rising edge of the absorbance front, in other words the falling edge of transmission, was thoroughly investi-

gated to confirm that the expansion velocity of the absorbance corresponds to the expected proton velocities. There is a variation in arrival time at the water cell with approximately 80 ps from the highest energy protons (~ 10 MeV corresponding to ~ 43 $\mu\text{m}/\text{ps}$) to the lowest energy protons (~ 5 MeV corresponding to ~ 32 $\mu\text{m}/\text{ps}$) that can penetrate through the 200 μm entrance window of teflon. When the proton pulse arrives inside the water cell, it is found that the absorbance first rises rapidly over the duration of the proton pulse, as expected from the swift processes that solvates electrons.²¹ The absorbance varies over the different propagation depths as expected from the discussion above, with the highest absorbance found where the highest dose is deposited.

A model has been developed to simulate how the absorbance changes as a function of depth in the water cell. The simulations are based on tabulated data from SRIM (The Stopping and Range of Ions in Matter)²² and the

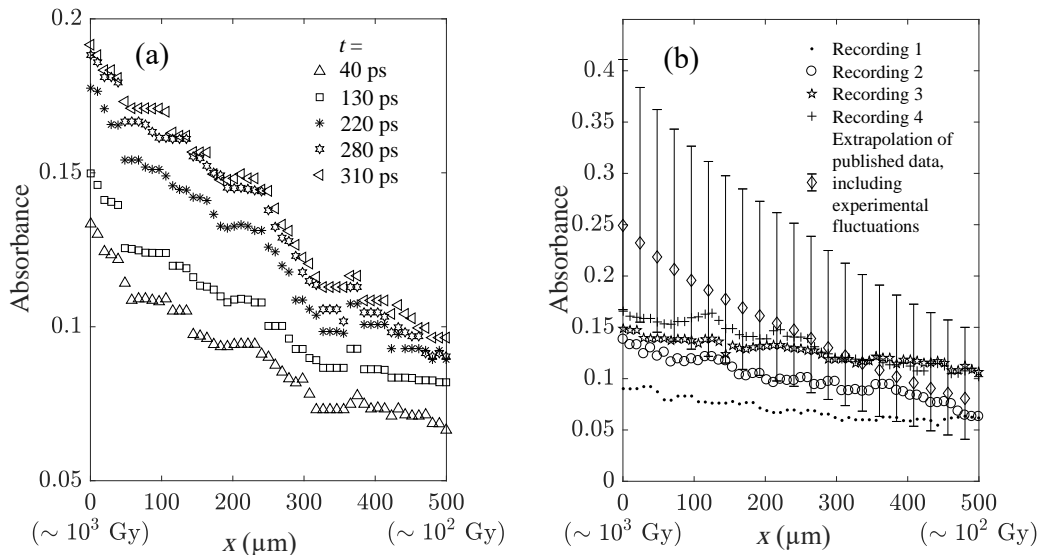


FIG. 3. (a) Absorbance of water as a function of the penetration depth, x , when exposed to a proton pulse at $t=0$ ps, at five different times. The proton pulse duration is below 80 ps for all values of x , but a clear increase in absorption is measured up to at least 200 ps. This trend is clearer for low values of x , i.e. higher doses. (b) Absorbance of water at $t=100$ ps as a function of the penetration depth, x , for four different recordings, when exposed to a proton pulse at $t=0$ ps. The diamonds mark expected absorbance according to the model displayed in Fig. 2b, based on extrapolation of yields of solvated electrons from publications^{6,8} with lower dose rates. The error bars take into account shot-to-shot fluctuations in the proton energy spectra, both in terms of maximum energy and number of protons for each energy. The shot to shot variations cannot fully explain the discrepancy between the model and the measured data for the highest doses, indicating that on the picosecond time scale, for sufficiently high dose rates, other physical processes take place compared to lower dose rates and longer time scales.

conversion efficiency from deposited energy into solvated electrons is taken from LaVerne et al.⁶ The molar attenuation coefficient, specific to our probe frequencies, is given in Assel et al.²³ The bandwidth of the chirped probe pulse is only a few nanometers and therefore the coefficient is, as a good approximation, constant throughout the whole pulse. Further, the small decay of solvated electrons at room temperature on the picosecond timescale, as presented by De Waele et al. and El Omar et al.^{19,20}, is included in the model. The protons are also assumed to have an initial energy distribution, before propagating through the teflon window, similar to what was measured during the experiment, i.e. an exponentially decaying proton energy spectrum from $\sim 10^{11}$ protons/MeV/sr at 1 MeV to $\sim 10^9$ protons/MeV/sr at 10 MeV. The results of these simulations are shown in Fig. 2 together with corresponding experimental recordings.

A comparison between the model and the experimental findings, see Fig. 3, shows reasonable agreement for the level of absorbance for the expected doses, especially for the lower doses. In Fig. 3b the errorbars in the model represent likely shot-to-shot fluctuations in the proton energy spectra, both considering variations in maximum

energy (20 %) and number of protons for each energy interval (50 %). For lower doses all the recordings fall within the errorbars. For the highest doses, i.e. where the protons enter the water cell, there is however a clear discrepancy. One possible explanation for this is that the model does not take into account any intertrack effects. A high energy proton passing through water will deposit energy along its track in so called spurs of radiolytic species. In this experiment the track radius is in the order of a few nm²⁴ at the times considered. The area density, where the protons enter the water cell, is approximately 5000 protons/ μm^2 , indicating that track structures of 5 nm radius would fill nearly half the water volume. Kreipl et al.²⁵ show through simulations a decrease in yield of solvated electrons in the tracks of 20 MeV protons propagating through water, when the protons are in close proximity of one another. This effect increases with the temporal and spatial density of the proton tracks. Since the linear energy transfer for protons of lower energy increases, giving an even higher density of radiolytic species in their tracks, it seems reasonable to assume that intertrack reactions would be at least as important for protons of 10 MeV or below. This may explain why the difference in absorbance between

the lowest and the highest dose is slightly smaller in the experiment than predicted by the model, suggesting that for sufficiently high dose rates the yield of solvated electrons is decreased. Given the linear relation between absorbance and concentration of solvated electrons, see Eq. 1, the comparison in Fig. 3b between our experimental data and the model, extrapolating data from previous publications, indicates that the correction in yields of solvated electrons for high dose rates (kGy/80 ps) could be as large as a factor of two.

The proton pulse duration is approximately 80 ps when entering the water, but also at later times the absorbance continues to slowly increase, see Fig. 3a, in contrast to what would be expected from the swift solvation process of electrons²¹ and the decay kinetics involved^{19,20,26}. Towards 300 ps this increase levels out. To avoid shot-to-shot fluctuations affecting the results in Fig. 3a, the data from each of the different times is taken from one single recording. This further confirms that an extrapolation of yields of solvated electrons from longer times and lower dose rates does not fully describe the scenario.

In conclusion we have presented experimental data of how picosecond bunches of high energy protons interact with water. This enables further understanding of how ultrahigh dose rates affect the energy deposition into water. Our experimental scheme provides a unique tool to study high energy proton/water interactions and gather information that previously was primarily accessible through simulations.

ACKNOWLEDGMENTS

L. S., O. L. and C.-G. W. acknowledge support from Knut and Alice Wallenberg Foundation (including PLIONA project) and from the Swedish Research Council. L. S. acknowledges financial support from SILMI, European Science Foundation (ESF). B. D. acknowledges support from the EPSRC (EP/L02327X/1 and EP/P016960/1).

¹A. Macchi, M. Borghesi, and M. Passoni, *Rev. Mod. Phys.* **85**, 751 (2013).

²H. Daido, M. Nishiuchi, and A. S. Pirozhkov, *Rep. Prog. Phys.* **75**, 056401 (2012).

³J. Fuchs, P. Antici, E. d'Humieres, E. Lefebvre, M. Borghesi, E. Brambrink, C. A. Cecchetti, M. Kaluza, V. Malka,

M. Manclossi, S. Meyroneinc, P. Mora, J. Schreiber, T. Toncian, H. Pepin, and P. Audebert, *Nat. Phys.* **2**, 48 (2006).

⁴B. Dromey, M. Coughlan, L. Senje, M. Taylor, S. Kuschel, B. Villagomez-Bernabe, R. Stefaniuk, G. Nersisyan, L. Stella, J. Kohanoff, M. Borghesi, F. Currell, D. Riley, D. Jung, C.-G. Wahlström, C. Lewis, and M. Zepf, *Nat. Commun.* **7**, 10642 (2016).

⁵M. Borghesi, A. Schiavi, D. H. Campbell, M. G. Haines, O. Willi, A. J. MacKinnon, L. A. Gizzi, M. Galimberti, R. J. Clarke, and H. Ruhl, *Plasma Phys. Contrl. F.* **43**, A267 (2001).

⁶J. A. LaVerne, I. Štefanić, and S. M. Pimblott, *J. Phys. Chem. A* **109**, 9393 (2005).

⁷S. Uehara and H. Nikjoo, *J. Radiat. Res.* **47**, 69 (2006).

⁸G. Baldacchino, *Radiat. Phys. Chem.* **77**, 1218 (2008).

⁹B. Abel, U. Buck, A. L. Sobolewski, and W. Domcke, *Phys. Chem. Chem. Phys.* **14**, 22 (2011).

¹⁰R. E. Larsen, W. J. Glover, and B. J. Schwartz, *Science* **329**, 65 (2010).

¹¹L. Turi and A. Madarasz, *Science* **331**, 1387 (2011).

¹²L. D. Jacobson and J. M. Herbert, *Science* **331**, 1387 (2011).

¹³E. Alizadeh and L. Sanche, *Chem. Rev.* **112**, 5578 (2012).

¹⁴S. P. Hatchett, C. G. Brown, T. E. Cowan, E. A. Henry, J. S. Johnson, M. H. Key, J. A. Koch, A. B. Langdon, B. F. Lasinski, R. W. Lee, A. J. Mackinnon, D. M. Pennington, M. D. Perry, T. W. Phillips, M. Roth, T. C. Sangster, M. S. Singh, R. A. Snively, M. A. Stoyer, S. C. Wilks, and K. Yasuike, *Phys. Plasmas* **7**, 2076 (2000).

¹⁵S. C. Wilks, A. B. Langdon, T. E. Cowan, M. Roth, M. Singh, S. Hatchett, M. H. Key, D. Pennington, A. MacKinnon, and R. A. Snively, *Phys. Plasmas* **8**, 542 (2001).

¹⁶F. Nürnberg, M. Schollmeier, E. Brambrink, A. Blazevic, D. C. Carroll, K. Flippo, D. C. Gautier, M. Geissel, K. Harres, B. M. Hegelich, O. Lundh, K. Markey, P. McKenna, D. Neely, J. Schreiber, and M. Roth, *Rev. Sci. Instrum.* **80**, 033301 (2009).

¹⁷I. A. Shkrob, D. A. Oulianov, R. A. Crowell, and S. Pommeret, *J. Appl. Phys.* **96**, 25 (2004).

¹⁸V. De Waele, U. Schmidhammer, J. R. Marquès, H. Monard, J.-P. Larbre, N. Bourgeois, and M. Mostafavi, *Rad. Phys. Chem.* **78**, 1099 (2009).

¹⁹V. De Waele, S. Sorges, P. Pernot, J.-L. Marignier, H. Monard, J.-P. Larbre, and M. Mostafavi, *Chem. Phys. Lett.* **423**, 30 (2006).

²⁰A. K. El Omar, U. Schmidhammer, P. Jeunesse, J.-P. Larbre, M. Lin, Y. Muroya, Y. Katsumura, P. Pernot, and M. Mostafavi, *J. Phys. Chem. A* **115**, 12212 (2011).

²¹V. Cobut, Y. Frongillo, J. P. Patau, T. Goulet, M.-J. Fraser, and J.-P. Jay-Gerin, *Radiat. Phys. Chem.* **51**, 229 (1998).

²²www.srim.org.

²³M. Assel, R. Laenen, and A. Laubereau, *J. Chem. Phys.* **111**, 6869 (1999).

²⁴Y. Frongillo, T. Goulet, M.-J. Fraser, V. Cobut, J. P. Patau, and J.-P. Jay-Gerin, *Radiat. Phys. Chem.* **51**, 245 (1998).

²⁵M. S. Kreipl, W. Friedland, and H. G. Paretzke, *Radiat. Environ. Biophys.* **48**, 349-359 (2009).

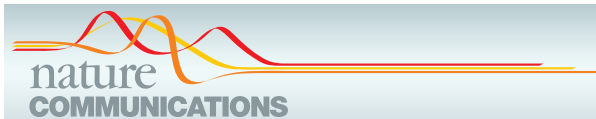
²⁶W. G. Burns, R. May, G. V. Buxton, and G. S. Tough, *Farad. Discuss.* **63**, 47 (1977).

PAPER VI

Picosecond metrology of laser-driven proton bursts

B. Dromey, M. Coughlan, L. Senje, M. Taylor, S. Kuschel, B. Villagomez-Bernabe, R. Stefanuik, G. Nersisyan, L. Stella, J. Kohanoff, M. Borghesi, F. Currell, D. Riley, D. Jung, C.-G. Wahlström, C. L. S. Lewis, & M. Zepf.

Nature Communications 7, 10642 (2016).



ARTICLE

Received 22 Oct 2015 | Accepted 7 Jan 2016 | Published 10 Feb 2016

DOI: 10.1038/ncomms10642

OPEN

Picosecond metrology of laser-driven proton bursts

B. Dromey¹, M. Coughlan¹, L. Senje², M. Taylor¹, S. Kuschel³, B. Villagomez-Bernabe¹, R. Stefanuik⁴, G. Nersisyan¹, L. Stella⁵, J. Kohanoff⁵, M. Borghesi¹, F. Currell¹, D. Riley¹, D. Jung¹, C.-G. Wahlström², C.L.S. Lewis¹ & M. Zepf^{1,3}

Tracking primary radiation-induced processes in matter requires ultrafast sources and high precision timing. While compact laser-driven ion accelerators are seeding the development of novel high instantaneous flux applications, combining the ultrashort ion and laser pulse durations with their inherent synchronicity to trace the real-time evolution of initial damage events has yet to be realized. Here we report on the absolute measurement of proton bursts as short as 3.5 ± 0.7 ps from laser solid target interactions for this purpose. Our results verify that laser-driven ion acceleration can deliver interaction times over a factor of hundred shorter than those of state-of-the-art accelerators optimized for high instantaneous flux. Furthermore, these observations draw ion interaction physics into the field of ultrafast science, opening the opportunity for quantitative comparison with both numerical modelling and the adjacent fields of ultrafast electron and photon interactions in matter.

¹Centre for Plasma Physics, School of Mathematics and Physics, Queens University Belfast, Belfast BT7 1NN, UK. ²Department of Physics, Lund University, PO Box 118, S-221 00 Lund, Sweden. ³Helmholtz-Institut Jena, Frobelstieg 3, 07743 Jena, Germany. ⁴School of Physics, University College Dublin, Belfield, Dublin 4, Ireland. ⁵Atomistic Simulation Centre, School of Mathematics and Physics, Queens University Belfast, Belfast BT7 1NN, UK. Correspondence and requests for materials should be addressed to B.D. (email: b.dromey@qub.ac.uk).

To date the experimental investigation of exactly how matter recovers in response to ion damage, and the emerging pathways for the resultant reactive species generated during the interaction, has been limited by pulse length in conventional accelerators and probe timing jitter¹. When a pulse of ions (with kinetic energy > 1 MeV per nucleon) interacts with condensed matter the individual particles generate nanometre-wide tracks of ionization with correspondingly steep energy density gradients^{2–6}. The generation of steep energy density gradients drives a rapid diffusion of the hot electron population that tends to homogenize the dose distribution^{3,4}. This process leads to secondary ionization cascades and the formation of long-lived excited states/chemically reactive species, which equilibrate with the background material over picosecond timescales^{7,8}. Studying the lifetime of these states is critical for understanding the relationship between the incident ion flux and time-dependent defect concentration in ion-irradiated matter⁹ and cell death/repair rate for radiobiology driven by ultrafast energy deposition¹⁰. This interaction, and subsequent evolution of dose, is unambiguously distinct from the near-homogeneous excitation that results from both X-ray and electron interactions due to significantly different stopping powers of the different ionizing species in matter.

While pump–probe measurements can in principle reveal these inherently multi-scale processes, they require that the ion pump pulse is significantly shorter than the mean lifetime of the species under investigation and that there is a comparatively high degree of synchronicity between the pump and probe sources. As mentioned above, the corresponding few picosecond bunch duration is not routinely available from conventional accelerators^{1,11} and so an alternative source is required. One method to overcome this problem is to capitalize on the ultrafast acceleration phase provided during the interaction of high-power lasers with thin, solid-density foils^{12–14}. The high instantaneous flux is suitable for a host of high energy density applications^{15–18} but to date the excellent synchronicity between the pulse of protons (pump) and the driving laser (probe) has not been exploited to directly investigate ultrafast damage processes in matter^{8,10,19}.

Here we demonstrate an absolute duration measurement of proton pulses generated during high-power laser solid target interactions that overcomes these limitations. Our technique relies on the observation of prompt ionization dynamics^{8,20} in high-purity SiO₂ glass (a transparent wide bandgap dielectric) irradiated by laser-driven protons using highly synchronized optical laser pulses. As part of this measurement we are also able to place an upper limit on the mean free lifetime of the excited electron population in the conduction band of < 0.2 ps for our experimental conditions. It is this ultrafast response of SiO₂ that permits the single-shot temporal characterization (with < 0.5 ps resolution for our entire detection system) of the proton pulse driving the ionization dynamics. In addition we demonstrate the general applicability of this technique by extending our measurements to perform jitter-free tracking of ion-induced dynamics in an alternative sample dielectric sample (borosilicate glass). This is made possible because the absolute proton pulse duration has been established. In future this technique can be combined with equally synchronized laser-driven coherent ultraviolet/X-ray probes^{21,22} to allow for metrology of ion interactions on timescales of the rising edge of the interaction and potentially detailed studies of the initial damage track structure in the medium.

Results

Experimental procedure. To date the duration of laser-accelerated proton bunches has only been inferred from proton radiography^{17,18}. For ultrafast applications, however, a more direct method of pulse metrology is desirable. In this section we show

that the absolute measurement of laser-driven ion pulses is made possible by studying ultrafast ionization dynamics^{8,9,20} in ion-irradiated SiO₂ (Fig. 1). We also demonstrate the application of this method to novel studies of the lifetime of excited conduction band electrons in proton-irradiated matter.

First we examine the temporal characteristics of protons accelerated via the target normal sheath acceleration (TNSA) mechanism (see Methods), although the technique described below is also applicable to ion bursts from alternative laser-driven acceleration schemes^{14,23}. TNSA is an inherently broadband generation mechanism, producing a Maxwellian spectrum with a sharp, high-energy cutoff (E_{co}). For nonrelativistic proton energies (MeV scale) this large energy spread causes the initially short ion pulse to stretch rapidly due to velocity dispersion, as it drifts from the source. The initial short pulse duration is still, however, preserved in narrow energy slices (bandwidths) of the spectrum. One way to recover this bandwidth is by stopping²⁴ the lower-energy protons in bulk SiO₂ (Fig. 1). The pulse duration $\tau(D)$ can then simply be estimated from time-of-flight considerations for the fastest and slowest edges of the bandwidth remaining at a given depth in the SiO₂ (Fig. 1b). See Methods for further details on bandwidth narrowing and the corresponding pulse duration.

To measure $\tau(D)$ experimentally we study the lifetime of electrons excited into the conduction band of SiO₂ by proton stopping. The schematic in the inset of Fig. 1 (dashed box) shows how this can provide the basis for an ultrafast detector. Prompt ($< 10^{-15}$ s) ionization by protons (i) results in the excitation of

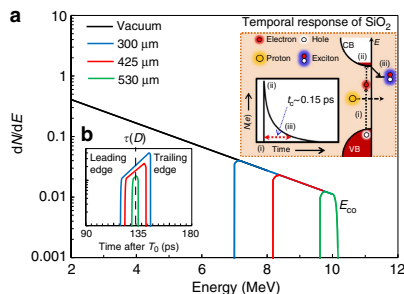


Figure 1 | Ultrafast proton pulse metrology in SiO₂. The dashed inset shows a schematic of the intraband dynamics and temporal response of an excited electron in α -SiO₂. VB and CB are the valance and conduction bands, respectively, and E is the energy. Exciton formation provides the ultrafast de-excitation pathway for electrons in the CB⁹. The time constant for exciton formation is ~ 0.15 ps (refs 8,20). **(a)** Schematic of a TNSA proton spectrum (black trace) represented by a truncated exponential, with a proton temperature $T = 2$ MeV and a high-energy spectral cutoff $E_{\text{co}} = 10$ MeV. The coloured traces show the bandwidth of the original spectrum that remains after proton stopping at different depths D , in bulk SiO₂ (density 2.66 g cm^{-3}) from stopping and range of ions in matter (SRIM) calculations²⁴ (see Methods for more details). This returns a continuously decreasing bandwidth with respect to D (up to the stopping depth for E_{co} , here $\sim 570 \mu\text{m}$). The proton pulse duration $\tau(D)$ **(b)** is then simply the difference in time of flight for vacuum propagation (chosen here to be 5 mm) plus D for both the leading and trailing (high and low kinetic energy) edges of the remaining proton bandwidth. This illustrative schematic shows only the cumulative bandwidth narrowing of the originally broadband spectrum to reveal how short pulses can in principle be retrieved. It does not account for other aspects of the TNSA mechanism, such as energy-dependent cone narrowing^{12–14} critical for determination of the detailed proton pulse profile for a particular D .

electrons into the conduction band (ii), where the Roman numerals correspond to labels in the inset of Fig. 1. Previous experiments based on uniform photoexcitation in SiO₂ demonstrate a decay time constant of ~ 0.15 ps for moderate excitation densities ($\sim 10^{19}$ cm⁻³)^{8,20,25}, with recombination being driven by ultrafast defect formation (iii) in the material^{8,9,20}. Before recombination, however, these excited electrons are available to take part in free-free absorption of optical radiation (~ 1 eV). It is this rapid switching in the optical transmission properties of irradiated SiO₂ (transient opacity) that provides the platform for ultrafast metrology of proton pulses.

Observation of the proton pulse duration. Figure 2 shows a schematic for the optical streaking technique used to temporally resolve the transient opacity in SiO₂ induced by laser-driven ion pulses. To experimentally verify this technique the TARANIS laser facility at Queens University Belfast²⁷ is used to accelerate protons via the TNSA mechanism to a spectral cutoff energy (E_{co}) of 10 ± 0.5 MeV. This pulse then interacts with a high-purity SiO₂ sample placed 5 ± 0.5 mm behind the generation point. A typical optical streak obtained from this setup is shown in Fig. 3a. In agreement with full modelling for the optical streak (based on Monte Carlo simulations, Fig. 3b), the duration of the transient opacity gets successively shorter with respect to D due to bandwidth narrowing as a result of low-energy proton stopping. For $D = 530 \pm 10$ μm the duration of the opacity is measured to be 3.5 ± 0.7 ps (Fig. 4a). This is in excellent agreement with the expected proton pulse duration $\tau(D)$ of ~ 3.3 ps from both calculations (green trace, Fig. 1b) and modelling (Fig. 3b).

In fact, using this modelling of the optical streak we can analyse the temporal profile of the measured proton pulse in some detail. The resolution of this measurement is 0.45 ± 0.05 ps, which corresponds to a proton pulse bandwidth of < 0.1 MeV for the conditions described in Fig. 4a. We find that best agreement

between experiment and modelling is obtained for an assumed detector response time t_d of 0.45 ps (green dashed trace, inset, Fig. 4a). This places an upper bound of 0.1 MeV on the decay constant of the TNSA spectral intensity above E_{co} and an upper limit of < 0.2 ps on the lifetime of excited electrons in the conduction band of the irradiated sample SiO₂ (from temporal profile fitting, inset, Fig. 4a). Furthermore, this analysis demonstrates that proton straggling does not lead to a significant increase in the observed pulse duration beyond what is expected due to slowing in SiO₂. In all, this analysis confirms the efficacy of SiO₂ as a sub-picosecond resolution detector for proton bursts. Finally, our ultrafast metrology verifies that there is negligible thermal spread imposed on the nascent bunch during the acceleration mechanism for the fastest protons (> 6 MeV), that is, the protons are accelerated from an initially cold cathode for our experimental conditions. The observation of emission from a cold cathode is in agreement with previous experimental measurements of the transverse emittance of the TNSA beam on similar specification systems²⁸.

It is worth noting that for proton bunches with an inherently narrow energy spread, stopping in bulk SiO₂ is not required to achieve ultrafast temporal resolution. In this scenario the bulk sample can be replaced by a thin SiO₂ pellicle and the proton pulse duration can be obtained using a near-collinear probing geometry²⁰. For proton beams with sufficiently high kinetic energy this will have a negligible effect on beam quality and is a possible route to online temporal metrology. In addition, this near-collinear geometry can provide information on the two-dimensional beam spatial/angular distribution by imaging the opacity induced by the proton-SiO₂ interaction directly onto a charge-coupled device as an ultrafast replacement for comparatively slow scintillation screens.

Ultrafast ion damage in matter. Next we demonstrate how this technique can be applied more generally to study ultrafast

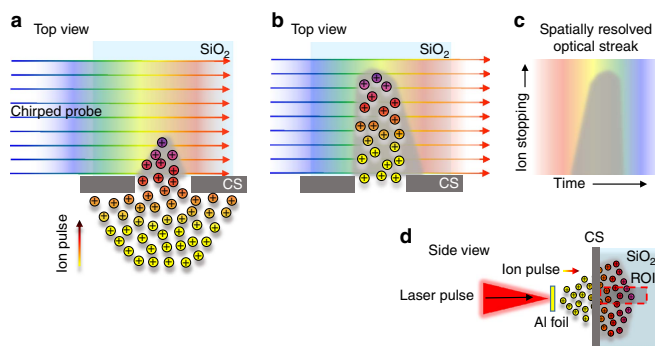


Figure 2 | Schematic of the optical streaking technique for laser-driven proton bursts. Protons accelerated from a thin contamination layer on the rear surface of 10- μm -thick Au foils via the TNSA mechanism undergo electronic stopping in a high-purity SiO₂ sample at ~ 300 K placed 5 mm behind the interaction. The corresponding transient opacity (grey) is recorded using a synchronized 1,053-nm probe pulse with a variable linear frequency sweep, or chirp²⁶. This permits observation of the interaction over time windows ranging from 0.4 ± 0.02 (fully compressed pulse for direct imaging of interaction and represents the fundamental temporal resolution of this system) to $\sim 1,400$ ps (maximum chirp for optical streaking). In **a** and **b** the proton bunch is incident from below and collimated to a width of 100 μm using a 1-mm-thick Al slit collimating slit (CS). Co-propagating keV electrons are stopped with the use of a 50- μm Al foil at the interaction facing surface of the SiO₂ (not shown). A chirped pulse (> 50 ps) is incident from the left. Different frequency components traverse the irradiated region at different times, thus encoding the temporal evolution in the observed spectrum. It is important to note that the bandwidth of the optical probe (4 nm) is narrow compared with the width of the absorption spectrum for conduction band electrons in SiO₂. The optical streak is obtained by spectrally resolving the chirped pulse (**c**) using a 1-m imaging spectrometer with a $1,200$ mm^{-1} grating (dimensions 10×10 cm). The region of interest (ROI, **d**) for the ion burst interaction is a 10- μm scale slice along the central axis of the driving laser pulse. This is imaged onto the entrance slit of the spectrometer with a magnification of ~ 10 . The fundamental temporal resolution of the system described here is limited only by the resolution of the spectrometer²⁶. For a 200-ps probe this system provides a resolution of 0.45 ± 0.05 ps.

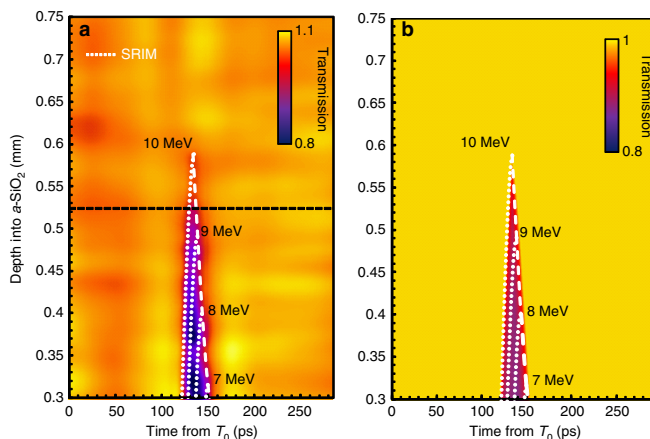


Figure 3 | Optical streaking of transient ion-induced opacity in SiO_2 . (a) An experimentally obtained optical streak for opacity induced in SiO_2 by the stopping of a TNSA proton pulse with a spectral endpoint energy of 10 ± 0.5 MeV generated by the TARANIS laser. The data are normalized to the average full transmission. The on-laser axis proton flux in the SiO_2 ranges from $250 \pm 50 \mu\text{m}^{-2}$ for $D = 300 \mu\text{m}$ to $100 \pm 50 \mu\text{m}^{-2}$ for $D = 530 \mu\text{m}$ as inferred from radiochromic film measurements. The average excited electron density is measured to be $< 10^{19} \text{cm}^{-2}$ from interferometry of the interaction region using a fully compressed probe pulse and Wollaston prism. In **a** and **b** the colour scale goes from full transmission (light) to 80% transmission (0.8, dark). There is a slight modulation due to noise on the experimentally obtained streak. The data are shown for depths $> 300 \mu\text{m}$ due to small bevelled edge ($\sim 100 \mu\text{m}$) on the SiO_2 sample increasing uncertainty in the measured transmitted light. It is important to note however that the signal due to ions (starting at ~ 120 ps) is not compromised by earlier opacity from prompt electrons/X-rays at this depth. The white dotted lines represent stopping and range of ions in matter (SRIM)²⁴ calculations for monoenergetic protons (labelled) stopping in SiO_2 . The white dashed line corresponds to the $1/e$ level of the peak in the stopping curve at the end of range for these calculations. (b) Modelling for the expected temporal evolution of opacity in SiO_2 for the proton spectrum. This modelling takes into account the energy-dependent cone angle of the emission as measured using radiochromic film stacks¹⁴. The key assumptions made for **b** are that the opacity generated is linear with stopping power²⁴ and that the response time of the detector is 0.45 ps.

dynamics in proton-irradiated condensed matter. In Fig. 4b we show a direct comparison of the lifetime of conduction band electrons in SiO_2 and borosilicate glass (BK7) for identical proton pulse conditions to those presented in Fig. 3a. BK7 is a multi-component derivative of SiO_2 , representing a low-cost alternative for laboratories due to its similar thermal shock and optical properties. However, as can be seen, the proton-induced transient opacity is observed to have a > 400 -ps recovery time to full transmission (red dotted trace, Fig. 4b). Photoexcitation experiments in BK7 suggest that this long recovery can be interpreted as being due to occupied interstitial levels preventing rapid relaxation of the hot electron population²⁹. However, those experiments also indicate that the lifetime of photoexcited electrons is $\sim 5,000$ ps. Our measurement of 430 ± 20 ps, while being ~ 100 times longer than that of SiO_2 , is significantly shorter than 5,000 ps.

Discussion

One hypothesis for this discrepancy lies in the nature of proton interactions in condensed matter. Monte Carlo modelling for damage tracks in SiO_2 shows that an instantaneous proton flux (that is, time = 0 fs) of $50 \mu\text{m}^{-2}$ produces a strongly inhomogeneous dose distribution with excited electron densities falling from $> 10^{21} \text{cm}^{-3}$ to equilibrium level over transverse widths < 4 nm (Fig. 4c). From simple electronic diffusivity considerations this distribution will evolve rapidly over ps timescales in comparison with homogenous photoexcitation³. While a detailed study of this evolution is beyond the scope of the work presented here, the observation of significantly reduced recovery timescales

in BK7 provides an example of the new insights into physical processes this metrology can provide for transient dynamics resulting from proton-matter interactions. Furthermore, the high degree of synchronicity between the proton and probe sources means that our technique can be readily extended to study the evolution of specific transient defects by changing the probe wavelength, either through frequency conversion in crystals or nonlinear conversion using either gas or relativistic plasma^{21,22} sources, to temporally resolve absorption bands for specific excited species.

Looking to the future, the prospect of generating narrow-bandwidth proton spectra with femtosecond duration driving lasers¹⁴ offers the possibility of extending this technique to timescales suitable for investigating primary radiation events during the rising edge of the interaction using femtosecond scale probing. Another possibility is the potential to extend work examining energy transfer in non-equilibrium warm dense matter generated through isochoric heating using laser-accelerated protons³⁰. For the present TNSA source, schemes that require the maintenance of high proton beam quality can be realized using a simple magnetic spectrometer and slit arrangement, or more complicated chromatic focusing schemes using a laser-driven electrostatic lens³¹ to select the desired flux and energy bandwidth (or pulse duration) instead of via stopping in bulk material. This will permit ultrafast studies of proton implantation and resulting damage at well-specified depths in materials.

Methods

Target normal sheath acceleration. During intense laser-foil (μm scale thickness) interactions an accelerating potential at the rear surface of the foil is rapidly

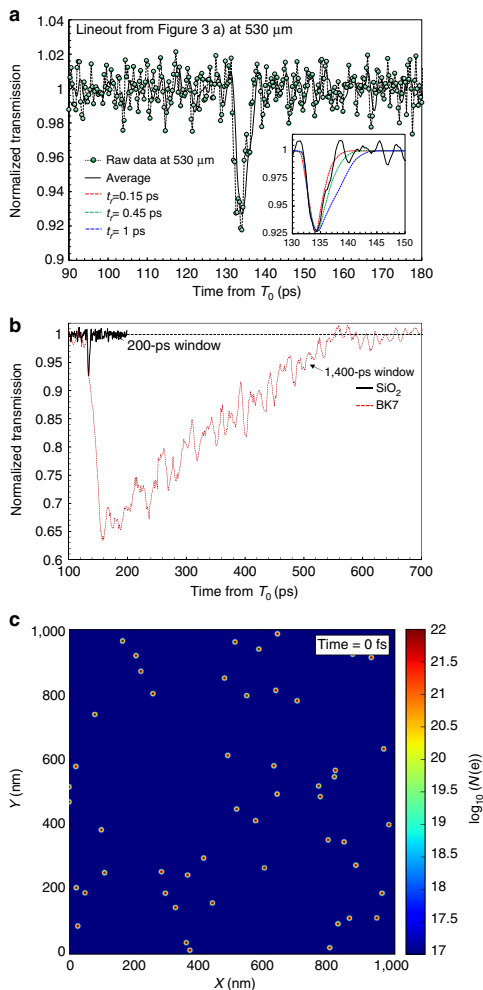


Figure 4 | Ultrafast metrology of proton bursts and their interactions in condensed matter. (a) Background corrected data (points) and moving average signal over seven adjacent points (solid black line) for the transient opacity at a depth of 530 μm in optical streak presented in Fig. 3a. All times are shown with respect to the interaction time, T_0 . The observed duration of the transient opacity is 3.5 ± 0.7 ps. The inset of **a** shows a comparison of the average signal level with modelling of the optical streaking adjusted for different detector response times, t_r . The best fit for the observed temporal profile is found to correspond to $t_r = 0.45$ ps, which is close to the resolution limit of the optical pulse^{26,27}. (b) A direct comparison between the response time for TNSA pulse interactions in SiO₂ (black line, as in **a** and BK7 (red dotted line) at depths of 530 μm and 610 μm to account for the slightly different densities of the two media—2.66 and 2.31 g cm⁻³, respectively. The horizontal dashed line represents the mean of full transmission. (c) The result of Monte-Carlo-based modelling for the instantaneous dose distribution at a depth of 530 μm for a proton flux of 50 μm⁻². The colour scale is in log of free electron density ($N(e)$).

established by electrons driven through the target from the front surface by the intense laser field. As they exit the foil, these electrons ionize a thin hydrocarbon contamination layer on the rear surface leaving a net positive charge in their wake. Simulations show that this process leads to the formation of a charge separation sheath producing a strong electrostatic field exceeding 1 TV m^{-1} , which provides a transient accelerating potential for the rear-surface ions¹⁴. However, since the fastest electrons only contribute to this sheath for a fraction of the driving laser duration, the peak in this accelerating potential is very short-lived. It is this ultrafast evolution of the accelerating potential that provides the basis for ultrashort ion pulse generation during TNSA.

Stopping of protons in SiO₂ for TNSA bandwidth/pulse duration selection.

As the broad bandwidth of TNSA protons transverses the SiO₂ sample, they continuously lose kinetic energy, that is, a 10-MeV proton in vacuum has $< < 1$ eV kinetic energy after ~ 570 μm of SiO₂. This implies that the bandwidth of the TNSA spectrum continually narrows and shifts towards lower energies with respect to D . At a given depth the remaining bandwidth is bounded on the leading edge by the fastest protons. These protons have a well-defined energy (E_{co} before entering the SiO₂). Next the trailing/slowest edge is bounded by the lowest-energy protons that have yet to be stopped at that depth²⁴. Together these edges define a sharply bounded, depth-dependent bandwidth that narrows as the fastest protons slow to thermal energies (which implies that all protons with lower initial kinetic energy are already stopped). This is illustrated in Fig. 1b where the pulse duration (obtained from the bandwidth) is shown to reduce with respect to D .

References

- Baldacchino, G. Pulse radiolysis in water with heavy-ion beams. A short review. *Rad. Phys. Chem.* **77**, 1218–1223 (2008).
- Murat, M., Akkerman, A. & Barak, J. Spatial distribution of electron-hole pairs induced by electrons and protons in SiO₂. *IEEE Trans. Nucl. Sci.* **51**, 3211–3218 (2004).
- Osmani, O., Medvedev, N., Schlegel, M. & Rethfeld, B. Energy dissipation in dielectrics after swift heavy-ion impact: a hybrid model. *Phys. Rev. B* **84**, 214105 (2011).
- Medvedev, N. *et al.* Early stage of the electron kinetics in swift heavy ion tracks in dielectrics. *Phys. Rev. B* **82**, 125425 (2010).
- Schiwietz, G., Czernski, K., Roth, M., Staufienbiel, F. & Grande, P. L. Femtosecond dynamics—snapshots of the early ion-track evolution. *Nucl. Instrum. Methods Phys. Res. B* **225**, 4–26 (2004).
- Kluth, P. *et al.* Fine structure in swift heavy ion tracks in amorphous SiO₂. *Phys. Rev. Lett.* **101**, 175503 (2008).
- Chipman, D. M. Absorption spectrum of OH radical in water. *J. Phys. Chem. A* **112**, 13372–13381 (2008).
- Guizard, J. *et al.* Time resolved study of colour centre formation SiO₂. *J. Phys. Condens. Matter* **8**, 1281–1290 (1996).
- Hosono, H., Kawazoe, H. & Matsunami, N. Experimental evidence for frenkel defect formation in amorphous SiO₂ by electronic excitation. *Phys. Rev. Lett.* **80**, 317–320 (1998).
- Rigaud, O. *et al.* Exploring ultrashort high-energy electron-induced damage in human carcinoma cells. *Cell Death Dis.* **1**, e73 (2010).
- Baudrenghien, P. & Mastoridis, T. Longitudinal emission blowup in the large hadron collider. *Nucl. Instrum. Methods Phys. Res. A* **726**, 181–190 (2013).
- Clark, E. L. *et al.* Energetic heavy-ion and proton generation from ultra-intense laser-plasma interactions with solids. *Phys. Rev. Lett.* **85**, 1654–1657 (2000).
- Snively, R. A. *et al.* Intense high-energy proton beams from petawatt-laser irradiation of solids. *Phys. Rev. Lett.* **85**, 2945–2948 (2000).
- Macchi, A., Borghesi, M. & Passoni, M. Ion acceleration by superintense laser-plasma interaction. *Rev. Mod. Phys.* **85**, 751–793 (2013).
- Yogo, A. Application of laser-accelerated protons to the demonstration of DNA double-strand breaks in human cancer cells. *Appl. Phys. Lett.* **94**, 181502 (2009).
- Pelka, A. *et al.* Ultrafast melting of carbon induced by intense proton beams. *Phys. Rev. Lett.* **105**, 265701 (2010).
- Borghesi, M. *et al.* Electric field detection in laser-plasma interaction experiments via the proton imaging technique. *Phys. Plasmas* **9**, 2214–2220 (2002).
- Abicht, F. *et al.* Tracing ultrafast dynamics of strong fields at plasma-vacuum interfaces with longitudinal proton probing. *Appl. Phys. Lett.* **105**, 034101 (2014).
- Correa, A. A. *et al.* Nonadiabatic forces in ion-solid interactions: the initial stages of radiation damage. *Phys. Rev. Lett.* **108**, 213201 (2012).
- Audebert, P. *et al.* Space-time observation of an electron gas in SiO₂. *Phys. Rev. Lett.* **73**, 1990–1993 (1994).

21. Kiefer, D. *et al.* Relativistic electron mirrors from nanoscale foils for coherent frequency upshift to the extreme ultraviolet. *Nat. Commun.* **4**, 1763 (2013).
22. Dromey, B. *et al.* Coherent synchrotron emission from electron nanobunches formed in relativistic laser-plasma interactions. *Nat. Phys.* **8**, 804–808 (2012).
23. Jung, D. *et al.* Scaling of ion energies in the relativistic-induced transparency regime. *Laser Part. Beams* **33**, 695–703 (2015).
24. Ziegler, J. F., Ziegler, M. D. & Biersack, J. P. SRIM—the stopping and range of ions in matter. *Nucl. Instrum. Methods B* **268**, 1027–1036 (2010).
25. Riedel, R. *et al.* Single-shot pulse duration monitor for extreme ultraviolet and X-ray free-electron lasers. *Nat. Commun.* **4**, 1731 (2013).
26. Polli, D., Brida, D., Mukamel, S., Lanzani, G. & Cerullo, G. Effective temporal resolution in pump-probe spectroscopy with strongly chirped pulses. *Phys. Rev. B* **82**, 053809 (2010).
27. Dzelzainis, T. *et al.* The TARANIS laser: a multi-Terawatt system for laser-plasma investigations. *Laser Part. Beams* **28**, 451–461 (2010).
28. Cowan, T. E. *et al.* Ultralow emittance, multi-MeV proton beams from a laser virtual-cathode plasma accelerator. *Phys. Rev. Lett.* **92**, 204801 (2004).
29. Horn, A., Kreutz, E. W. & Poprawe, R. Ultrafast time-resolved photography of femtosecond laser induced modifications in BK7 glass and fused silica. *Appl. Phys. A* **79**, 923–925 (2004).
30. White, T. G. *et al.* Observation of inhibited electron-ion coupling in strongly heated graphite. *Sci. Rep.* **2**, 889 (2012).
31. Kar, S. *et al.* Dynamic control of laser-produced proton beams. *Phys. Rev. Lett.* **100**, 105004 (2008).

Acknowledgements

We acknowledge support for this work from the EPSRC through the following grants EP/L02327X/1 and EP/K022415/1. R.S. acknowledges support from SFI. We acknowledge insightful discussions with Prof. Pdraig Dunne (University College Dublin).

Author contributions

This work was conceived and implemented by B.D. and M.Z.; the experimental work was performed by B.D., M.C., L.S., D.J., M.T., G.S., R.S. and D.M.; numerical simulations were performed by S.K. and B.V.-B.; all other authors contributed directly to the data analysis and discussion phase.

Additional information

Competing financial interests: The authors declare no competing financial interests.

Reprints and permission information is available online at <http://npg.nature.com/reprintsandpermissions/>

How to cite this article: Dromey, B. *et al.* Picosecond metrology of laser-driven proton bursts. *Nat. Commun.* **7**:10642 doi: 10.1038/ncomms10642 (2016).



This work is licensed under a Creative Commons Attribution 4.0 International License. The images or other third party material in this article are included in the article's Creative Commons license, unless indicated otherwise in the credit line; if the material is not included under the Creative Commons license, users will need to obtain permission from the license holder to reproduce the material. To view a copy of this license, visit <http://creativecommons.org/licenses/by/4.0/>

PAPER VII

Supersonic jets of hydrogen and helium for laser wakefield acceleration

K. Svensson, M. Hansson, F. Wojda, L. Senje, M. Burza, B. Aurand, G. Genoud, A. Persson, C.-G. Wahlström, & O. Lundh.

Physical Review Accelerators and Beams **19**, 051301 (2016).

Supersonic jets of hydrogen and helium for laser wakefield acceleration

K. Svensson,^{*} M. Hansson, F. Wojda, L. Senje, M. Burza, B. Aurand, G. Genoud,
A. Persson, C.-G. Wahlström, and O. Lundh[†]

Department of Physics, Lund University, P.O. Box 118, SE-221 00 Lund, Sweden

(Received 1 December 2015; published 2 May 2016)

The properties of laser wakefield accelerated electrons in supersonic gas flows of hydrogen and helium are investigated. At identical backing pressure, we find that electron beams emerging from helium show large variations in their spectral and spatial distributions, whereas electron beams accelerated in hydrogen plasmas show a higher degree of reproducibility. In an experimental investigation of the relation between neutral gas density and backing pressure, it is found that the resulting number density for helium is $\sim 30\%$ higher than for hydrogen at the same backing pressure. The observed differences in electron beam properties between the two gases can thus be explained by differences in plasma electron density. This interpretation is verified by repeating the laser wakefield acceleration experiment using similar plasma electron densities for the two gases, which then yielded electron beams with similar properties.

DOI: 10.1103/PhysRevAccelBeams.19.051301

The development of bright and ultrashort sources of particles and x rays is an important area of research. Such sources are of interest in many domains, including materials science, chemistry, biology, and medicine. Currently, emerging sources based on laser-plasma acceleration [1] are attracting significant attention. The accelerator can be very compact, and the particle beams have several unique characteristics. Recent achievements include the generation of electron beams with high energies (few GeV) [2], short pulse duration (few femtoseconds) [3], high peak current (few kA) [4], low energy spread ($< 1.5\%$) [5], and low emittance (few $\text{mm} \times \text{mrad}$) [6]. For most demanding applications, however, the stability of the source is also very important. A critical issue for laser wakefield accelerator (LWFA) research is to find ways to decrease shot-to-shot fluctuations.

In a typical LWFA, an intense laser pulse is focused in a neutral gas medium and atoms, or molecules, are rapidly ionized by the leading edge of the laser pulse. The main part of the pulse interacts with a plasma, and free electrons are displaced by the laser ponderomotive force which leads to a significant charge separation and a copropagating plasma wave. Strong accelerating electric fields ($\sim 100 \text{ GV/m}$) are present in the plasma wave, and copropagating electrons can be accelerated to high energies if they have sufficient initial kinetic energy and are located in an appropriate phase of the plasma wave. In the so-called bubble regime [7], the injection of electrons can be

achieved by driving the plasma wave to such a high amplitude that the wave breaks. This occurs as the velocity of the electrons exceeds the phase velocity of the plasma wave and results in self-injection of electrons from the background plasma into the accelerating phase of the plasma wave.

The threshold for wave breaking can be described as a laser power threshold [8] as well as a laser energy threshold [9] for a given plasma electron density n_e . Thus, for a given set of laser parameters, the self-injection threshold can be found by adjusting n_e . Assuming ideal gas behavior, the neutral gas number density n in a supersonic jet is proportional to the pressure p_0 supplied to the nozzle and for a fully ionized gas $n_e = N_e n$, where N_e is the number of electrons per atom, or molecule, depending on the gas species. Thus, for fully ionized gases, $n_e \propto p_0$. In this article, we present, to our knowledge, the first comparative study of electron beams emerging from supersonic jets of H_2 and He. These gases were chosen since they will be fully ionized for the present experimental conditions.

The experimental investigations were conducted using the multiterawatt laser at the Lund Laser Centre. This Ti:sapphire-based system produced 37 fs duration laser pulses with 650 mJ of energy on target during the present study. An $f/15$ parabolic mirror focused the laser pulse to a $16 \mu\text{m}$ (FWHM) spot measured in vacuum, which yielded a peak intensity of $5.7 \times 10^{18} \text{ W/cm}^2$. The beam waist was positioned, within one Rayleigh length, at the front edge of a supersonic gas flow released from a 2 mm diameter nozzle. Behind the interaction medium, along the laser propagation axis, a permanent dipole magnet dispersed the accelerated electrons according to energy. The dispersed electron beams impacted on a scintillating screen, imaged using a 16-bit digital camera. The integrated charge above

^{*}kristoffer.svensson@fysik.lth.se

[†]olle.lundh@fysik.lth.se

Published by the American Physical Society under the terms of the Creative Commons Attribution 3.0 License. Further distribution of this work must maintain attribution to the author(s) and the published article's title, journal citation, and DOI.

the spectrometer threshold energy (40 MeV) was also estimated using the measured response of the scintillator screen [10,11].

In Fig. 1, two five-image sequences of electron beams accelerated in 2 mm gas jets of H₂ and He operated at $p_0 = 9.5$ bar are presented. It is apparent that electron beams originating from H₂ [Fig. 1(a)] were, compared to those accelerated in He plasmas [Fig. 1(b)], more stable in terms of maximum electron energy, position, and spatial divergence, as well as integrated beam charge. Most electron energy spectra contained a single peak with a relatively large energy spread, corresponding to the dispersed electron beams shown in Fig. 1(a). Also, the individual images shown in Fig. 1(a) are similar to the average of the full sequence, consisting of ten images, which is shown in Fig. 1(c). However, the electron beams emerging from He [Fig. 1(b)] fluctuated significantly and suffered from filamentation, which was not the case for

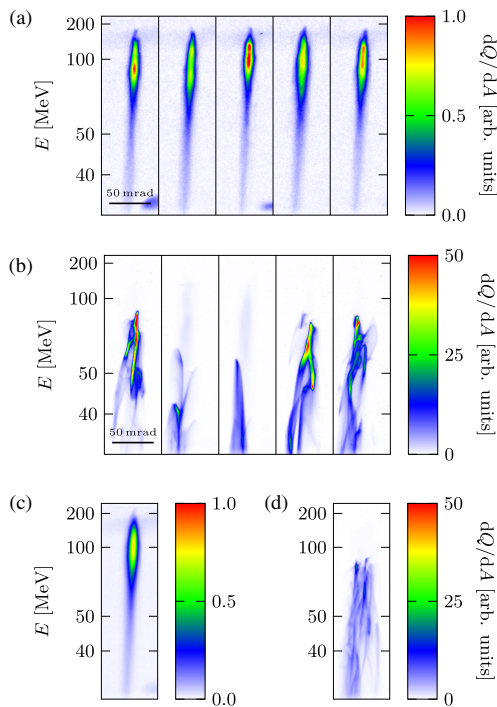


FIG. 1. False-color images of five electron beams emerging from (a) H₂ and (b) He dispersed by a permanent dipole magnet. In both cases, a 2 mm nozzle was used at a fixed backing pressure of 9.5 bar. The reproducibility of the data is shown by the average of ten individual images of electron spectra for beams emerging from (c) H₂ and (d) He. All color scales are normalized to the maximum signal in (a).

beams from H₂. Most of the energy spectra of the beams originating in He had multiple peaks, each often having very small energy spreads. It is also apparent that the sequence average [see Fig. 1(d)] is not similar to any of the individual images shown in Fig. 1(b). When comparing the two series, it can also be deduced that the integrated charge of beams accelerated in He is significantly larger than those accelerated in H₂.

The integrated beam charge was measured in a sequence of pulses while varying the pressure in the range 3–15 bar, and the results are shown in Fig. 2. As can be seen, the threshold for self-injection, which is the point where beam charge increases rapidly, is at 9 bar for He but occurs at 11 bar for H₂, indicating differences between the two media.

We have evaluated several phenomena in order to explain our observations, such as differences in the neutral gas ionization and the corresponding ionization-induced defocusing [12]. However, the intensity needed [13] for He \rightarrow He⁺ is 1.4×10^{15} W/cm², and for He⁺ \rightarrow He²⁺ is 8.8×10^{15} W/cm², which are at least 2 orders of magnitude below the peak laser intensity used in this experiment. Thus, this effect should have been noticeable only at the front of the laser pulse and in the wings. Simulations of the laser-pulse evolution performed using the code WAKE [14], which included ionization of neutral gases, did not show any significant differences in pulse characteristics when propagating through H₂ compared to He at identical n_e .

Another possible cause for the behavior in Fig. 2 could be weaker accelerating fields for H₂ than for He. Since H₂ is a molecular gas, the background of positively charged ions in the bubble behind the laser pulse might not be homogenous, as is expected for monatomic gases such as He. Assuming that the protons of the fully ionized H₂ ions

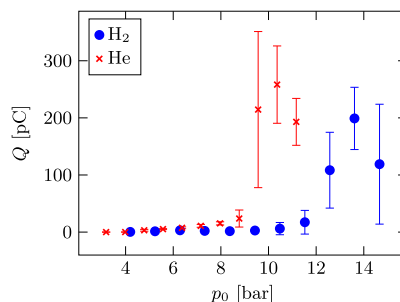


FIG. 2. Measured charge Q in the electron beams accelerated in a 2 mm gas jet over the scanned pressure range 3–15 bar in H₂ (blue circles) and He (red crosses) plotted as functions of the backing pressure. Each point represents the average of ten individual measurements with error bars indicating one standard deviation in each direction. Note that only electrons with an energy exceeding the cutoff (40 MeV) contributes to Q in this figure.

are separated by their molecular bond distance (0.074 nm), Coulomb repulsion will cause an explosion. However, in a H₂ plasma, the initial ion speed (~ 4.5 nm/fs) is too small to have a noticeable effect on the ion density in the bubble.

Finally, the differences between the gases seen in Figs. 1 and 2 can be due to fluid mechanical differences between the gases. To determine the magnitude of such an influence on the resulting n_e , a simple model of a converging-diverging nozzle was investigated. The relation between the nozzle throat sizes and flow Mach number M is [15]

$$\left(\frac{r_0}{r^*}\right)^2 = \frac{1}{M} \left[\frac{2 + (\kappa - 1)M^2}{(\kappa + 1)} \right]^{\frac{\kappa + 1}{2(\kappa - 1)}}, \quad (1)$$

where r_0 is the nozzle exit radius, r^* is the critical radius where the flow reaches sonic speeds inside the nozzle, and κ is the ratio of specific heats of the gas with numerical values 1.41 for H₂ and 1.66 for He [16]. For the specified $r^* = 0.39$ mm of the 2.0 mm diameter nozzle used in the experiments, Eq. (1) yields $M = 3.5$ and $M = 4.2$, for H₂ and He, respectively. Assuming that the gas can be described as an ideal gas, it is also possible to express the density at the nozzle exit, n_{exit} , as [17]

$$n_{\text{exit}} = \frac{p_0}{k_B T_0} \left[1 + \frac{\kappa - 1}{2} M^2 \right]^{-\frac{1}{\kappa - 1}}, \quad (2)$$

where k_B is Boltzmann's constant and $T_0 = 293$ K the temperature. As the flow exits the nozzle, it will diverge with half-angle φ given by $\varphi = \alpha + \theta$, where $\alpha = \arcsin M^{-1}$ is the Mach cone half-angle and θ the nozzle expansion angle. This means that, using cylindrical symmetry, the radius of the gas flow can be written as $r = r_0 + h \tan \varphi$, where h is the vertical distance from the nozzle exit. Assuming that φ remains constant, the gas density at a specific h close to the nozzle exit can be estimated as $n = n_{\text{exit}}(r_0/r)^2$.

As is seen from Eqs. (1) and (2), there is a nontrivial relation between n_{exit} and the gas-species-dependent κ . Therefore, characterizing the relation between p_0 and n for both gases released from the nozzle was necessary and performed experimentally. The phase shift introduced by He at $n = 5 \times 10^{18} \text{ cm}^{-3}$ over 2 mm for 633 nm light is 0.14 rad (corresponding to a 14 nm optical path length difference), which is difficult to measure with an ordinary interferometer. Therefore, n was measured as a function of p_0 with a setup consisting of an expanded HeNe-laser beam and a wave-front sensor [18], which is sensitive enough to determine the phase shift introduced by He. By assuming full ionization, n_e is then plotted as a function of p_0 for the two gases in Fig. 3, which clearly shows that they resulted in different n_e at all p_0 . Using r^* as a fitting parameter in Eq. (1) to simultaneously fit the theoretical model to experimental results obtained for both H₂ and He yielded $r^* \approx 0.35$ mm, which is close to the specified critical radius

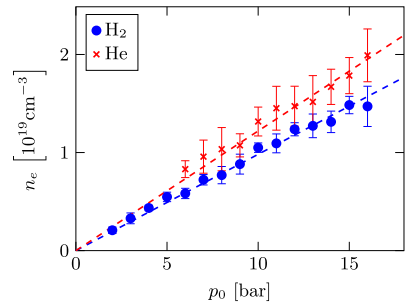


FIG. 3. The plasma electron number density n_e , 1 mm from the nozzle orifice (2 mm diameter) as a function of the applied backing pressure (p_0) for H₂ (blue circles) and He (red crosses). Assuming full ionization, the plateau electron number density n_e along the center axis in the laser propagation direction is determined from measurements of the neutral gas number density (n) using a setup consisting of an expanded HeNe beam and a wave-front sensor. Each point represents the average of 10–20 individual measurements, and the error bars indicate one standard deviation in each direction. The dashed lines are the theoretical results fitted with regards to r^* .

of the nozzle. The fitted results, shown as dashed lines in Fig. 3, are in excellent agreement with the experimental data.

From the theoretical model, it was found that $n_{\text{He}} \approx 1.3n_{\text{H}_2}$. Thus, n_e in He is $\sim 30\%$ higher than for H₂ at any specific p_0 . Compensating for this difference and plotting the data in Fig. 2 as a function of n_e instead of p_0 results in Fig. 4(a). Now it can be seen that the rapid increase in Q occurs at the same n_e for both gas species. The effect observed in Fig. 1 is therefore not significantly due to any of the previously discussed differences between the two gas species but can be explained by the relation between n_e and p_0 in Fig. 3. In Fig. 1, the electrons were accelerated in gas jets with $p_0 = 9.5$ bar which corresponds to $n_e = 9.3 \times 10^{18} \text{ cm}^{-3}$ for H₂ and $n_e = 1.2 \times 10^{19} \text{ cm}^{-3}$ for He. Using a similar n_e for He as for H₂ in Fig. 1(a) results in Fig. 4(b). Now, the accelerated electron beams emerging from He are very similar to the ones from H₂, which is also seen when comparing the averages of ten individual images in Figs. 1(c) (H₂) and 4(c) (He). Laser self-focusing inside the plasma becomes stronger with increasing n_e , resulting in a smaller spot size w_0 and a higher normalized vector potential a_0 for He than for H₂. For small w_0 and high a_0 , it is expected that self-injection LWFA results in unstable, high charge electron beams, since transversal injection dominates over longitudinal injection [19]. When longitudinal injection is the dominant injection mechanism (large w_0 and small a_0), the accelerated electron beams becomes very stable, but with low charge. Thus, the differences seen in Fig. 1 can be explained by the differences in n_e between H₂ and He at

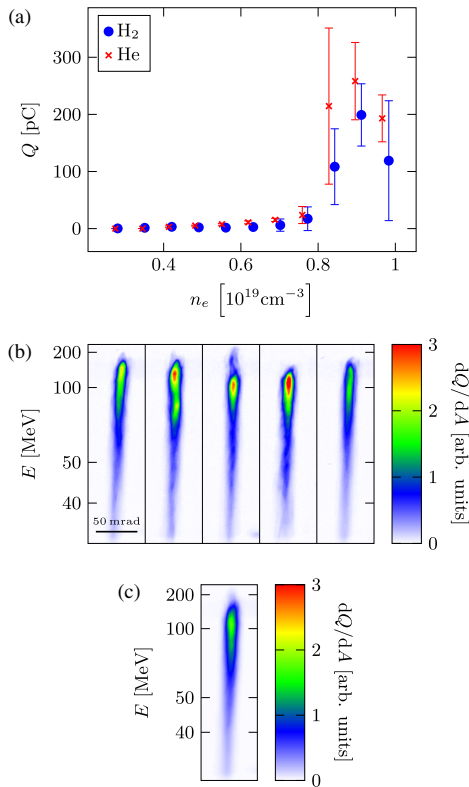


FIG. 4. (a) Measured charge Q from Fig. 2 plotted against plasma electron density n_e (assuming full ionization) instead of backing pressure p_0 , by using the results of Fig. 3. Again, only electrons with energies exceeding the cutoff energy of the spectrometer setup contribute to Q . Each point represents the average of ten individual measurements with error bars indicating one standard deviation. (b) False-color images of five electron beams emerging from He at $n_e = 9.8 \times 10^{18} \text{ cm}^{-3}$ dispersed by a permanent dipole magnet, showing a high resemblance to electron beams accelerated in H_2 at similar n_e . (c) Average of the full ten-image sequence which is partly shown in (b). The color scales are normalized to the maximum signal in Fig. 1(a).

identical p_0 , since the two series have different injection mechanisms.

In this study, we have shown that electron beams emerging from H_2 and He at identical nozzle backing pressures have different properties. This is found to be primarily a result of the supersonic gas jet number density dependence on a specific heat ratio which, generally, differs between gas species. Repeating the experiment using similar n_e for both gases confirms these findings, since the resulting beams of accelerated electrons then showed similar properties regardless of gas species. Thus, both

gases resulted in stable, low charge electron beams for $n_e < 8 \times 10^{18} \text{ cm}^{-3}$, which can be deduced from Fig. 4. It is also believed that this effect can have implications when using gas mixtures as an acceleration medium and should be studied further.

We acknowledge the support of the Swedish Research Council, the Knut and Alice Wallenberg Foundation, the Swedish Foundation for Strategic Research, Laserlab-Europe/CHARPAC (Grant Agreement No. 284464, EC's 7th Framework Programme) and EuCARD2/ANAC2 (Grant Agreement No. 312453, EC's 7th Framework Programme).

- [1] T. Tajima and J. M. Dawson, Laser Electron Accelerator, *Phys. Rev. Lett.* **43**, 267 (1979).
- [2] W. P. Leemans, A. J. Gonsalves, H. S. Mao, K. Nakamura, C. Benedetti, C. B. Schroeder, C. Toth, J. Daniels, D. E. Mittelberger, S. S. Bulanov, J. L. Vay, C. G. R. Geddes, and E. Esarey, Multi-GeV Electron Beams from Capillary-Discharge-Guided Subpetawatt Laser Pulses in the Self-Trapping Regime, *Phys. Rev. Lett.* **113**, 245002 (2014).
- [3] A. Buck, M. Nicolai, K. Schmid, C. M. S. Sears, A. Sävert, J. M. Mikhailova, F. Krausz, M. C. Kaluza, and L. Veisz, Real-time observation of laser-driven electron acceleration, *Nat. Phys.* **7**, 543 (2011).
- [4] O. Lundh, J. Lim, C. Rechatin, L. Ammoura, A. Ben-Ismaïl, X. Davoine, G. Gallot, J.-P. Goddet, E. Lefebvre, V. Malka, and J. Faure, Few femtosecond, few kiloampere electron bunch produced by a laser-plasma accelerator, *Nat. Phys.* **7**, 219 (2011).
- [5] C. Rechatin, J. Faure, A. Ben-Ismaïl, J. Lim, R. Fitour, A. Specka, H. Videau, A. Tafzi, F. Burgy, and V. Malka, Controlling the Phase-Space Volume of Injected Electrons in a Laser-Plasma Accelerator, *Phys. Rev. Lett.* **102**, 164801 (2009).
- [6] R. Weingartner, S. Raith, A. Popp, S. Chou, J. Wenz, K. Khrennikov, M. Heigoldt, A. R. Maier, N. Kajumba, M. Fuchs, B. Zeitler, F. Krausz, S. Karsch, and F. Grüner, Ultralow emittance electron beams from a laser-wakefield accelerator, *Phys. Rev. Accel. Beams* **15**, 111302 (2012).
- [7] A. Pukhov and J. Meyer-ter-Vehn, Laser wake field acceleration: The highly non-linear broken-wave regime, *Appl. Phys. B* **74**, 355 (2002).
- [8] D. H. Froula, C. E. Clayton, T. Döppner, K. A. Marsh, C. P. J. Barty, L. Divol, R. A. Fonseca, S. H. Glenzer, C. Joshi, W. Lu, S. F. Martins, P. Michel, W. B. Mori, J. P. Palastro, B. B. Pollock, A. Pak, J. E. Ralph, J. S. Ross, C. W. Siders, L. O. Silva, and T. Wang, Measurements of the Critical Power for Self-Injection of Electrons in a Laser Wakefield Accelerator, *Phys. Rev. Lett.* **103**, 215006 (2009).
- [9] S. P. D. Mangles, G. Genoud, M. S. Bloom, M. Burza, Z. Najmudin, A. Persson, K. Svensson, A. G. R. Thomas, and C.-G. Wahlström, Self-injection threshold in self-guided laser wakefield accelerators, *Phys. Rev. Accel. Beams* **15**, 011302 (2012).

- [10] Y. Glinec, J. Faure, A. Guemnie-Tafo, V. Malka, H. Monard, J. P. Larbre, V. De Waele, J. L. Marignier, and M. Mostafavi, Absolute calibration for a broad range single shot electron spectrometer, *Rev. Sci. Instrum.* **77**, 103301 (2006).
- [11] A. Buck, K. Zeil, A. Popp, K. Schmid, A. Jochmann, S. D. Kraft, B. Hidding, T. Kudyakov, C. M. S. Sears, L. Veisz, S. Karsch, J. Pawelke, R. Sauerbrey, T. Cowan, F. Krausz, and U. Schramm, Absolute charge calibration of scintillating screens for relativistic electron detection, *Rev. Sci. Instrum.* **81**, 033301 (2010).
- [12] T. Auguste, P. Monot, L.-A. Lompré, G. Mainfray, and C. Manus, Defocusing effects of a picosecond terawatt laser pulse in an underdense plasma, *Opt. Commun.* **89**, 145 (1992).
- [13] P. Gibbon, *Short Pulse Laser Interactions with Matter, An Introduction* (Imperial College Press, London, 2005).
- [14] P. Mora and J. Thomas M. Antonsen, Kinetic modeling of intense, short laser pulses propagating in tenuous plasmas, *Phys. Plasmas* **4**, 217 (1997).
- [15] S. Semushin and V. Malka, High density gas jet nozzle design for laser target production, *Rev. Sci. Instrum.* **72**, 2961 (2001).
- [16] C. Nordling and J. Österman, *Physics Handbook*, 7th ed. (Studentlitteratur, Lund, 2004).
- [17] K. Schmid and L. Veisz, Supersonic gas jets for laser-plasma experiments, *Rev. Sci. Instrum.* **83**, 053304 (2012).
- [18] G. R. Plateau, N. H. Matlis, C. G. R. Geddes, A. J. Gonsalves, S. Shiraishi, C. Lin, R. A. van Mourik, and W. P. Leemans, Wavefront-sensor-based electron density measurements for laser-plasma accelerators, *Rev. Sci. Instrum.* **81**, 033108 (2010).
- [19] S. Corde, C. Thauray, A. Lifschitz, G. Lambert, K. Ta Phuoc, X. Davoine, R. Lehe, D. Douillet, A. Rousse, and V. Malka, Observation of longitudinal and transverse self-injections in laser-plasma accelerators, *Nat. Commun.* **4**, 1501 (2013).

PAPER VIII

Dynamics of ionization-induced electron injection in the high density regime of laser wakefield acceleration

F. G. Desforges, B. S. Paradkar, M. Hansson, J. Ju, L. Senje, T. L. Audet, A. Persson, S. Dobosz-Dufrénoy, O. Lundh, G. Maynard, P. Monot, J.-L. Vay, C.-G. Wahlström, & B. Cros.

Physics of Plasmas **21**, 120703 (2014).



Dynamics of ionization-induced electron injection in the high density regime of laser wakefield acceleration

F. G. Desforges,¹ B. S. Paradkar,^{1,a)} M. Hansson,² J. Ju,¹ L. Senje,² T. L. Audet,¹ A. Persson,² S. Dobosz-Dufrénoy,³ O. Lundh,² G. Maynard,¹ P. Monot,³ J.-L. Vay,⁴ C.-G. Wahlström,² and B. Cros^{1,b)}

¹Laboratoire de Physique des Gaz et des Plasmas, CNRS-Université Paris-Sud, 91405 Orsay, France

²Department of Physics, Lund University, P. O. Box 118, S-22100 Lund, Sweden

³Laboratoire Interactions, Dynamique et Lasers, CEA Saclay, 91191 Gif-sur-Yvette, France

⁴Lawrence Berkeley National Laboratory, Berkeley, California 94720, USA

(Received 23 September 2014; accepted 23 November 2014; published online 8 December 2014)

The dynamics of ionization-induced electron injection in high density ($\sim 1.2 \times 10^{19} \text{ cm}^{-3}$) regime of laser wakefield acceleration is investigated by analyzing the betatron X-ray emission. In such high density operation, the laser normalized vector potential exceeds the injection-thresholds of both ionization-injection and self-injection due to self-focusing. In this regime, direct experimental evidence of early on-set of ionization-induced injection into the plasma wave is given by mapping the X-ray emission zone inside the plasma. Particle-In-Cell simulations show that this early on-set of ionization-induced injection, due to its lower trapping threshold, suppresses the trapping of self-injected electrons. A comparative study of the electron and X-ray properties is performed for both self-injection and ionization-induced injection. An increase of X-ray fluence by at least a factor of two is observed in the case of ionization-induced injection due to increased trapped charge compared to self-injection mechanism. © 2014 AIP Publishing LLC.

<http://dx.doi.org/10.1063/1.4903845>

One of the exciting applications of Laser Wakefield Acceleration (LWFA)¹ is the development of next generation compact X-ray sources with femtosecond pulse duration and source size of the order of few microns. For this application, LWFA is operated in the extremely non-linear regime, typically known as the bubble regime,² where electrons from the background plasma are injected and accelerated in the ion cavity formed by the near-total expulsion of electrons initially located in the path of the laser. Accelerated electrons emit X-rays while performing transverse oscillatory betatron motion due to the radial focusing force exerted by the ions.³

For the successful realization of a practical LWFA based X-ray source, it is crucial to improve the efficiency of X-ray generation (from laser to X-ray). Typically, current experiments,^{4–8} relying on self-injection mechanism, have been able to produce a maximum of $\sim 10^9$ photons with peak spectral brightness in the range of $10^{20} - 10^{22}$ photons/(s mm² mrad² 0.1%BW) using 50–100 TW laser systems. For given laser parameters, wavelength (λ_L), and power (P_L), the self-injection mechanism is controlled by varying the parameter $P_{eff} = \alpha P_L / P_c$, where α is the fraction of laser energy within full-width-at-half-maximum (FWHM) intensity of focal spot and P_c is the critical power for self-focusing. Therefore, in order to achieve a specific P_{eff} for a given laser power αP_L , the required plasma density (n_0) can be calculated as $n_0 (\text{cm}^{-3}) \simeq 1.94 P_{eff} \times 10^{19} / [\alpha P_L (\text{TW}) \lambda_L^2 (\mu\text{m}^2)]$. Recent experiments⁹ have shown that self-injection mechanism starts at $P_{eff} \simeq 2$ whereas the injected charge saturates at $P_{eff} \geq 4$ due to the beam-loading effect. For example,

for a 20 TW Gaussian laser pulse ($\alpha=0.5$) operating at $0.8 \mu\text{m}$ wavelength, self-injection is expected to start at $n_0 \simeq 6 \times 10^{18} \text{ cm}^{-3}$ whereas beam-loading should occur for $n_0 \geq 1.2 \times 10^{19} \text{ cm}^{-3}$. Since X-ray production is directly proportional to trapped charge, high density operation near beam loading limit is essential to maximize the trapped charge and X-ray fluence.

In addition to high-density operation near beam loading limit, the ionization-induced injection mechanism^{11–15} offers an attractive alternative to the self-injection mechanism for the optimization of X-ray generation. In this mechanism, inner shell electrons of high atomic number gas are preferentially trapped into the plasma wave. Although these electrons are ionized near the laser axis, they have a non-zero transverse momentum which is necessary for betatron oscillations. In addition, the number of trapped electrons can be controlled by adjusting the length of the plasma column. On this background, we examined the use of this injection mechanism for the optimization of X-ray beam properties. This offers a new perspective as previous experimental studies of the ionization-induced injection mechanism^{12–14} were so far focused on electron acceleration to produce low emittance, quasi-monoenergetic GeV energy electron bunches.

In this letter, we present a comparative study of electron and X-ray properties for both self-injection and ionization-induced injection mechanisms in the high density regime near beam-loading threshold. In this regime, for moderate laser intensity, self-focusing plays an important role to control ionization-induced injection.^{16,17} Here, self-focusing is used to initiate both ionization-induced injection and self-injection with a laser initially having an intensity below the

^{a)}Electronic mail: bsparadkar@gmail.com

^{b)}Electronic mail: brigitte.cros@u-psud.fr

injection thresholds. By analysing betatron radiation, we give the first experimental demonstration of an early onset of ionization-induced injection due its lower injection threshold compared to self-injection. This result is obtained by using a technique similar to pinhole imaging of the betatron radiation inside a long dielectric capillary tube.^{8,18,19} Previous experiments^{11–14} have demonstrated ionization-induced injection by operating below self-injection threshold. With the help of numerical simulations, we demonstrate that this early ionization-induced injection of electrons in the ion cavity suppresses self-injection. We also report a significant increase, by at least a factor of two, of X-ray fluence when ionization-induced injection is used compared to self-injection. The improvement of the X-ray yield is pre-dominantly due to an increase of trapped charge.

Experiments were performed using the Lund Laser Centre (LLC) multi-terawatt titanium-doped sapphire (Ti:Sa) laser, delivering pulses with a duration of 40 fs FWHM at a wavelength of 800 nm. The laser beam was focused to a spot with radius (w_0) at e^{-2} of the maximum intensity of 17 μm . The energy in the focal plane was measured²⁰ to be $E_L = (830 \pm 30)$ mJ, 88% of which was contained within a circle of radius equal to the waist size (w_0). The corresponding peak intensity and normalized vector potential are estimated to be $I_L = (38 \pm 02) \times 10^{18}$ W/cm² and $a_0 \approx 1.3$ –1.4, respectively. A glass capillary tube, with a length of 20 mm and an inner radius $r_{\text{cap}} = 73$ μm was used to confine and control the gas distribution.²¹ The gas was let in through two slits located at 2.5 mm from the tube exits, providing a 15 mm long plateau with constant pressure between the two slits. The gas used for studying self-injection was pure hydrogen whereas it was a mixture composed of 99% hydrogen (H_2) and 1% nitrogen (N_2) for ionization-induced injection. The gas density was calibrated off-line;²¹ the corresponding electron number density of the plateau, with and without nitrogen, is $n_0 = (12 \pm 2) \times 10^{18}$ cm⁻³, assuming a complete ionization of the atoms. Note that this density is the same as the estimated density for near beam-loading limit operation for 20 TW laser system. The electron bunch energy characterization was performed by combining a deflecting dipole magnet with a scintillating screen imaged by a 16-bit CCD camera. The lowest energy that could be measured was about 40 MeV. The charge was calculated from the image of the scintillating screen using published calibration factors.²² The X-ray emission was recorded with a 16-bit X-ray CCD camera located 1.20 meter away from the emission source. An array of thin metallic filters²³ was inserted between the source and the camera in order to allow estimation of the critical energy, assuming a synchrotron-like spectrum.⁶

The energy spectra of electron bunches accelerated in pure H_2 (blue curves) and mixture (red curves) media are given in Fig. 1(a). The mean spectra obtained from a sequence of 30 shots for the same parameters are represented by solid and dashed lines. The shaded areas illustrate the standard deviation of electron spectra from the mean curves. For these experimental parameters, electron bunches with broad energy spectra were measured, indicating a continuous injection. The resulting detected charge was estimated to be

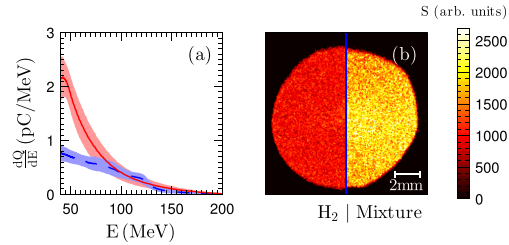


FIG. 1. (a) Mean energy spectra of electron bunches for a sequence of 30 shots performed at $n_0 = (12 \pm 2) \times 10^{18}$ cm⁻³ with pure H_2 (blue dashed line) and gas mixture (red solid line). The colored areas indicate the standard deviation from the mean spectra. (b) Typical X-ray half-beam images for H_2 (left part) and gas mixture (right part).

55 pC for pure H_2 and 100 pC for mixture whereas the average energy was found to be approximately 70 MeV for both gases. The X-ray beams generated during the acceleration process are illustrated by two typical X-ray half-beam images in Fig. 1(b) for pure H_2 (left part) and mixture (right part). It shows that the amplitude of the X-ray signal (S) is at least twice higher when the gas mixture is used, leading to a maximum peak fluence of $\sim 10^5$ ph/mrad². The fluence of betatron radiation emitted by an electron bunch oscillating within an ion plasma channel scales as³ $\Gamma_X \propto N_\beta \gamma_e^2 Q$ where Q and γ_e are the bunch charge and energy, respectively. The number of oscillations can be estimated as $N_\beta = L_\phi / \lambda_\beta \propto n_0^{-1} \gamma_e^{-1/2}$, where L_ϕ is the dephasing length of electrons and λ_β is the betatron oscillation wavelength. As γ_e and n_0 are similar for both gases, the higher fluence observed in the presence of the mixture is pre-dominantly due to an increase of the electron bunch charge.

The characterization of the X-ray beam provides a valuable insight on the electron injection and dynamics during acceleration. The critical energy is defined²⁵ as $E_c = 3\gamma_e^2 r_\beta \hbar \omega_p^2 / 2$, where r_β and ω_p are the source size and the plasma frequency, respectively. The critical energy was found to be independent of the type of gas. The average critical energy for all the shots shown in Fig. 1(a) was computed to be 5.2 ± 1.0 keV. Assuming a synchrotron-like spectrum, it was estimated from a least squares method⁷ using the transmission data of the filters and the sensitivity of the imaging system. The corresponding X-ray source size is estimated to be $r_\beta \approx 2.6 \pm 0.5$ μm , using the critical energy definition given above.

By analyzing the spatial distribution of the X-ray signal as detailed in Refs. 18 and 19, we can determine the betatron X-ray radiating zone inside the plasma. As the capillary tube plays a role similar to a pinhole for X-rays, the radial variation of the X-ray signal in the detector plane is directly transformed into the longitudinal variation (dI/dz) of the X-ray emission intensity inside the plasma, assuming emission on the capillary axis.

The azimuthal average of the X-ray signal on the detector (Fig. 2(a)) shows that the peak value of the X-ray fluence for the mixture (red solid and dotted-dashed lines) is twice that of pure H_2 (blue dashed line), as it can be seen in Fig. 1(b). The corresponding emission lengths (Fig. 2(b)) for

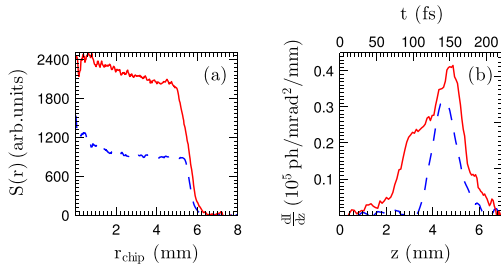


FIG. 2. Experimental profiles of X-ray beams for pure H_2 (blue dashed line) and gas mixture (red solid line) at $(11 \pm 1) \times 10^{18} \text{ cm}^{-3}$: (a) Azimuthal average of the X-ray signal on the detector, and (b) corresponding calculated longitudinal profile of emission.

mixture and pure H_2 are about 5 mm and 3 mm, respectively. Typically, a single electron injected at a position “ z ” inside the plasma will radiate over a distance of the order of the dephasing length. Beyond dephasing length, the radiated power by the electron should reduce considerably due to the reduction in energy.¹⁰ Therefore, an X-ray emission length significantly larger than the dephasing length²⁴ ($L_\phi \simeq 400 \mu\text{m}$), is indicative of multiple electron injections as the laser pulse propagates through the plasma. In addition, Fig. 2(b) shows that the typical variation of the measured emission occurs on a scale length much longer than the longitudinal bunch size of electrons, which is of the order of the plasma wavelength. Therefore, the X-ray source can be assumed to be a point source moving inside the plasma with the group velocity of the laser pulse (v_{gr}). Consequently, photons emitted at longitudinal locations separated by distance dz will reach the detector with a time difference of $dt = dz(v_{gr}^{-1} - c^{-1})$. In other words, we can compute the temporal profile of the X-ray pulse from the longitudinal spatial profile using the transformation $t = z(v_{gr}^{-1} - c^{-1})$. The corresponding time scale is shown on the top horizontal axis of Fig. 2(b). The analysis of 10 shots for each gas type shows that, on average, ionization-induced injection is triggered earlier than self-injection by around 1 mm. The FWHM of X-ray emission duration is found to be on average 47 fs for pure H_2 and 53 fs for the mixture. The corresponding peak brightness for gas mixture case is estimated to be $\sim 5 \times 10^{20}$ photons/($\text{s mm}^2 \text{ mrad}^2 0.1\% \text{ BW}$) and the number of photons $\sim 10^9$.

These experimental results are qualitatively analyzed using Particle-In-Cell (PIC) simulations in two dimensional Cartesian geometry (2DXZ) with the code WARP.²⁶ Ionization dynamics is described by a field ionization model²⁷ implemented in WARP. Different electron species for each possible ionization state are created in order to identify the electrons coming from inner shell ionization. For example, for the simulation of H_2 and N_2 gas mixture, we have a total of 8 electron species, 1 for H_2 and 7 for N_2 . The glass capillary tube (dielectric constant = 2.25) is modelled by two dielectric slabs separated by a distance equal to the inner diameter of the capillary tube. The longitudinal profile of plasma density, shown by the grey area in Fig. 3, is modelled as a linear density ramp near the capillary entrance

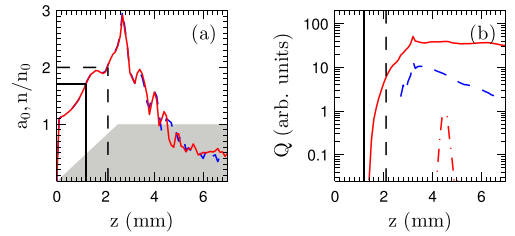


FIG. 3. Simulated normalized vector potential of the laser beam and gas profile (grey area) (a), bunch charge (b) as functions of plasma length for a pure H_2 (blue dashed line) and a 99% H_2 +1% N_2 gas (red solid and dotted-dashed lines for inner and outer shell electrons, respectively). The black dashed and solid lines indicate the theoretical thresholds of self-injection and ionization-induced injection, respectively.

followed by a plateau of density $n_0 = 11 \times 10^{18} \text{ cm}^{-3}$. Here, the density at the entrance rises from zero to n_0 in 2.5 mm. The laser pulse with $a_0 = 1.3$, waist size $w_0 = 17 \mu\text{m}$ and duration (FWHM) $\tau = 40$ fs is focused at $z = 1$ mm. The grid resolution in Z and X directions is $0.04 \mu\text{m}$ and $0.33 \mu\text{m}$, respectively, with 4 macro-particles per cell.

The simulated evolution of the laser a_0 and accelerated charge (with energy above 40 MeV) along the longitudinal direction are plotted in Fig. 3 for pure H_2 (blue dashed line) and gas mixture (red solid line). In both cases, self-focusing of the laser causes a_0 to increase above the thresholds of self-injection and ionization-induced injection (see Fig. 3(a)). Typically, for our operating conditions, the ionization-induced injection is expected¹⁵ at $a_0 \approx 1.7$ whereas the self-injection will occur for²⁴ $a_0 \geq 2$. In the case of gas mixture, all the electrons above 40 MeV energy are found to come from N_2 inner shell (N^{5+} , N^{6+}) ionization. Indeed, the amount of these electrons is two orders of magnitude higher than the quantity of accelerated electrons coming from outer shell ionization (H and N to N^{4+}), as illustrated by the comparison of the red dotted-dashed and solid lines in Fig. 3(b). These negligibly small number of outer shell electrons (shown by red dotted-dashed line) are trapped in a wakefield produced by a beam of trapped inner shell electrons. This result indicates that ionization-induced injection of N_2 inner shell electrons suppresses the self-injection of H_2 electrons. We observe that the ionization-induced injection starts ~ 1 mm before self-injection (see Fig. 3(b)) which is consistent with the experimental results. In both cases, the process of injection stops with the decrease of a_0 after 3 mm. The continuous injection of inner shell electrons over a longer distance results in the observed increase of trapped charge in ionization-induced injection compared to the self-injection process.

One important consequence of early injection due to ionization-induced injection is the suppression of self-injection of electrons coming from outer shell ionization (H and N to N^{4+}). The mechanism of such suppression is shown in Fig. 4. PIC simulations studies²⁴ have demonstrated that in the case of self-injection, trapped electrons typically enter the bubble transversely to the laser pulse propagation. This is referred as transverse injection whereas the injection of

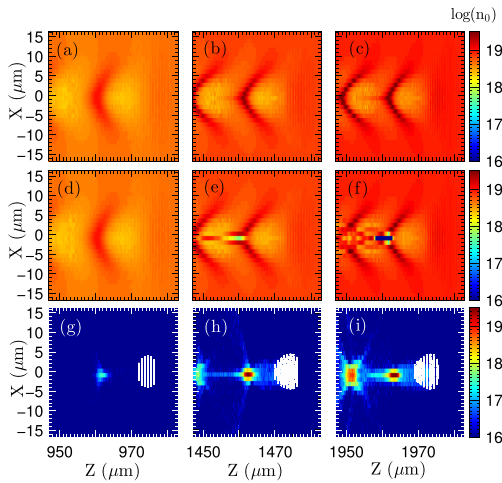


FIG. 4. Modification of wakefield structure leading to suppression of transverse injection by ionization-induced injection. For different longitudinal locations, the densities of electrons in pure Hydrogen case are plotted in (a), (b), and (c). Corresponding densities of electrons coming from outer shell ionization (H^+ and N^+) are plotted in (d), (e), and (f) while the electron densities from inner shell ionization (N^{5+} and N^{6+}) are shown in (g), (h), and (i). The laser pulse is shown by white contour lines in the bottom plots.

electrons along the axis of the laser propagation is called longitudinal injection.⁴ In Figs. 4(a)–4(c), the electron densities for the pure Hydrogen case are plotted at three different longitudinal locations whereas outer shell electron densities in the gas mixture case are shown in Figs. 4(d)–4(f). The corresponding inner shell electron densities in the gas mixture case can be seen in Figs. 4(g)–4(i). The laser pulse is shown by white contour lines in the bottom graphs. During the onset of ionization-induced injection at $Z \sim 950 \mu\text{m}$, the outer shell electron density is identical to the pure hydrogen case as can be seen from Figs. 4(a) and 4(d). The inner shell electrons (Fig. 4(g)) are injected longitudinally as they are ionized inside the bubble near $X=0$ at the peak intensity of the laser pulse. During the laser pulse propagation, the laser self-focusing (see Fig. 3(a)) makes the plasma wave increasingly non-linear as can be seen from Figs. 4(a)–4(c). However, in the case of gas mixture, due to the presence of longitudinally injected inner shell trapped electrons near the axis (Figs. 4(h) and 4(i)), the outer shell electrons coming transversely to the axis are repelled. This can be seen by comparing Figs. 4(b) and 4(c) with Figs. 4(e) and 4(f). The reduction in electron density near the axis seen in Figs. 4(c) and 4(f) is due to the expulsion of outer-shell electrons by the already injected inner-shell electrons. This modification of transverse wakefield structure eventually results in the suppression of transverse injection due to longitudinal ionization-induced injection.

In conclusion, by observing betatron X-ray radiation we have experimentally demonstrated early onset of ionization-induced injection in a LWFA regime in which both ionization-induced injection and self-injection are possible.

We found that a higher X-ray fluence ($\sim 10^5 \text{ ph/mrad}^2$) is achieved in the case of ionization-induced injection compared to the case of self-injection. The FWHM X-ray pulse duration was estimated to be approximately 53 fs. The increase in X-ray fluence is primarily due to the increased amount of trapped charge in the case of ionization-induced injection, attributed to a longer injection length due to its lower injection threshold. Finally, we observe that in the regime where both self-injection and ionization-induced injection are possible, the early on-set of ionization-induced injection suppresses the transverse self-injection process thereby leading to pre-dominantly longitudinal injection. These are key results for understanding the dynamics of ionization-induced injection, and also for the development of future X-ray sources based on betatron radiation, as it demonstrates that the efficiency of X-ray generation can be significantly increased by using ionization-induced injection instead of self-injection.

This project has benefited from financial support from the Triangle de la Physique, the Labex PALM, ARC, the Swedish Research Council, the Knut and Alice Wallenberg Foundation, the Swedish Foundation for Strategic Research, the Lund University X-ray Centre (LUXC), Laserlab-Europe/CHARPAC (Grant Agreement No. 284464, EC's 7th Framework Programme), EuCARD2/ANAC2 (Grant Agreement No. 312453, EC's 7th Framework Programme), and US-DOE (Contract No. DE-AC02-05CH11231). J. Ju acknowledges financial support from the Chinese Scholarship Council (CSC).

¹E. Esarey, C. B. Schroeder, and W. P. Leemans, *Rev. Mod. Phys.* **81**, 1229 (2009).

²A. Pukhov and J. Meyer-ter-Vehn, *Appl. Phys. B* **74**, 355 (2002).

³I. Kostyukov, S. Kiselev, and A. Pukhov, *Phys. Plasma* **10**, 4818 (2003).

⁴S. Corde, C. Thauray, A. Lifschitz, G. Lambert, K. Ta Phuoc, X. Davoine, R. Lehe, D. Douillet, A. Rousse, and V. Malka, *Nat. Commun.* **4**, 1501 (2013).

⁵A. Rousse, K. Ta Phuoc, R. Shah, A. Pukhov, E. Lefebvre, V. Malka, S. Kiselev, F. Burgy, J. Rousseau, D. Umstadter *et al.*, *Phys. Rev. Lett.* **93**, 135005 (2004).

⁶S. Fourmaux, S. Corde, K. Ta Phuoc, P. Leguay, S. Payeur, P. Lassonde, S. Gnedyuk, G. Lebrun, C. Fourment, V. Malka *et al.*, *New. J. Phys.* **13**, 033017 (2011).

⁷S. Kneip, S. R. Nagel, C. Bellei, N. Bourgeois, A. E. Dangor, A. Gopal, R. Heathcote, S. P. D. Mangles, J. F. Marques, A. Maksimchuk *et al.*, *Phys. Rev. Lett.* **100**, 105006 (2008).

⁸J. Ju, K. Svensson, H. Ferrari, A. Döpp, G. Genoud, F. Wojda, M. Burza, A. Persson, O. Lundh, C-G. Wahlström *et al.*, *Phys. Plasmas* **20**, 083106 (2013).

⁹S. P. D. Mangles, G. Genoud, M. S. Bloom, M. Burza, Z. Najmudin, A. Persson, K. Svensson, A. G. R. Thomas, and C-G. Wahlström, *Phys. Rev. ST Accel. Beams* **15**, 011302 (2012).

¹⁰S. Corde, K. Ta Phuoc, G. Lambert, R. Fitour, V. Malka, A. Rousse, A. Beck, and E. Lefebvre, *Rev. Mod. Phys.* **85**, 1 (2013).

¹¹M. Chen, Z.-M. Sheng, Y.-Y. Ma, and J. Zhang, *J. Appl. Phys.* **99**, 056109 (2006).

¹²C. McGuffey, A. G. R. Thomas, W. Schumaker, T. Matsuoka, V. Chvykov, F. J. Dellar, G. Kalintchenko, V. Yanovsky, A. Maksimchuk, K. Krushelnick *et al.*, *Phys. Rev. Lett.* **104**, 025004 (2010).

¹³C. E. Clayton, J. E. Ralph, F. Albert, R. A. Fonseca, S. H. Glenzer, C. Joshi, W. Lu, K. A. Marsh, S. F. Martins, W. B. Mori *et al.*, *Phys. Rev. Lett.* **105**, 105003 (2010).

¹⁴A. Pak, K. A. Marsh, S. F. Martins, W. Lu, W. B. Mori, and C. Joshi, *Phys. Rev. Lett.* **104**, 025003 (2010).

¹⁵M. Chen, E. Esarey, C. B. Schroeder, C. G. R. Geddes, and W. P. Leemans, *Phys. Plasmas* **19**, 033101 (2012).

- ¹⁶C. Xia, J. Liu, W. Wang, H. Lu, W. Cheng, A. Deng, W. Li, H. Zhang, X. Liang, Y. Leng *et al.*, *Phys. Plasmas* **18**, 113101 (2011).
- ¹⁷M. Zeng, M. Chen, Z.-M. Sheng, W. B. Mori, and J. Zhang, *Phys. Plasmas* **21**, 030701 (2014).
- ¹⁸G. Genoud, K. Cassou, F. Wojda, H. E. Ferrari, C. Kamperidis, M. Burza, A. Persson, J. Uhlig, S. Kneip, S. P. D. Mangles *et al.*, *Appl. Phys. B* **105**, 309 (2011).
- ¹⁹S. Corde, C. Thaury, K. T. Phuoc, A. Lifschitz, G. Lambert, J. Faure, O. Lundh, E. Benveniste, A. Ben-Ismaïl, L. Arantchuk *et al.*, *Phys. Rev. Lett.* **107**, 215004 (2011).
- ²⁰F. G. Desforges, M. Hansson, J. Ju, L. Senje, T. L. Audet, S. Dobosz-Dufrénoy, A. Persson, O. Lundh, C.-G. Wahlström, and B. Cros, *Nucl. Instrum. Methods Phys. Res., Sect. A* **740**, 54 (2013).
- ²¹J. Ju and B. Cros, *J. Appl. Phys.* **112**, 113102 (2012).
- ²²A. Buck, K. Zeil, A. Popp, K. Schmid, A. Jochmann, S. D. Kraft, B. Hidding, T. Kudyakov, C. M. S. Sears, L. Veisz *et al.*, *Rev. Sci. Instrum.* **81**, 033301 (2010).
- ²³P. Kirkpatrick, *Rev. Sci. Instrum.* **10**, 186 (1939).
- ²⁴W. Lu, M. Tzoufras, C. Joshi, F. S. Tsung, W. B. Mori, J. Vieira, R. A. Fonseca, and L. O. Silva, *Phys. Rev. ST Accel. Beams* **10**, 061301 (2007).
- ²⁵E. Esarey, B. A. Shadwick, P. Catravas, and W. P. Leemans, *Phys. Rev. E* **65**, 056505 (2002).
- ²⁶J.-L. Vay, D. P. Grote, R. H. Cohen, and A. Friedman, *Comput. Sci. Discovery* **5**, 014019 (2012).
- ²⁷G. L. Yudin and M. Y. Ivanov, *Phys. Rev. A* **64**, 013409 (2001).

PAPER IX

Enhanced stability of laser wakefield acceleration using dielectric capillary tubes

M. Hansson, L. Senje, A. Persson, O. Lundh, C.-G. Wahlström, F. G. Desforges, J. Ju, T. L. Audet, B. Cros, S. Dobosz Dufrénoy, and P. Monot.
Physical Review Special Topics Accelerators and Beams 17, 031303 (2014).

Enhanced stability of laser wakefield acceleration using dielectric capillary tubes

M. Hansson,* L. Senje, A. Persson, O. Lundh, and C.-G. Wahlström
Department of Physics, Lund University, P.O. Box 118, S-22100 Lund, Sweden

F. G. Desforges, J. Ju, T. L. Audet, and B. Cros
Laboratoire de Physique des Gaz et des Plasmas, CNRS-Université Paris-Sud 11, 91405 Orsay, France

S. Dobosz Dufrénoy, and P. Monot
Service des Photons, Atomes et Molécules, CEA Saclay, 91191 Gif-sur-Yvette, France
 (Received 25 October 2013; published 17 March 2014)

The stability of beams of laser wakefield accelerated electrons in dielectric capillary tubes is experimentally investigated. These beams are found to be more stable in charge and pointing than the corresponding beams of electrons accelerated in a gas jet. Electron beams with an average charge of 43 pC and a standard deviation of 14% are generated. The fluctuations in charge are partly correlated to fluctuations in laser pulse energy. The pointing scatter of the electron beams is measured to be as low as 0.8 mrad (rms). High laser beam pointing stability improved the stability of the electron beams.

DOI: 10.1103/PhysRevSTAB.17.031303

PACS numbers: 41.75.Jv, 52.35.-g, 52.38.-r, 52.50.Jm

Laser wakefield accelerators, first proposed in 1979 [1], appear promising as sources of highly relativistic electrons and associated X-ray radiation, in particular since experiments have demonstrated the possibility of generating high-quality quasimonochromatic pulses of electrons [2–4].

Laser wakefield accelerators benefit from the much higher electric field that can be sustained in electron plasma waves compared to conventional accelerators, and thus hold promise for size and cost reduction. The beams of laser wakefield accelerated electrons have properties that are complementary to those of conventional accelerators, and thus open doors to novel applications. These sources therefore attract worldwide interest from many different areas of science, technology, and medicine, e.g., X-ray free-electron lasers, high-energy particle physics, and oncology. However, laser-plasma accelerators are still at their early stage of development and are hampered by, in particular, limited reproducibility and stability, restricting their use in applications.

Much current research in this field is focused on increasing the maximum energy of the electrons, for example by extending the acceleration length through the use of different laser waveguiding structures [5,6], or by using multiple accelerator stages [7]. Large efforts are also made to control the injection of electrons into the

accelerating structure to increase the quality of the electron pulses and to gain better control of the mechanism.

In this paper we report on a study of the stability of beams of laser-plasma accelerated electrons using dielectric capillary tubes as laser waveguides. This type of waveguide [8] has three main advantages: (i) The plasma density inside the tubes can be arbitrarily low, as the laser beam is then guided purely by reflection from the tube walls [6]. The absence of a minimum density requirement for guiding [9] makes the capillary tube relevant for laser wakefield acceleration over long distance since the maximum achievable electron energy scales with the inverse electron density assuming the process is limited by dephasing [1]. (ii) When the laser focal spot is smaller than the matched focal spot for coupling to the capillary tube, and for laser power larger than the critical power for self-focusing, the laser energy outside the main peak of the focal spot can be reflected from the tube wall back to the laser axis, which helps to sustain relativistic self-focusing and laser guiding over a longer distance than in a gas jet or in a gas cell with similar plasma density [9,10]. (iii) the capillary tube provides a shock-free gas medium [11]. In this study electrons from the background plasma are trapped and accelerated in the so-called bubble regime of laser plasma acceleration. This mechanism is simple to achieve experimentally, and has been observed by numerous groups in gas jet, gas cell, or waveguides. Using hydrogen filled capillary tubes, we have performed a statistical analysis of the stability of the parameters of the electrons accelerated by a laser beam which pointing position is stabilized in the focal plane.

The experiments were conducted at the Lund Laser Centre, using a Ti:Sapphire based multi-terawatt laser

*martin.hansson@fysik.lth.se

Published by the American Physical Society under the terms of the Creative Commons Attribution 3.0 License. Further distribution of this work must maintain attribution to the author(s) and the published article's title, journal citation, and DOI.

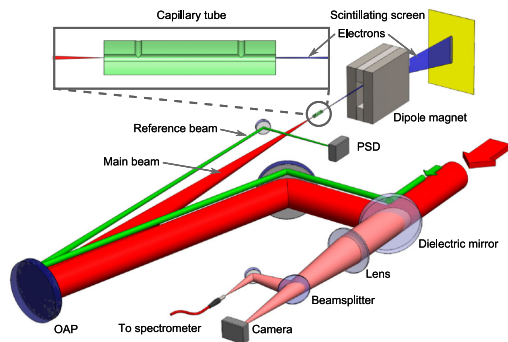


FIG. 1. Sketch of the experimental setup. The main laser pulse (red) is focused by an off-axis parabolic mirror (OAP) into a dielectric capillary tube (or a gas jet) filled with hydrogen gas. The accelerated electrons are dispersed by a dipole magnet before reaching a scintillating screen. The leakage from a dielectric mirror in the beam path is used to record spatial and spectral intensity distributions of every laser pulse. A continuous reference beam (marked in green for clarity, but in reality of the same wavelength as the main beam) is used in combination with a position sensitive detector (PSD) for feedback to a system for active pointing stabilization.

system. A sketch of the experimental setup is shown in Fig. 1. Typically, the laser was set to deliver pulses with energy of 750 mJ on target with a pulse duration of 40 fs at a center wavelength of 800 nm, giving a peak power of 18 TW. The laser beam was focused by an $f = 76$ cm off-axis parabolic mirror. Using a closed looped optimization system, consisting of a wavefront sensor and a deformable mirror in the beam path, a focal spot with a FWHM of $19 \mu\text{m}$, close to the diffraction limit (Strehl ratio ≥ 0.95), was achieved. An estimated peak intensity of $4.4 \times 10^{18} \text{ W/cm}^2$ was thus achieved in the focus of the beam, corresponding to a peak normalized vector potential of $a_0 = 1.4$.

An active system for stabilization of the transverse position of the focus [12] was used to minimize laser pointing errors. This system uses an analog position sensitive device to measure the position of the focus from a reference beam, and a large (100 mm) piezoelectric actuated mirror in the beam path to steer the beam. With this system a short-term scatter of the focal spot position with a rms distance from the average position of $\approx 4 \mu\text{rad}$ was achieved, while any long-term drift of the transverse focal position was essentially eliminated.

The laser pulses were focused one millimeter inside different glass capillary tubes, with diameters in the range 76 to $254 \mu\text{m}$ and lengths in the range 8 to 20 mm, carefully aligned to the laser beam axis [9]. The capillaries were filled with hydrogen gas from a reservoir with variable backing pressure, 35 ms before each laser pulse. The resulting molecular density of the gas inside each capillary

was deduced from interferometric studies [13] performed off-line. The gas inside the capillary tubes became fully ionized into a plasma by the leading edge of the laser pulse. Alternatively, a gas nozzle could be moved under vacuum to replace the capillary tube to create a cylindrical jet of hydrogen gas with a diameter of 3 mm at the laser focus for comparison with capillary tubes.

The accelerated electrons were observed on a scintillating screen (Kodak Lanex Regular), using a 16-bit CCD camera. This way the electron beam profile and pointing could be studied. In addition, a 120 mm long rectangular dipole magnet with a peak magnetic field of 0.7 T could be inserted into the electron beam path to disperse the electrons according to energy and thus allow the energy spectrum of the electrons to be determined. The energy axis of the spectra was absolutely calibrated by numerically tracing electrons through a map of the measured magnetic field. The physical boundaries of the dipole magnet set a lower limit on the energy of the electrons that could be observed to ≈ 40 MeV taking into account the electron beam divergence. The energy resolution of the spectrometer is decreasing with increasing energy. For the divergence of the electron beams observed in this experiment, the energy resolution is $\approx 8\%$ at 80 MeV. The total amount of charge impacting the scintillating screen was determined by integrating the images and using published calibration factors [14] for the scintillating screen.

Furthermore, the laser pulses were sampled, using the leakage through a dielectric mirror in the laser beam path, and focused using an achromatic lens (see Fig. 1). An image of this focus was acquired at each shot, which provided an absolutely calibrated measurement of the laser pulse energy on target and also an estimate of the scatter of the laser focus position and size. In addition, the spectral intensity distribution of each laser pulse was acquired using an optical spectrometer. Neglecting shot-to-shot fluctuations in spectral phase, these spectral intensity variations allow an estimate of shot-to-shot variations in pulse duration to be made through an inverse Fourier transform.

The data presented in Fig. 2 were acquired during a sequence of 130 consecutive pulses with identical settings. The delay between pulses was 30 s in order to allow the pumps to evacuate the target vacuum chamber from the gas load. Thus, these data points were acquired over 65 min. The measured pulse energy, shown in Fig. 2(a) as a function of the shot number, indicates a slight drift toward lower energy during the sequence of shots. However, the standard deviation of the laser pulse energy is only 1.9%. The estimated laser pulse duration showed similar stability, with a standard deviation of 1.9%, but without any drift. After the first 90 pulses, marked in red in the figures, the active pointing stabilization system was turned off, marked in blue in the figures. As expected, no change in stability of laser energy or pulse duration was observed when turning off the active pointing stabilization system.

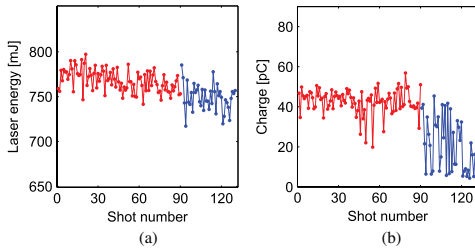


FIG. 2. Laser pulse energy delivered to the entrance of a 20 mm long, 152 μm diameter capillary tube (a) and the corresponding accelerated charge with an energy above 40 MeV (b) as a function of shot number. The active stabilization system is on during the first 90 pulses, and thereafter off. The stability of the electron bunch charge is significantly decreased by turning this system off.

During this sequence, the laser pulses were focused into a 20 mm long dielectric capillary tube with a diameter of 152 μm filled with hydrogen gas at a backing pressure of 340 mbar, resulting in a fully ionized plasma density of $1.3 \times 10^{19} \text{ cm}^{-3}$. At this plasma electron density and the given peak power, the ratio between the peak power and the critical power for relativistic self-focusing [15,16] is $P/P_c \approx 7$. Under these experimental conditions, the laser pulse is expected to self-focus soon after entering the plasma, resulting in an increased peak intensity. The laser pulse expels electrons from regions of high intensity, leading to a bubble structure following the laser pulse, in which electrons are self-injected at multiple locations along the propagation through the plasma [10,17]. The density threshold for injection of electrons into the accelerating structure was experimentally determined to be $\approx 0.85 \times 10^{19} \text{ cm}^{-3}$.

The amount of charge in the resulting electron beams, with energy above 40 MeV, is shown in Fig. 2(b) as a function of the shot number. The electron beam parameters show larger fluctuations than the laser pulse parameters. Immediately after the active pointing system is turned off, the quality and stability of the electron beams degrade significantly and after ~ 25 shots the capillary tube is damaged beyond being operational. This shows that controlling the scatter and drift of the laser focal spot is crucially important when accelerating electrons in dielectric capillary tubes using laser pulses of high intensity and energy. The active stabilization system employed in the present study enabled long sequences of data collection and an enhanced endurance of the capillaries.

The average charge for the first 90 shots in the sequence was determined to 43 pC with a standard deviation of only 14%. This small spread in charge was found to be typical also for dielectric capillary tubes of different dimension after similar optimization. For example, in another sequence the charge of electrons, with energy above 40 MeV, accelerated inside a capillary tube with a larger

diameter, 254 μm , and a shorter length, 10 mm, was measured to be higher, 107 pC, while the standard deviation was still only 18%. We did not observe any significant correlation between the amount of accelerated charge and the dimensions of the capillary tube. The difference in amount of accelerated charge between the different series of data reported here can instead be attributed to small differences in experimental parameters, such as laser energy and plasma density, that affect the amount of accelerated charge [17,18]. The experimental parameters were optimized for best stability before acquiring each series of data, which resulted in slightly different values of these parameters.

The stability in charge using the capillary tube is very good compared to the results achieved when, in the same setup and with identical laser parameters, the capillary tube is replaced with a 3 mm gas jet as a target, which showed a standard deviation in charge of 55%, with an average value of 68 pC. The charge stability of beams accelerated in capillary tubes is very good also when compared to published studies on laser wakefield acceleration in gas jets and gas cells showing stable beams [11,19,20]. The average value and stability of measured parameters of the beams of electrons accelerated in dielectric capillary tubes of different sizes, and in a gas jet, are summarized in Table I.

The energy stability of the accelerated electron beams is shown in Fig. 3. False color images of traces of the dispersed electrons on the scintillating screen, from 15 consecutive laser shots (number 25 to 39 in Fig. 2), are shown in Fig. 3(a) using the same color scale for all images. The electron energy spectra in this study show continuous energy distribution, as shown in Fig. 3(b), rather than

TABLE I. Summary of electron beam stability parameters acquired in three series using capillaries of different diameter (ϕ) and lengths (l) (A–C) in comparison with one series of data acquired using gas jet. The stabilities of the electron beams were studied using the same regime of acceleration. Before acquiring each series of data, the experimental conditions were optimized for best stability, yielding slightly different values of, e.g., backing pressure and laser intensity. The average and standard deviation of charge (Q) corresponds to electrons with an energy above 40 MeV measured with the dispersing dipole magnet in the electron beam path. The divergence (θ) and the RMS pointing stability (ϕ) was measured without the dispersing dipole in the electron beam path.

Parameter	A	B	C	Gas jet
ϕ [μm]	152	178	254	...
l [mm]	20	10	10	3
$\langle Q \rangle$ [pC]	43	88	107	68
std (Q) [%]	14	14	18	55
$\langle \theta \rangle$ [mrad]	11	10	10	14
std (θ) [%]	13	14	11	64
$\langle \phi \rangle$ [mrad]	1.2	...	0.8	4.4

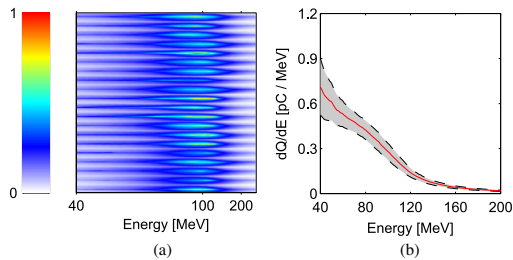


FIG. 3. False color images of the dispersed electrons on the scintillating screen from 15 consecutive shots are shown in (a), all using the same color scale. The average electron spectrum of all shots in the sequence is plotted as a solid red line in (b). The shaded area, bounded by dashed lines, shows the corresponding standard deviation from the average spectrum. Over the full energy range, the maximum standard deviation from the average spectrum is 27%.

features of peaks, indicating that the acceleration process is dominated by injection at multiple locations in space and time [10,17]. Previous studies [9] report on electron beams from dielectric capillary tubes with quasimonoenergetic energy spectra, but with lower charge, when experimental parameters were instead optimized in order to achieve self-injection in a well-localized phase-space volume and to avoid dephasing. The parameters of the present study were selected for their capability to produce, on every shot, an accelerated beam with a significant amount of charge, interesting for example for the study of X-ray generation or other applications.

The energy spectrum of the beams of accelerated electrons in dielectric capillary tubes are reproducible, as indicated by Fig. 3. The standard deviation from the average spectrum is less than 27% over the full measured energy range. This standard deviation is below 15% for energies between 65 and 80 MeV and has a minimum of 14% at 72 MeV.

The dependence of the amount of accelerated charge, with an energy above 40 MeV, on the laser pulse energy on target is shown in Fig. 4(a). This figure shows a clear dependence between the charge and laser pulse energy. This behavior is expected since higher laser energy for the same pulse parameters implies a higher probability of self-injection due to the higher amplitude of the plasma wave [18]. The data points are scattered along the solid line, which is fitted from the experimental data, and indicates that the stability in charge can be improved by a better stability in laser pulse energy. Although a certain amount of fluctuations in beam charge is clearly due to variations in laser pulse energy, these variations account only for part of the total charge fluctuations within a given series. However, the figure shows that small variations in laser energy can explain the observed difference in accelerated charge between different series.

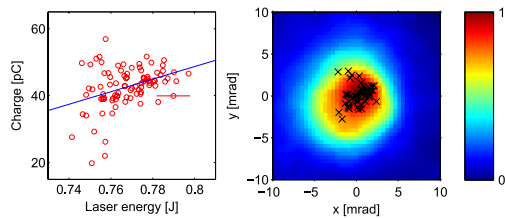


FIG. 4. In (a), the charge of the electrons in the beam, with energy above ~ 40 MeV, is plotted as a function of laser pulse energy for the first 90 shots in Fig. 2, with the active pointing stabilization system on. The estimated measurement error in laser energy of 1% is marked as a solid red line only in one data point for clarity. This figure shows a clear correlation to laser energy. In (b), a typical beam profile is shown together with a scatter map of the centroids of a sequence of 30 shots with the pointing stabilization system on.

We could not find any significant correlation between the electron beam parameters and intrinsic variations in focal spot size or width of the laser pulse spectrum. Although this might be due to insufficient accuracy of the measurement, it can also be due to the nonlinear laser pulse evolution in the plasma, such as self-phase modulation and relativistic self-focusing. Thus, fluctuations in laser pulse duration and spot size after propagation in plasma are not necessarily the same as the measured initial values.

A typical electron beam charge distribution in the transverse plane is shown in Fig. 4(b) acquired during a sequence of 30 shots using the same setup as above, but without the dispersing dipole magnet in the electron beam path. The average divergence (FWHM) for these shots was measured to 11 mrad with a standard deviation of 13%. This divergence is larger than the opening angle of the capillary tube as viewed from the entrance plane, which is 7.6 mrad. Similar divergence of the electron beam was measured on electron beams accelerated inside capillaries tubes of other dimensions as shown in Table I, which suggests that the beam is not limited by the aperture of the capillary tube. The divergence of the beams of electrons accelerated inside the capillary tubes is also similar to divergence of the beams accelerated inside a gas jet (see Table I).

The pointing scatter of the electron beams accelerated inside the capillary with diameter $152 \mu\text{m}$ and length of 10 mm is also shown in Fig. 4(b), where the center of each beam profile is marked by a cross. The rms distance from the average beam position is only 1.2 mrad for this sequence. This is significantly less than the corresponding value of 4.4 mrad measured for the beams of electrons accelerated inside a gas jet during this experiment. Small pointing scatter was observed also using capillaries of other dimensions. For example, during a sequence of 100 pulses in a capillary with a diameter of $254 \mu\text{m}$ and a length of

10 mm, the rms pointing scatter was as low as 0.8 mrad and no shot deviated more than 2.7 mrad from the average beam position.

The beams of electrons accelerated during this experiment have been shown to be very stable in charge, divergence, and pointing. The stable and uniform gas density distribution, which is also shockfree, that can be achieved in a dielectric capillary tube, or a gas cell of similar dimensions, is expected to contribute to this stability of the resulting electron beams.

In conclusion, we have shown an enhanced stability of beams of electrons accelerated in dielectric capillary tubes compared to electrons accelerated using a gas jet as target. Very good laser beam pointing stability has been shown to be necessary in order to carry out the studies reported in this paper. In the present study, such stability was achieved using an active beam pointing stabilization system. The measured beam charge variations are shown to be partly due to laser pulse energy fluctuations. The stability of the electron beam parameters appears to be similar for the different sizes of capillary tubes used in this experiment. The enhanced stability of laser wakefield acceleration using dielectric capillary tubes indicates a path toward applications of these electron beams.

We acknowledge the support of the Swedish Research Council, the Knut and Alice Wallenberg Foundation, the Swedish Foundation for Strategic Research, the Lund University X-ray Centre (LUXC), Laserlab-Europe/CHARPAC (Grant Agreement No. 284464, EC's 7th Framework Programme) and EuCARD2/ANAC2 (Grant Agreement No. 312453, EC's 7th Framework Programme). J. Ju acknowledges financial support from the Chinese Scholarship Council (CSC). This project has benefited from financial support from ARC.

- [1] T. Tajima and J. M. Dawson, *Phys. Rev. Lett.* **43**, 267 (1979).
- [2] C. G. R. Geddes, C. Toth, J. van Tilborg, E. Esarey, C. B. Schroeder, D. Bruhwiler, C. Nieter, J. Cary, and W. P. Leemans, *Nature (London)* **431**, 538 (2004).
- [3] J. Faure, Y. Glinec, A. Pukhov, S. Kiselev, S. Gordienko, E. Lefebvre, J.-P. Rousseau, F. Burgy, and V. Malka, *Nature (London)* **431**, 541 (2004).
- [4] S. P. D. Mangles, C. D. Murphy, Z. Najmudin, A. G. R. Thomas, J. L. Collier, A. E. Dangor, E. J. Divall, P. S. Foster, J. G. Gallacher, C. J. Hooker, D. A. Jaroszynski, A. J. Langley, W. B. Mori, P. A. Norreys, F. S. Tsung, R. Viskup, B. R. Walton, and K. Krushelnick, *Nature (London)* **431**, 535 (2004).
- [5] D. J. Spence, A. Butler, and S. M. Hooker, *J. Phys. B* **34**, 4103 (2001).
- [6] B. Cros, C. Courtois, G. Matthieussent, A. Di Bernardo, D. Batani, N. Andreev, and S. Kuznetsov, *Phys. Rev. E* **65**, 026405 (2002).
- [7] C. B. Schroeder, E. Esarey, C. G. R. Geddes, C. Benedetti, and W. P. Leemans, *Phys. Rev. ST Accel. Beams* **13**, 101301 (2010).
- [8] F. Wojda, K. Cassou, G. Genoud, M. Burza, Y. Glinec, O. Lundh, A. Persson, G. Vieux, E. Brunetti, R. P. Shanks, D. Jaroszynski, N. E. Andreev, C.-G. Wahlström, and B. Cros, *Phys. Rev. E* **80**, 066403 (2009).
- [9] G. Genoud, K. Cassou, F. Wojda, H. Ferrari, C. Kamperidis, M. Burza, A. Persson, J. Uhlig, S. Kneip, S. Mangles, A. Lifschitz, B. Cros, and C.-G. Wahlström, *Appl. Phys. B* **105**, 309 (2011).
- [10] H. E. Ferrari, A. F. Lifschitz, and B. Cros, *Plasma Phys. Controlled Fusion* **53**, 014005 (2011).
- [11] J. Osterhoff, A. Popp, Z. Major, B. Marx, T. P. Rowlands-Rees, M. Fuchs, M. Geissler, R. Hörlein, B. Hidding, S. Becker, E. A. Peralta, U. Schramm, F. Grüner, D. Habs, F. Krausz, S. M. Hooker, and S. Karsch, *Phys. Rev. Lett.* **101**, 085002 (2008).
- [12] G. Genoud, F. Wojda, M. Burza, A. Persson, and C.-G. Wahlström, *Rev. Sci. Instrum.* **82**, 033102 (2011).
- [13] J. Ju and B. Cros, *J. Appl. Phys.* **112**, 113102 (2012).
- [14] A. Buck, K. Zeil, A. Popp, K. Schmid, A. Jochmann, S. D. Kraft, B. Hidding, T. Kudyakov, C. M. S. Sears, L. Veisz, S. Karsch, J. Pawelke, R. Sauerbrey, T. Cowan, F. Krausz, and U. Schramm, *Rev. Sci. Instrum.* **81**, 033301 (2010).
- [15] P. Sprangle, C.-M. Tang, and E. Esarey, *IEEE Trans. Plasma Sci.* **15**, 145 (1987).
- [16] G.-Z. Sun, E. Ott, Y. C. Lee, and P. Guzdar, *Phys. Fluids* **30**, 526 (1987).
- [17] J. Ju, K. Svensson, H. Ferrari, A. Dopp, G. Genoud, F. Wojda, M. Burza, A. Persson, O. Lundh, C.-G. Wahlström, and B. Cros, *Phys. Plasmas* **20**, 083106 (2013).
- [18] S. P. D. Mangles, G. Genoud, M. S. Bloom, M. Burza, Z. Najmudin, A. Persson, K. Svensson, A. G. R. Thomas, and C.-G. Wahlström, *Phys. Rev. ST Accel. Beams* **15**, 011302 (2012).
- [19] S. Corde, C. Thauray, A. Lifschitz, G. Lambert, K. Ta Phuoc, X. Davoine, R. Lehe, D. Douillet, A. Rousse, and V. Malka, *Nat. Commun.* **4**, 1501 (2013).
- [20] S. Banerjee, S. Y. Kalmykov, N. D. Powers, G. Golovin, V. Ramanathan, N. J. Cunningham, K. J. Brown, S. Chen, I. Ghebregziabher, B. A. Shadwick, D. P. Umstadter, B. M. Cowan, D. L. Bruhwiler, A. Beck, and E. Lefebvre, *Phys. Rev. ST Accel. Beams* **16**, 031302 (2013).